Université de Montréal

Studying Biological Assembly of Ion Channel Complexes

Par

Lena Moeller

Département de Biochimie

Faculté de Médecine

Thèse présentée en vue de l'obtention du grade de *Philosophiae Doctor* (PhD)
en biochimie
option Cellular Dynamics of Molecular Complexes

Août, 2020

Université de Montréal

Faculté de Médecine

Cette thèse intitulée

Studying Biological Assembly of Ion Channel Complexes

Présenté par

Lena Moeller

A été évaluée par un jury composé des personnes suivantes

Michel Bouvier
Président-rapporteur

Rikard Blunck
Directeur de recherche

Jurgen Sygusch
Codirecteur

Rafael Najmanovich
Membre du jury

Gerhard Thiel
Examinateur externe

Julie Hussin
Représentant de la doyenne

Resumé

Les canaux ioniques sont des complexes macromoléculaires clés exprimés dans tous les types de cellules et sont impliqués dans divers processus physiologiques, y compris la génération et la propagation de potentiels d'action. Des canaux défectueux conduisent à des maladies graves, notamment l'épilepsie, des arythmies et des syndromes douloureux, ce qui en fait une cible potentielle intéressante pour le développement de médicaments. Pour améliorer notre compréhension de ces assemblages biologiques et éventuellement trouver des traitements spécifiques pour les canalopathies, il est crucial d'étudier la structure et la fonction des canaux ioniques. L'objectif principal de cette thèse a été d'étudier ce type de détails structurels et fonctionnels pour trois canaux ioniques associés aux domaines des capteurs de douleur et des canaux potassiques voltage-dépendants en utilisant des techniques de fluorescence et d'électrophysiologie.

Dans le premier projet, nous avons étudié la stœchiométrie des canaux hétéromères Kv2.1 / 6.4 (chapitre trois). La technique du décompte de sous-unités isolées (*single subunit counting* :ssc) permet de compter les sous-unités marquées par fluorescence d'un complexe isolé en déterminant le nombre d'événements de photoblanchiment, qui apparaissent en sauts irréversibles vers le bas sur les traces de fluorescence. Pour désigner la stœchiométrie la plus probable, nous avons utilisé des calculs de probabilités pondérées et avons constaté que les canaux Kv2.1 / 6.4 s'expriment dans un arrangement 2 : 2. Plus précisément, les études fonctionnelles des canaux concatémériques montrent que les sous-unités Kv6.4 et 2.1 doivent être disposées de manière alternée.

Le deuxième projet était également basé sur des expériences de SSC et visait à déterminer l'état oligomérique du nouveau canal ionique TACAN (chapitre quatre). Nous avons trouvé une portion significative de canaux intracellulaires, ce qui a provoqué une fluorescence de fond dans les expériences de SSC traditionnelles réalisées avec les cellules mammifères. Pour améliorer le rapport du signal sur bruit de fond, nous avons effectué des expériences de SSC sur des canaux purifiés qui ont été immobilisés sur des lamelles de verre fonctionnalisées Ni-NTA. En utilisant la méthode de calcul décrite dans le premier projet, nous avons trouvé différents états

oligomériques et proposons que les canaux TACAN natifs s'assemblent en tétramères qui sont instables lorsqu'ils sont solubilisés dans un détergent.

Dans le dernier projet, nous avons étudié la relation structure-fonction de la sous-unité auxiliaire DPP6 pour les canaux Kv4.2 (chapitre cinq). Ici, nous avons progressivement tronqué le grand domaine extracellulaire de 700 acides aminés de DPP6 et étudié son effet sur les courants macroscopiques en utilisant la technique du *cut-open voltage clamp*. Nous avons constaté que les sous-unités DPP6 avec un domaine extracellulaire court ne parviennent pas à moduler les propriétés du canal aussi efficacement que la DPP6 pleine longueur. Plus précisément, la seconde moitié du domaine extracellulaire *β-propeller* de DPP6 est responsable d'une inactivation du canal considérablement accélérée. Sur la base de la structure cristalline du domaine extracellulaire, nous avons proposé qu'un domaine *β-propeller* stable et possiblement la formation de dimères DPP6 sont responsables de la déstabilisation efficace de l'état du canal ouvert.

Mots-clés : canaux ioniques, Kv2.1 / Kv6.4, TACAN, Kv4.2, DPP6, *single subunit counting*, *cut-open oocyte voltage clamp*, fluorométrie en voltage imposé.

Abstract

Ion channels are key macromolecular complexes expressed in all cell types and are involved in various physiological processes including the generation and propagation of action potentials. Defective channels lead to severe diseases including epilepsy, arrhythmias and pain syndromes making them an interesting potential drug target. To improve our understanding of these biological assemblies and eventually find specific treatments for channelopathies, it is crucial to study the structure and function of ion channels. The main purpose of this thesis has been to investigate such structural and functional details of three ion channel complexes from the field of pain sensors and voltage-gated potassium channels using fluorescence and electrophysiological techniques.

In the first project, we studied the stoichiometry of heteromeric Kv2.1/6.4 channel complexes (chapter three). Single subunit counting (SSC) allows to directly count the number of fluorescently labeled subunits by determining the number of irreversible, step-wise photobleaching events. To determine the most probable stoichiometry, we used weighted likelihood calculations and found that Kv2.1/6.4 channels express in a 2:2 arrangement. More precisely, functional studies of concatemeric channels (performed by our collaborators) illustrate that Kv6.4 and 2.1 subunits need to be arranged in an alternating fashion.

The second project was also based on SSC experiments and aimed at determining the oligomeric state of the novel ion channel TACAN (chapter four). We found a significant amount of channels in the intracellular which caused background fluorescence in traditional SSC experiments performed in cells. To improve the signal to background ratio, we performed SSC experiments on purified channels that were immobilized on Ni-NTA functionalized glass coverslips. Using the model selection method described in the first project, we found different oligomeric states and propose that native TACAN channels assemble as tetramers which are unstable when solubilized in detergent.

In the last project, we investigated the structure-function relation of the auxiliary DPP6 subunit in Kv4.2 channel complexes (chapter five). Here, we progressively truncated DPP6's 700

amino acids long extracellular domain and studied its effect on macroscopic currents using the cut-open voltage clamp technique. We found that DPP6 subunits with a short extracellular domain fail to modulate the channel properties as efficiently as the full length DPP6. More precisely, the second half of the extracellular β-propeller domain of DPP6 is responsible for drastically accelerated channel inactivation. Based on the crystal structure of the extracellular domain, we proposed that a stable β-propeller domain and possibly DPP6 dimer formation is responsible for destabilizing the open channel state efficiently.

Keywords : ion channels, Kv2.1/Kv6.4, TACAN, Kv4.2, DPP6, single subunit counting, cut-open oocyte voltage clamp, voltage-clamp fluorometry.

Table of contents

List of tables

List of figures

List of abbreviations

aa – amino acid

AB-NTA – aminobutyl-nitrilotriacetic acid

ANOVA – Analysis of variance

arb. u. – arbitrary units

Cav – voltage-gated calcium channel

CHO – Chinese hamster ovary

COVC – cut open oocyte voltage clamp

CSI – closed state inactivation

CTI – C-type inactivation

DDM – n-Dodecyl β-D-maltoside

dF – change in fluorescence

DMEM – Dulbecco's modified eagle medium

DNA – Deoxyribonucleic acid

DPP – dipeptidyl peptidase

DRG – dorsal root ganglia

EDTA – ethylenediaminetetraacetic acid

eGFP – enhanced GFP

EM – extracellular matrix

EMCCD – electron-multiplying charge-coupled device

ER – endoplasmic reticulum

F – fluorescence

FBS – fetal bovine serum

FC14 – Fos-Choline-14

Fig – figure

FP – fluorescent protein

GFP – green fluorescent protein

GluCl – glutamate-gated chloride channel

GluK2 – ionotropic glutamate receptor kainite type subunit 2

GPCR – G-protein coupled receptor

GPTMS – (3-Glycidyloxypropyl)-trimethoxysilane

HEK – human embryonic kidney

HEPES – (4-(2-hydroxyethyl)-1-piperazineethanesulfonic acid

His – histidine

HL – hemolysin

I – current

IMAC – Immobilized metal affinity chromatography

K_{2P} – two P domain potassium

KChIP – Kv channel-interacting protein

kDA – kilodalton

kHz – kilohertz

Kv – voltage-gated potassium channel

KvS – electrically silent Kv subunit

min – minute

mg – miligram

mL – milliliter

mm – milimeter

mM – millimolar

ms – millisecond

MscL – large conductance mechanosensitive channel

MscS – small conductance mechanosensitive channel

mV – millivolt

mW – milliwatt

NA – numerical aperture

Nav – voltage-gated sodium channel

Ni – nickel

nm – nanometer

NTA – nitrilotriacetic acid

NTI – N-type inactivation

OD_{600} – optical density measured at 600 nm

OSI – open state inactivation

pA – picoampere

PBS – phosphate buffered saline

p_{col} – probability of colocalization

pF – picofarad

p_f – probability of fluorescence

PM – plasma membrane

RE – restriction enzyme

RNA – Ribonucleic acid

SBR – signal-to-background ratio

SEC – size exclusion chromatography

SEM – standard error of the mean

sfmGFP – super-folder monomeric GFP

SSC – single subunit counting

T1 domain – tetramerization domain 1

T – temperature

TEA – tetraethylammonium

TMR – tetramethylrhodamine

TRP - transient receptor potential

VCF – voltage clamp fluorometry

VSD – voltage sensing domain

WT – wild-type

Å – angstrom

λ – wavelength

τ – time constant tau

You must never think of the whole street at once, understand?
You must only concentrate on the next step,
the next breath, the next stroke of the broom,
and the next, and the next.
Nothing else.

That way you enjoy your work,
which is important,
because then you make a good job of it.
And that's how it ought to be.

And all at once,
before you know it,
you find you've swept the whole street clean,
bit by bit.
What's more, you aren't out of breath.
That's important, too.

— Michael Ende, Momo

Acknowledgements

No other decision had such a huge impact on my life as coming to Montreal and starting a Master's program under the supervision of Rikard. So, first and foremost, I would like to thank you, Rikard, for giving me the opportunity to stay on and conduct my PhD in your lab and freely explore what it means to be a researcher. Thank you for giving me many different projects. Even though not all of them made it into this thesis, I am grateful to have had the chance to familiarize myself with a variety of techniques. Your continuous support and advise were of invaluable importance to successfully bring this chapter of my life to a close. I would also like to acknowledge my co-supervisor Jurgen Sygusch. Thank you for all the advice and helpful comments. Additionally, I want to thank the jury for having accepted to evaluate this thesis.

I owe much gratitude to past and present lab members, neighbors and collaborators. You made the many hours spent in the "dark room" so much more enjoyable. Thank you for all your help.

Thank you to my friends and family, whom I wish I could have spent more time with in the last years. Thanks for all your encouragement, support and love!

Chapter 1 – Introduction

The brain is the most complex organ of the vertebrate's body and therefore probably the most challenging to understand. 86 billion neurons with trillions of connections form the vast network of cells in the central nervous system that governs our body (1). While imaging and electrophysiological techniques uncovered the anatomical details and many of the molecular key players, the intricacies of countless processes remain unknown, ranging from broad questions such as, how does the brain work and what makes up our consciousness, to specific ones, such as which molecular structures are involved and how they influence each other. Naturally, these unsolved puzzles attract attention in many diverse scientific fields and studying the brain and nervous system has developed into an interdisciplinary research pursuit.

The electrical signals in the nervous system are generated primarily by ion channels. Ion channels are estimated to make up more than 1 % of the human protein-coding genes (2-4), which can be grouped into four major groups according to their gating mechanism: mechanically-gated, voltage-gated, ligand-gated, and constitutively open (figure 1.1). All ion channels are membrane proteins that have an ion conducting pore spanning from one side of the membrane to the other. Through this pore, ions flow selectively or non-selectively along the electrochemical gradient depending on the structural details of the pore. Each ion channel group can be subdivided into families of channels that have distinct structural and electrophysiological properties. Heteromerization of channel subunits and variable recruitment of auxiliary subunits further diversify the ion channel landscape. As such, the process of assembly of the ion channel complexes have come into the focus of biophysical and -chemical research. In this thesis, I will present my work on the structural details of the assembly of different ion channel complexes.

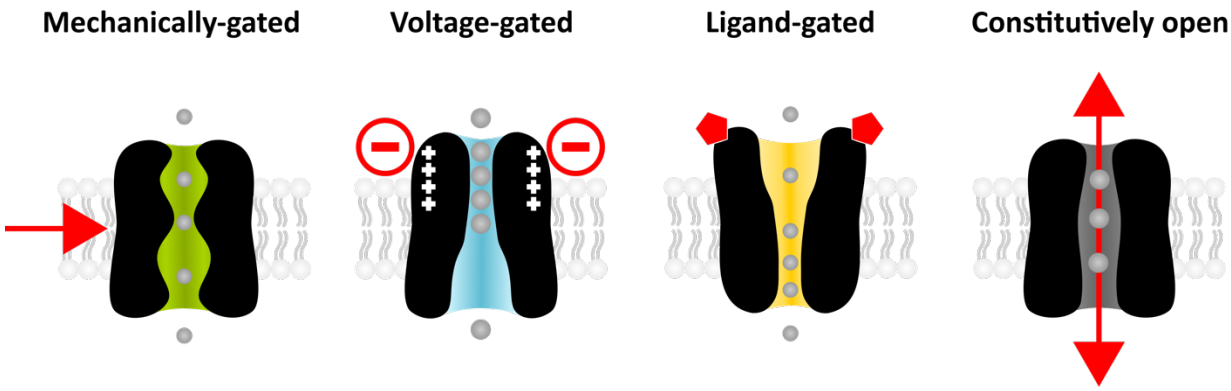

Figure 1.1 Ion channel groups
Cartoon representation of mechanically-gated, voltage-gated, ligand-gated and constitutively open ion channels. Channels are differentiated by their structure and mode of activation, highlighted in red: pressure, change in the membrane potential, binding of ligands.

Missing or insufficient structural data form a key obstacle researchers need to overcome to better interpret channel function and rationally design new therapeutics. Ion channels are a vital component of the nervous system and disturbed channel function can result in severe neurological diseases (5-7) making them an interesting potential drug target. However, some of these ion channels are ubiquitously expressed rendering the development of new treatments that do not cause severe side effects extremely difficult. This is why fundamental research that aims at elucidating structural details is not only integral for the advancement of knowledge in the respective field but also for the development of new treatments. Therefore, it is worthwhile to study the structure-function relation of channels with their tissue-specific modulatory subunits (chapter five), the stoichiometry of heteromeric channel complexes (chapter three) and particularly the structural basis of novel proteins (chapter four). This thesis presents the structural investigation of three different ion channel complexes from the field of pain sensors and voltage gated potassium channels. I will provide the background to each after introducing biological assemblies of ion channels.

1.1 Biological Assemblies of Ion Channels

Determining the number of subunits within an ion channel complex is key for understanding structure-function relationship, especially for novel proteins that could serve as attractive drug targets. On the most basic level, homomeric channel structures dictate the intrinsic mechanisms before modulatory subunits alter the channel structure and function. Generally, distinct ion channels are assembled by up to eight subunits (figure 1.2). Mechanosensitive Piezo channels and ATP-gated P2X receptors ion channel family members form trimeric structures (8-10). Many ion channel families, including the large superfamily of voltage-gated ion channel members, but also the transient receptor potential (TRP) channel family (11) and ionotropic glutamate receptors (12, 13) feature four subunits. Pentameric arrangements have been demonstrated for the ligand-gated cys-loop receptor ion channel family (14, 15), while gap junction proteins (connexin) and the volume-regulated SWELL1 channel are composed of six subunits (16, 17). Channel arrangements with up to eight subunits are also possible and have been reported for other gap junction components and pore forming toxins like Anthrax and hemolysins (18-25).

More specifically, channels can be either formed by separate subunits or form pseudo-multimers. For example, the voltage-gated potassium (Kv) channels are tetramers, comprising four separate subunits that form a single central ion conducting pore (26-29). We can call these “true” tetramers in comparison to the voltage-gated sodium (Nav) and calcium (Cav) channels that form pseudo-tetrameric structures from a single polypeptide chain but containing four analogous repeats (30-32). Two pore domain potassium (K_{2P}) channels like the mechanosensitive TRAAK also form pseudo-tetrameric channels but contain two individual polypeptide chains (33, 34).

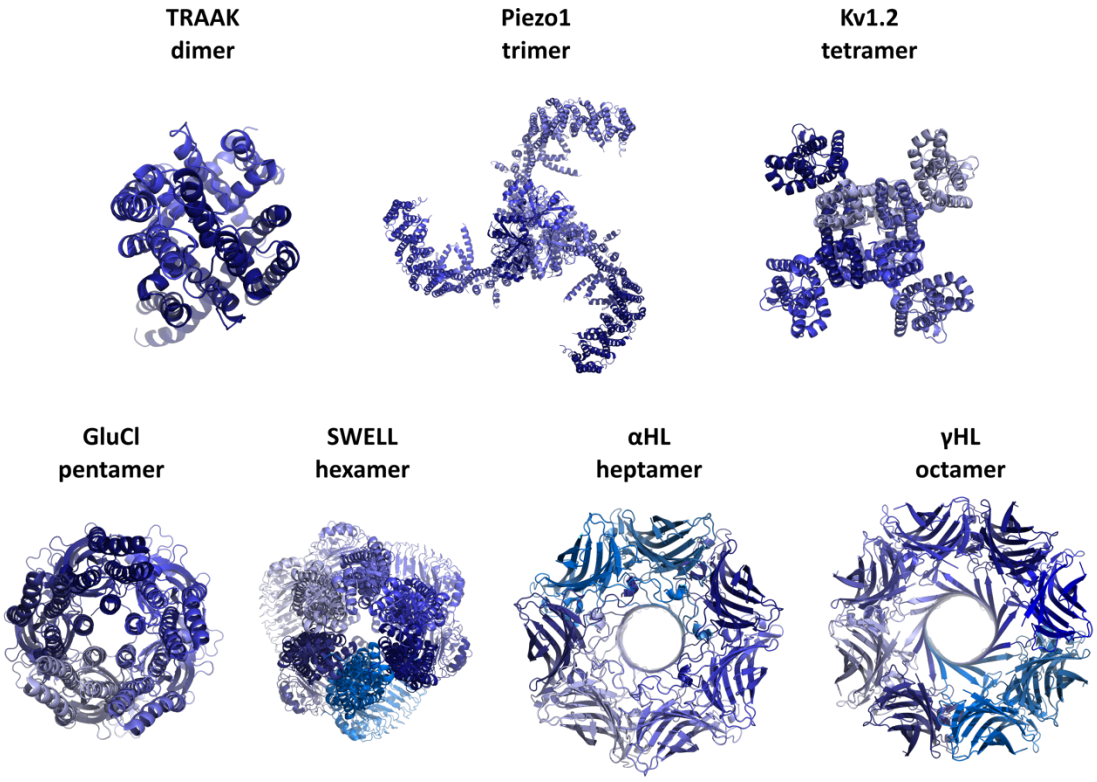

Figure 1.2 Examples of homomers with distinct subunit arrangements
High resolution crystal or EM-structures, individual subunits are coloured in shades of blue. Structures were obtained from following pdb files 3UM7 (TRAAK (33)), 5Z10 (Piezo1 (35)), 2R9R (Kv1.2 (27)), 4TNV (glutamate-gated chloride channel (GluCl) (36)), 6DJB (SWELL1 (16)), 7AHL (αHL (α-Hemolysin) (19)), 3B07 (γHL (γ-Hemolysin) (37)).

The structure and function of ion channels in the body are diversified by heteromerization. This enables cells to produce channels with modified properties by breaking the channel's symmetry and regulating channel function by changing the subunit's stoichiometric arrangement (38). Such a diversification has been demonstrated for many ion channels including K_{2P} channels, voltage-gated potassium channels, the ligand-gated cys-loop receptor ion channel family and connexins (38-43).

Additionally to heteromerization, channel functions are further finetuned by coassembly with auxiliary (β-) subunits. These β-subunits are diverse and can be localized in the plasma membrane or soluble in the cytoplasm. Their functions range from aiding trafficking and stabilizing channels in the membrane (44-46) to modulating channel gating (47-49). The underlying mechanisms of these modulating effects on channel gating often remain unclear. However, since ion channels cycle between ion permeable and non-permeable conformations and the relative stability of each state impacts the channel's function, allosteric interactions with auxiliary subunits might bias the equilibrium by

stabilizing or destabilizing the different channel states (50, 51). Such allosteric interactions are of course not limited to auxiliary subunits but play a vital role within the channels themselves. Especially gated ion channels feature spatially distinct domains that are either covalently linked or interact through non-covalent interactions. Conformational changes in one domain can then allosterically modulate the conformation of another domain over a long range (13, 52-55). This makes gating mechanisms complex and difficult to fully decipher.

1.2 Pain

One of the major research questions has always been how we interact with our surroundings. The transmission and reaction to external information is essential to our survival but also crucial for social interactions. Our five basic senses keep us informed about our immediate environment and the research of the last decades has provided some insights into how our basic senses function. However, many fundamental questions remain unanswered.

The molecular determinants for sight, smell and taste were identified first and their workings have since been intensively studied (56-62). In all three of these senses, the external stimulus — a photon, odorous or taste molecule — activates specific photo- and chemoreceptors, respectively (63-65). These receptors belong to the G-protein coupled receptor (GPCR) family, the largest class of cell surface proteins. Receptor activation results in the cascade of signal transduction (66), which in sensory cells, ultimately triggers action potentials in nerve fibers that relay information to the brain (67). But not all senses rely on this mechanism. Indeed, the sensation of salty and sour tastes relies on ion channels (68-71). Furthermore, GPCR activation and signal transduction via secondary messengers are too slow to explain the temporal resolution necessary for the two remaining basic senses, touch and hearing. Early on, researchers proposed that in this case, ion channels must be involved (figure 1.3) (72-74).

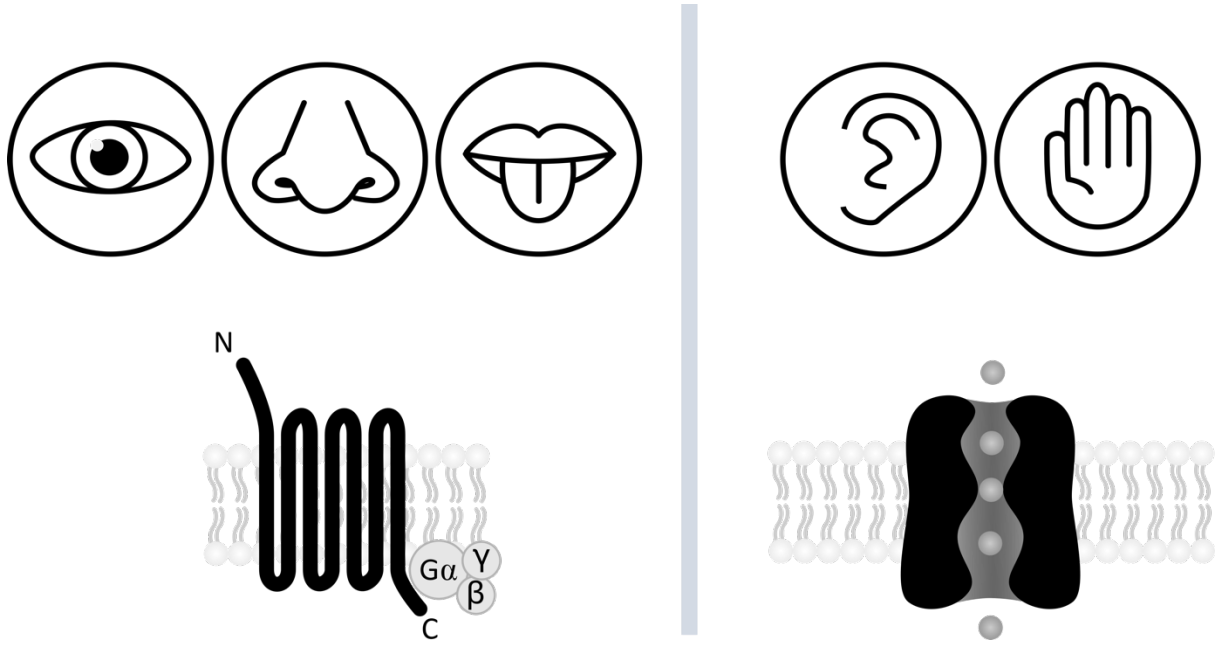

Figure 1.3 Molecular determinants of the five basic senses
Sight, smell and taste (with the exception for salty and sour taste) receptors are GPCRs (left). Touch and sound transduction is mediated by ion channels (right).

Despite the early discovery of sensory cells in the skin, the identity of mechanosensitive ion channels responsible for the sensation of touch remained elusive for a long time (75). In the meantime, researchers focused on identifying neuronal pathways from the periphery to the central nervous system. Generally, three neurons are involved in the transmission of sensory stimuli to the brain. The cell bodies of primary afferent neurons are located in the Dorsal Root Ganglia (DRG). Their axons innervate the skin and project to the dorsal horn of the spinal cord. Here, axons take different routes to the brain. The fast-conducting, heavily myelinated Aβ nerve fibers of primary neurons involved in fine touch take the phylogenetically new route from the spinal cord to the brain (76). They immediately turn upwards in the dorsal horn to the brainstem, where they synapse with secondary neurons that decussate and relay information to the thalamus. A third neuron continues to the somatosensory cortex. On the other hand, neurons involved in mechanically induced pain sensing, also called nociceptors, do not ascend immediately, but synapse in the dorsal horn with second order neurons that decussate to the contralateral site of the spinal cord and ascend through the phylogenetically older (anterolateral spinothalamic) tract from the spine to the thalamus. Again, a third neuron relays the sensory information from the brainstem and thalamus to the limbic system and the somatosensory cortex, respectively (figure 1.4) (77-79). Nociceptive fibers are divided into thinly myelinated Aδ- and

unmyelinated C-fibers, which conduct pain-induced impulses at medium and slow speed, respectively. This duality results in the perception of a first, well localized sharp and a second, dull and lasting pain sensation (80-84). Inhibitory neurons and nerve damage can further modify the propagation of impulses.

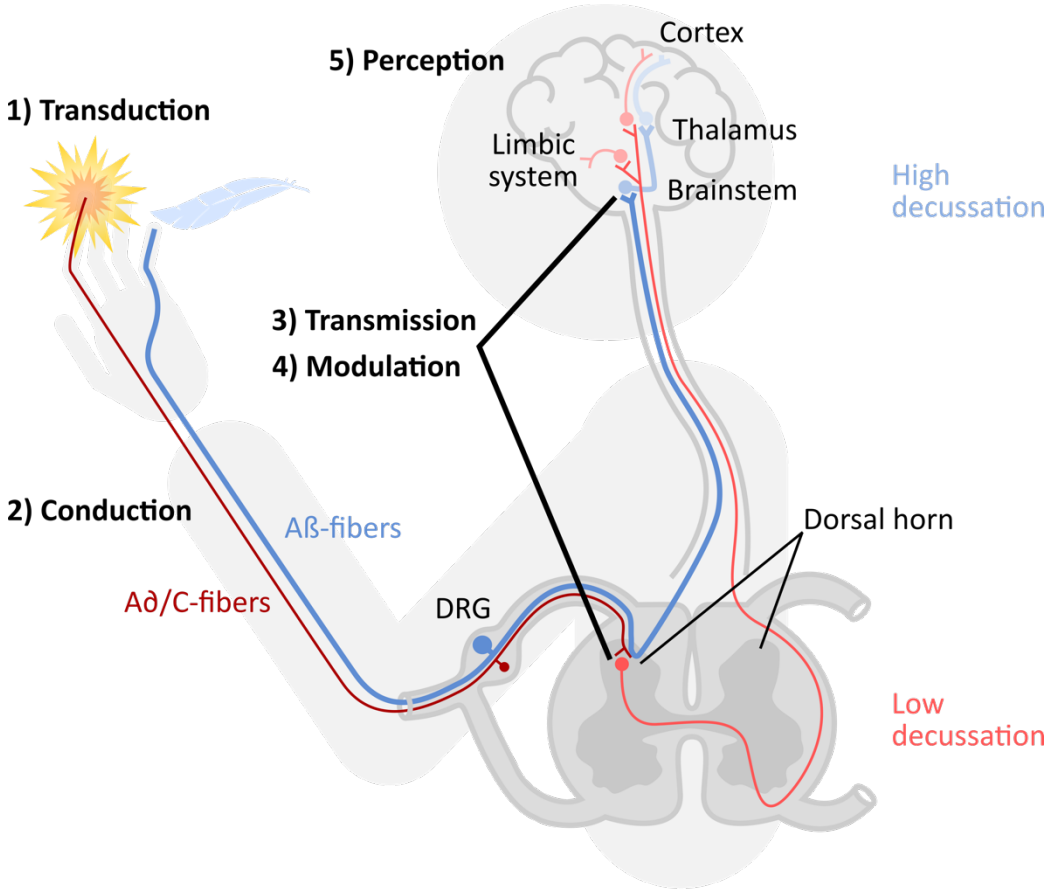

Figure 1.4 Schematic diagram of ascending somatosensory pathway
Non-noxious and noxious stimuli are transduced by specific molecules that activate different pathways, blue and red respectively. Three neurons are involved in the ascending pathways, coloured dark to light. Cell bodies of first order neurons are located in the dorsal root ganglia (DRG). Impulses of light touch are conducted along thick Aβ-fibers (blue), which enter the dorsal horn and directly turn upwards in the spinal cord. In the brainstem, they synapse with the second order neuron, which decussates to the contralateral side (high decussation) and synapses with the third order neuron on the thalamus. Impulses of painful stimuli are conducted along thinner Aδ and C-fibers (red), which synapse with second order neurons in the dorsal horn. The second order neuron decussates to the contralateral side of the dorsal horn (low decussation) and ascend to the brainstem and thalamus. Third order neurons terminate in the structures of the limbic system and somatosensory cortex. Interneurons (not shown) can modulate the transmission of impulses between neurons.

The search of molecular determinants responsible for the transduction of touch stimuli, led to the discovery of several potential mechanotransducers (85, 86) However, until recently, little was known

about the identity of the molecular determinants of touch and noxious touch transduction in humans. In 2010 the Patapoutian laboratory discovered the mechanically activated ion channels Piezo1 and Piezo2 (87). These channels are structurally distinct from other mechano-sensitive ion channels and form gigantic propeller-shaped trimers with a cation-conductive pore at the center. Each subunit consists of at least 26 transmembrane helices (8, 35, 88, 89) (figure 1.5). Functionally, Piezo2 has been identified as the key player for the transduction of non-noxious mechanical forces in the skin. However, Piezo2 is not involved in the transduction of painful mechanical forces (90). Piezo1 is also no candidate for such a pain-sensor, but is expressed in endothelial cells and required for vascular development (91).

Efforts to identify the elusive molecular determinant for mechanically induced pain transduction led most recently to the discovery of a new mechano-sensitive ion channel called TACAN (92). This channel is expressed in a subgroup of nociceptors and a knockout of this channel reduces the response to noxious touch but not to gentle touch (92). Intensive investigation of TACAN's functions validate its candidacy as mechanical pain transducer. Electrophysiological studies demonstrate the presence of a cation-conducting pore and opening of the channel results in the depolarization of somatosensory neuron, triggering action potential propagation along the nerve fibers to the brain (92). TACAN subunits are proposed to feature six transmembrane helices but no detailed structural information is yet available (figure 1.5). In chapter four, I will present research aimed at determining the number of subunits of this important new ion channel.

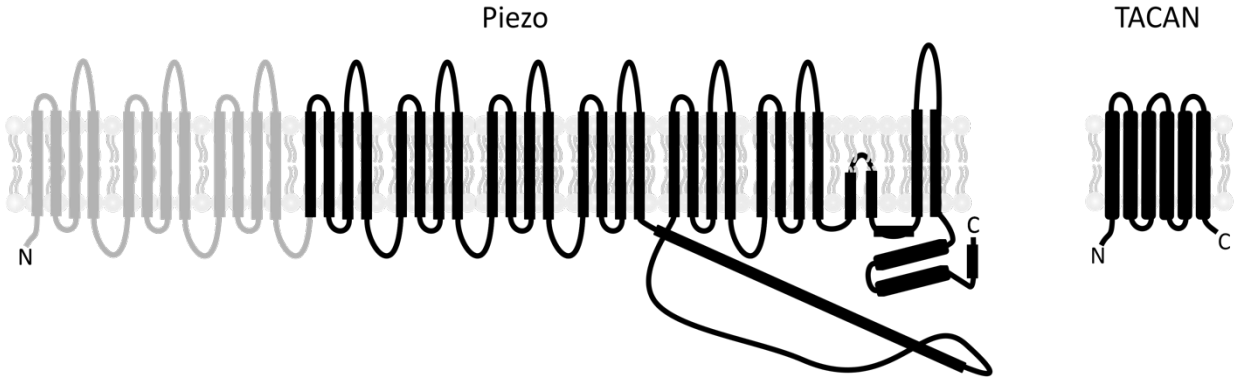

Figure 1.5 Structures of different mechano-sensitive channels
Cartoon representation of single subunits. Amino- and C-termini are marked by N and C, respectively. Piezo features at least 26 transmembrane helices (TMs) (black) arranged into six transmembrane helical units of four TMs plus two pore forming helices at the C-terminus, three more transmembrane helical units (grey) were unresolved in Piezo1 (35), but resolved for Piezo2 (89). TACAN is predicted to comprise six TMs.

1.3 Voltage-gated Potassium Channels

The other class of ion channels whose assembly properties I have studied belong to the family of voltage-gated potassium (Kv) channels. Typical Kv channels have four subunits, each consisting of six transmembrane helices and a pore loop. The first four helices (S1-S4) of each subunit make up the peripheral voltage sensing domains, featuring a positively charged S4 helix that moves following the electric field. The transmembrane helices S5, S6 and a so-called "pore loop" between S5 and S6 of all four subunits form a single ion conducting pathway in the center of the ion channel (figure 1.6) (26, 93). The S4-S5 linker couples the VSD to the pore domain. In Kv1-7, the voltage-sensing domains are positioned adjacent to the pore helices from neighboring subunits resulting in a domain-swapped arrangement (figure 1.6) (26, 27, 94, 95). However, Kv10-12 and Slo1, a voltage-gated potassium channel that can also be activated by Ca^{2+}, adopt non-domain-swapped channel architectures, where the VSD is positioned adjacent to the pore helices of the same rather than the neighboring subunit (96-98).

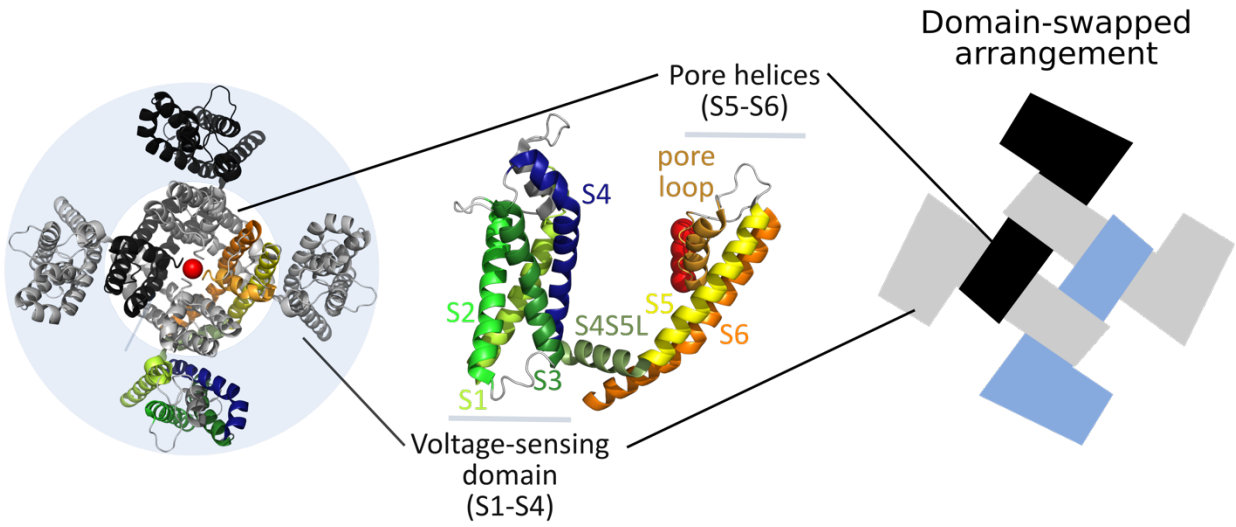

Figure 1.6 Representative structure of a voltage-gated channel
Crystal structure (2R9R) of the tetrameric Kv1.2 channel arrangement viewed from the extracellular (left) and the single subunit viewed from the side (middle) (27). Each subunit comprises six transmembrane helices (S1-S6) and a pore loop. The voltage-sensing domains (S1-S4) are located in the periphery, the pore helices (S5-S6) form a central ion-conducting pore. Four potassium ions (red spheres) are stabilized by the pore loop. The long S4-S5 linker helix is nearly parallel to the lipid bilayer and connects the VSD and pore helices. Cartoon representation (right) of the tetramer illustrates the domain swapped arrangement, where the VSD of one subunit is adjacent to the S5-S6 pore helices of the neighboring subunit.

Kv channels make up the most extensive group of voltage-gated channels, with 40 members belonging to 12 subgroups (Kv1-12). Members are renowned for shaping action potentials in the nervous system. However, they are ubiquitously expressed and are involved in various other tasks such as regulation of neuronal excitability and dendritic signal transduction, proliferation, apoptosis and determining the heart rate (99-106). It is obvious then, that altered functions of these channels can lead to a variety of diseases ranging from ataxia and epilepsy to heart diseases and pain syndromes (7, 107-113).

The electrical signal conduction in neurons depends on different voltage-gated ion channels, including Kv channels, that together generate action potentials. The initial discovery of action potentials by Bernstein and the subsequent model by Hodgkin and Huxley demonstrate the nerve cell's selective permeability of potassium and sodium ions (114-116). The rising phase of the action potential is governed by fast-opening voltage-gated sodium channels. Their activation leads to sodium influx and depolarization of the membrane. At more depolarized potentials, sodium channels inactivate and more slowly activating voltage-gated potassium channels open, which leads to an outflux of potassium ions and the repolarization of the membrane (figure 1.7).

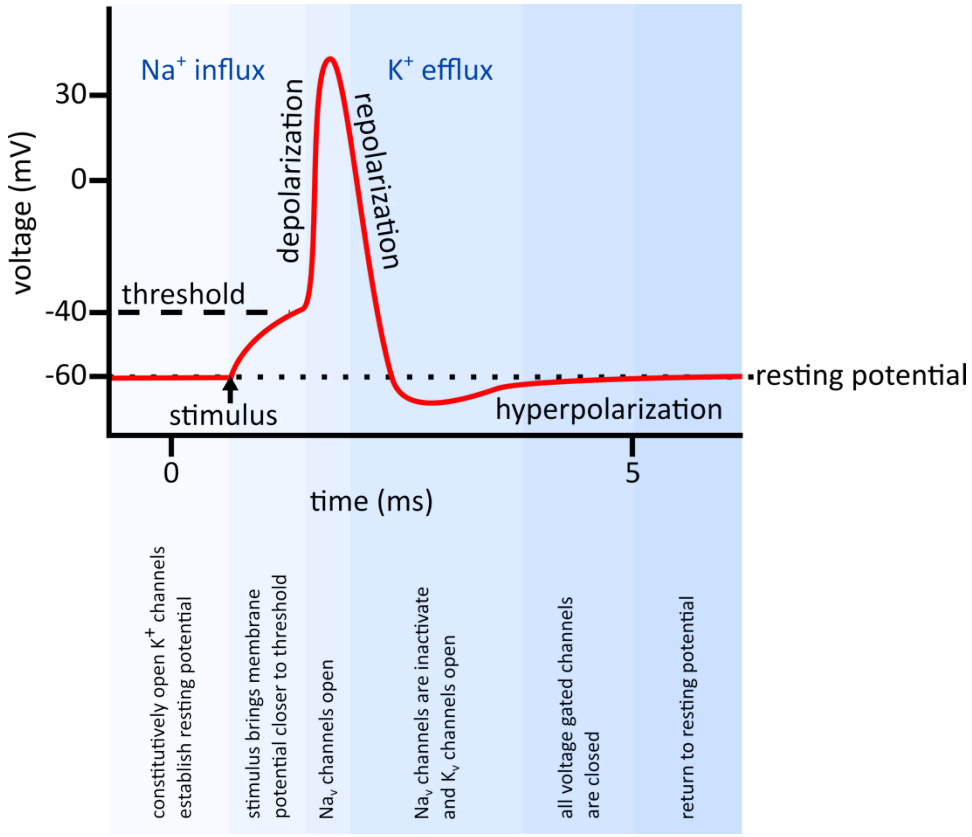

Figure 1.7 Basic steps of the action potential
The action potential can be described by six steps (left to right). 1) Pre-stimulus, the membrane is at resting potential. 2) An incoming stimulus depolarises the membrane, 3) when the threshold is reached Na_v channels open, further depolarizing the membrane. 4) At very positive membrane potentials, K_v channels activate and Na_v channels inactivate, resulting in the repolarization and hyperpolarization of the membrane. 5) All voltage-gated channels are closed and 6) constitutively open K-channels re-establish the resting potential.

The rich firing patterns of the human brain depend on the localized expression and finetuned activation of 145 voltage-gated ion channels as well as calcium-activated and constitutively open potassium channels (117-120). One important voltage-gated potassium channel family member is Kv2.1, studied in chapter three, which is dominantly expressed in the hippocampus and cortex (121, 122) and renowned for its key role in learning and memory formation (123). Kv2.1 channels belong to the group of delayed rectifiers; they activate after significant depolarization and only slowly inactivate (124). The resulting potassium currents regulate action potential repolarization, influence neuronal excitability and prevent action potential back propagation due the channel's localized expression at the axon initiation segment as well as on the soma and proximal dendrites of neurons (figure 1.8) (122, 125). Kv4.2, studied in chapter five, is another voltage-gated potassium channel subunit that influences action potentials and prohibits backpropagation. In neurons of the central nervous system, Kv4.2

channels are, opposed to Kv2.1, expressed in more distal dendrites (figure 1.8) where they activate at small depolarizing voltages and feature fast inactivating A-type currents. Kv2.1 and 4.2 channels in the nervous system act as molecular “breaks”. Channel modifications that result in reduced potassium efflux are the molecular equivalent to taking the “foot of the break” and contribute to neuronal hyperexcitability, which has been linked to seizures, learning deficiencies and chronic neuropathic pain (121, 123, 126-128).

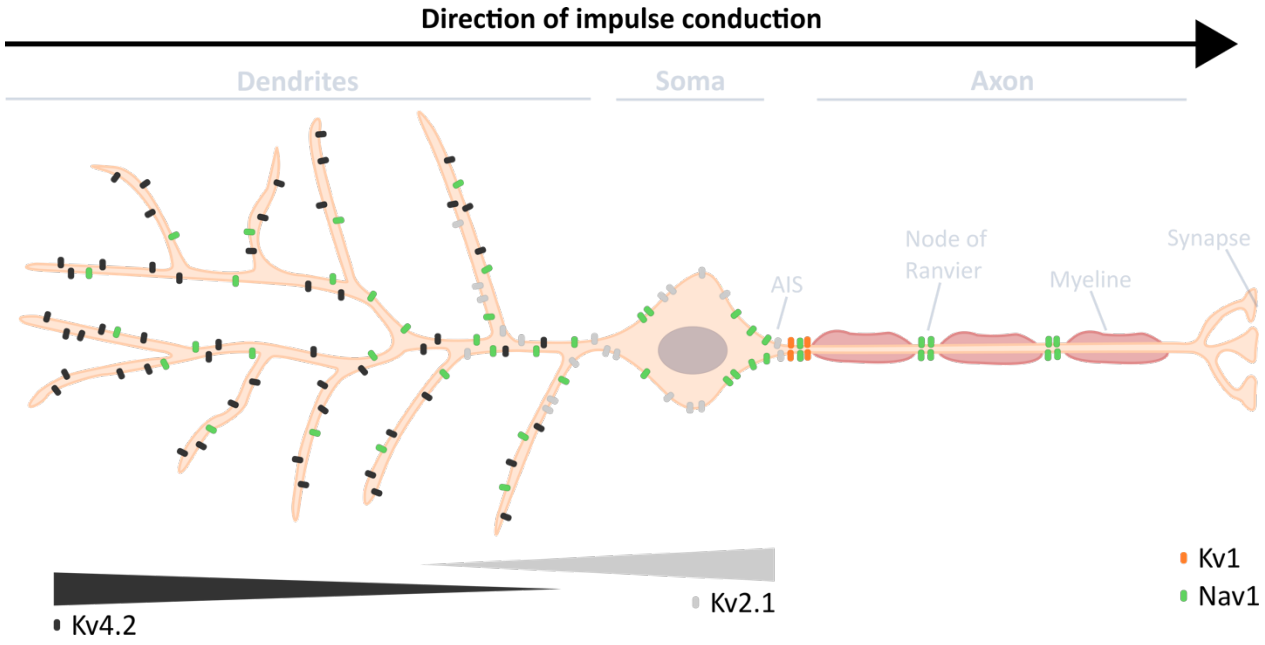

Figure 1.8 Expression of voltage-gated channels in neurons of the CNS
Cartoon of a neuron illustrating the localized expression of Kv4.2 (black) in distal dendrites, Kv2.1 (grey) at the axon initial segment (AIS) as well as on the soma and proximal dendrites, Kv1 (orange) at the AIS and Nav1 (green). The localized expression and finetuned voltage-dependent opening of the different channels results in the conduction of impulses from dendrites to the synapses. Figure adapted from Dumenieu et al., 2017 (129).

1.3.1 Biological Assemblies of Kv Channels

Ion channels are expressed ubiquitously in the body, where their properties are further finetuned to the tissue specific requirements by alternative splicing (130-134), post-translational modifications (135-138), formation of heteromeric complexes (139-143) and co-expression with auxiliary subunits (48, 144-150). Below, I will further introduce the diversification and modulation of Kv channel assemblies, that are relevant to this body of work.

1.3.1.1 Silent Subunits

Kv channel subunits are closely related and specific interactions between the subunits dictate their oligomerization compatibility. Members Kv1-6, -8 and -9 of the voltage gated potassium channel family feature an amino-terminal tetramerization (T1) domain that helps discriminating between different subunits (151-153). For Kv1-4, this domain mediates subunit interactions between members of the same subfamily that form functional homo- or heterotetrameric channels while prohibiting heteromerization between members of these four subfamilies (153-157). The interaction between two compatible T1 domains in the endoplasmic reticulum is thought to be the first step in Kv channel assembly, since these domains interact while the nascent protein is still attached to the ribosome (158). Dimerized Kv subunits subsequently form tetrameric channel structures and it has been shown, that the interaction sites of the monomer-monomer interface differ from the sites that later mediate tetramer formation (159).

Not all members of the voltage-gated potassium channel superfamily form functional channels by themselves but act as channel modulators. Of the 12 Kv channel subfamilies, Kv5, -6, -8, and -9 constitute the distinct group of such modulatory subunits. Despite their general sequence similarity to Kv1-4 subunits, these subunits fail to form functional homotetramers and are therefore referred to as electrically “silent” KvS subunits (160, 161). While their tetramerization (T1) domains are self-incompatible, replacing the T1 domain of KvS subunits with T1 domains that otherwise mediate homotetrameric channel formation, does not result in KvS homotetramers in the plasma membrane, indicating that other sites are crucial for subunit interaction and trafficking (162-164). However, extensive mutational analysis did not yet succeed at producing a conductive homotetrameric KvS channel (162-164). KvS subunits act as channel modulators by forming heterotetramers with Kv2 subunits, which further diversifies Kv channel functions (139). Compared to Kv2 tetramers, Kv2/KvS heterotetramers feature altered electrophysiological channel properties (figure 1.9) (161, 165-169). More specifically, heteromerization with Kv6.4 results in reduced current densities and a hyperpolarizing shift in the voltage-dependence of channel inactivation thereby making neurons more excitable when Kv6.4 is expressed (151, 162).

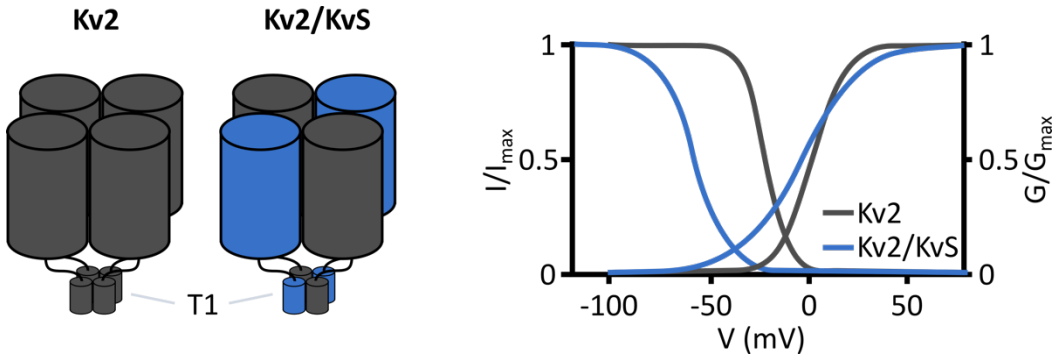

Figure 1.9 Effect of silent Kv subunits
Cartoon illustrating the homotetrameric Kv2 (left) and heterotetrameric Kv2/KvS (right) channel arrangements mediated by the tetramerization domains T1 (left). KvS subunits (blue) modulate the voltage dependence of Kv2 activation and inactivation as indicated by the GV and IV curve, respectively (right). Figure adapted from Bocksteins, 2016 (39).

To comprehend the mechanistic basis underlying altered channel properties, electrophysiological and fluorescence based structural investigations have been conducted. Electrophysiological investigations on the voltage sensor movement in Kv2.1/6.4 heteromers demonstrated that the hyperpolarizing shift in inactivation is accompanied by a distinct movement of the voltage-sensing S4 helix at hyperpolarized potentials, linking voltage sensor movement to channel inactivation (170). Understanding the channel complex architecture is vital and the first stoichiometric investigation was performed on Kv2.1/Kv9.3 channels which reported a single silent subunit per heterotetramer (171). Researchers tacitly assumed that distinct Kv2/KvS heteromers adopt identical subunit stoichiometries, but we (172) and others (173) observed a more flexible channel arrangement which will be presented in chapter 3.

1.3.1.2 Auxiliary Subunits of Kv4

Heterologous Kv4 channel expression does not result in macroscopic currents matching the neuronal Kv4 currents and co-expression with auxiliary proteins is necessary to modulate the gating kinetics and reconcile the observed currents (47, 48, 144, 174-179). Kv Channel Interacting Proteins (KChIPs) and Dipeptidyl Peptidase (DPP) like proteins are the two major auxiliary subunits modulating native Kv4 currents through distinct mechanisms (174, 178).

Kv Channel Interacting Proteins (KChIP) are soluble proteins, that bind to the proximal N-terminus of Kv4 subunits and thereby impair fast inactivation (175). Sites in the tetramerization domain T1 and

C-terminus of the channel subunit further stabilize the clamp-like binding of the auxiliary subunit (180-182). The degree of modulation of the channel's properties is linked to the variable number of bound KChIP subunits (183). KChIP associates to the channel subunits early in the biosynthetic pathway and increases trafficking to the plasma membrane (178, 184-186). The binding of maximal four KChIP proteins to the Kv4 tetramer thus results in increased current densities, slowing of the early stage of macroscopic current inactivation and accelerated recovery from inactivation (47, 175).

Dipeptidyl peptidase (DPP)-like proteins are large, enzymatically inactive single transmembrane proteins, that are integral to the native Kv4 channel complexes but are also found in the plasma membrane in the absence of Kv4 subunits (130, 131, 176, 177, 187-189). The exact structure of the Kv4/DPP complex is unknown, but the importance of the transmembrane and short cytoplasmic N-terminal domain for the interaction with the channel and its modulation has been demonstrated (132, 177, 179, 188, 190, 191). The stoichiometry of DPPs and Kv4 channels is flexible and, as for KChIPs, up to four auxiliary DPP subunits can bind (192, 193). Distinct interaction sites between DPPs, KChIPs and Kv4 subunits allow for simultaneous binding of the two auxiliary proteins to the channel complex (figure 1.10) (188). DPP's primarily interact through their transmembrane helix with the voltage sensing domain of the channel. This promotes the voltage dependent S4 movement, boosting the voltage sensing conformational change (194). As a result, DPPs cause a hyperpolarizing shift in the conductance-voltage relationship and inactivation. Like KChIP, DPP expression increases trafficking to the plasma membrane leading to elevated macroscopic Kv4 currents. But contrary to the modulation by KChIPs, DPPs also increase the single channel conductance of Kv4 channels (48, 144, 195). Furthermore, DPP subunits accelerate not only recovery from inactivation like KChIPs, but also accelerate inactivation kinetics themselves (48, 195).

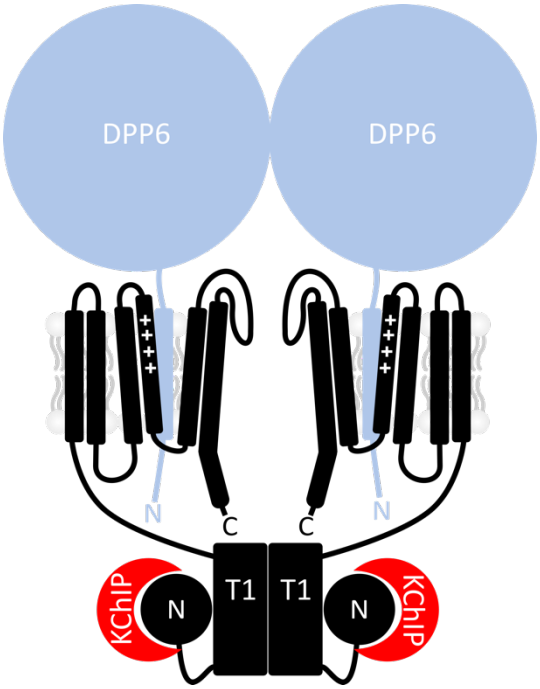

Figure 1.10 Model of Kv4/DPP6/KChIP channel complex
Cartoon modelling the channel complex composed of Kv4 (black), DPP6 (blue) and KChIP (red). Two subunits of each component are shown. The transmembrane helix of DPP6 interacts with the VSD while KChIP sequesters the N-terminal ball of Kv4 in a clamp-like structure.

The modulatory effect of the large extracellular domain of DPPs on Kv4 channels remains unclear. The crystal structure of the isolated domain demonstrates two distinct structural features; a non-functional α/ß-hydrolase domain closer to the transmembrane helix and an eight-bladed ß-propeller structure (196). The extracellular domain mediates contacts with the extracellular matrix and is involved in cell adhesion and motility (45). It is also important for channel trafficking from the endoplasmic reticulum to the plasma membrane and stabilization of the channel complex at the cell surface, (197) but the role of the extracellular domain on channel gating remained unchallenged. As a first step in understanding the effect of the extracellular domain on channel complexes, we aimed at identifying which part of the approximately 700 amino acid long extracellular domain confers the gating modulation. This research is presented in chapter five and lays a foundation for finding specific interactions sites that could serve as drug targets.

1.3.1 Gating of Voltage-gated Potassium Channels

In order to explain how coexpression of silent and auxiliary subunits might result in functional changes of the voltage-gated ion channels, it is important to understand the basic gating mechanism. Extensive studies focused on the structure-function relation of Kv channels, but various details remain unclear. Ion channels can adopt four main states: resting, partially activated, open and inactivated (figure 1.11). The kinetic properties of transitions between these states govern the open probability of the channel and thereby the shape of the macroscopic current.

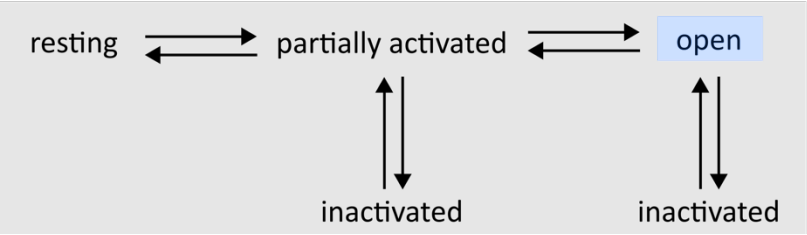

Figure 1.11 Simplified model of conformational states of Kv channels
Kv2 and Kv4 channels can be in four main conformational states: resting, partially activated, open and inactivated. Kv2.1 and 4.2 channels preferentially inactivated from a pre-open, partially activated state. Vestigial inactivation from the open state can occur in Kv4.2 channels. Only the open state (blue) allows for ion conduction through the pore.

1.3.2.1 Channel Activation and Selectivity

Channel activation describes the transition from the closed to open state (figure 1.12). As mentioned above, each channel features four voltage sensing domains (VSDs) at the outer edge of the channel. They independently change their conformation according to the electric field. The S4 helix of K_V channels is the key feature involved in voltage-sensing. Four to six positively charged side chains in the helix detect changes in the electric field. Upon depolarization of the membrane, the positive charges of the S4 are driven away from the now more positively charged intracellular and lead to a conformational change (198-200). Rather than displacing the gating charges across the entire bilayer, water-filled openings project the electric field into the lipid bilayer, so that the helices vertically and radially displace, rotate and tilt in the membrane to accommodate for the change in the electric field (201-207).

Once all four VSDs are in an activated conformation, they open the S6 channel gate cooperatively in two steps (29, 208, 209). The molecular mechanism through which the movement of the VSD results in pore opening is not fully understood. In the closed state, the C-terminal ends of the S6 segments adopt a crossed conformation on the intracellular side of the pore, blocking ions from passing through. The displacement of the S4 helix conveys force directly onto the intracellular S4-S5 linker, which covalently links the VSD to the outer pore helix and more importantly anneals with the C-terminal S6 (53, 210, 211), alluding to the importance of this structural feature for coupling voltage sensing and pore opening. Indeed, the linker motion is complex and displaces in distinct steps during gating (212). Furthermore, numerous non-covalent intersubunit interactions between the VSD, S4-S5 linker and the pore helices are crucial for stabilizing both closed and open pore conformations (208, 213-215).

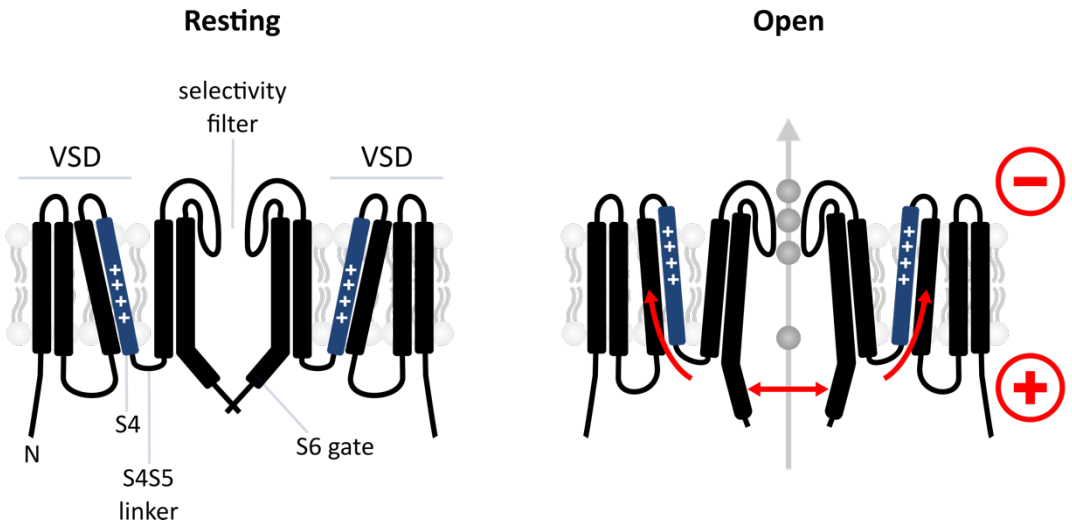

Figure 1.12 Channel activation
Cartoon illustrating the activation of voltage-gated ion channels. Two of four subunits are shown. In the resting state (left), the voltage-sensing S4 helix is deactivated and the S6 gate is closed. Upon depolarization of the membrane, the VSD is activated and the S6 gate is open. Red arrows highlight the main conformational changes leading to pore opening.

Once the intracellular S6 gate is opened, K^+ ions can pass from the intracellular side, through the selectivity filter of the pore to the extracellular side of the channel. The selectivity filter is the narrow part of the pore close to the extracellular side of the channel responsible for the efficient and selective K^+ conductance along the electrochemical gradient. Key feature of this structure is the re-entrant loop between segments S5 and S6, which carries the signature GYG motif. The corresponding carbonyl oxygens of the peptide backbone are oriented towards the lumen of the pore, where they replace the

hydration shell of K^+ ions (Figure 1.13) (216, 217). K^+ ions are stabilized by the selectivity filter in a single file and at the same time are destabilized by repulsive forces of neighboring K^+ ions, resulting in rapid ion conductance close to the diffusion limit (218). The specific structure of the selectivity filter disfavors the passage of anions, divalent cations and Na^+.

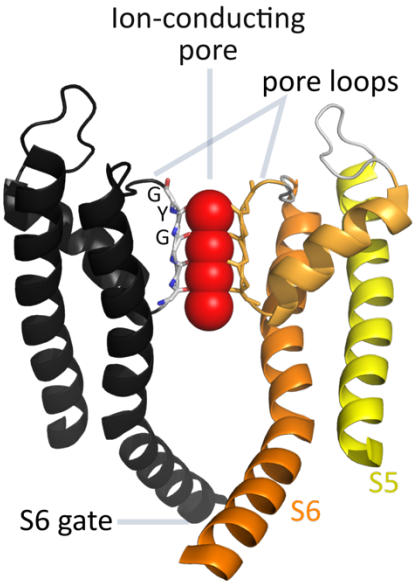

Figure 1.13 Ion channel pore
Crystal structure (2R9R) of the Kv1.2 channel pore (27). Two of four subunits are shown. The re-entrant pore loops form the selectivity filter. The carbonyl oxygens (sticks) of the XXGYG motive stabilize the potassium ions (red spheres) in the pore.

1.3.2.2 Channel Inactivation

Independent of the conformational state of the internal gate, channels can inactivate, i.e. become non-conductive through multiple possible mechanisms (figure 1.14 and 1.15). These diverse inactivation mechanisms influence the threshold and waveform of action potentials as well as neuronal firing frequencies. According to the S6 conformation, inactivation can be divided into two main groups; open state and closed state inactivation. The former is a prevalent feature of many K_V channels and describes the mechanism of inactivation after the channel pore opened. Closed state inactivation (CSI) on the other hand describes the mechanism of inactivation that takes place before the pore becomes conductive. Time courses of the different mechanism vary widely and macroscopic currents reflect a complicated combination of different inactivation mechanisms overlapping in time. According to the inactivation kinetics, Kv-channel-mediated currents can be divided into non- or slow-inactivating

"delayed rectifiers" (over seconds) like Kv2.1 and fast-inactivating "A-type" currents (over milliseconds) like Kv4.2. This variety in gating kinetics adds to the diversity of voltage-gated ion channel properties, thereby refining macroscopic currents and action potential characteristics to the tissue specific requirements.

Open state inactivation can be, according to the molecular mechanism, further divided into N-type and C-type inactivation. N-type inactivation (NTI) is defined by the obstruction of the conducting pore typically by the N-terminal structure of the channel subunit (figure 1.14A). This cytoplasmic structure features a tethered ball-like conformation and hydrophobic interactions between this ball and the pore result in the obstruction of ion flow (219-221). The model K_V Shaker channel from *Drosophila*, as well as Kv1.4, 3.4 and 4.2 feature such N-terminal ball and chain structures that enable them to undergo intrinsic NTI (222-225). However, in native Kv4.2 channel complexes, KChIP sequesters the N-terminal ball, suppressing NTI (175).

The typically slower C-type inactivation (CTI) mechanism includes conformational changes at the selectivity filter that result in a non-conductive state (figure 1.14B). A series of crystal structures of the bacterial KcsA channel, which is structurally analogous to the pore domain of K_V channels, demonstrate the flexibility of the selectivity filter during CTI (216, 226, 227). Steric clashes caused by the opening of the intracellular S6 gate result in the rearrangement of the selectivity filter, linking pore opening directly to the non-conductive state (228). The stable inactivated conformation of the selectivity filter destabilizes K^+ ions inside the conductive pathway and is further characterized by the presence of water molecules trapped behind the filter, which need to be released in order for the channel to recover (228-230). Besides the opening of the intracellular S6 gate, mutations around the selectivity filter as well as changes in the ionic composition of the extracellular solution and pore blockers further influence C-type inactivation (231-234).

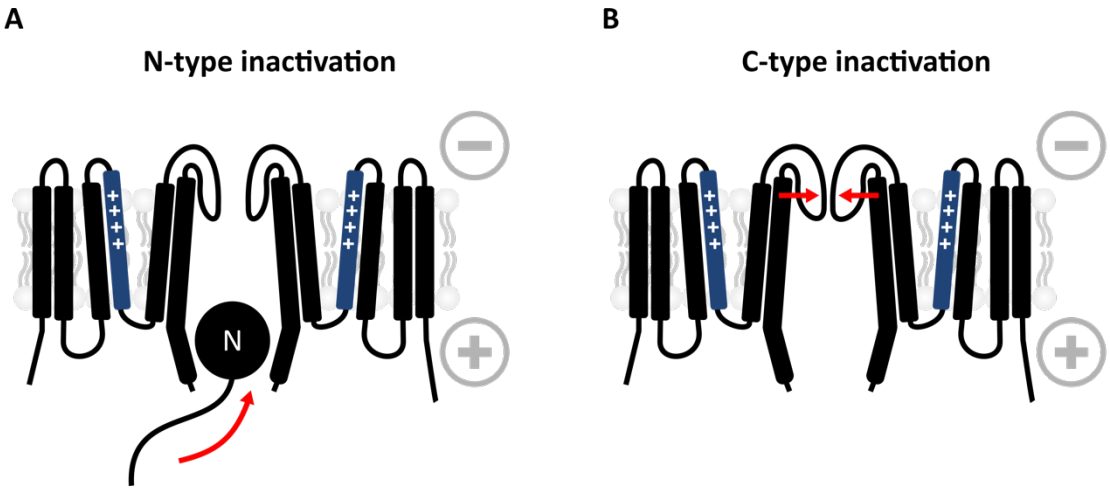

Figure 1.14 Open state inactivation
Cartoon illustrating the inactivation of voltage-gated ion channels after opening. Two of four subunits are shown. **A)** The intracellular N-terminal ball enters the pore and blocks ion flux resulting in N-type inactivation. **B)** Conformational changes of the selectivity filter obstruct the extracellular part of the pore and block ion flux resulting in C-type inactivation.

Rather than entering a non-conductive state from an open channel conformation, closed state inactivation (CSI) describes the state in which channels are partially activated but reluctant to open. As opposed to open state N- and C-type inactivation, the molecular details of CSI or U-type inactivation remained for a long time elusive. U-type inactivation refers to the characteristic voltage-dependence of inactivation that channels featuring CSI exhibit; they preferentially inactivate at sub-threshold depolarization (235). Channels featuring CSI include Shaker, K_V1.5, K_V2.1, K_V3.1 and K_V4 members (124, 236-240). A recent study conducted on Kv2.1 and Kv3.1 demonstrates that an allosteric coupling between the S6 gate and the selectivity filter is not only involved in C-type inactivation but also in U-type inactivation (241). However, the exact molecular mechanism remains poorly understood.

K_V4 channels are a useful model to study the underlying molecular basis for closed-state inactivation in K_V channels (242). Opposed to other Kv-channels, K_V4 channels undergo preferential CSI even at strong depolarization and although the N-terminal ball-and-chain structure can inactivate the channel through open state N-type inactivation, due to the binding of KChIP in native channel complexes, NTI only plays a minor role (222, 239). Moreover, K_V4 open state inactivation is only transient and channels accumulate in a closed-inactivated state upon long depolarization (239, 243). Early on in the investigations studying the underlying mechanisms of CSI, it became clear that the voltage sensing domain adopts a dual role and is involved not only in channel activation but also in

inactivation (211, 244). Dougherty et al. demonstrated that CSI is accompanied by the immobilization of the positive gating charges in the voltage sensing S4 helix. This immobilization of gating charges is thought to be caused by a slow conformational change of the helix to a stable conformation that differs from the resting position. As a result, the voltage sensing domain becomes desensitized to depolarizing voltages and fails to reliably open the intracellular S6 gate (244). Mutations that affect the gating charges in the S4 helix influence CSI and further support the hypothesized involvement of the VSD in closed-state inactivation (245-247). In Shaker channel activation, the movement of the voltage sensor is directly coupled to the opening of the S6 gate meditated by non-covalent interactions between the S4-S5 linker and the pore helices of neighboring subunits (208, 213-215). In Kv4 channels, homologous binding sites interact dynamically and mediate transient activation as well as closed-state inactivation (248-250). These dynamic interactions occur within individual subunits and between neighboring subunits (248). Taken together, these findings paint a picture of a "slippery" S6 gate causing CSI. Upon weak depolarization the voltage-sensing S4 helix adopts a relaxed conformation, the S4-S5 linker subsequently does not interact strongly enough with the S6 gate failing to open it and thus uncoupling voltage sensor movement from pore opening (figure 1.15) (251). Strong depolarization on the other hand, increases the opening probability, but due to the preferential CSI, opened Kv4 channels end-up in closed-inactivated states after long depolarization. Despite the progress in understanding the molecular mechanism underlying CSI in individual Kv4 channels, we do not fully understand how modulations of the channel complex under physiological conditions alter the structure-function relation.

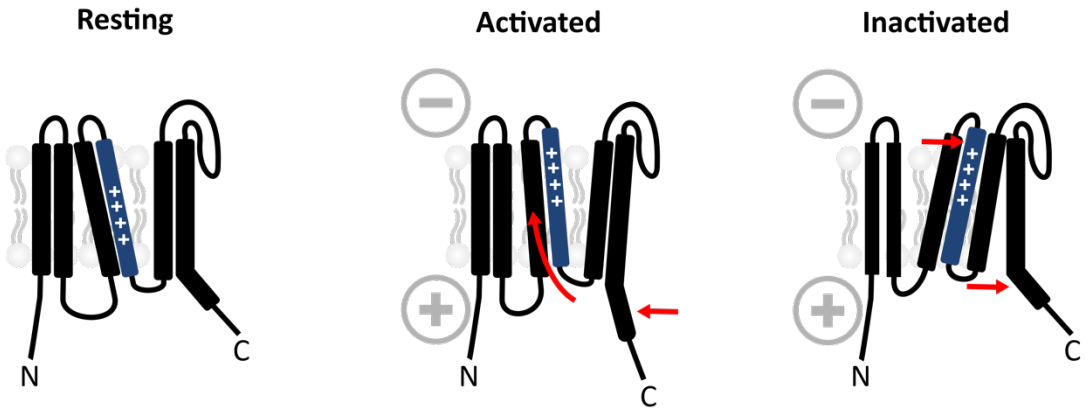

Figure 1.15 Closed state inactivation
Cartoon illustrating the inactivation of voltage-gated ion channels after opening. One of four subunits is shown. In the resting state (left), the voltage-sensing S4 helix is deactivated and the S6 gate is closed. Upon

depolarization of the membrane, the VSD is activated and the S6 gate is open (middle). Conformational changes of the VSD to a more stable position result in the uncoupling of the S6 pore helix and the VSD resulting in an closed-inactivated state (right). Red arrows highlight the main conformational changes involved in CSI. Figure adapted from Barghaan and Bähring, 2009 (250)

1.4 Thesis Format

Elucidating the structure-function relations of any protein complex in the body is fundamental for the advancement of our understanding of the healthy and pathological bodily functions. Many potential therapeutic drugs target these ubiquitously expressed channels but interact broadly and non-specifically and are never approved due to undesirable side effects. It is therefore crucial to identify specific interaction sites that can serve as pharmaceutical drug targets. The research presented in this thesis lays a foundation for improving our comprehension about the structure and structure-function relation of three ion channel complexes.

This thesis comprises one published article and two articles that are ready for submission. Chapter 3 and 4 present the structural investigation of Kv2.1/6.4 and TACAN ion channels, respectively. Chapter 3 will introduce a rigorous analysis of subunit counting data obtained from Kv2.1/6.4 expression in a heterologous expression system. This exhaustive analysis accompanied by a parallel electrophysiological evaluation by our collaborators aims at minimizing confirmation bias, a neglected issue often observed in studies presenting subunit counting data. Chapter 4 utilizes the same analysis approach on subunit counting data obtained from purified and immobilized TACAN channels. Chapter 5 presents the work on Kv4 channel complexes. Here, data obtained from electrophysiological investigations helps comprehend the elusive modulatory effect of DPP6's extracellular domain on the Kv4 channel. Before presenting the research, chapter two will introduce the relevant electrophysiological and fluorescence-based techniques used during this body of work.

1.5 References

1. F. A. Azevedo *et al.*, Equal numbers of neuronal and nonneuronal cells make the human brain an isometrically scaled-up primate brain. *J Comp Neurol* **513**, 532-541 (2009).
2. T. J. Jegla, C. M. Zmasek, S. Batalov, S. K. Nayak, Evolution of the human ion channel set. *Comb Chem High Throughput Screen* **12**, 2-23 (2009).
3. T. Klassen *et al.*, Exome sequencing of ion channel genes reveals complex profiles confounding personal risk assessment in epilepsy. *Cell* **145**, 1036-1048 (2011).
4. M. Pertea *et al.*, CHESS: a new human gene catalog curated from thousands of large-scale RNA sequencing experiments reveals extensive transcriptional noise. *Genome Biol* **19**, 208 (2018).
5. J. P. Adelman, C. T. Bond, M. Pessia, J. Maylie, Episodic ataxia results from voltage-dependent potassium channels with altered functions. *Neuron* **15**, 1449-1454 (1995).
6. M. R. Rose, Neurological channelopathies. *BMJ* **316**, 1104-1105 (1998).
7. P. Imbrici *et al.*, Therapeutic Approaches to Genetic Ion Channelopathies and Perspectives in Drug Discovery. *Front Pharmacol* **7**, 121 (2016).
8. K. Saotome *et al.*, Structure of the mechanically activated ion channel Piezo1. *Nature* **554**, 481-486 (2018).
9. T. Kawate, J. C. Michel, W. T. Birdsong, E. Gouaux, Crystal structure of the ATP-gated P2X(4) ion channel in the closed state. *Nature* **460**, 592-598 (2009).
10. A. Nicke *et al.*, P2X1 and P2X3 receptors form stable trimers: a novel structural motif of ligand-gated ion channels. *EMBO J* **17**, 3016-3028 (1998).
11. N. Kedei *et al.*, Analysis of the native quaternary structure of vanilloid receptor 1. *J Biol Chem* **276**, 28613-28619 (2001).
12. C. Rosenmund, Y. Stern-Bach, C. F. Stevens, The tetrameric structure of a glutamate receptor channel. *Science* **280**, 1596-1599 (1998).
13. A. I. Sobolevsky, M. P. Rosconi, E. Gouaux, X-ray structure, symmetry and mechanism of an AMPA-subtype glutamate receptor. *Nature* **462**, 745-756 (2009).
14. K. Brejc *et al.*, Crystal structure of an ACh-binding protein reveals the ligand-binding domain of nicotinic receptors. *Nature* **411**, 269-276 (2001).
15. H. McGuire, M. R. Aurousseau, D. Bowie, R. Blunck, Automating single subunit counting of membrane proteins in mammalian cells. *J Biol Chem* **287**, 35912-35921 (2012).
16. J. M. Kefauver *et al.*, Structure of the human volume regulated anion channel. *Elife* **7** (2018).
17. S. Maeda *et al.*, Structure of the connexin 26 gap junction channel at 3.5 A resolution. *Nature* **458**, 597-602 (2009).

18. K. Michalski *et al.*, The Cryo-EM structure of pannexin 1 reveals unique motifs for ion selection and inhibition. *Elife* **9** (2020).

19. L. Song *et al.*, Structure of staphylococcal alpha-hemolysin, a heptameric transmembrane pore. *Science* **274**, 1859-1866 (1996).

20. J. E. Gouaux *et al.*, Subunit stoichiometry of staphylococcal alpha-hemolysin in crystals and on membranes: a heptameric transmembrane pore. *Proc Natl Acad Sci U S A* **91**, 12828-12831 (1994).

21. G. Miles, L. Movileanu, H. Bayley, Subunit composition of a bicomponent toxin: staphylococcal leukocidin forms an octameric transmembrane pore. *Protein Sci* **11**, 894-902 (2002).

22. D. B. Lacy, D. J. Wigelsworth, R. A. Melnyk, S. C. Harrison, R. J. Collier, Structure of heptameric protective antigen bound to an anthrax toxin receptor: a role for receptor in pH-dependent pore formation. *Proc Natl Acad Sci U S A* **101**, 13147-13151 (2004).

23. A. F. Kintzer, H. J. Sterling, Tang, II, E. R. Williams, B. A. Krantz, Anthrax toxin receptor drives protective antigen oligomerization and stabilizes the heptameric and octameric oligomer by a similar mechanism. *PLoS One* **5**, e13888 (2010).

24. A. F. Kintzer *et al.*, The protective antigen component of anthrax toxin forms functional octameric complexes. *J Mol Biol* **392**, 614-629 (2009).

25. H. Katayama *et al.*, Three-dimensional structure of the anthrax toxin pore inserted into lipid nanodiscs and lipid vesicles. *Proc Natl Acad Sci U S A* **107**, 3453-3457 (2010).

26. S. B. Long, E. B. Campbell, R. Mackinnon, Crystal structure of a mammalian voltage-dependent Shaker family K+ channel. *Science* **309**, 897-903 (2005).

27. S. B. Long, X. Tao, E. B. Campbell, R. MacKinnon, Atomic structure of a voltage-dependent K+ channel in a lipid membrane-like environment. *Nature* **450**, 376-382 (2007).

28. S. Y. Lee, A. Lee, J. Chen, R. MacKinnon, Structure of the KvAP voltage-dependent K+ channel and its dependence on the lipid membrane. *Proc Natl Acad Sci U S A* **102**, 15441-15446 (2005).

29. W. N. Zagotta, T. Hoshi, R. W. Aldrich, Shaker potassium channel gating. III: Evaluation of kinetic models for activation. *J Gen Physiol* **103**, 321-362 (1994).

30. M. Noda *et al.*, Primary structure of Electrophorus electricus sodium channel deduced from cDNA sequence. *Nature* **312**, 121-127 (1984).

31. J. Payandeh, T. Scheuer, N. Zheng, W. A. Catterall, The crystal structure of a voltage-gated sodium channel. *Nature* **475**, 353-358 (2011).

32. M. Takahashi, M. J. Seagar, J. F. Jones, B. F. Reber, W. A. Catterall, Subunit structure of dihydropyridine-sensitive calcium channels from skeletal muscle. *Proc Natl Acad Sci U S A* **84**, 5478-5482 (1987).

33. S. G. Brohawn, J. del Marmol, R. MacKinnon, Crystal structure of the human K2P TRAAK, a lipid- and mechano-sensitive K+ ion channel. *Science* **335**, 436-441 (2012).

34. A. N. Miller, S. B. Long, Crystal structure of the human two-pore domain potassium channel K2P1. *Science* **335**, 432-436 (2012).

35. Q. Zhao, H. Zhou, X. Li, B. Xiao, The mechanosensitive Piezo1 channel: a three-bladed propeller-like structure and a lever-like mechanogating mechanism. *FEBS J* **286**, 2461-2470 (2019).

36. T. Althoff, R. E. Hibbs, S. Banerjee, E. Gouaux, X-ray structures of GluCl in apo states reveal a gating mechanism of Cys-loop receptors. *Nature* **512**, 333-337 (2014).

37. K. Yamashita *et al.*, Crystal structure of the octameric pore of staphylococcal gamma-hemolysin reveals the beta-barrel pore formation mechanism by two components. *Proc Natl Acad Sci U S A* **108**, 17314-17319 (2011).

38. A. P. Stewart *et al.*, The Kv7.2/Kv7.3 heterotetramer assembles with a random subunit arrangement. *J Biol Chem* **287**, 11870-11877 (2012).

39. E. Bocksteins, Kv5, Kv6, Kv8, and Kv9 subunits: No simple silent bystanders. *J Gen Physiol* **147**, 105-125 (2016).

40. J. Grudzinska *et al.*, The beta subunit determines the ligand binding properties of synaptic glycine receptors. *Neuron* **45**, 727-739 (2005).

41. C. H. Cho, E. M. Hwang, J. Y. Park, Emerging Roles of TWIK-1 Heterodimerization in the Brain. *Int J Mol Sci* **19** (2017).

42. J. Levitz *et al.*, Heterodimerization within the TREK channel subfamily produces a diverse family of highly regulated potassium channels. *Proc Natl Acad Sci U S A* **113**, 4194-4199 (2016).

43. G. T. Cottrell, J. M. Burt, Functional consequences of heterogeneous gap junction channel formation and its influence in health and disease. *Biochim Biophys Acta* **1711**, 126-141 (2005).

44. H. Abriel, J. S. Rougier, J. Jalife, Ion channel macromolecular complexes in cardiomyocytes: roles in sudden cardiac death. *Circ Res* **116**, 1971-1988 (2015).

45. L. Lin *et al.*, DPP6 regulation of dendritic morphogenesis impacts hippocampal synaptic development. *Nat Commun* **4**, 2270 (2013).

46. A. C. Jackson, R. A. Nicoll, The expanding social network of ionotropic glutamate receptors: TARPs and other transmembrane auxiliary subunits. *Neuron* **70**, 178-199 (2011).

47. W. F. An *et al.*, Modulation of A-type potassium channels by a family of calcium sensors. *Nature* **403**, 553-556 (2000).

48. M. S. Nadal *et al.*, The CD26-related dipeptidyl aminopeptidase-like protein DPPX is a critical component of neuronal A-type K+ channels. *Neuron* **37**, 449-461 (2003).

49. S. H. Heinemann, J. Rettig, H. R. Graack, O. Pongs, Functional characterization of Kv channel beta-subunits from rat brain. *The Journal of physiology* **493 (Pt 3)**, 625-633 (1996).

50. Q. Liang *et al.*, Positive Allosteric Modulation of Kv Channels by Sevoflurane: Insights into the Structural Basis of Inhaled Anesthetic Action. *PLoS One* **10**, e0143363 (2015).

51. J. Krieger, J. Y. Lee, I. H. Greger, I. Bahar, Activation and desensitization of ionotropic glutamate receptors by selectively triggering pre-existing motions. *Neurosci Lett* **700**, 22-29 (2019).

52. J. P. Changeux, A. Christopoulos, Allosteric Modulation as a Unifying Mechanism for Receptor Function and Regulation. *Cell* **166**, 1084-1102 (2016).

53. G. A. Haddad, R. Blunck, Mode shift of the voltage sensors in Shaker K+ channels is caused by energetic coupling to the pore domain. *J Gen Physiol* **137**, 455-472 (2011).

54. C. Kapsalis *et al.*, Allosteric activation of an ion channel triggered by modification of mechanosensitive nano-pockets. *Nat Commun* **10**, 4619 (2019).

55. F. T. Horrigan, J. Cui, R. W. Aldrich, Allosteric voltage gating of potassium channels I. Mslo ionic currents in the absence of Ca(2+). *J Gen Physiol* **114**, 277-304 (1999).

56. F. Boll (1876) Zur Anatomie und Physiologie der Retina. in *Monatsberichte der Ko« niglichen Preussischen Akademie der Wissenschaften zu Berlin*, pp 783-787.

57. P. A. Hargrave *et al.*, The structure of bovine rhodopsin. *Biophys Struct Mech* **9**, 235-244 (1983).

58. R. A. Dixon *et al.*, Cloning of the gene and cDNA for mammalian beta-adrenergic receptor and homology with rhodopsin. *Nature* **321**, 75-79 (1986).

59. J. L. Fuller, Single-locus control of saccharin preference in mice. *J Hered* **65**, 33-36 (1974).

60. M. A. Hoon *et al.*, Putative mammalian taste receptors: a class of taste-specific GPCRs with distinct topographic selectivity. *Cell* **96**, 541-551 (1999).

61. H. Matsunami, J. P. Montmayeur, L. B. Buck, A family of candidate taste receptors in human and mouse. *Nature* **404**, 601-604 (2000).

62. L. Buck, R. Axel, A novel multigene family may encode odorant receptors: a molecular basis for odor recognition. *Cell* **65**, 175-187 (1991).

63. T. Olender, D. Lancet, D. W. Nebert, Update on the olfactory receptor (OR) gene superfamily. *Hum Genomics* **3**, 87-97 (2008).

64. A. Terakita, The opsins. *Genome Biol* **6**, 213 (2005).

65. P. Mombaerts, Genes and ligands for odorant, vomeronasal and taste receptors. *Nat Rev Neurosci* **5**, 263-278 (2004).

66. U. Gether, B. K. Kobilka, G protein-coupled receptors. II. Mechanism of agonist activation. *J Biol Chem* **273**, 17979-17982 (1998).

67. H. K. Hartline, Graham, C. H., Nerve Impulses from Single Receptors in the Eye of Limulus. *Proceedings of the Society for Experimental Biology and Medicine* **29**, 613-615 (1932).

68. A. Bigiani, V. Ghiaroni, F. Fieni, Channels as taste receptors in vertebrates. *Prog Biophys Mol Biol* **83**, 193-225 (2003).

69. A. L. Huang *et al.*, The cells and logic for mammalian sour taste detection. *Nature* **442**, 934-938 (2006).

70. B. Lindemann, Receptors and transduction in taste. *Nature* **413**, 219-225 (2001).

71. N. D. LopezJimenez *et al.*, Two members of the TRPP family of ion channels, Pkd1l3 and Pkd2l1, are co-expressed in a subset of taste receptor cells. *J Neurochem* **98**, 68-77 (2006).

72. D. P. Corey, A. J. Hudspeth, Ionic basis of the receptor potential in a vertebrate hair cell. *Nature* **281**, 675-677 (1979).

73. R. Alvarez-Buylla, J. Ramirez de Arellano, Local responses in Pacinian corpuscles. *Am J Physiol* **172**, 237-244 (1953).

74. J. Hu, G. R. Lewin, Mechanosensitive currents in the neurites of cultured mouse sensory neurones. *The Journal of physiology* **577**, 815-828 (2006).

75. F. S. Merkel, Tastzellen und Tastkörperchen bei den Hausthieren und beim Menschen. *Archiv für mikroskopische Anatomie* **11**, 636-652 (1875).

76. D. Purves, Augustine,G.J., Fitzpatrick,D., Katz,L.C., LaMantia,A., McNamara, J.O., Williams,S.M., "Neuroscience". (Sinauer Associates, Inc., Sunderland (MA), 2001), chap. The Major Afferent Pathway for Mechanosensory Information: The Dorsal Column-Medial Lemniscus System.

77. W. D. Willis, K. N. Westlund, Neuroanatomy of the pain system and of the pathways that modulate pain. *J Clin Neurophysiol* **14**, 2-31 (1997).

78. A. K. Jones, W. D. Brown, K. J. Friston, L. Y. Qi, R. S. Frackowiak, Cortical and subcortical localization of response to pain in man using positron emission tomography. *Proc Biol Sci* **244**, 39-44 (1991).

79. B. Kulkarni *et al.*, Attention to pain localization and unpleasantness discriminates the functions of the medial and lateral pain systems. *Eur J Neurosci* **21**, 3133-3142 (2005).

80. G. H. Bishop, The relation between nerve fiber size and sensory modality: phylogenetic implications of the afferent innervation of cortex. *J Nerv Ment Dis* **128**, 89-114 (1959).

81. H. S. Gasser, The classification of nerve fibers. *Ohio Journal of Science* **41**, 145-159 (1941).

82. D. D. Price, Characteristics of second pain and flexion reflexes indicative of prolonged central summation. *Exp Neurol* **37**, 371-387 (1972).

83. H. E. Torebjork, R. G. Hallin, Perceptual changes accompanying controlled preferential blocking of A and C fibre responses in intact human skin nerves. *Exp Brain Res* **16**, 321-332 (1973).

84. R. A. Mackenzie, D. Burke, N. F. Skuse, A. K. Lethlean, Fibre function and perception during cutaneous nerve block. *J Neurol Neurosurg Psychiatry* **38**, 865-873 (1975).

85. R. G. Walker, A. T. Willingham, C. S. Zuker, A Drosophila mechanosensory transduction channel. *Science* **287**, 2229-2234 (2000).

86. M. Huang, M. Chalfie, Gene interactions affecting mechanosensory transduction in Caenorhabditis elegans. *Nature* **367**, 467-470 (1994).

87. B. Coste *et al.*, Piezo1 and Piezo2 are essential components of distinct mechanically activated cation channels. *Science* **330**, 55-60 (2010).

88. Y. Wang *et al.*, A lever-like transduction pathway for long-distance chemical- and mechano-gating of the mechanosensitive Piezo1 channel. *Nat Commun* **9**, 1300 (2018).

89. L. Wang *et al.*, Structure and mechanogating of the mammalian tactile channel PIEZO2. *Nature* **573**, 225-229 (2019).

90. S. S. Ranade *et al.*, Piezo2 is the major transducer of mechanical forces for touch sensation in mice. *Nature* **516**, 121-125 (2014).

91. S. S. Ranade *et al.*, Piezo1, a mechanically activated ion channel, is required for vascular development in mice. *Proc Natl Acad Sci U S A* **111**, 10347-10352 (2014).

92. L. Beaulieu-Laroche *et al.*, TACAN Is an Ion Channel Involved in Sensing Mechanical Pain. *Cell* **180**, 956-967 e917 (2020).

93. F. Bezanilla, Voltage-gated ion channels. *IEEE Trans Nanobioscience* **4**, 34-48 (2005).

94. S. B. Long, E. B. Campbell, R. Mackinnon, Voltage sensor of Kv1.2: structural basis of electromechanical coupling. *Science* **309**, 903-908 (2005).

95. J. Sun, R. MacKinnon, Cryo-EM Structure of a KCNQ1/CaM Complex Reveals Insights into Congenital Long QT Syndrome. *Cell* **169**, 1042-1050 e1049 (2017).

96. J. R. Whicher, R. MacKinnon, Structure of the voltage-gated K(+) channel Eag1 reveals an alternative voltage sensing mechanism. *Science* **353**, 664-669 (2016).

97. W. Wang, R. MacKinnon, Cryo-EM Structure of the Open Human Ether-a-go-go-Related K(+) Channel hERG. *Cell* **169**, 422-430 e410 (2017).

98. X. Tao, R. K. Hite, R. MacKinnon, Cryo-EM structure of the open high-conductance Ca(2+)-activated K(+) channel. *Nature* **541**, 46-51 (2017).

99. J. M. Post, J. R. Hume, S. L. Archer, E. K. Weir, Direct role for potassium channel inhibition in hypoxic pulmonary vasoconstriction. *Am J Physiol* **262**, C882-890 (1992).

100. G. R. Li, M. Q. Dong, Pharmacology of cardiac potassium channels. *Adv Pharmacol* **59**, 93-134 (2010).

101. D. Singer-Lahat *et al.*, K+ channel facilitation of exocytosis by dynamic interaction with syntaxin. *J Neurosci* **27**, 1651-1658 (2007).

102. L. K. Kaczmarek, Non-conducting functions of voltage-gated ion channels. *Nat Rev Neurosci* **7**, 761-771 (2006).

103. D. Johnston *et al.*, Dendritic potassium channels in hippocampal pyramidal neurons. *The Journal of physiology* **525 Pt 1**, 75-81 (2000).

104. L. A. Pardo, Voltage-gated potassium channels in cell proliferation. *Physiology (Bethesda)* **19**, 285-292 (2004).

105. C. Serrano-Novillo *et al.*, Implication of Voltage-Gated Potassium Channels in Neoplastic Cell Proliferation. *Cancers (Basel)* **11** (2019).

106. A. O. Grant, Cardiac ion channels. *Circ Arrhythm Electrophysiol* **2**, 185-194 (2009).

107. H. Lee, M. C. Lin, H. I. Kornblum, D. M. Papazian, S. F. Nelson, Exome sequencing identifies de novo gain of function missense mutation in KCND2 in identical twins with autism and seizures that slows potassium channel inactivation. *Hum Mol Genet* **23**, 3481-3489 (2014).

108. S. E. Tomlinson, M. G. Hanna, D. M. Kullmann, S. V. Tan, D. Burke, Clinical neurophysiology of the episodic ataxias: insights into ion channel dysfunction in vivo. *Clin Neurophysiol* **120**, 1768-1776 (2009).

109. S. M. Zuberi *et al.*, A novel mutation in the human voltage-gated potassium channel gene (Kv1.1) associates with episodic ataxia type 1 and sometimes with partial epilepsy. *Brain : a journal of neurology* **122 (Pt 5)**, 817-825 (1999).

110. B. Singh *et al.*, A Kv4.2 truncation mutation in a patient with temporal lobe epilepsy. *Neurobiol Dis* **24**, 245-253 (2006).

111. A. Abd-Elsayed, M. Jackson, S. L. Gu, K. Fiala, J. Gu, Neuropathic pain and Kv7 voltage-gated potassium channels: The potential role of Kv7 activators in the treatment of neuropathic pain. *Molecular pain* **15**, 1744806919864256 (2019).

112. X. Du, N. Gamper, Potassium channels in peripheral pain pathways: expression, function and therapeutic potential. *Curr Neuropharmacol* **11**, 621-640 (2013).

113. J. Busserolles, C. Tsantoulas, A. Eschalier, J. A. Lopez Garcia, Potassium channels in neuropathic pain: advances, challenges, and emerging ideas. *Pain* **157 Suppl 1**, S7-14 (2016).

114. J. Bernstein, Ueber den zeitlichen Verlauf der negativen Schwankung des Nervenstroms. *Pflüger Archiv für die Gesammte Physiologie des Menschen und der Thiere* **1**, 173–207 (1868).

115. J. Bernstein, Untersuchungen zur Thermodynamik der bioelektrischen Ströme - Erster Theil. *Pflüger Archiv für die Gesammte Physiologie des Menschen und der Thiere* **92**, 521-562 (1902).

116. A. L. Hodgkin, A. F. Huxley, A quantitative description of membrane current and its application to conduction and excitation in nerve. *The Journal of physiology* **117**, 500-544 (1952).

117. H. C. Lai, L. Y. Jan, The distribution and targeting of neuronal voltage-gated ion channels. *Nat Rev Neurosci* **7**, 548-562 (2006).

118. J. S. Trimmer, Subcellular localization of K+ channels in mammalian brain neurons: remarkable precision in the midst of extraordinary complexity. *Neuron* **85**, 238-256 (2015).

119. R. Ranjan *et al.*, A Kinetic Map of the Homomeric Voltage-Gated Potassium Channel (Kv) Family. *Front Cell Neurosci* **13**, 358 (2019).

120. B. P. Bean, The action potential in mammalian central neurons. *Nat Rev Neurosci* **8**, 451-465 (2007).

121. H. Murakoshi, J. S. Trimmer, Identification of the Kv2.1 K+ channel as a major component of the delayed rectifier K+ current in rat hippocampal neurons. *J Neurosci* **19**, 1728-1735 (1999).

122. J. Du, L. L. Haak, E. Phillips-Tansey, J. T. Russell, C. J. McBain, Frequency-dependent regulation of rat hippocampal somato-dendritic excitability by the K+ channel subunit Kv2.1. *The Journal of physiology* **522 Pt 1**, 19-31 (2000).

123. D. J. Speca *et al.*, Deletion of the Kv2.1 delayed rectifier potassium channel leads to neuronal and behavioral hyperexcitability. *Genes Brain Behav* **13**, 394-408 (2014).

124. K. G. Klemic, C. C. Shieh, G. E. Kirsch, S. W. Jones, Inactivation of Kv2.1 potassium channels. *Biophys J* **74**, 1779-1789 (1998).

125. P. D. Sarmiere, C. M. Weigle, M. M. Tamkun, The Kv2.1 K+ channel targets to the axon initial segment of hippocampal and cortical neurons in culture and in situ. *BMC Neurosci* **9**, 112 (2008).

126. P. A. Castro, E. C. Cooper, D. H. Lowenstein, S. C. Baraban, Hippocampal heterotopia lack functional Kv4.2 potassium channels in the methylazoxymethanol model of cortical malformations and epilepsy. *J Neurosci* **21**, 6626-6634 (2001).

127. G. Bagetta, G. Nistico, J. O. Dolly, Production of seizures and brain damage in rats by alpha-dendrotoxin, a selective K+ channel blocker. *Neurosci Lett* **139**, 34-40 (1992).

128. D. S. Kim, J. O. Choi, H. D. Rim, H. J. Cho, Downregulation of voltage-gated potassium channel alpha gene expression in dorsal root ganglia following chronic constriction injury of the rat sciatic nerve. *Brain Res Mol Brain Res* **105**, 146-152 (2002).

129. M. Dumenieu, M. Oule, M. R. Kreutz, J. Lopez-Rojas, The Segregated Expression of Voltage-Gated Potassium and Sodium Channels in Neuronal Membranes: Functional Implications and Regulatory Mechanisms. *Front Cell Neurosci* **11**, 115 (2017).

130. H. H. Jerng, A. D. Lauver, P. J. Pfaffinger, DPP10 splice variants are localized in distinct neuronal populations and act to differentially regulate the inactivation properties of Kv4-based ion channels. *Mol Cell Neurosci* **35**, 604-624 (2007).

131. J. Maffie, T. Blenkinsop, B. Rudy, A novel DPP6 isoform (DPP6-E) can account for differences between neuronal and reconstituted A-type K(+) channels. *Neurosci Lett* **449**, 189-194 (2009).

132. M. S. Nadal, Y. Amarillo, E. Vega-Saenz de Miera, B. Rudy, Differential characterization of three alternative spliced isoforms of DPPX. *Brain Res* **1094**, 1-12 (2006).

133. N. Zandany *et al.*, Alternative splicing modulates Kv channel clustering through a molecular ball and chain mechanism. *Nat Commun* **6**, 6488 (2015).

134. M. Fury, S. O. Marx, A. R. Marks, Molecular BKology: the study of splicing and dicing. *Sci STKE* **2002**, pe12 (2002).

135. K. Takimoto, E. K. Yang, L. Conforti, Palmitoylation of KChIP splicing variants is required for efficient cell surface expression of Kv4.3 channels. *J Biol Chem* **277**, 26904-26911 (2002).

136. H. Misonou *et al.*, Regulation of ion channel localization and phosphorylation by neuronal activity. *Nat Neurosci* **7**, 711-718 (2004).

137. M. D. Benson *et al.*, SUMO modification regulates inactivation of the voltage-gated potassium channel Kv1.5. *Proc Natl Acad Sci U S A* **104**, 1805-1810 (2007).

138. R. Martinez-Marmol *et al.*, Ubiquitination mediates Kv1.3 endocytosis as a mechanism for protein kinase C-dependent modulation. *Sci Rep* **7**, 42395 (2017).

139. E. Bocksteins, D. J. Snyders, Electrically silent Kv subunits: their molecular and functional characteristics. *Physiology (Bethesda)* **27**, 73-84 (2012).

140. P. M. Jenkins *et al.*, Subunit-dependent axonal trafficking of distinct alpha heteromeric potassium channel complexes. *J Neurosci* **31**, 13224-13235 (2011).

141. R. W. Aldrich, Potassium channels. Mixing and matching. *Nature* **345**, 475-476 (1990).

142. E. Y. Isacoff, Y. N. Jan, L. Y. Jan, Evidence for the formation of heteromultimeric potassium channels in Xenopus oocytes. *Nature* **345**, 530-534 (1990).

143. M. Sheng, Y. J. Liao, Y. N. Jan, L. Y. Jan, Presynaptic A-current based on heteromultimeric K+ channels detected in vivo. *Nature* **365**, 72-75 (1993).

144. Y. A. Kaulin *et al.*, The dipeptidyl-peptidase-like protein DPP6 determines the unitary conductance of neuronal Kv4.2 channels. *J Neurosci* **29**, 3242-3251 (2009).

145. M. A. Peltola, J. Kuja-Panula, S. E. Lauri, T. Taira, H. Rauvala, AMIGO is an auxiliary subunit of the Kv2.1 potassium channel. *EMBO Rep* **12**, 1293-1299 (2011).

146. Y. L. Kuo *et al.*, K(+) Channel Modulatory Subunits KChIP and DPP Participate in Kv4-Mediated Mechanical Pain Control. *J Neurosci* **37**, 4391-4404 (2017).

147. K. J. Rhodes *et al.*, Voltage-gated K+ channel beta subunits: expression and distribution of Kv beta 1 and Kv beta 2 in adult rat brain. *J Neurosci* **16**, 4846-4860 (1996).

148. M. Roura-Ferrer *et al.*, Impact of KCNE subunits on KCNQ1 (Kv7.1) channel membrane surface targeting. *J Cell Physiol* **225**, 692-700 (2010).

149. L. Sole *et al.*, KCNE4 suppresses Kv1.3 currents by modulating trafficking, surface expression and channel gating. *J Cell Sci* **122**, 3738-3748 (2009).

150. Y. A. Kuryshev, B. A. Wible, T. I. Gudz, A. N. Ramirez, A. M. Brown, KChAP/Kvbeta1.2 interactions and their effects on cardiac Kv channel expression. *Am J Physiol Cell Physiol* **281**, C290-299 (2001).

151. E. Bocksteins *et al.*, Conserved negative charges in the N-terminal tetramerization domain mediate efficient assembly of Kv2.1 and Kv2.1/Kv6.4 channels. *J Biol Chem* **284**, 31625-31634 (2009).

152. N. V. Shen, P. J. Pfaffinger, Molecular recognition and assembly sequences involved in the subfamily-specific assembly of voltage-gated K+ channel subunit proteins. *Neuron* **14**, 625-633 (1995).

153. T. E. Lee, L. H. Philipson, A. Kuznetsov, D. J. Nelson, Structural determinant for assembly of mammalian K+ channels. *Biophys J* **66**, 667-673 (1994).

154. M. Li, Y. N. Jan, L. Y. Jan, Specification of subunit assembly by the hydrophilic amino-terminal domain of the Shaker potassium channel. *Science* **257**, 1225-1230 (1992).

155. D. M. Papazian, Potassium channels: some assembly required. *Neuron* **23**, 7-10 (1999).

156. N. V. Shen, P. J. Pfaffinger, Molecular recognition and assembly sequences involved in the subfamily-specific assembly of voltage-gated K^+ channel subunit proteins. *Neuron* **14**, 625-633 (1995).

157. J. Xu, W. Yu, Y. N. Jan, L. Y. Jan, M. Li, Assembly of voltage-gated potassium channels. Conserved hydrophilic motifs determine subfamily-specific interactions between the alpha-subunits. *J Biol Chem* **270**, 24761-24768 (1995).

158. J. Lu, J. M. Robinson, D. Edwards, C. Deutsch, T1-T1 interactions occur in ER membranes while nascent Kv peptides are still attached to ribosomes. *Biochemistry* **40**, 10934-10946 (2001).

159. L. Tu, C. Deutsch, Evidence for dimerization of dimers in K+ channel assembly. *Biophys J* **76**, 2004-2017 (1999).

160. J. A. Drewe, S. Verma, G. Frech, R. H. Joho, Distinct spatial and temporal expression patterns of K+ channel mRNAs from different subfamilies. *J Neurosci* **12**, 538-548 (1992).

161. A. Castellano *et al.*, Identification and functional characterization of a K+ channel alpha-subunit with regulatory properties specific to brain. *J Neurosci* **17**, 4652-4661 (1997).

162. N. Ottschytsch, A. L. Raes, J. P. Timmermans, D. J. Snyders, Domain analysis of Kv6.3, an electrically silent channel. *The Journal of physiology* **568**, 737-747 (2005).

163. J. P. Hugnot *et al.*, Kv8.1, a new neuronal potassium channel subunit with specific inhibitory properties towards Shab and Shaw channels. *EMBO J* **15**, 3322-3331 (1996).

164. M. Stocker, M. Hellwig, D. Kerschensteiner, Subunit assembly and domain analysis of electrically silent K+ channel alpha-subunits of the rat Kv9 subfamily. *J Neurochem* **72**, 1725-1734 (1999).

165. N. Ottschytsch, A. Raes, D. Van Hoorick, D. J. Snyders, Obligatory heterotetramerization of three previously uncharacterized Kv channel alpha-subunits identified in the human genome. *Proc Natl Acad Sci U S A* **99**, 7986-7991 (2002).

166. A. J. Patel, M. Lazdunski, E. Honore, Kv2.1/Kv9.3, a novel ATP-dependent delayed-rectifier K+ channel in oxygen-sensitive pulmonary artery myocytes. *EMBO J* **16**, 6615-6625 (1997).

167. M. Salinas, F. Duprat, C. Heurteaux, J. P. Hugnot, M. Lazdunski, New modulatory alpha subunits for mammalian Shab K+ channels. *J Biol Chem* **272**, 24371-24379 (1997).

168. X. R. Zhu, R. Netzer, K. Bohlke, Q. Liu, O. Pongs, Structural and functional characterization of Kv6.2 a new gamma-subunit of voltage-gated potassium channel. *Receptors Channels* **6**, 337-350 (1999).

169. Y. Sano *et al.*, Molecular cloning and characterization of Kv6.3, a novel modulatory subunit for voltage-gated K(+) channel Kv2.1. *FEBS Lett* **512**, 230-234 (2002).

170. E. Bocksteins, A. J. Labro, D. J. Snyders, D. P. Mohapatra, The electrically silent Kv6.4 subunit confers hyperpolarized gating charge movement in Kv2.1/Kv6.4 heterotetrameric channels. *PLoS One* **7**, e37143 (2012).

171. D. Kerschensteiner, F. Soto, M. Stocker, Fluorescence measurements reveal stoichiometry of K+ channels formed by modulatory and delayed rectifier alpha-subunits. *Proc Natl Acad Sci U S A* **102**, 6160-6165 (2005).

172. L. Moller, G. Regnier, A. J. Labro, R. Blunck, D. J. Snyders, Determining the correct stoichiometry of Kv2.1/Kv6.4 heterotetramers, functional in multiple stoichiometrical configurations. *Proc Natl Acad Sci U S A* 10.1073/pnas.1916166117 (2020).

173. A. Pisupati *et al.*, The S6 gate in regulatory Kv6 subunits restricts heteromeric K(+) channel stoichiometry. *J Gen Physiol* **150**, 1702-1721 (2018).

174. Y. Amarillo *et al.*, Ternary Kv4.2 channels recapitulate voltage-dependent inactivation kinetics of A-type K+ channels in cerebellar granule neurons. *The Journal of physiology* **586**, 2093-2106 (2008).

175. E. J. Beck, M. Bowlby, W. F. An, K. J. Rhodes, M. Covarrubias, Remodelling inactivation gating of Kv4 channels by KChIP1, a small-molecular-weight calcium-binding protein. *The Journal of physiology* **538**, 691-706 (2002).

176. B. D. Clark *et al.*, DPP6 Localization in Brain Supports Function as a Kv4 Channel Associated Protein. *Front Mol Neurosci* **1**, 8 (2008).

177. H. H. Jerng, P. J. Pfaffinger, Incorporation of DPP6a and DPP6K variants in ternary Kv4 channel complex reconstitutes properties of A-type K current in rat cerebellar granule cells. *PLoS One* **7**, e38205 (2012).

178. E. Seikel, J. S. Trimmer, Convergent modulation of Kv4.2 channel alpha subunits by structurally distinct DPPX and KChIP auxiliary subunits. *Biochemistry* **48**, 5721-5730 (2009).

179. E. Zagha *et al.*, DPP10 modulates Kv4-mediated A-type potassium channels. *J Biol Chem* **280**, 18853-18861 (2005).

180. B. Callsen *et al.*, Contribution of N- and C-terminal Kv4.2 channel domains to KChIP interaction [corrected]. *The Journal of physiology* **568**, 397-412 (2005).

181. M. Pioletti, F. Findeisen, G. L. Hura, D. L. Minor, Jr., Three-dimensional structure of the KChIP1-Kv4.3 T1 complex reveals a cross-shaped octamer. *Nat Struct Mol Biol* **13**, 987-995 (2006).

182. H. Wang *et al.*, Structural basis for modulation of Kv4 K+ channels by auxiliary KChIP subunits. *Nat Neurosci* **10**, 32-39 (2007).

183. M. Kitazawa, Y. Kubo, K. Nakajo, The stoichiometry and biophysical properties of the Kv4 potassium channel complex with K+ channel-interacting protein (KChIP) subunits are variable, depending on the relative expression level. *J Biol Chem* **289**, 17597-17609 (2014).

184. B. Hasdemir, D. J. Fitzgerald, I. A. Prior, A. V. Tepikin, R. D. Burgoyne, Traffic of Kv4 K+ channels mediated by KChIP1 is via a novel post-ER vesicular pathway. *J Cell Biol* **171**, 459-469 (2005).

185. N. C. Foeger, W. Wang, R. L. Mellor, J. M. Nerbonne, Stabilization of Kv4 protein by the accessory K(+) channel interacting protein 2 (KChIP2) subunit is required for the generation of native myocardial fast transient outward K(+) currents. *The Journal of physiology* **591**, 4149-4166 (2013).

186. K. Kunjilwar, Y. Qian, P. J. Pfaffinger, Functional stoichiometry underlying KChIP regulation of Kv4.2 functional expression. *J Neurochem* **126**, 462-472 (2013).

187. Y. Kin, Y. Misumi, Y. Ikehara, Biosynthesis and characterization of the brain-specific membrane protein DPPX, a dipeptidyl peptidase IV-related protein. *J Biochem* **129**, 289-295 (2001).

188. N. C. Foeger, A. J. Norris, L. M. Wren, J. M. Nerbonne, Augmentation of Kv4.2-encoded currents by accessory dipeptidyl peptidase 6 and 10 subunits reflects selective cell surface Kv4.2 protein stabilization. *J Biol Chem* **287**, 9640-9650 (2012).

189. B. M. Nadin, P. J. Pfaffinger, Dipeptidyl peptidase-like protein 6 is required for normal electrophysiological properties of cerebellar granule cells. *J Neurosci* **30**, 8551-8565 (2010).

190. X. Ren, Y. Hayashi, N. Yoshimura, K. Takimoto, Transmembrane interaction mediates complex formation between peptidase homologues and Kv4 channels. *Mol Cell Neurosci* **29**, 320-332 (2005).

191. H. H. Jerng, K. Dougherty, M. Covarrubias, P. J. Pfaffinger, A novel N-terminal motif of dipeptidyl peptidase-like proteins produces rapid inactivation of KV4.2 channels by a pore-blocking mechanism. *Channels (Austin)* **3**, 448-461 (2009).

192. H. Soh, S. A. Goldstein, I SA channel complexes include four subunits each of DPP6 and Kv4.2. *J Biol Chem* **283**, 15072-15077 (2008).

193. M. Kitazawa, Y. Kubo, K. Nakajo, Kv4.2 and accessory dipeptidyl peptidase-like protein 10 (DPP10) subunit preferentially form a 4:2 (Kv4.2:DPP10) channel complex. *J Biol Chem* **290**, 22724-22733 (2015).

194. K. Dougherty, M. Covarrubias, A dipeptidyl aminopeptidase-like protein remodels gating charge dynamics in Kv4.2 channels. *J Gen Physiol* **128**, 745-753 (2006).

195. H. H. Jerng, Y. Qian, P. J. Pfaffinger, Modulation of Kv4.2 channel expression and gating by dipeptidyl peptidase 10 (DPP10). *Biophys J* **87**, 2380-2396 (2004).

196. P. Strop, A. J. Bankovich, K. C. Hansen, K. C. Garcia, A. T. Brunger, Structure of a human A-type potassium channel interacting protein DPPX, a member of the dipeptidyl aminopeptidase family. *J Mol Biol* **343**, 1055-1065 (2004).

197. L. Lin, L. K. Long, M. M. Hatch, D. A. Hoffman, DPP6 domains responsible for its localization and function. *J Biol Chem* **289**, 32153-32165 (2014).

198. E. R. Liman, P. Hess, F. Weaver, G. Koren, Voltage-sensing residues in the S4 region of a mammalian K+ channel. *Nature* **353**, 752-756 (1991).

199. D. M. Papazian, L. C. Timpe, Y. N. Jan, L. Y. Jan, Alteration of voltage-dependence of Shaker potassium channel by mutations in the S4 sequence. *Nature* **349**, 305-310 (1991).

200. A. Cha, F. Bezanilla, Characterizing voltage-dependent conformational changes in the Shaker K+ channel with fluorescence. *Neuron* **19**, 1127-1140 (1997).

201. D. M. Starace, F. Bezanilla, A proton pore in a potassium channel voltage sensor reveals a focused electric field. *Nature* **427**, 548-553 (2004).

202. V. Yarov-Yarovoy, D. Baker, W. A. Catterall, Voltage sensor conformations in the open and closed states in ROSETTA structural models of K(+) channels. *Proc Natl Acad Sci U S A* **103**, 7292-7297 (2006).

203. L. Catacuzzeno, F. Franciolini, Simulation of Gating Currents of the Shaker K Channel Using a Brownian Model of the Voltage Sensor. *Biophys J* **117**, 2005-2019 (2019).

204. P. Bjelkmar, P. S. Niemela, I. Vattulainen, E. Lindahl, Conformational changes and slow dynamics through microsecond polarized atomistic molecular simulation of an integral Kv1.2 ion channel. *PLoS Comput Biol* **5**, e1000289 (2009).

205. R. Blunck, Z. Batulan, Mechanism of electromechanical coupling in voltage-gated potassium channels. *Front Pharmacol* **3**, 166 (2012).

206. E. Faure, G. Starek, H. McGuire, S. Berneche, R. Blunck, A limited 4 A radial displacement of the S4-S5 linker is sufficient for internal gate closing in Kv channels. *J Biol Chem* **287**, 40091-40098 (2012).

207. E. Vargas, F. Bezanilla, B. Roux, In search of a consensus model of the resting state of a voltage-sensing domain. *Neuron* **72**, 713-720 (2011).

208. M. Pathak, L. Kurtz, F. Tombola, E. Isacoff, The cooperative voltage sensor motion that gates a potassium channel. *J Gen Physiol* **125**, 57-69 (2005).

209. T. Kalstrup, R. Blunck, Dynamics of internal pore opening in K(V) channels probed by a fluorescent unnatural amino acid. *Proc Natl Acad Sci U S A* **110**, 8272-8277 (2013).

210. Z. Lu, A. M. Klem, Y. Ramu, Ion conduction pore is conserved among potassium channels. *Nature* **413**, 809-813 (2001).

211. Z. Lu, A. M. Klem, Y. Ramu, Coupling between voltage sensors and activation gate in voltage-gated K+ channels. *J Gen Physiol* **120**, 663-676 (2002).

212. T. Kalstrup, R. Blunck, S4-S5 linker movement during activation and inactivation in voltage-gated K(+) channels. *Proc Natl Acad Sci U S A* **115**, E6751-E6759 (2018).

213. J. L. Ledwell, R. W. Aldrich, Mutations in the S4 region isolate the final voltage-dependent cooperative step in potassium channel activation. *J Gen Physiol* **113**, 389-414 (1999).

214. G. J. Soler-Llavina, T. H. Chang, K. J. Swartz, Functional interactions at the interface between voltage-sensing and pore domains in the Shaker K(v) channel. *Neuron* **52**, 623-634 (2006).

215. Z. Batulan, G. A. Haddad, R. Blunck, An intersubunit interaction between S4-S5 linker and S6 is responsible for the slow off-gating component in Shaker K+ channels. *J Biol Chem* **285**, 14005-14019 (2010).

216. D. A. Doyle *et al.*, The structure of the potassium channel: molecular basis of K+ conduction and selectivity. *Science* **280**, 69-77 (1998).

217. S. Y. Noskov, S. Berneche, B. Roux, Control of ion selectivity in potassium channels by electrostatic and dynamic properties of carbonyl ligands. *Nature* **431**, 830-834 (2004).

218. S. Berneche, B. Roux, Energetics of ion conduction through the K+ channel. *Nature* **414**, 73-77 (2001).

219. T. Hoshi, W. N. Zagotta, R. W. Aldrich, Biophysical and molecular mechanisms of Shaker potassium channel inactivation. *Science* **250**, 533-538 (1990).

220. S. D. Demo, G. Yellen, The inactivation gate of the Shaker K+ channel behaves like an open-channel blocker. *Neuron* **7**, 743-753 (1991).

221. M. Zhou, J. H. Morais-Cabral, S. Mann, R. MacKinnon, Potassium channel receptor site for the inactivation gate and quaternary amine inhibitors. *Nature* **411**, 657-661 (2001).

222. M. Gebauer *et al.*, N-type inactivation features of Kv4.2 channel gating. *Biophys J* **86**, 210-223 (2004).

223. C. Antz, B. Fakler, Fast Inactivation of Voltage-Gated K(+) Channels: From Cartoon to Structure. *News Physiol Sci* **13**, 177-182 (1998).

224. J. A. Encinar *et al.*, Inactivating peptide of the Shaker B potassium channel: conformational preferences inferred from studies on simple model systems. *Biochem J* **331 (Pt 2)**, 497-504 (1998).

225. G. J. Stephens, B. Robertson, Inactivation of the cloned potassium channel mouse Kv1.1 by the human Kv3.4 'ball' peptide and its chemical modification. *The Journal of physiology* **484 (Pt 1)**, 1-13 (1995).

226. H. Schrempf *et al.*, A prokaryotic potassium ion channel with two predicted transmembrane segments from Streptomyces lividans. *EMBO J* **14**, 5170-5178 (1995).

227. L. G. Cuello, V. Jogini, D. M. Cortes, E. Perozo, Structural mechanism of C-type inactivation in K(+) channels. *Nature* **466**, 203-208 (2010).

228. L. G. Cuello *et al.*, Structural basis for the coupling between activation and inactivation gates in K(+) channels. *Nature* **466**, 272-275 (2010).

229. J. Ostmeyer, S. Chakrapani, A. C. Pan, E. Perozo, B. Roux, Recovery from slow inactivation in K+ channels is controlled by water molecules. *Nature* **501**, 121-124 (2013).

230. J. D. Lueck *et al.*, Atomic mutagenesis in ion channels with engineered stoichiometry. *Elife* **5** (2016).

231. J. Lopez-Barneo, T. Hoshi, S. H. Heinemann, R. W. Aldrich, Effects of external cations and mutations in the pore region on C-type inactivation of Shaker potassium channels. *Receptors Channels* **1**, 61-71 (1993).

232. Y. Yang, Y. Yan, F. J. Sigworth, How does the W434F mutation block current in Shaker potassium channels? *J Gen Physiol* **109**, 779-789 (1997).

233. T. W. Claydon, M. Vaid, S. Rezazadeh, S. J. Kehl, D. Fedida, 4-aminopyridine prevents the conformational changes associated with p/c-type inactivation in shaker channels. *J Pharmacol Exp Ther* **320**, 162-172 (2007).

234. K. L. Choi, R. W. Aldrich, G. Yellen, Tetraethylammonium blockade distinguishes two inactivation mechanisms in voltage-activated K+ channels. *Proc Natl Acad Sci U S A* **88**, 5092-5095 (1991).

235. R. W. Aldrich, Inactivation of voltage-gated delayed potassium current in molluscan neurons. A kinetic model. *Biophys J* **36**, 519-532 (1981).

236. Y. M. Cheng *et al.*, Molecular determinants of U-type inactivation in Kv2.1 channels. *Biophys J* **101**, 651-661 (2011).

237. K. G. Klemic, G. E. Kirsch, S. W. Jones, U-type inactivation of Kv3.1 and Shaker potassium channels. *Biophys J* **81**, 814-826 (2001).

238. H. T. Kurata, K. W. Doerksen, J. R. Eldstrom, S. Rezazadeh, D. Fedida, Separation of P/C- and U-type inactivation pathways in Kv1.5 potassium channels. *The Journal of physiology* **568**, 31-46 (2005).

239. R. Bahring, L. M. Boland, A. Varghese, M. Gebauer, O. Pongs, Kinetic analysis of open- and closed-state inactivation transitions in human Kv4.2 A-type potassium channels. *The Journal of physiology* **535**, 65-81 (2001).

240. E. J. Beck, M. Covarrubias, Kv4 channels exhibit modulation of closed-state inactivation in inside-out patches. *Biophys J* **81**, 867-883 (2001).

241. L. Coonen *et al.*, The Selectivity Filter Is Involved in the U-Type Inactivation Process of Kv2.1 and Kv3.1 Channels. *Biophys J* **118**, 2612-2620 (2020).

242. R. Bahring, J. Barghaan, R. Westermeier, J. Wollberg, Voltage sensor inactivation in potassium channels. *Front Pharmacol* **3**, 100 (2012).

243. J. D. Fineberg, D. M. Ritter, M. Covarrubias, Modeling-independent elucidation of inactivation pathways in recombinant and native A-type Kv channels. *J Gen Physiol* **140**, 513-527 (2012).

244. K. Dougherty, J. A. De Santiago-Castillo, M. Covarrubias, Gating charge immobilization in Kv4.2 channels: the basis of closed-state inactivation. *J Gen Physiol* **131**, 257-273 (2008).

245. M. R. Skerritt, D. L. Campbell, Role of S4 positively charged residues in the regulation of Kv4.3 inactivation and recovery. *Am J Physiol Cell Physiol* **293**, C906-914 (2007).

246. M. R. Skerritt, D. L. Campbell, Non-native R1 substitution in the s4 domain uniquely alters Kv4.3 channel gating. *PLoS One* **3**, e3773 (2008).

247. M. R. Skerritt, D. L. Campbell, Contribution of electrostatic and structural properties of Kv4.3 S4 arginine residues to the regulation of channel gating. *Biochim Biophys Acta* **1788**, 458-469 (2009).

248. J. Wollberg, R. Bahring, Intra- and Intersubunit Dynamic Binding in Kv4.2 Channel Closed-State Inactivation. *Biophys J* **110**, 157-175 (2016).

249. O. Yifrach, R. MacKinnon, Energetics of pore opening in a voltage-gated K(+) channel. *Cell* **111**, 231-239 (2002).

250. J. Barghaan, R. Bahring, Dynamic coupling of voltage sensor and gate involved in closed-state inactivation of kv4.2 channels. *J Gen Physiol* **133**, 205-224 (2009).

251. R. Bahring, M. Covarrubias, Mechanisms of closed-state inactivation in voltage-gated ion channels. *The Journal of physiology* **589**, 461-479 (2011).

Chapter 2 – Technical Basis

2.1 Electrophysiology

The third and fifth chapter present electrophysiological investigation of ion channels. Biological membranes form barriers between the cell intracellular and extracellular or compartments within the cell and exhibit specific permeabilities to ions through embedded ion channels. The asymmetric distribution of ions between the separated compartments results in a concentration gradient and an electrical potential difference, i.e. membrane potential ($V_{membrane}$). The ion flux across the membrane is driven by this electrochemical gradient and changes the respective concentrations of the separated compartments. This, in turn, changes the membrane potential. Depending on the experiment, the ionic current or the change in the membrane potential can be measured.

2.1.1 Classical Patch-clamp Method

The patch clamp technique (1-3) enables researchers to record changes in the membrane potential or ionic currents from cells and isolated membranes. Changes in the membrane potential are recorded in the current-clamp mode, which is typically used when recording action potentials in excitable cells. The voltage-clamp mode, on the other hand, allows to record ionic currents and is used in the research presented in this thesis. The underlying principle is to seal off the plasma membrane with a “patch pipette” and record changes in the ionic conductance (figure 2.1A). In the voltage-clamp mode, the voltage is kept constant by injecting current into the system to compensate the ionic current across the membrane. The injected current is recorded. The patch pipette, used in these experiments to seal off the plasma membrane, is a narrow glass microelectrode, filled with electrolyte solution which is in contact with an Ag/AgCl-electrode. The tight seal between membrane and recording electrode results in a high resistance, which is necessary to minimize noise and any leakage between the solutions inside and outside the pipette and isolate ionic currents that flow directly through the membrane via ion channels. The recording electrode of the patch pipette connects to an amplifier to measure the current and to control the voltage. A second “reference” electrode is placed in the bath solution surrounding the cell, setting it to ground potential.

Three main configurations are commonly used to study either macroscopic or single channel currents: cell-attached, whole cell and excised patch (figure 2.1B). The cell-attached configuration leaves the membrane in the recording pipette intact and records ionic currents that originate from flux through this sealed-off area of the membrane, which is typically 1-3 µm in diameter. When the channel of interest is expressed at very low levels, currents obtained from cell-attached recordings are from single (or very few) ion channels. Another way to record single channel currents is from excised patches, where a small part of the plasma membrane is pulled out from the rest of the cell by pulling the pipette backwards. According to the orientation of the membrane, excised patches can be "inside-out" or "outside-out". Furthermore, excised patches allow for a direct control of the composition of not only the extracellular, but also the intracellular solution. If more suction is applied in the cell-attached mode, the membrane breaks and the whole-cell configuration is obtained. Here, the patch pipette provides low-resistance access to the whole cell so that the transmembrane voltage of the entire plasma membrane can be controlled. All ion channels in the membrane thus contribute to the ion flux, resulting in macroscopic currents.

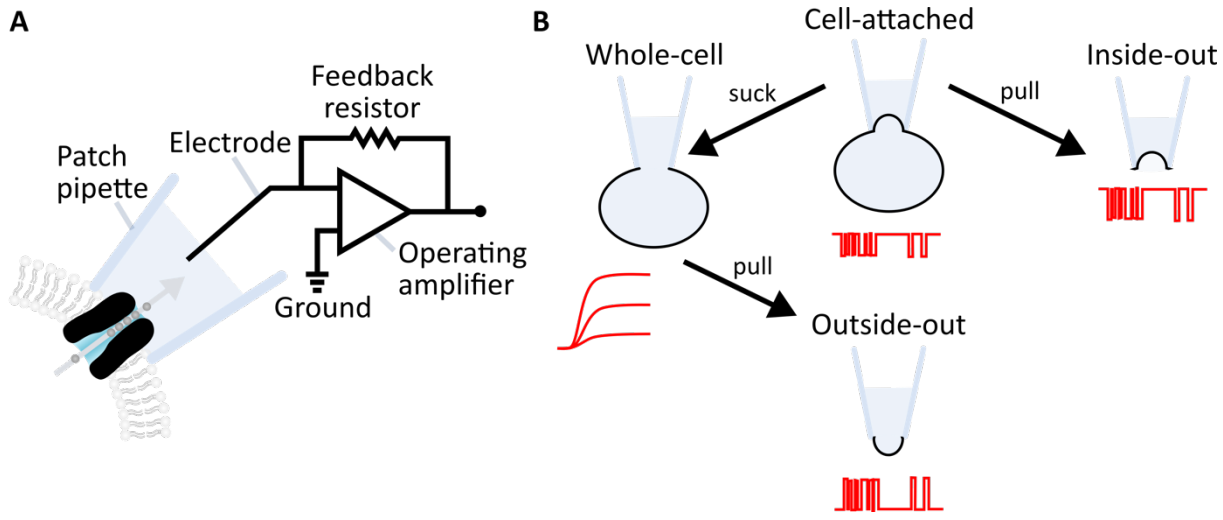

Figure 2.1 Patch clamp method
A) Illustration of the voltage-clamp technique. A patch pipette seals off a portion of the plasma membrane and the recording electrode measures the ionic current through the ion channel imbedded in the membrane. **B)** Different patch clamp modes. Cell-attached mode measures single channel currents through the membrane isolated by the patch pipette. Pulling the patch pipette away from the cell breaks the plasma membrane and results in an excised inside-out patch allowing for high signal to noise single channel recordings. Applying negative pressure (suck) through the patch pipette breaks the cell membrane open, resulting in the whole-cell mode, which allows for macroscopic currents to be recorded. Pulling the patch pipette away from the cell in whole cell mode breaks the plasma membrane and results in an excised outside-out patch allowing for high signal to noise single channel recordings.

To record large macroscopic currents from big cells like *Xenopus* oocytes, the two electrode voltage clamp (TEVC) technique is often used. As the name suggests, two electrodes, one for voltage sensing, the other for current injection, are used to impale the large cell and monitor the current. Due to the localized injection of current, the large membrane of a *Xenopus* oocytes might not be uniformly charged. This makes it impossible to resolve fast kinetics as channels are exposed to a heterogenous membrane voltage and currents therefore reflect the ensemble of differently clamped channels. To circumvent this problem, the cut open voltage clamp (COVC) technique was developed (4-7).

2.1.2 Cut Open Oocyte Voltage Clamp

The cut-open voltage clamp technique allows for high temporal resolution of electrophysiological recordings with fast kinetics. Rather than injecting current from a small localized position, as in the TEVC technique, this technique matches the size of the current injection site to the size of the clamped membrane, resulting in the quick and uniformly charged membrane (figure 2.2A). The oocyte is mounted onto a chamber dividing the membrane into three areas (figure 2.2B). The ionic current is recorded from the top region. The extracellular, i.e. the top and middle compartment, is clamped to 0 mV. Clamping the chamber's middle compartment to the same potential as the top chamber, guards against any leakage currents through the seals. The bottom chamber is continuous with the cell's interior. This is accomplished by chemically permeabilizing or physically opening (cut open) of the membrane. The bottom chamber and the intracellular of the oocyte are clamped to the command voltage ($V_{membrane}$) as differentially recorded between the impaling microelectrode V1 and the extracellular V2 electrode. The current is directly injected through the permeabilized membrane exposed to the bottom chamber, eliminating the high access resistance of a microelectrode. In this configuration, the membrane can be uniformly charged in sub-milliseconds and allows for high-resolution recordings of fast charge movements. The physical access to the intracellular solution also allows for intracellular solution exchange. Mounting this setup on an upright fluorescence microscope make it possible to simultaneously record functional changes of the channel through ionic currents and conformational changes through site-directed fluorescence measurements. This specialized COVC technique is termed voltage clamp fluorometry (VCF), which will be introduced below (2.2.1 *Voltage-clamp Fluorometry*).

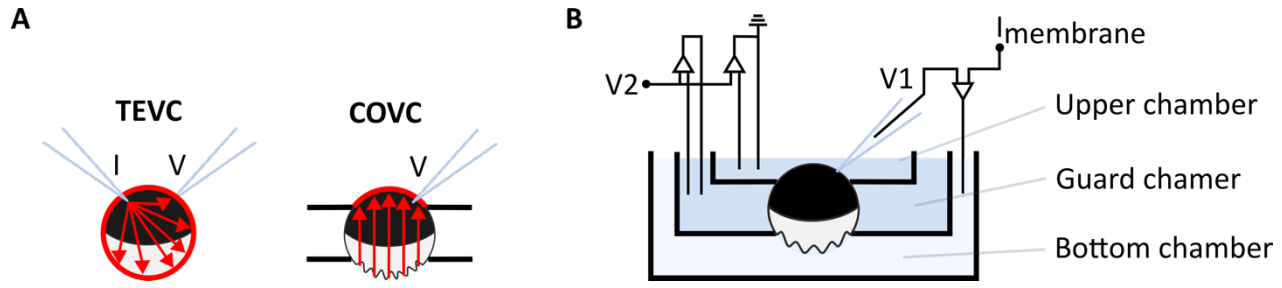

Figure 2.2 Cut open voltage clamp technique
A) Cartoon illustrating the current injection (red arrows) and clamped membrane (red line) in TEVC and COVC. **B)** The COVC setup is comprised of three chambers. The upper and guard chamber are clamped to 0 mV (measured by V2), while the bottom chamber is clamped at the command voltage (measured by V1). Current is injected into the permeabilized oocyte via the bottom chamber.

In this thesis, electrophysiological measurements are used to study the properties of ion channel complexes. In chapter three, we study the effect of the modulatory subunit Kv6.4 on Kv2.1/6.4 heteromeric channels. To this aim, our collaborators performed whole cell patch clamp recordings. In chapter five, we investigate the effect of the DPP6 auxiliary subunit on Kv4.2 channel complexes using the COVC technique.

2.2 Basis of Fluorescence Techniques

Research presented in the third, fourth and fifth chapter includes studies based on fluorescence measurements unveiling information about the structural details of protein complexes. This section introduces the underlying concepts of fluorescence.

The Jablonski diagram illustrates the process of light absorption and emission (figure 2.3A) (8). Fluorophores can have different energies depending on their excitation and populate either the ground state S_0 or when excited, a higher electronic state S_1 or S_2. Each of these states has distinct vibrational energy levels. Due to the large energetic difference between ground S_0 and the excited S_1 state, the higher state cannot be induced by heat but only by light. The absorption of a photon of the right energy thus results in the excitation of an electron to the higher energy level. From there, the fluorophore relaxes to the lowest vibrational energy level of S_1 before it returns to a higher vibrational state of the ground state S_0, followed by relaxation of the vibrational energy. This return can be non-radiative, when the energy is dissipated into the molecule or the surrounding, or result in the emission of a photon of lower energy compared to the photon that was initially absorbed. This energy difference of absorbed

and emitted photon is the basis for the Stokes shift from higher energy (shorter) absorption wavelength toward lower energy (longer) emission wavelengths in the spectra (figure 2.3B).

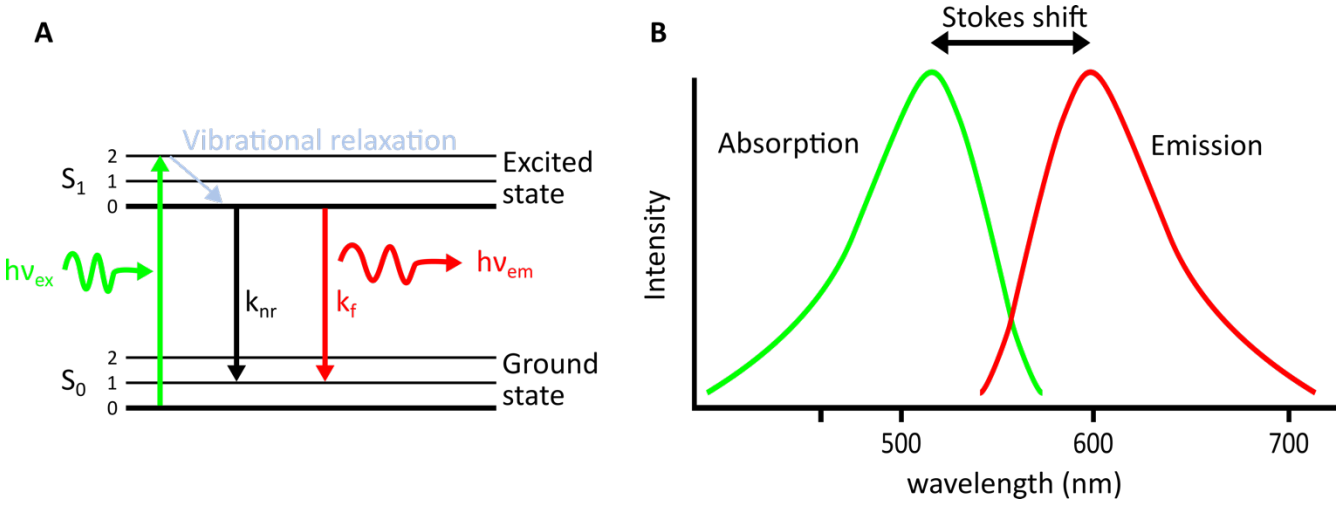

Figure 2.3 Fluorescence spectroscopy
A) Jablonski diagram illustrating the process of fluorescence. Electrons in the ground state S_0 are excited by photons ($h\nu_{ex}$, green representing the wavelength) to a vibrational level of the S_1 state from where it relaxes to the lowest S_1 state before returning to the ground state. The return can be non-radiative (black, k_{nr}) or result in fluorescence (k_f), i.e. the emittance of a lower energy photon ($h\nu_{em}$, red representing the wavelength). **B)** Representative absorption (green) and emission (red) spectra highlighting the stokes shift between absorption and emission.

Depending on the requirements, researchers can choose from a multitude of different fluorophores, which can be grouped into biological fluorophores, organic dyes and quantum dots. Quantum dots are nanoscale semiconductors, whereas biological fluorophores and organic dyes are organic molecules and feature a system of delocalized electrons through conjugated double bonds (8). Biological fluorophores such as the green fluorescent protein (GFP) and its derivatives can be directly conjugated to proteins of interest through genetic engineering (9). GFPs are valued for their autocatalytic chromophore formation eliminating the need of further manipulation. GFP's chromophore is formed by the tripeptide S65, Y66 and G67, which is located at the center of a cylinder-shaped ß-barrel structure and undergoes a process of chromophore formation that is referred to as maturation (figure 2.4A and B). This maturation process consists of protein folding, peptide cyclisation, oxidation and dehydration and depends on several factors, including temperature and aeration (10). Even in improved derivatives like the superfolder GFP (sfGFP) (11), a fraction of proteins fails to maturate and remain "dark". Two major drawbacks of using GFP as a fluorescent marker are this

possibility of incomplete maturation and the size of the fluorescent protein. Opposed to fluorescent proteins, organic dyes like tetramethylrhodamine (TMR) are much smaller and therefore better suited for linking to proteins without interfering with their function (figure 2.4C). Moreover, optimized organic dyes are typically brighter and more stable which makes them ideal markers when exciting for extended times. Inaccessible regions, e.g. transmembrane segments and intracellular parts, can be specifically labeled by site-directed incorporation of fluorescent unnatural amino acids (12).

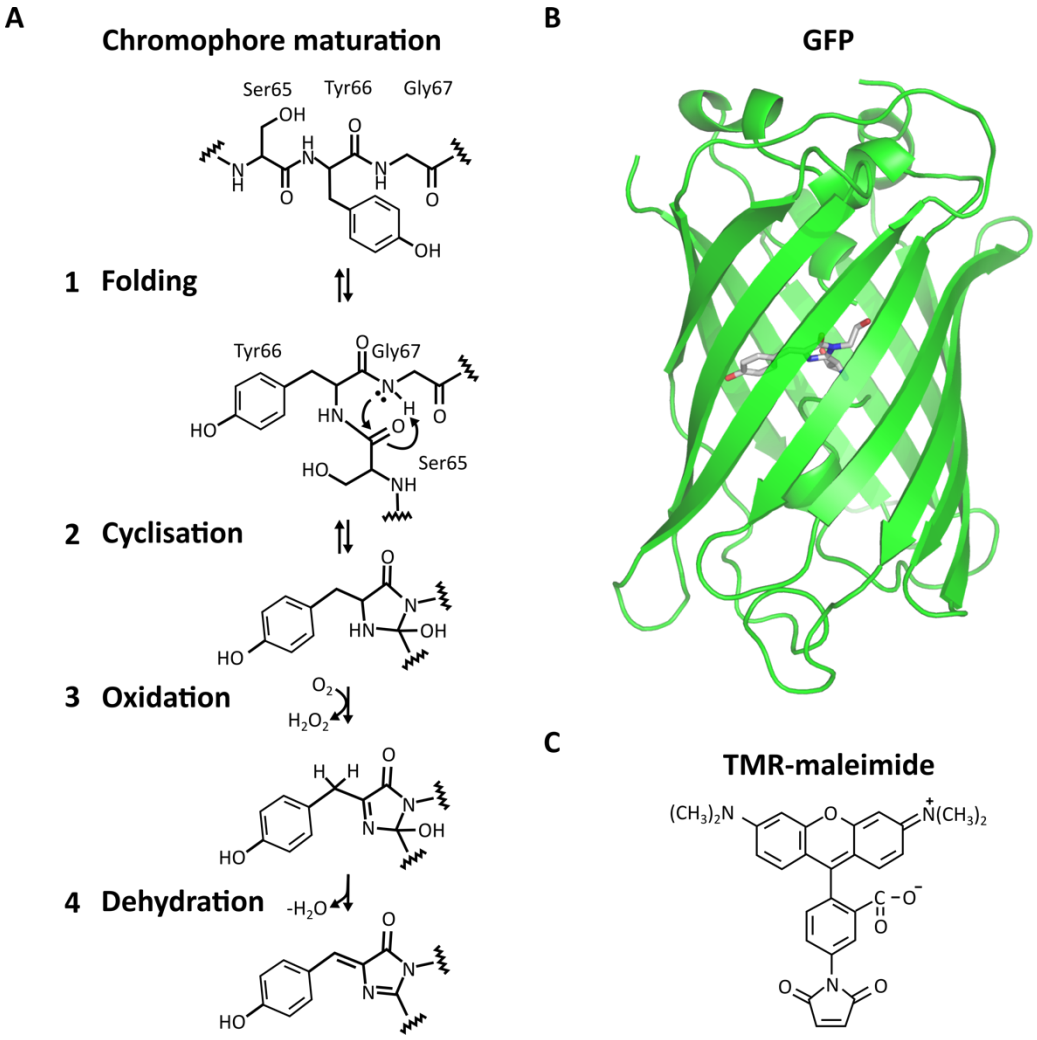

Figure 2.4 Fluorescent molecules
A) Maturation of GFP from the tripeptide to the chromophore, adapted from Craggs et al. (10). **B)** Crystal structure of GFP in cartoon representation featuring the matured chromophore in the center of the β-barrel structure (structure obtained from pdb 1EMB (13)). **C)** Chemical structure of TMR with a thiol-reactive maleimide-tag that allows covalent binding of the fluorophore to cysteines.

The brightness of the fluorophore depends on many factors. It is characterized by its molar extinction coefficient, i.e. the amount of light that can be absorbed at a specific wavelength, and its quantum yield (QY) (8). The QY is defined as the ratio of emitted to absorbed photons and can depend on the fluorophore's interaction with its environment. When the fluorophore interacts with another molecule, its fluorescence can be decreased. Generally, the process of decreasing the fluorescence intensity is referred to as *quenching*, which can be static or dynamic. Static quenching is characterized by the formation of a nonfluorescent stable complex of fluorophore and quencher. During dynamic quenching, on the other hand, the fluorophore collides with the quencher and temporarily transfers its energy from the excited state to the quencher. Dynamic quenchers need to be within 2-3 Å of the fluorophore to absorb its energy. As a result of dynamic quenching, the fluorophore returns from its excited state to the ground state without emitting a photon. The presence of static or dynamic quenchers can be used to study protein-protein interactions and conformational changes. In these experiments, one can further distinguish between quenchers that are in solution, such as oxygen, and quenchers that are part of the protein (14). Aromatic amino acids, especially tryptophan and tyrosine, are strong quenchers and have been used to study protein structures (15-18). Apart from changing the fluorophore's intensity temporarily, its fluorescence can be permanently lost. The photochemical destruction of the fluorophore is referred to as photobleaching. Upon prolonged and high intensity illumination, the chromophore is chemically destroyed rendering the molecule non-fluorescent. This photobleaching characteristic as well as the fluorophore's sensitivity to the local environment make them a powerful tool in studying protein structures.

Apart from electrophysiological investigations, the work presented in this thesis is based on fluorescence measurements. Single subunit counting experiments on Kv2.1/6.4 heterotetramers and TACAN channels, presented in chapter three and four, respectively, are based on the photobleaching properties of GFP. The technique is further introduced below (2.2.2 *Single Subunit Counting*). Chapter five presents quenching/unquenching fluorescence traces of TMR-labeled Kv4 channels obtained by voltage-clamp fluorometry, which will be introduced next.

2.2.1 Voltage-clamp Fluorometry

Voltage-clamp fluorometry (VCF) is a variation of the cut-open voltage clamp technique and requires labeling of the ion channel complex (19, 20). In addition to recording the current of the ion

channel to study their function, simultaneous fluorescence measurements from the clamped region of the oocyte provide structural data. In order to do so, the protein of interest needs to be fluorescently labeled prior to performing the experiment. An endogenous or engineered cysteine of the protein can be labeled with thiol-reactive maleimide dyes like TMR-maleimide (TMRM). This labeling is restricted to cysteines that are extracellular and accessible. Removal of other accessible cysteines of the heterologously expressed protein reduces unspecific labeling. Cysteines of endogenous membrane proteins are also labeled, resulting in low signal to background ratios (SBR) if the protein of interest is expressed at low levels. In addition, endogenous background fluorescence from the oocyte further decreases the SBR. This endogenous background is lower when fluorescence measurements are taken from the dark animal pole of the oocyte. This side of the oocyte is dark brown in appearance due to expressing melanin in the cortex. This pigmentation shields from fluorescence background that originates from the intracellular compartment. The opposite side of the oocyte, i.e. vegetal pole, is white, since it does not express melanin. Consequently, recordings made on the vegetal side suffer more from endogenous background fluorescence. Exposure to light prior to the experiment, especially in the range of the excitation wavelength of the fluorophore, results in photobleaching and decrease the fluorescence signal of the fluorophore. Taken together, high expression levels, protection from pre-bleaching and recording from the dark animal pole of the oocytes are necessary to maximize the signal to background ratio.

The fluorescently labeled oocyte is placed in a COVC setup, as described in 2.1.2 *Cut Open Oocyte Voltage Clamp*. To enable fluorescence recordings, an upright fluorescence microscope in conjunction with a photodiode detection system is added to the setup (figure 2.5). A halogen lamp serves as light source and an electronic shutter synchronizes the voltage pulse protocol with the excitation of the fluorophore. When the voltage pulse is applied to the oocyte, the shutter is opened and the light passes through an excitation filter that transmits light of the desired excitation wavelength. The light is then directed by a dichroic mirror through a 40x water-immersion objective (NA=0.8). The objective focuses the light onto the oocyte's surface where it excites the fluorescent labels. The emitted light from the fluorophore is collected through the objective, passed through an emission filter and detected by the photodiode.

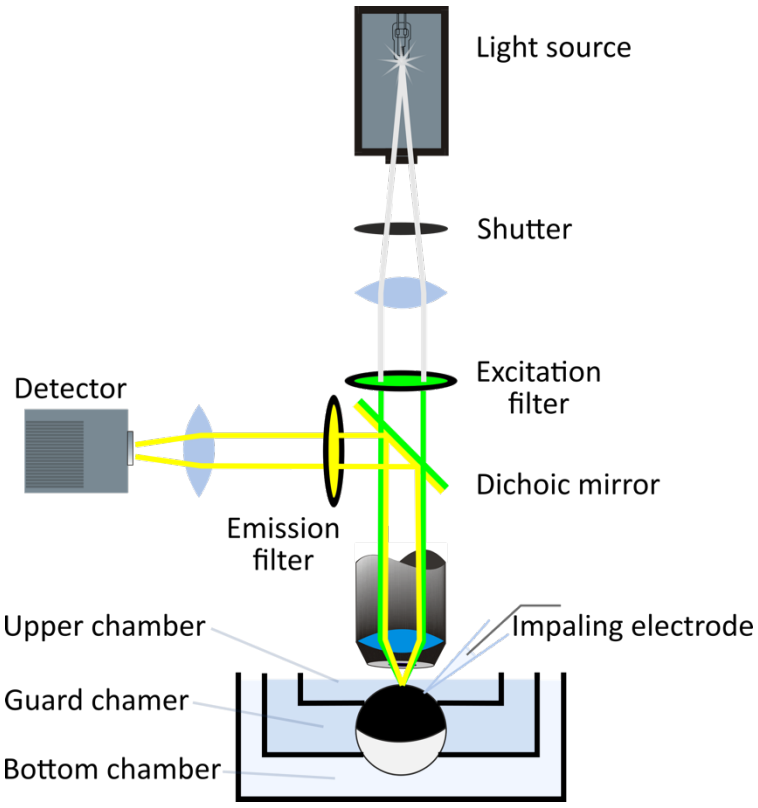

Figure 2.5 VCF setup
The COVC setup is adjusted to allow the simultaneous recording of electrophysiological and fluorescence data. The excitation light (green) is directed towards the oocyte membrane via a dichroic mirror and the emitted light (yellow) is collected through the same objective and reflected towards the detector.

The VCF technique is a powerful tool to study the structure-function relation of ion channels. As described above, ion channels undergo various conformational changes during gating. Due to the fluorophore's sensitivity to its environment, fluorescent labels can detect conformational changes of the protein. However, this is only possible, if the conformational change results in quenching or unquenching of the fluorophore. Therefore, not all positions that are involved in the structural change are suitable labeling positions. While typically, VCF is applied to analyze the dynamics of structural rearrangements and correlate them with functional data, which is simultaneously recorded, we utilized the VCF technique to probe protein-protein interactions rather than exploring kinetics (presented in chapter 5).

2.2.2 Single Subunit Counting

Single-subunit counting (SSC) is a powerful technique to determine the number of multimeric complex components. Although recent advancements in electron microscopy helped defining new protein structures at a rapid rate, membrane protein structures remain difficult to obtain and other techniques like SSC are employed to complement the available structural data. Chapter three and four present data on SSC experiments performed on heteromeric Kv2.1/Kv6.4 and homomeric TACAN ion channels, respectively.

The SSC technique is based on single molecule fluorescence microscopy and photobleaching (21, 22). The subunit of interest in the biological assembly studied is fluorescently labeled, typically using a genetically engineered N- or C-terminal GFP-tag. Usually, the tagged protein is expressed in *Xenopus* oocytes or in cultured immortalized mammalian cell lines, such as the human embryonic kidney (HEK) 293T or Chinese hamster ovary (CHO) cell line (22-30). Independent of the expression system, the expression density has to be adjusted to resolve single channel complexes with optical microscopy (i.e. ½ wavelength of visible light). Alternatively to expressing and counting the subunits of interest in heterologous expression systems, one can perform SSC on purified complexes that have been immobilized on a glass coverslip. Complexes can be directly tethered to the glass through different linkers, such as biotin (31, 32), antibodies (33, 34) or nickel nitrilotriacetic acid (Ni-NTA) (35). One of the advantages of using purified proteins, is the control over spot density, as it can be adjusted by altering the concentration and incubation time.

In single subunit counting experiments, a single channel complex is observed as a single fluorescent spot. To observe fluorescently tagged complexes in the plasma membrane, cultured cell lines can be grown directly on glass coverslips, whereas oocytes need to be mechanically peeled prior to being placed onto the coverslip, as their plasma membrane is surrounded by a second membrane, i.e. the vitelline membrane. Once this second membrane is remove and the oocyte is placed onto the coverslip, the plasma membrane is in direct contact with the glass and single channel complexes can be observed. The camera's resolution is not sufficient to resolve individual subunits of these complexes, so that the recorded fluorescence from one diffraction-limited spot originates from all labeled subunits within the complex. In SSC experiments, the fluorescent tags are excited at high intensities for a prolonged time,

which leads to photobleaching of the fluorophore. Opposed to observing exponential bleaching of the ensemble of all labeled complexes, the analysis is performed for each individual fluorescent spot, which can be detected automatically to reduce observer bias (28). In theory, each spot is composed of only one channel complex, so that the fluorescence time trace exhibits a distinct bleaching step every time one of the fluorescent tags is irreversibly destroyed (figure 2.6A). In an ideal setting, a labeled tetrameric complex would thus result in four bleaching steps for all observed spots (figure 2.6B, red). However, GFP maturation is not complete and pre-bleaching of the fluorophore prior to the experiment further reduces the number of observable fluorescent tags. This reduced probability of fluorescence (p_f) results in the binomial distribution of step frequency histograms. The order of the binomial distribution corresponds to the maximum number of labeled subunits in the complex (figure 2.6B, grey). Colocalization of channel complexes within the diffraction limited spot, on the other hand, artificially increase the apparent subunit count (figure 2.6B, black), so that it can be difficult to distinguish between two colocalized dimers and a tetrameric complex for example. When interpreting the obtained frequency histograms, the probability of fluorescence (p_f) and colocalization (p_c) need to be considered. Rigorous and careful analysis is crucial for the interpretation of any SSC data, but unfortunately, confirmation bias can lead to the disregard of data. Chapter three will discuss a much needed, advanced analysis method of SSC data.

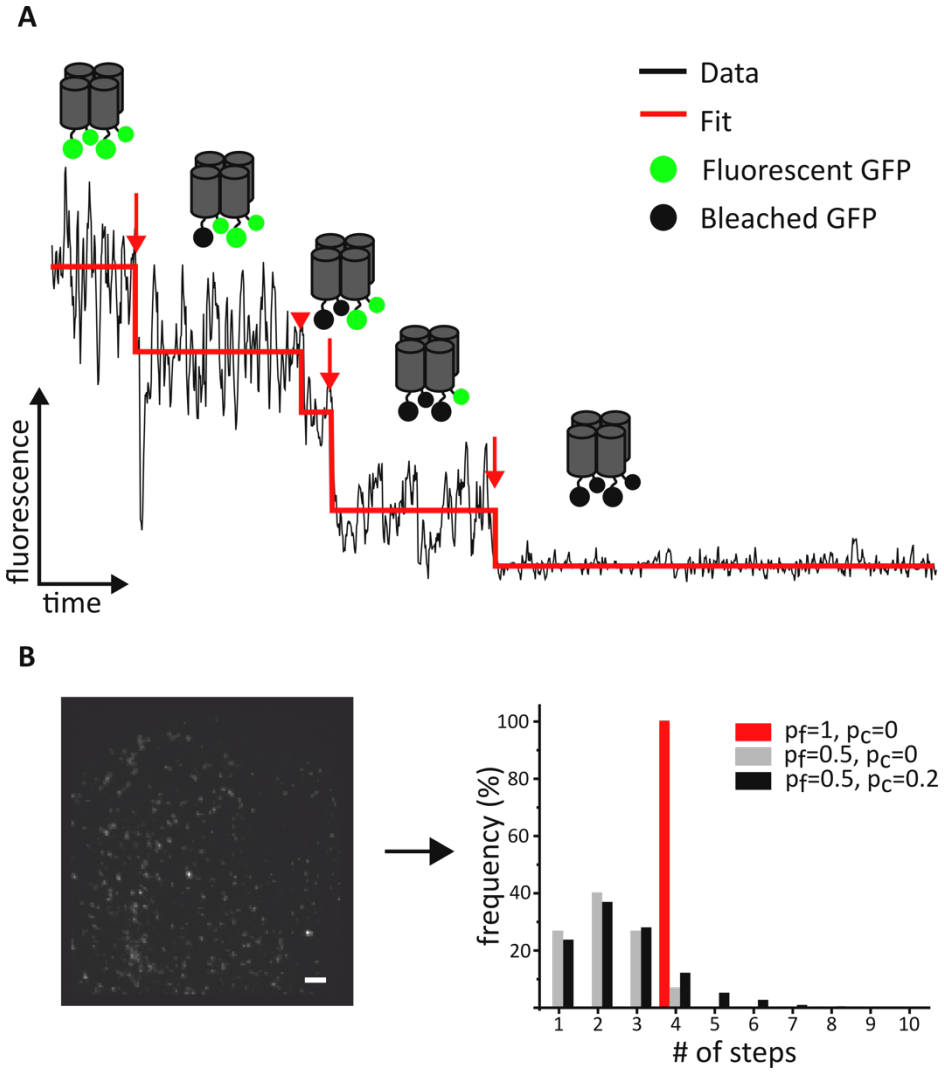

Figure 2.6 Single subunit counting principle
A) Representative photobleaching trace obtained from a single fluorescently labeled tetrameric complex. The cartoon on top represents the complex, fluorescent GFP tags (green) are permanently destroyed (black). Red arrows further highlight each bleaching step **B)** Bleaching traces of all fluorescent spots of a recorded bleaching movie (left) are analyzed and result in a step frequency histogram. If all tags of a tetrameric channel were fluorescent and no colocalization of labeled complexes is accounted for (red), all analyzed spots would feature four bleaching steps. If a fraction of the GFP tags are dark before the recording of the movie (grey), the step frequency histogram is binomially distributed. More than four bleaching steps are observed for tetrameric complexes, when complexes are colocalized in a diffraction limited spot (black).

Background fluorescence originating from the intracellular can be reduced by using total internal reflection fluorescence (TIRF) microscopy (36). This background fluorescence often originates from untrafficked fluorescently tagged proteins (28). As the name suggests, TIRF microscopy is based on the total reflection inside the glass of the excitation light beam at the interface of the coverslip and the basolateral membrane or solution and is achieved by an increased angle of the incoming light

(figure 2.7). When the critical angle is reached, the excitation beam does not propagate into the sample chamber atop the coverslip but is to 100% reflected back into the glass. As a result, an evanescent wave illuminates the sample at the point of TIRF excitation. The intensity of this restricted electromagnetic field decreases exponentially with the distance from the interface (z-direction), illuminating approximately 200 nm (37). This drastically reduces background fluorescence from intracellular compartments and therefore increases the signal to background ratio.

Background fluorescence can also be reduced by expressing the protein of interest in *Xenopus* oocytes, rather than smaller cells, because, here, the intracellular compartments are located further from the plasma membrane. Additionally, placing the dark melanin-expressing animal pole, opposed to the bright vegetal pole onto the coverslip further shields from disturbing background fluorescence (figure 2.7). Moreover, performing SSC experiments on purified and subsequently immobilized complexes practically eliminates fluorescence background. Here, background from unbound fluorescent complexes can be removed by washing these unbound complexes off prior to recording bleaching movies.

In this thesis, SSC experiments are performed in oocytes, immortalized cell lines and on purified proteins. In chapter three, Kv2.1/6.4 heterotetramers are expressed in *Xenopus* oocytes. Chapter four presents SSC experiments on TACAN channels obtained from HEK293T and CHO cells. Here, we also show Kv2.1/6.4 channels expressed in HEK293T cells as a control. Due to high background fluorescence in cells, we investigate the oligomeric state of TACAN in purified form, tethered to glass coverslips via Ni-NTA. The experimental details are presented in the Method section of the corresponding chapters.

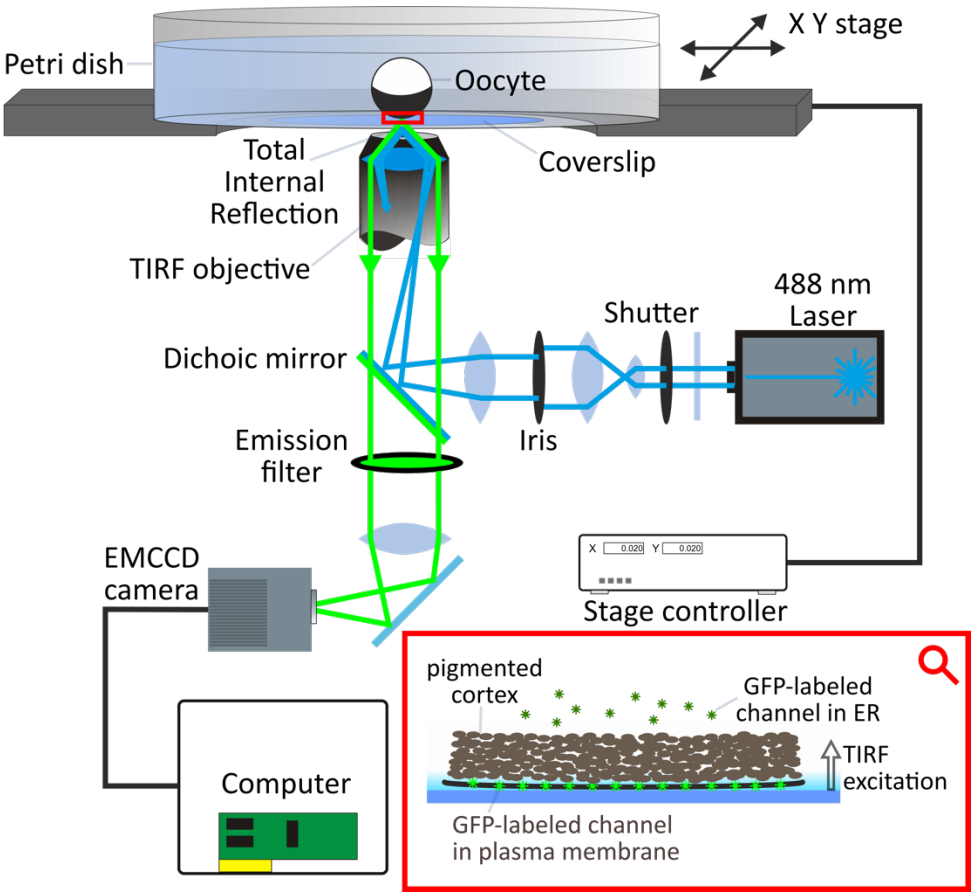

Figure 2.7 Single subunit counting setup
The oocyte is placed onto a glass coverslip and excited in TIRF illumination. The excitation light (blue) is directed towards the oocyte membrane via a dichroic mirror and the emitted light (green) is collected through the same objective and reflected towards the camera. The inset to the right illustrates how the limited excitation in TIRF and the melanin containing pigmented cortex of the oocyte limit background fluorescence from labeled proteins in the intracellular.

2.3 References

1. E. Neher, B. Sakmann, Single-channel currents recorded from membrane of denervated frog muscle fibres. *Nature* **260**, 799-802 (1976).

2. E. Neher, B. Sakmann, J. H. Steinbach, The extracellular patch clamp: a method for resolving currents through individual open channels in biological membranes. *Pflugers Arch* **375**, 219-228 (1978).

3. B. Sakmann, E. Neher, Patch clamp techniques for studying ionic channels in excitable membranes. *Annu Rev Physiol* **46**, 455-472 (1984).

4. E. Stefani, L. Toro, E. Perozo, F. Bezanilla, Gating of Shaker K+ channels: I. Ionic and gating currents. *Biophys J* **66**, 996-1010 (1994).

5. F. Bezanilla, E. Perozo, D. M. Papazian, E. Stefani, Molecular basis of gating charge immobilization in Shaker potassium channels. *Science* **254**, 679-683 (1991).

6. M. Taglialatela, L. Toro, E. Stefani, Novel voltage clamp to record small, fast currents from ion channels expressed in Xenopus oocytes. *Biophys J* **61**, 78-82 (1992).

7. E. Stefani, F. Bezanilla, Cut-open oocyte voltage-clamp technique. *Methods Enzymol* **293**, 300-318 (1998).

8. J. R. Lakowicz, *Principles of fluorescence spectroscopy* (Springer Science+Business Media,LLC, New York, USA, ed. 3, 2006).

9. M. Chalfie, Y. Tu, G. Euskirchen, W. W. Ward, D. C. Prasher, Green fluorescent protein as a marker for gene expression. *Science* **263**, 802-805 (1994).

10. T. D. Craggs, Green fluorescent protein: structure, folding and chromophore maturation. *Chem Soc Rev* **38**, 2865-2875 (2009).

11. J. D. Pedelacq, S. Cabantous, T. Tran, T. C. Terwilliger, G. S. Waldo, Engineering and characterization of a superfolder green fluorescent protein. *Nat Biotechnol* **24**, 79-88 (2006).

12. T. Kalstrup, R. Blunck, Voltage-clamp Fluorometry in Xenopus Oocytes Using Fluorescent Unnatural Amino Acids. *J Vis Exp* 10.3791/55598 (2017).

13. K. Brejc *et al.*, Structural basis for dual excitation and photoisomerization of the Aequorea victoria green fluorescent protein. *Proc Natl Acad Sci U S A* **94**, 2306-2311 (1997).

14. R. Blunck, "Investigation of ion channel structure using fluorescence spectroscopy" in Handbook of Ion Channels, J. Zheng, Trudeau, M.C., Ed. (CRC Press, 2015), chap. 9, pp. 113-134.

15. N. Marme, J. P. Knemeyer, M. Sauer, J. Wolfrum, Inter- and intramolecular fluorescence quenching of organic dyes by tryptophan. *Bioconjug Chem* **14**, 1133-1139 (2003).

16. S. E. Mansoor, H. S. McHaourab, D. L. Farrens, Mapping proximity within proteins using fluorescence spectroscopy. A study of T4 lysozyme showing that tryptophan residues quench bimane fluorescence. *Biochemistry* **41**, 2475-2484 (2002).

17. A. Pantazis, K. Westerberg, T. Althoff, J. Abramson, R. Olcese, Harnessing photoinduced electron transfer to optically determine protein sub-nanoscale atomic distances. *Nat Commun* **9**, 4738 (2018).

18. L. D. Islas, W. N. Zagotta, Short-range molecular rearrangements in ion channels detected by tryptophan quenching of bimane fluorescence. *J Gen Physiol* **128**, 337-346 (2006).

19. A. Cha, F. Bezanilla, Characterizing voltage-dependent conformational changes in the Shaker K+ channel with fluorescence. *Neuron* **19**, 1127-1140 (1997).

20. L. M. Mannuzzu, M. M. Moronne, E. Y. Isacoff, Direct physical measure of conformational rearrangement underlying potassium channel gating. *Science* **271**, 213-216 (1996).

21. S. K. Das, M. Darshi, S. Cheley, M. I. Wallace, H. Bayley, Membrane protein stoichiometry determined from the step-wise photobleaching of dye-labelled subunits. *Chembiochem* **8**, 994-999 (2007).

22. M. H. Ulbrich, E. Y. Isacoff, Subunit counting in membrane-bound proteins. *Nat Methods* **4**, 319-321 (2007).

23. N. Durisic *et al.*, Stoichiometry of the human glycine receptor revealed by direct subunit counting. *J Neurosci* **32**, 12915-12920 (2012).

24. P. M. Haggie, A. S. Verkman, Monomeric CFTR in plasma membranes in live cells revealed by single molecule fluorescence imaging. *J Biol Chem* **283**, 23510-23513 (2008).

25. P. Hastie *et al.*, AMPA receptor/TARP stoichiometry visualized by single-molecule subunit counting. *Proc Natl Acad Sci U S A* **110**, 5163-5168 (2013).

26. W. Ji *et al.*, Functional stoichiometry of the unitary calcium-release-activated calcium channel. *Proc Natl Acad Sci U S A* **105**, 13668-13673 (2008).

27. Y. Lussier *et al.*, Disease-linked mutations alter the stoichiometries of HCN-KCNE2 complexes. *Sci Rep* **9**, 9113 (2019).

28. H. McGuire, M. R. Aurousseau, D. Bowie, R. Blunck, Automating single subunit counting of membrane proteins in mammalian cells. *J Biol Chem* **287**, 35912-35921 (2012).

29. L. D. Plant *et al.*, One SUMO is sufficient to silence the dimeric potassium channel K2P1. *Proc Natl Acad Sci U S A* **107**, 10743-10748 (2010).

30. L. A. Veliz *et al.*, Near-membrane dynamics and capture of TRPM8 channels within transient confinement domains. *PLoS One* **5**, e13290 (2010).

31. D. Cherny *et al.*, Stoichiometry of a regulatory splicing complex revealed by single-molecule analyses. *EMBO J* **29**, 2161-2172 (2010).

32. H. Yokota, Y. A. Chujo, Y. Harada, Single-molecule imaging of the oligomer formation of the nonhexameric Escherichia coli UvrD helicase. *Biophys J* **104**, 924-933 (2013).

33. Z. Shen *et al.*, Dynamic association of ORCA with prereplicative complex components regulates DNA replication initiation. *Mol Cell Biol* **32**, 3107-3120 (2012).

34. M. S. Panter, A. Jain, R. M. Leonhardt, T. Ha, P. Cresswell, Dynamics of major histocompatibility complex class I association with the human peptide-loading complex. *J Biol Chem* **287**, 31172-31184 (2012).

35. W. Cheng *et al.*, Ultrasensitive scanometric strategy for detection of matrix metalloproteinases using a histidine tagged peptide-Au nanoparticle probe. *Chem Commun (Camb)* **47**, 2877-2879 (2011).

36. T. Hirschfeld, Total reflection fluorescence. *Can. Spectrosc.*, 128 (1965).

37. D. Axelrod, Evanescent excitation and emission in fluorescence microscopy. *Biophys J* **104**, 1401-1409 (2013).

Chapter 3

Determining the Correct Stoichiometry of Kv2.1/Kv6.4 Heterotetramers, Functional in Multiple Stoichiometrical Configurations

Lena Möller*[,1], Glenn Regnier*[,2], Alain J. Labro[2], Rikard Blunck[#,3,1], and Dirk J. Snyders[#,2]

1 Department of Biochemistry, Université de Montréal, Montréal, Canada, **2** Laboratory for Molecular, Cellular and Network Excitability, Department of Biomedical Sciences, University of Antwerp, Antwerp, Belgium, **3** Department of Physics, Université de Montréal, Montréal, Canada

Received for review September 17, 2019 and approved March 5, 2020

Published Online April 13, 2020

Proc Natl Acad Sci USA, vol. 117 no. 17, p. 9365-9376, April 28, 2020

Keywords: Kv channels, single subunit counting, silent subunits, model selection

[#] To whom correspondence may be addressed. Email: rikard.blunck@umontreal.ca or dirk.snyders@ua.ac.be.

*** L.M. and G.R. contributed equally to this work.**

Author Contributions

Alain J. Labro, Rikard Blunck and Dirk J. Snyders designed the research.

The research was carried out by Glenn Regnier, Rikard Blunck and myself. I performed single subunit counting experiments as well as the initial data analysis to obtain step frequency histograms and wrote the respective parts of the first version of the manuscript. Rikard Blunck particularly contributed to the single subunit counting part by designing and implementing maximum likelihood calculations as a rigorous model selection method. Furthermore, he performed simulations on model selection and wrote the respective parts of the manuscript. Glenn Regnier collected electrophysiology data, which was analyzed by himself, Alain J. Labor, Dirk J. Snyders and Rikard Blunck. Glenn Regnier wrote the respective parts of first version of the manuscript.

Alain J. Labro, Rikard Blunck and Dirk J. Snyders edited the first version of the article and all authors contributed to writing the final version.

3.1 Abstract

The electrically silent (KvS) members of the voltage-gated potassium subfamilies Kv5, Kv6, Kv8 and Kv9 selectively modulate Kv2 subunits by forming heterotetrameric Kv2/KvS channels. Based on the reported 3:1 stoichiometry of Kv2.1/Kv9.3 channels, we tested the hypothesis that Kv2.1/Kv6.4 channels express, in contrast to the assumed 3:1, in a 2:2 stoichiometry. We investigate the Kv2.1/Kv6.4 stoichiometry using single subunit counting and functional characterization of tetrameric concatemers. For selecting the most probable stoichiometry, we introduce a model selection method that is applicable for any multimeric complex by investigating the stoichiometry of Kv2.1/Kv6.4 channels. Weighted likelihood calculations bring rigor to a powerful technique. Using the weighted-likelihood model selection method and analysis of electrophysiological data, we show that Kv2.1/Kv6.4 channels express, in contrast to the assumed 3:1, in a 2:2 stoichiometry. Within this stoichiometry the Kv6.4 subunits have to be positioned alternating with Kv2.1 to express functional channels. The variability in Kv2/KvS assembly increases the diversity of heterotetrameric configurations and extends the regulatory possibilities of KvS by allowing presence of more than one silent subunit.

3.2 Significance Statement

Voltage-gated potassium (Kv) channels play a key role in cellular electrical excitability. While various Kv subunits assemble to homotetrameric functional channels, the silent subfamilies KvS exclusively form heterotetramers with Kv2 subunits and thus regulate their biophysical properties in a tissue-specific way. Despite the vast functional research, key aspects of the heterotetrameric architecture remain controversial, including the stoichiometry with which KvS and Kv2 can assemble. We used concatemers and single subunit counting in combination to show that Kv2/Kv6 assemble in a 2:2 stoichiometry following the general dimer of dimer mechanism for channel formation. We demonstrate how to objectively choose the most likely model for single subunit counting data, which is applicable for any multimeric complex and will help choosing models confidently.

3.3 Introduction

Single subunit counting, the progressive stepwise photobleaching of fluorescently labeled monomers in a biological complex, has been the method of choice to determine stoichiometries in biological assemblies (1). This technique is based on the irreversible photobleaching of green fluorescent protein (GFP) tags, which are fused to the protein of interest (Fig. 3.1 A and F) (1). During prolonged excitation, each GFP progressively loses its ability to fluoresce by photochemical destruction, leading to stepwise bleaching events. Since only a fraction of the GFPs mature to become fluorescent, one obtains a binomial distribution of N-th order, where N is the number of monomers in the biological assembly. More rigorous evaluation revealed GFP-maturation rates in the range between 0.4 and 0.9 (1-12). With increasing N, it becomes difficult to distinguish between the different orders of binomial distributions in this range. Often, one must rely on the highest step count; for instance, observation of a small number of five bleaching steps automatically leads to a pentamer and excludes a tetramer. While this logic is theoretically true, it can be misleading if more than one complex colocalize within one diffraction-limited spot. This situation is unavoidable even in fully stochastic distribution of the single complexes. What has been lacking to date is an objective manner of selecting the correct model based on *a-posteriori* probabilities. Here, we show how to evaluate different models and use this method to determine the stoichiometry of Kv2.1/Kv6.4 complexes.

Voltage-gated K^+ (Kv) channels regulate the selective flux of K^+ ions across the cell membrane by opening, closing, and/or inactivating in response to changes in membrane voltage (13). A fully assembled Kv channel consists of four α-subunits, with the NH_2-terminus containing the T1-domain as a key determinant in controlling tetramerization of compatible subunits (14, 15). To tune the native Kv currents to tissue-specific requirements, each tissue expresses a characteristic set of α-subunits, which are divided into several subfamilies based on sequence homology. In the case of the *Shaker*-related subunits, eight different subfamilies can be distinguished: Kv1-Kv6 and Kv8-Kv9 (16). Within each of the Kv1-Kv4 subfamilies, subunits cannot only oligomerize into homotetramers but also into heterotetramers, increasing the diversity of Kv channel complexes. Members of the Kv5, Kv6, Kv8 and Kv9 subfamilies, on the other hand, are unable to form

functional channels, even though they have the typical topology of a Kv α-subunit, and are therefore designated silent Kv (KvS) subunits (17). However, they do selectively interact with members of the Kv2 subfamily, forming functional Kv2/KvS heterotetramers that possess unique biophysical and pharmacological properties. Generally, they slow the activation and deactivation kinetics, shift the voltage dependency of activation and inactivation and reduce in heterologous expression systems the current density relative to Kv2 homotetramers. Therefore, these KvS subunits are considered modulatory α-subunits of the Kv2 subfamily.

Oligomerization of Kv subunits into a functional channel is thought not to occur by the sequential addition of monomers to the channel complex, but by dimerization of dimers, in which the dimeric interaction sites differ from those mediating monomer-monomer interactions (18). Therefore, heterotetramers are expected to assemble with a 2:2 stoichiometry, which has been confirmed in the case of the Kv4 homolog jShal1 and jShalγ1 (19). In contrast, for Kv2.1/Kv9.3 heterotetramers a stoichiometry of three Kv2.1 subunits and one Kv9.3 subunit has been reported (20), alluding that a similar 3:1 stoichiometry could be applicable to all Kv2/KvS channels. This would imply assembly of each one homodimer and one heterodimer, assuming the channels are assembled from dimers (21).

On the other hand, several studies have shown subunit stoichiometry of heteromeric Kv channel complexes to vary dependent on the relative expression of the different subunits (22-26). It is also important to study only the configuration of functionally expressed Kv2/KvS channel complexes excluding temporary aggregations that might be formed due to overexpression but that are retained in the endoplasmic reticulum (ER) in a physiological context. Therefore, KvS subunits might be more diverse than assumed leading to the idea that, in addition to a 3:1 ratio, Kv2/KvS channels assemble in a 2:2 ratio, i.e., as a dimer of dimers.

We explored the distribution of stoichiometries with two experimentally independent approaches. To probe the internal arrangement of the different stoichiometries, we compared the *biophysical properties* of concatemers with corresponding monomeric constructs. With the latter approach, ion-channel stoichiometries have been successfully studied (27-29). Possible stoichiometries are 3:1, 2:2, or a population mixing both stoichiometries. In *single subunit*

counting experiments, we directly counted the number of Kv6.4 subunits in Kv2.1/Kv6.4 heteromers expressed in *Xenopus oocytes*. Since maturation of GFP, whose photobleaching steps are detected, is not complete, each stoichiometry will lead to a characteristic bleaching-step distribution histogram. Choosing the most likely distribution is, therefore, a prominent problem for the analysis and interpretation of single subunit counting data. Here, we provide the framework for objectively choosing the most likely (mixture of) stoichiometry of a multimeric arrangement, applicable to any single subunit counting experiments of multimeric complexes.

3.4 Results

3.4.1 Heterotetramers Coexpress in a 2:2 Stoichiometry

Kv6.4 is a representative member of the KvS family given its profound modulating effect on the Kv2 channel properties (30). The direct way to investigate the stoichiometry of Kv2.1/Kv6.4 heterotetramers is by single subunit counting experiments, which provide directly the number of fluorescently labeled Kv6.4 subunits within a single channel assembly. For our studies, we chose the *Xenopus* oocyte expression system for the single subunit counting experiments because injection of RNA provides accurate control over expression level and expression-level ratios (31), not easily achieved by DNA transfection in mammalian cells. Furthermore, fluorescence originating from nontrafficked channel assemblies retained in the ER is efficiently blocked by the melanin pigmentation located between membrane and ER in *Xenopus* oocytes (Fig. 3.1F). We initially carried out the experiments in human embryonic kidney 293 (HEK293) cells and obtained high background fluorescence from Kv6.4–GFP-transfected cells trapped in the ER in the absence of Kv2.1 (9).

Not every GFP-fusion protein is detected. While photobleaching before the measurement can be limited by protecting the samples from light, the chromophore matures (i.e., develops its fluorescent properties) only in a fraction of the GFP population after protein folding. The fraction of mature GFP depends on the experimental conditions but not on the protein, the GFP is fused to (9). Therefore, we initially determined the probability of GFP maturation for the experimental

conditions used here by studying the Kv2.1 homotetramer in the absence of any silent subunits. The expression level was adjusted such that individual channels were clearly distinguishable as single spots, which is a prerequisite for reliably determining the stoichiometry of single channels (Fig. 3.1 A–E; please refer to *Methods* for a detailed explanation of the exclusion criteria). As a homotetramer, each Kv2.1 contains four GFP proteins per channel. Accordingly, the homogenous tetrameric population showed a step-number distribution following a binomial distribution of fourth order, consistent with each GFP having a finite probability of fluorescence $p_f = 0.48$ of being observed (Fig. 3.1C; n = 6,388 spots, 16 oocytes).

The histogram showed some spots with more than four bleaching steps. Intuitively, this may seem unexpected, but it is a result of the stochastic distribution of the channels. In order to obtain sufficient spots for a meaningful analysis, there is a 10 to 20% probability of finding two channels within the same diffraction-limited spot (~300-nm diameter). This colocalization of more than one channel within a diffraction-limited spot was consistently found in all our experiments independent of the protein of interest. While one might be tempted to exclude spots with more than the theoretically possible number of steps per protein from analysis as an artifact, such a selective exclusion would distort the determination of the remaining distribution; e.g., two tetramers would lead to a binomial distribution of eighth order, which have a finite probability not only for five to eight but also for one to four steps. Excluding the five to eight as an artifact would misrepresent the one to four distribution. As a result, the fluorescence probability p_f of the fluorophore would be overestimated. We will discuss below that colocalization is also essential to obtain reliable information if observing heterogenous populations.

We next studied the stoichiometry of the Kv2.1/Kv6.4 heteromers. To exclude any background of Kv2.1 homotetramers from our analysis, a Kv6.4-GFP fusion protein was coexpressed with wild-type (WT) Kv2.1, rendering the latter monomers invisible. *Xenopus laevis* oocytes were injected with untagged Kv2.1 and Kv6.4-GFP RNA in a 1:8 ratio. The ratio was biased toward the Kv6.4 subunit to be consistent with the electrophysiological experiments, where higher Kv2.1 fractions would result in a majority of homotetrameric Kv2.1 channels that would superpose the electrical signal of the heteromers. The majority of the photobleaching time traces showed one or two bleaching events consistent with a 2:2 stoichiometry (Fig. 3.1D). This

observation was confirmed when fitting the step-distribution histogram to a binomial distribution (Fig. 3.1E). The histogram (n = 8,675 spots, 28 oocytes) was fitted to binomial distributions of second, third, and fourth order as well as a Poisson distribution, representing expression of two, three, four and one Kv6.4 subunit per tetramer, respectively (see *Methods* for details).

With the colocalization of spots, we obtained typically up to four to eight bleaching steps per histogram. To evaluate the different stoichiometries against each other, we calculated weighted-likelihood ratios (for details, see *Single Subunit Counting Analysis* below). When the probability of fluorescence was fixed to the previously determined value $p_f = 0.48$, we found that a 2:2 stoichiometry best fit our data ($P > 0.9999$). Despite the relatively stable maturation rate, we preferred not to rely on a fixed parameter but, rather, let the fit confirm the previous knowledge. For this reason, we also fit the data, leaving the probability of fluorescence p_f free to vary. Under these conditions, the binomial distribution of second order was the best fit, and the 2:2 stoichiometry remained the most likely stoichiometry ($P > 0.99$; Fig. 3.1G). Although left free to vary, the p_f of the 2:2 stoichiometry did not alter significantly ($p_f = 0.49$), whereas it was inconsistent with the values for the other possible Kv2:Kv6 ratios: p_f (3:1) = 1; p_f (1:3) = 0.36; and p_f (0:4) = 0.3).

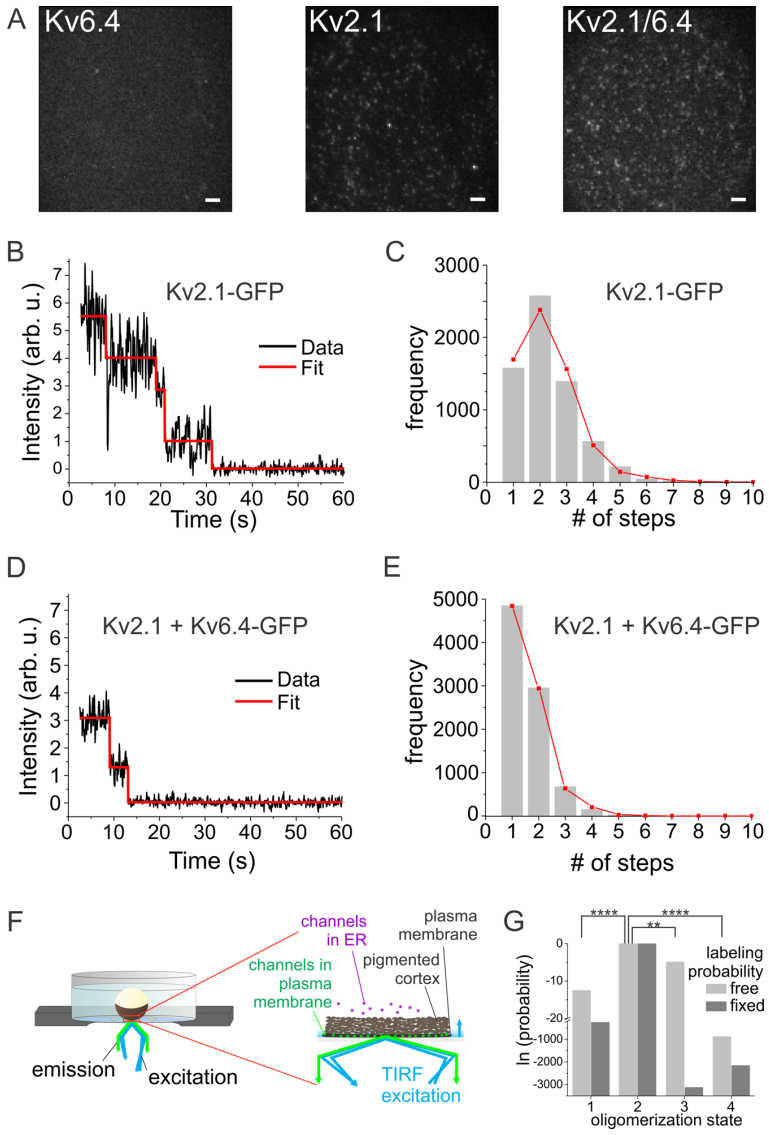

Figure 3.1 Single-channel subunit counting

A) Representative frames of a recorded movie of Kv6.4-GFP (Left), Kv2.1-GFP (Center) and Kv2.1/6.4-GFP (Right, 1:8 ratio) expressed in the *Xenopus* oocyte membrane recorded in TIRF configuration (scale bars: 2 µm). **B** and **D)** Representative intensity-time traces from single Kv2.1-GFP homomeric (B) and Kv2.1/Kv6.4-GFP heteromeric (D) channels with four and two bleaching steps, respectively. Arb. u., arbitrary units. **C** and **E)** PIF automated analysis: Each spot is analyzed, and number of steps recorded. The resulting distribution histograms (grey bars) from Kv2.1-GFP (C) and Kv2.1/Kv6.4-GFP (E) were fitted to binomial distributions of fourth order (tetramer) and second order (dimer), respectively. The probability to detect fluorescence from GFP was P = 0.48 and the fraction of colocalization was 10% and 29%, respectively. The ratio of Kv2.1:Kv6.4-GFP was 1:8 (weight:weight). **F)** Oocytes are illuminated by (TIRF) and fluorescence was recorded using an EMCCD camera. The pigmented cortex in *Xenopus* oocytes is positioned between plasma membrane and ER such that fluorescence from the ER is efficiently blocked. **G**) Log-likelihoods for the distribution in E for 3:1, 2:2, 1:3 and 4:0 Kv2:Kv6 stoichiometries. Significance was determined by AIC with respect to 2:2 stoichiometry (**** p>0.9999; ** p>0.99).

3.4.2 Kv2.1/Kv6.4 Heterotetramers Are Functional in a 2:2-Stoichiometrical Configuration

While the single subunit counting experiments indicated a 2:2 stoichiometry, they cannot provide an answer as to how the subunits are arranged within the tetramer. Therefore, we investigated the functionality of Kv2.1/Kv6.4 heterotetramers with different stoichiometry using concatemeric constructs. Since Kv channels assemble by the dimerization of dimers (18), we started by analyzing the dimeric constructs Kv2.1-Kv2.1, Kv2.1-Kv6.4 and Kv6.4-Kv2.1 (Fig. 3.2A), and compared their electrophysiological properties with those of the corresponding channels assembled from the WT monomeric subunits (Fig. 3.3A). To avoid limitations on channel assembly and conformational flexibility due to the covalent linking of subunits, a 10 to 12 amino-acid linker was inserted between them (Fig. 3.2A). Such a linker has prevented this potential problem in previous studies (27, 29, 32, 33). Western blot analysis confirmed that all dimeric constructs were expressed as an intact polypeptide (Fig. 3.2B), indicating that the dimeric constructs were not cleaved, and no single subunits were expressed. We did not draw any conclusions from the band intensities about expression levels, as transfection efficiencies typically varied widely.

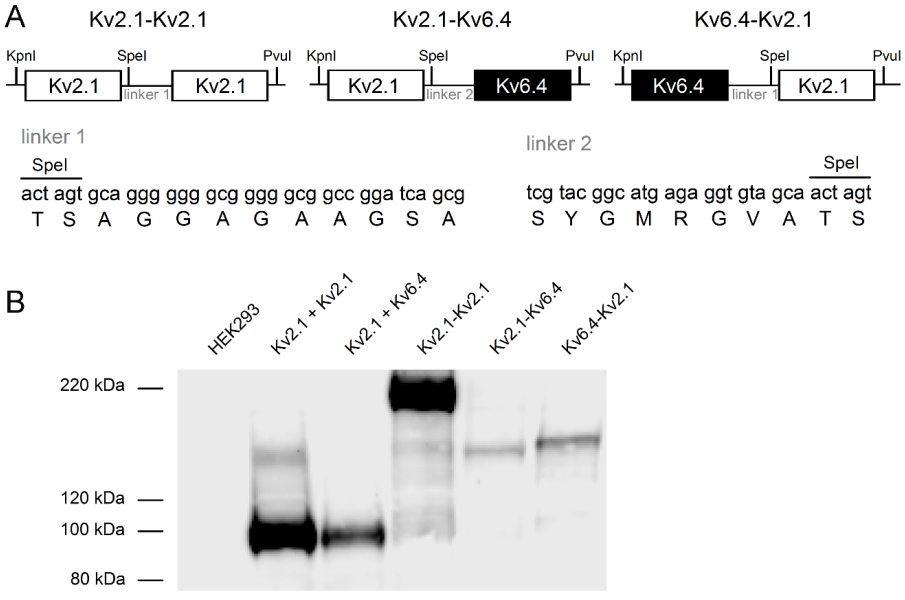

Figure 3.2 Overview and Western blot analysis of dimeric Kv2.1 and Kv2.1/Kv6.4 constructs
A) Design of Kv2.1-Kv2.1 (Left), Kv2.1-Kv6.4 (Center), and Kv6.4-Kv2.1 (Right) dimers. The Kv2.1 and Kv6.4 subunits are shown in white and black, respectively. Neighboring subunits had a common, unique RE site

enabling the linkage of subunits using specific RE digests. Subunits were covalently joined by a peptide linker of which the nucleotide and amino acid sequences are shown below in lower and upper case, respectively. **B)** Expression of dimers as a single polypeptide was examined with Western blotting using Kv2.1 antibodies. As a positive control, lysates of HEK293 cells (co)transfected with Kv2.1 and Kv6.4 or with Kv2.1 alone were used. In all lysates containing the positive controls or the dimers, a single band was noticeable which corresponded to the predicted molecular mass, while no signal was detected in lysates of nontransfected HEK293 cells. All dimeric constructs yielded one dominant protein band when probed with Kv2.1 antibodies with a molecular mass that approached their estimated weight.

To evaluate the effect of our concatemeric design, the Kv2.1 dimeric construct was studied first. The Kv2.1 dimer yielded functional channels with biophysical properties closely resembling those of Kv2.1 monomer-derived channels (Fig. 3.3 A and B). No significant differences were observed in the voltage dependencies of activation and inactivation or in the time constants of activation and deactivation (Fig. 3.3 C–E and Table 3.1), confirming that the covalent linker between the Kv2.1 subunits allowed enough conformational flexibility to yield functional channels without affecting their biophysical properties.

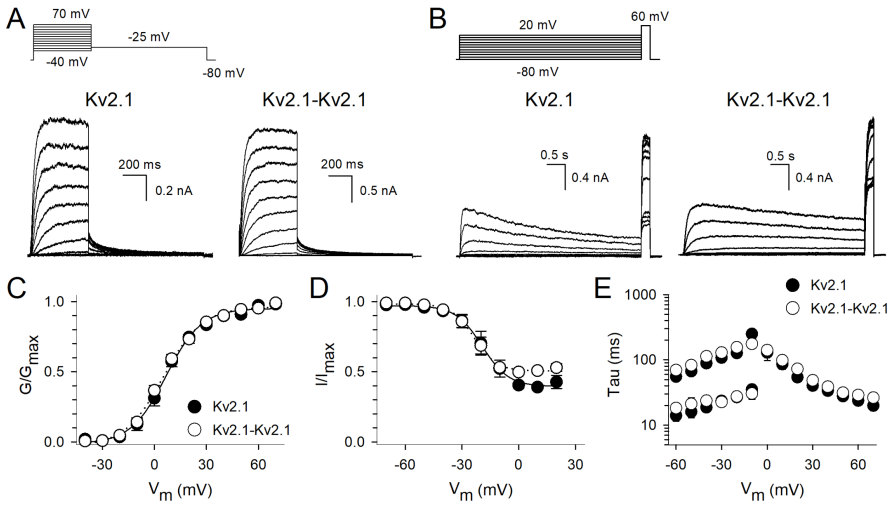

Figure 3.3 Biophysical properties of Kv2.1 monomers and dimers
A and B) Whole cell current recordings of Kv2.1 channels composed of Kv2.1 monomers (Left; 0.5 µg Kv2.1 transfected) or Kv2.1 dimers (Right; 1 µg transfected) used to determine the activation (A) and inactivation (B) properties. Voltage protocols are shown on top. **C)** Voltage dependence of activation for Kv2.1 channels composed of monomers (filled circles) or Kv2.1 dimers (open circles) derived from plotting the normalized tail current amplitudes at -25 mV (from recordings as shown in A) as a function of the prepulse potential. **D)** Voltage dependence of inactivation obtained from plotting the normalized peak current amplitude at +60 mV (from recordings as shown in B) as a function of the prepulse potential. **E)** Time constants of activation and deactivation obtained as described in *Methods*. Note that the biophysical properties of Kv2.1 channels composed of dimers were similar to those assembled from Kv2.1 monomers.

It was demonstrated previously that the biophysical properties of dimers containing two different subunits can be affected by the position of these subunits within the dimeric construct (34). Therefore, two different dimeric constructs were designed to investigate the functionality of Kv2.1/Kv6.4 channels in a 2:2 configuration: Kv2.1-Kv6.4 and Kv6.4-Kv2.1. Coexpression of Kv2.1 and Kv6.4 monomers yielded Kv2.1/Kv6.4 heterotetramers with biophysical properties that differed clearly from those of Kv2.1 homotetramers and the obtained kinetics were comparable to what has been reported before (Table 1) (30, 35-40). The most significant difference with Kv2.1 homotetramers is an approximately −40-mV shift in the voltage dependence of inactivation and an activation curve with a shallower slope factor k (Table 3.1). Both the Kv2.1-Kv6.4 and Kv6.4-Kv2.1 dimers each produced currents with characteristic Kv2.1/Kv6.4 heterotetrameric properties (Fig. 3.4 A and B and Table 3.1). Furthermore, also the activation and deactivation kinetics of both dimers were similar to those of Kv2.1/Kv6.4 heterotetramers assembled from coexpressing Kv2.1 and Kv6.4 monomers (Fig. 3.4C). The order of Kv2.1 and Kv6.4 within the dimer did not play a significant role consistent with our finding that the Kv2.1 concatemer behaves like the monomer (Fig. 3.4).

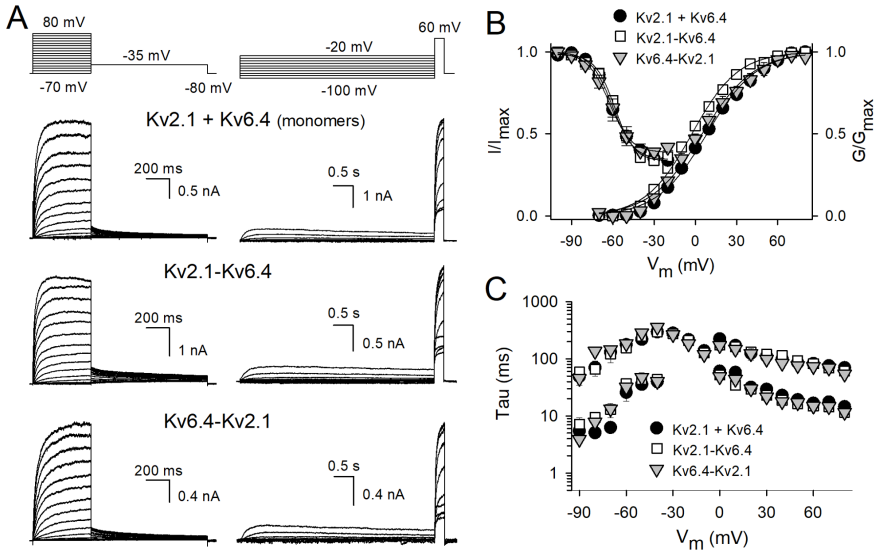

Figure 3.4 Biophysical properties of Kv2.1-Kv6.4 and Kv6.4-Kv2.1 dimers
A) Whole-cell current recordings after (co)transfection of Kv2.1 and Kv6.4 in 1:10 ratio (Top; black circles), 5 µg Kv2.1-Kv6.4 (Middle; white squares in B and C), and 5 µg Kv6.4-Kv2.1 (Bottom; gray inverted triangles in B and C) used to determine the activation (Left) and inactivation (Right) properties. Voltage protocols are shown on top. **B**) Voltage dependence of activation (normalized conduction G/G_{max}; right y axis) and inactivation (normalized current I/I_{max}; Left) for Kv2.1/Kv6.4 channels assembled from monomers (black

circles), Kv2.1-Kv6.4 dimer (white squares; $V_{1/2}$ = -58.4±0.7 mV, k = 18.4±0.6 mV/e-fold), and Kv6.4-Kv2.1 dimer (gray inverted triangles; $V_{1/2}$ = -62.5±1.9 mV, k = 21.6±2.5 mV/e-fold). Voltage dependence of activation was derived from plotting the normalized tail current amplitudes at -35 mV as a function of the prepulse potential. Voltage dependence of inactivation was obtained from the normalized peak current amplitude at +60 mV in function of the prepulse potential. **C)** Time constants of activation and deactivation obtained as described in *Methods*. Note that the biophysical properties of the Kv2.1-Kv6.4 and Kv6.4-Kv2.1 dimers were similar to those of the coexpressed Kv2.1 and Kv6.4 monomers.

Table 3.1: Biophysical properties of homotetrameric Kv2.1 and heterotetrameric Kv2.1/Kv6.4 channels composed of monomers, dimers or tetramers

	Activation			Inactivation		
	$V_{1/2}$	k	n	$V_{1/2}$	k	n
Monomer						
Kv2.1	6.1 ± 2.2	9.0 ± 0.4	7	-18.2 ± 2.3	6.4 ± 0.5	7
Kv2.1 + Kv**6.4**	7.9 ± 0.7	20.2 ± 0.7	3	-59.2 ± 2.5	7.4 ± 1.2	3
Dimer						
Kv2.1-Kv2.1	5.6 ± 2.4	10.9 ± 1.5	7	-23.4 ± 2.2	5.6 ± 0.9	7
Kv2.1-Kv**6.4**	-4.6 ± 1.0	18.4 ± 0.6	3	-58.4 ± 0.7	7.3 ± 0.3	3
Kv**6.4**-Kv2.1	2.4 ± 2.7	21.6 ± 2.5	4	-62.5 ± 1.9	7.3 ± 0.2	4
Tetramer						
Kv2.1-Kv2.1-Kv2.1-Kv2.1	1.8 ± 2.8	9.4 ± 0.6	5	-21.0 ± 1.9	5.6 ± 0.4	6
Kv2.1-Kv**6.4**-Kv2.1-Kv2.1 (3:1)	1.7 ± 2.9	14.9 ± 1.8	4	-54.8 ± 2.4	8.6 ± 0.7	10
Kv2.1-Kv**6.4**-Kv2.1-Kv**6.4** (2:2)	5.7 ± 3.1	21.9 ± 0.3	5	-62.8 ± 1.6	9.4 ± 0.9	9
Kv2.1-Kv**6.4**-Kv**6.4**-Kv2.1 (2:2)	ND					

Values are given as mean ± SEM and n is the number of cells analyzed. The midpoints of activation and inactivation ($V_{1/2}$), represented in millivolts, and the slope factor (k) were obtained from a single Boltzmann fit. ND, no data.

3.4.3 Kv2.1/Kv6.4 Heterotetramers Are Functional in an Alternating Arrangement

The results obtained from the dimer constructs indicated that Kv2.1/Kv6.4 channels are functional in a 2:2 configuration, consistent with the findings from the single subunit counting data. It remains unclear whether the arrangement of the silent subunits within the tetramer influences the function. Assuming that the channels are assembled as a dimer of dimers, the Kv2.1 and Kv6.4 subunits are likely arranged alternately within the heterotetrameric channel. However,

the Kv6.4 subunits can be positioned side by side instead of being separated from each other by Kv2.1 subunits. We will refer to these configurations as adjacent (side by side) and alternating, respectively. To evaluate the functional effect of different geometrical arrangements of Kv2.1/Kv6.4 channels with a 2:2 stoichiometry, the following tetrameric constructs were created: Kv2.1 tetramer, Kv2.1-Kv6.4-Kv2.1-Kv6.4, and Kv2.1-Kv6.4-Kv6.4-Kv2.1 (Fig. 3.5A). Similar to the dimeric constructs, neighboring subunits were covalently coupled with a 10 to 12 amino-acid linker. As for the dimeric constructs, band intensities of the Western blot analysis using Kv2.1 antibodies differed due to variation in transfection efficiencies, but revealed that all tetrameric constructs were expressed as a single polypeptide (Fig. 3.5B).

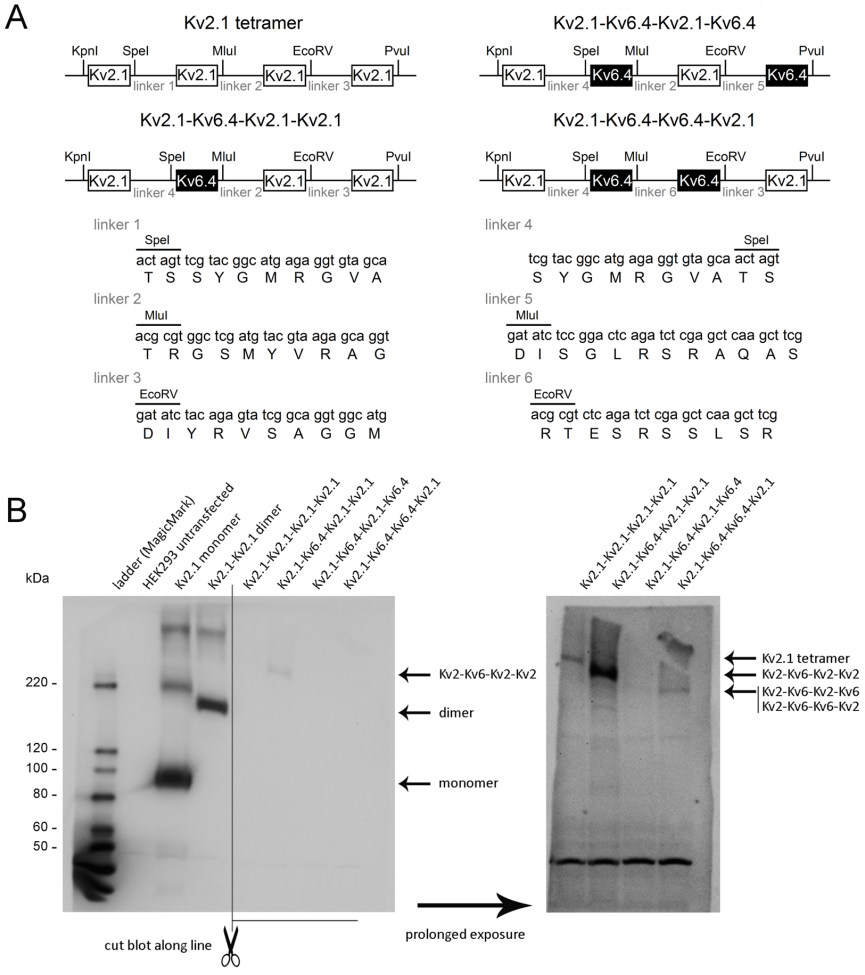

Figure 3.5 Overview and Western blot analysis of tetrameric constructs
A) Design of different tetrameric constructs composed of different unique rearrangements of Kv2.1 and Kv6.4 subunits which are shown in white and black, respectively. **B)** Expression of tetramers as a single

polypeptide was examined with Western blotting using Kv2.1 antibodies. The blot in B, Left was obtained after an exposure time of 1 minute. Because of an overload of Kv2.1 monomer and Kv2.1-Kv2.1 dimer protein compared to the different tetramers, the blot was cut, and the lanes with the different tetramer proteins were exposed for 10 minutes extra, yielding the blot in B, Right. In all lysates loaded (different lanes) a band was expected at the predicted molecular mass.

The functionality of the tetramers that represented the adjacent (Kv2.1-Kv6.4-Kv6.4-Kv2.1) and alternating (Kv2.1-Kv6.4-Kv2.1-Kv6.4) configurations were assessed, and their biophysical properties were compared with those of the Kv2.1 tetrameric construct. Tetramers in the alternating configuration produced ionic currents that displayed the biophysical signature of Kv2.1/Kv6.4 heterotetramers (Fig. 3.6 A-C and Table 3.1). Moreover, the kinetics of activation and deactivation differed from those of the Kv2.1 tetramer (Fig. 3.3D). The current density decreased from 360 ± 76 pA/pF (n = 7) to 160 ± 57 pA/pF (n = 6) at +30 mV for the Kv2.1 tetramer and Kv2.1-Kv6.4-Kv2.1-Kv6.4 (Fig. 3.6E), respectively. In contrast, tetramers representing the adjacent configuration produced no ionic currents yielding a current density of only 9 ± 3 pA/pF (n = 9; Fig. 3.6E). The results demonstrate that Kv2.1/Kv6.4 heterotetramers in a 2:2 stoichiometry function only when the Kv2.1 and Kv6.4 subunits alternate and not when the Kv6.4 subunits are positioned side by side (i.e., adjacent).

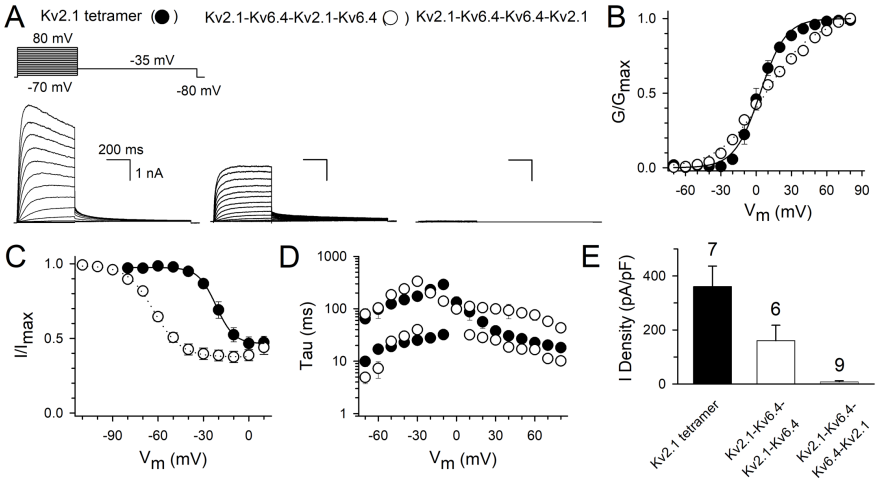

Figure 3.6 Biophysical Properties of Kv2.1/Kv6.4 tetrameric concatemers
A) Lower, Whole-cell current recordings after transfection of 5 µg of Kv2.1 tetramer (Left) (filled circles in B-D), Kv2.1-Kv6.4-Kv2.1-Kv6.4 (Center) (open circles in B-D), and Kv2.1-Kv6.4-Kv6.4-Kv2.1 (Right) elicited by the voltage protocol shown A, Upper. **B)** Plot shows the voltage dependence of activation determined for the Kv2.1 tetramer (filled circles; $V_{1/2}$ = -1.8±2.8 mV, k = 9.4±0.6 mV/e-fold) and Kv2.1-Kv6.4-Kv2.1-Kv6.4 tetramer (open circles; $V_{1/2}$ = -5.7±3.1 mV, k = 21.9±0.3 mV/e-fold). **C)** The voltage dependence of

inactivation is displayed for both the Kv2.1 ($V_{1/2}$ = -21.8±2.5 mV, k = 5.1±0.4 mV/e-fold) and Kv2.1-Kv6.4-Kv2.1-Kv6.4 tetramer ($V_{1/2}$ = -62.2±1.7 mV, k = 9.3±1.3 mV/e-fold). **D)** Time constants of activation and deactivation obtained as described in *Methods*. **E)** Current density of tetramers determined by normalizing the steady-state current at the end of a 500-ms pulse at +30 mV to the cell capacitance. The number of cells analyzed is indicated above every bar plot.

3.4.4 Kv2.1/Kv6.4 Channels Are Functional in a 3:1 Stoichiometrical Configuration

Since the above results suggested that the Kv6.4 subunits have no compatible interaction sites, it seems very unlikely that functional Kv2.1/Kv6.4 channels containing more than two Kv6.4 subunits can be formed under physiological conditions. However, it would leave the possibility to combine a homodimer with a heterodimer, leading to a 3:1 stoichiometry, as proposed for Kv2.1/Kv9.3. Although our single subunit counting data suggest a predominant 2:2 arrangement, we explored the functionality of Kv2.1/Kv6.4 channels in a 3:1 stoichiometry by constructing a Kv2.1-Kv6.4-Kv2.1-Kv2.1 tetramer. Under similar incubation conditions, this construct yielded ionic currents that displayed some hallmarks of Kv2.1/Kv6.4 heterotetrameric channels (Fig. 3.7). Compared to the Kv2.1 tetramer, the voltage dependence of inactivation was shifted into hyperpolarized direction and the voltage dependence of activation had a shallower slope factor k (Fig. 3.7 C and E and Table 3.1). Also, the time constants of activation displayed a fast and a slow component (Fig. 3.7D), typical for Kv2.1/Kv6.4 heterotetramers. However, comparing the properties to both the Kv2.1 homotetramer and the concatemers in 2:2 stoichiometry highlighted that the slope factor of activation and the shift of the inactivation of the concatemer in 3:1 stoichiometry differed significantly ($P \leq 0.003$; SI Appendix Fig. 3.S1) from the WT Kv2.1 tetramer and the Kv2.1-Kv6.4-Kv2.1-Kv6.4 tetramer (2:2 stoichiometry). The values of the 3:1 stoichiometry fell between both (Table 3.1). Thus, both parameters progressively alter with incorporation of more Kv6.4 subunits.

In comparison, the electrophysiological data of the Kv2.1/Kv6.4 heterotetramers assembled from monomeric subunits corresponded well to those of the 2:2 stoichiometry (Table 3.1 and Fig. 3.7 C and E). Statistical analysis indicated that the midpoint of inactivation of Kv2.1/Kv6.4 heterotetramers assembled from monomers resembled that of the Kv2.1-Kv6.4-Kv2.1-Kv6.4 tetramer (2:2 stoichiometry) and both differed significantly from that of the Kv2.1-Kv6.4-Kv2.1-Kv2.1 tetramer (3:1 stoichiometry, $P < 0.005$, Fig. 3.7F). This suggests that –

although a 3:1 stoichiometry is perfectly functional – coexpression of monomers prefers a 2:2 stoichiometry, consistent with an assembly as a dimer of dimers. The vast majority of the population has two silent Kv6.4 subunits, and only few (if any) have one Kv6.4.

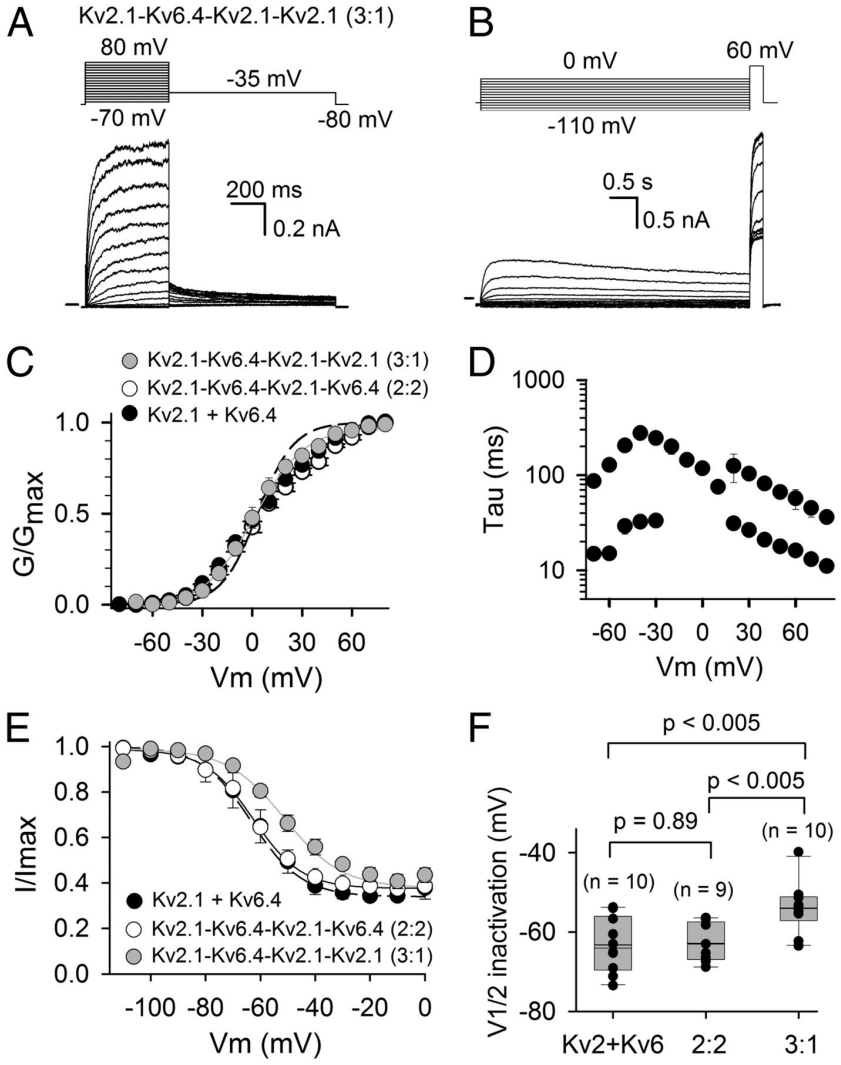

Figure 3.7 Biophysical properties of Kv2.1-Kv6.4-Kv2.1-Kv2.1 (3:1 stoichiometry)
A and B) Lower, representative whole-cell current recordings of Kv2.1-Kv6.4-Kv2.1-Kv2.1 used to determine the activation (A) and inactivation (B) properties. Voltage protocols are shown in A and B, Upper, and horizontal bar at the start of the recordings indicates the zero-current level. **C)** Plot displays the voltage dependence of activation for the Kv2.1-Kv6.4-Kv2.1-Kv2.1 (3:1) tetramer (grey circles; $V_{½}$ = 1.7±2.9, k = 14.9±1.8 mV/e-fold). As comparison the voltage dependence of activation for the Kv2.1+Kv6.4 heterotetramers assembled from monomeric subunits (Kv2+Kv6) and that of the Kv2.1-Kv6.4-Kv2.1-Kv6.4 (2:2) tetramer is retaken from Figs. 3.4 and 3.6 and represented with black and white circles respectively. **D)** Time constants of activation and deactivation of the Kv2.1-Kv6.4-Kv2.1-Kv2.1 tetramer are represented. **E)** Plot displays the voltage dependence of inactivation for the Kv2.1-Kv6.4-Kv2.1-Kv2.1 (3:1) tetramer (grey circles) compared to that of Kv2.1+Kv6.4 heterotetramers assembled from monomeric subunits (Kv2+Kv6; black circles) and that of the Kv2.1-Kv6.4-Kv2.1-Kv6.4 (2:2) tetramer (white circles). **F)** Box plot

represents the midpoint of channel inactivation values of Kv2.1+Kv6.4 heterotetramers assembled from monomers (Kv2+Kv6) and the Kv2.1-Kv6.4-Kv2.1-Kv6.4 (2:2) and Kv2.1-Kv6.4-Kv2.1-Kv2.1 (3:1) tetramers. One-way ANOVA with pairwise analysis between the three models was performed and the statistical significance was added to the figure. Values between parentheses indicate the number (n) of cells analyzed.

3.4.5 Tetraethylammonium Sensitivity Confirms Proper Assembly of Concatemers

Concatemers have been used successfully to investigate the stoichiometry of Kv channels (27, 28). However, due to the occurrence of T1-T1 interactions while the proteins are still attached to the ribosomes (41), it may be possible that multiple concatemers associate with each other, excluding some of the covalently attached subunits to be incorporated in the channel complex. In this case, the phenotype of the subunit positioned first in the construct will predominate, as they are more likely to be incorporated into the channel complex (34). The dimers used in this study did not seem to encounter this problem, as the biophysical properties of both Kv2.1-Kv6.4 and Kv6.4-Kv2.1 dimers were similar and comparable with those of coexpressed Kv2.1 and Kv6.4 monomers (Fig. 3.4 and Table 3.1).

Compared to the dimers, the tetrameric constructs might suffer more from this potential folding problem. However, two observations favor that the positional arrangement of the subunits were well constrained in our tetrameric constructs. First, the slope factor of the voltage dependence of activation becomes shallower and the midpoint of inactivation shifts towards more hyperpolarized potentials when more Kv6.4 subunits are included, and, second, the functionality of the tetrameric construct representing a 2:2 stoichiometry was abolished by changing the position of the Kv6.4 subunits from an alternating to an adjacent configuration. To unequivocally prove the proper folding of the tetramers, the sensitivity of the tetrameric constructs to extracellular applied tetraethylammonium (TEA) was determined. The binding site of extracellular TEA is well characterized in Kv channels, and a threonine residue in the pore loop of the Shaker-type Kv channel (residue T449, respectively) was identified as an important binding determinant (42). Kv2.1 and Kv6.4 have at the equivalent position a tyrosine and valine residue, respectively (Y384 in Kv2.1 and V425 in Kv6.4; Fig. 3.8A). Consequently, it was expected that Kv6.4 subunits are less sensitive to TEA than Kv2.1 subunits, which will decrease TEA sensitivity of the Kv2.1/Kv6.4 heterotetramers compared to Kv2.1 tetramers. Indeed, the concentration response

curve of the Kv2.1-Kv6.4-Kv2.1-Kv2.1 and the Kv2.1-Kv6.4-Kv2.1-Kv6.4 tetramer shifted gradually toward higher TEA concentrations with more Kv6.4 subunits being included (Fig. 3.8). Plotting the normalized remaining current as a function of applied TEA concentration yielded concentration effect curves with a half-maximal inhibitory concentration value of 2.5 ± 0.5 mM (n = 5), 5.4 ± 0.2 mM (n = 6), and 9.5 ± 1.3 mM (n = 5) for the Kv2.1, the Kv2.1-Kv6.4-Kv2.1-Kv2.1 (3:1), and the Kv2.1-Kv6.4-Kv2.1-Kv6.4 tetramer, respectively (SI Appendix, Fig. 3.S1). These data strengthen the argument that all four covalently coupled subunits of our tetrameric constructs were incorporated into the Kv2.1/Kv6.4 channels and that these heterotetrameric channels have, indeed, a different drug response compared to Kv2.1 homotetramers (40).

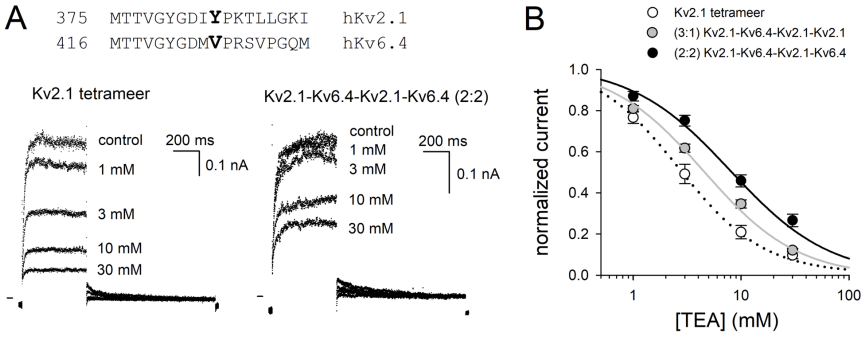

Figure 3.8 TEA sensitivity of tetrameric constructs
A) Upper, an alignment of a partial pore loop sequence of human Kv2.1 and hKv6.4 is shown. The corresponding residue identified to be important for TEA binding in Shaker-type Kv channels is highlighted in bold (Y385 and V425 in Kv2.1 and Kv6.4, respectively). A) Lower, representative steady-state current recordings are shown for the Kv2.1 (Left) and the Kv2.1-Kv6.4-Kv2.1-Kv6.4 tetramer (Right) in presence of different extracellular TEA drug concentrations. Whole-cell ionic currents were elicited by repetitively applying a +80 mV depolarizing step followed by a -35 mV repolarization before stepping to -80 mV holding potential (interpulse interval was 15 s). **B)** Concentration-effect curves for the Kv2.1 (white circles), the (3:1) Kv2.1-Kv6.4-Kv2.1-Kv2.1 (gray circles), and the (2:2) Kv2.1-Kv6.4-Kv2.1-Kv6.4 tetramer (black circles) obtained by normalizing the remaining steady-state currents from recordings shown in panel A as a function of applied TEA drug concentration. Note that the curve gradually shifts towards higher TEA concentrations when more Kv6.4 subunits are present in the tetramer.

3.4.6 Kv2.1/Kv6.4 Channels Intrinsically Prefer a 2:2 Stoichiometry

Considering that the concatemer containing a single silent subunit was functional, we should not exclude *ad hoc* the possibility of mixed populations. We demonstrated above that Kv2.1/Kv6.4 assemble predominantly in a 2:2 stoichiometry; however, it has been suggested

previously that the expression-level ratio between compatible Kv subunits can influence the stoichiometry of heterotetrameric channel complexes in heterologous expression systems (22-26). Our results above may, thus, be a consequence of the ratio in which Kv2.1 and Kv6.4(-GFP) were expressed. A fixed 3:1 stoichiometry has been suggested for Kv2.1/Kv9.3, and, recently, a preference for a 3:1 stoichiometry was also suggested for Kv2.1/Kv6.4 (43).

A pure or preferential 3:1 stoichiometry for Kv2.1/Kv6.4 would contradict our above results. However, if the assembly of the Kv2/KvS heteromers was concentration-dependent, then the distributions in the single subunit counting data should alter in a concentration-dependent manner, and we did not observe 3:1 stoichiometries because of an elevated Kv6.4 concentration. In this context, it is important to reflect upon the question of whether the single subunit counting data represent physiological conditions. To be able to observe single channels, we have to work at a relatively low expression level. However, the assembly of the channels into tetramers occurs already in the ER (41). It is, therefore, not the absolute number of channels expressed, but the Kv2.1/Kv6.4 ratio which are decisive for the biological assembly.

To test whether 3:1 stoichiometries occurred if less Kv6.4 subunits were present, we carried out the single subunit counting experiments at different expression ratios, altering the ratio of Kv2.1:Kv6.4 from 1:8 to 1:1, effectively increasing the relative amount of Kv2.1 (Fig. 3.9). In contrast to electrophysiological experiments, excess of Kv2.1 is possible here since the homotetrameric Kv2.1 channels are not fluorescently labeled and are, hence, silent in the optical measurements. No fluorescent spots were observed at the plasma membrane upon further increase of the Kv2.1:Kv6.4 ratio above 1:1, suggesting that Kv2.1 homotetramers were the ubiquitous form under those conditions.

To quantify the preference of a 2:2 over 3:1 stoichiometry, we calculated the weighted relative likelihoods at the different expression ratios. Under all conditions, including with probability of GFP fluorescence p_f free to vary, the probability of a 2:2 stoichiometry was $P > 0.9$. While it increased to even $P > 0.9999$ for expression ratios Kv2.1:Kv6.4 = 1:2 and 1:4 (Fig. 3.9). At the 1:1 ratio, we only observed a low number of spots (n = 610), which led to the lower certainty, indicating that, at all concentrations, the 2:2 stoichiometry was predominant.

We then evaluated the possibility of a mixed population of 3:1 and 2:2 stoichiometry, as suggested in Pisupati et al. (43). We assumed that channels of both compositions were able to colocalize, as colocalization occurs stochastically, and not due to a specific interaction. We used a convoluted distribution (see *Single Subunit Counting Analysis* section for details). As we outline below (see *Model Selection of Single Subunit Counting Data*), it is essential to have a sufficiently high expression to observe colocalization. Without it, the number of free parameters supersedes the number of data points, allowing any apparent ratio between the stoichiometries. The convoluted distribution of colocalized channels prevents this artifact. Our experimental results were best fitted by the resulting distribution function if the fraction of 3:1 channels was zero, i.e., by a pure 2:2 stoichiometry for all Kv2.1:Kv6.4 expression ratios tested (Table 3.2).

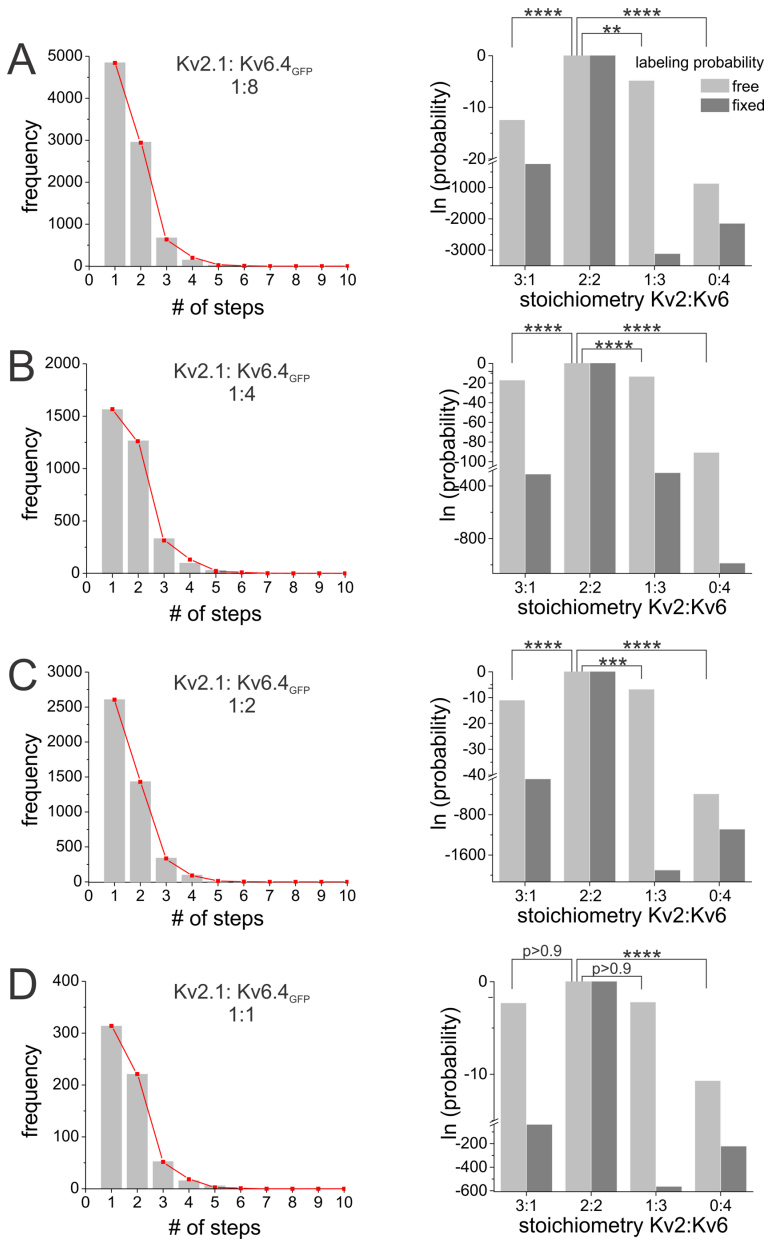

Figure 3.9 Concentration dependence of Kv2.1/Kv6.4 stoichiometry

Step distribution obtained from Kv2.1/Kv6.4-GFP heteromers expressed in *Xenopus* oocytes in weight:weight ratios 1:8 (**A**), 1:4 (**B**), 1:2 (**C**) and 1:1 (**D**) are shown. (Left) The grey bars indicate the observed distribution, the red trace the best fit for a 2:2 stoichiometry for fixed p_f and variable p_{col}. (*Right*) the relative likelihoods for homogenous populations for the given stoichiometries for fixed (*dark grey*) and free (*light grey*) probability of fluorescence p_f .** P > 0.99; ***P > 0.999; ****P >0.9999.n= 8,675 (A), 3,301 (B), 2,759 (C), 610 (D).

Table 3.2: Distribution of heterogenous populations

Kv2.1/Kv6.4 ratio	stoichiometry			p_{col}	p_f	significance
	3:1	2:2	1:3			
1:8	0	1	-	0.30	0.49	
	0	0.669	0.331	0.14	0.46	>0.999
1:4	0	1	-	0.30	0.57	
	0.01	0.741	0.252	0.18	0.55	>0.999
1:2	0.001	0.999	-	0.32	0.45	0.731
	0	1	0	0.32	0.45	0.269
1:1	0	1	-	0.29	0.53	0.58
	0.008	0.813	0.180	0.20	0.52	0.42

The single subunit counting distributions were fitted to distributions accounting for heterogenous populations. Each ratio was evaluated as a combination of 3:1 and 2:2 in absence (-) and presence of 1:3 stoichiometries. p_f represents the probability of GFP fluorescence and p_{col} the colocalization probability. The different stoichiometries were assumed to colocalize (e.g., one spot could contain one 2:2 and one 3:1 for a total of three potentially labelled Kv6.4). Significance was calculated as weighted likelihood ratios as previously.

We previously rejected the possibility of having three Kv6.4 and a single Kv2.1 subunit (i.e., a 1:3 Kv2.1:Kv6.4 stoichiometry) because T1 domains of Kv6.4 are not compatible, and it has been suggested that only heteromers with opposing silent subunits are functional (30, 37, 43-46). However, 1:3 channels might express as nonfunctional channels that are trafficked to the membrane as silent channels and, thus, appear in the single subunit counting data, leading to a heterogenous mixture of 3:1, 2:2, and 1:3 heteromers. We, therefore, also evaluated the possibility of a mixed population as above, now allowing 3:1, 2:2, and 1:3 stoichiometries (Table 3.2). While at expression ratios 1:1 and 1:2 the fit did not improve significantly compared to a pure 2:2 population, at high Kv6.4-GFP amounts (1:4 and 1:8), the fit improved when including a fraction up to 33% of Kv2.1/Kv6.4-GFP heteromers in the 1:3 stoichiometry. It should be noted that these distributions have an additional degree of freedom (the fraction of trimers), so it is not clear whether the improvement is owed to this. The results, thus, leave open the possibility, that at very high Kv6.4 expression levels nonfunctional heteromers in the 1:3

stoichiometry are trafficked to the plasma membrane. It is doubtful, however, that this has any physiological relevance. So, under physiological conditions, we propose that Kv2.1/Kv6.4 express in a preferred 2:2 stoichiometry consistent with both the single subunit counting and the electrophysiological data.

3.4.7 Model Selection of Single Subunit Counting Data

While our study suggests a fixed 2:2 Kv2.1/Kv6.4 stoichiometry, Pisupati et al. (43) reported a preferential 3:1 stoichiometry for the identical heteromer. Considering that the experimental data of both studies were quite similar, these contradicting interpretations raise the question how to objectively extract the correct stoichiometry (or mixture thereof) from the experimental data.

Single subunit counting data have, in general, the disadvantage of a low number of experimental data points (typically one to eight bleaching steps) and a strong similarity between the resulting distributions. The statistics have been improved after introduction of automated detection and analysis algorithms, which allowed a large number of spots to be analyzed, and, incidentally, also removed unconscious user bias to the “bestlooking” spots. To find the true stoichiometry, it is essential to not only show that a chosen model (stoichiometry or mixture thereof) fits the data well, but also that an alternative model, i.e., a different stoichiometry, shows less agreement. Our considerations of the heterogenous populations above also demonstrate that hidden populations (like 1:3) may be overlooked if no further alternatives are explored.

3.4.8 Model Selection in a Homogenous Population

When choosing the most likely model in a homogenous population, the task is to determine the true number of subunits N contained in each macromolecule with the highest probable confidence. Due to the probability of fluorescence (p_f), a single macromolecule can show 0 to N bleaching steps, which means that a dimeric protein would only show two nonzero data points. For a higher number of subunits, more nonzero data points would be observed, which prevents a direct comparison of different models. This problem is circumvented by allowing colocalization of two or more macromolecules within one diffraction-limited spot. Even if the colocalization

probability is close to zero, this allows an easier comparison among different models. All resulting distributions are described by three free parameters and contain an infinite number of nonzero points independent of the number of subunits per macromolecule N (*Methods* and Eq. 5). Accordingly, *a-posteriori* likelihoods can be directly compared, and we can determine the relative probabilities of the different models with weighted relative likelihoods, as described in *Methods*.

3.4.9 Characterizing Heterogenous Populations

The situation is different in heterogenous populations. Here, we do not decide which model is the most appropriate, but, rather, combine the different stoichiometries into a single function. The challenge for heterogenous populations is to determine the correct fractions of all three stoichiometries that best describe the heterogenous population (parameter fitting).

A mixture between monomers and dimers (as is the case here) is particularly challenging because two colocalized monomers are equivalent to a single dimer, and, vice versa, a dimer with only one fluorescent fluorophore is equivalent to a monomer. Consequently, a superposition of one- and two-step distributions can analytically be converted into a pure two-step population. This leads to the situation that, in the absence of colocalization, the distribution is described by more free parameters than it contains data points. Therefore, an infinite number of exact solutions exist. In the presence of colocalization, on the other hand, a single solution exists for the correct distribution between stoichiometries as shown in the minimum of the error landscape of a simulated distribution (Fig. 3.10 A and B).

But even in the presence of colocalization, the stochastic variations may be too large to obtain the correct parameters. Since the stochastic variations reduce with increasing sample size, we asked how many spots need to be analyzed to obtain a reliable result. We simulated heterogenous populations of a given ratio (0.7) between 3:1 and 2:2 stoichiometries comprising a variable number of channels, which were stochastically labeled (probability of fluorescence p_f) and colocalized (p_{col}). If we leave all three parameters free to vary within realistic values ($0 \leq \text{ratio} \leq 1$, $0.4 \leq p_f \leq 0.8$ and $0 \leq p_{col} \leq 0.3$), the ratios found were broadly distributed around the correct value with a 1-σ (68%) variation (or SD) of ±0.25 if 100 spots are analyzed (Fig. 3.10 C, *black*). This improves to only ±0.2 if 10^6 spots are analyzed.

Restricting p_f improves the accuracy significantly, but only if at least 1,000 spots were analyzed. 100 spots would not improve better than ±0.18, even if we had exact knowledge of p_f. If we allow p_f to vary by 10% and 5% around its predetermined value and increase the number of spots to 1,000, the SD reduces to ±0.13 and ±0.08, respectively (Fig. 3.10 C, *green and purple*). For Δp_f = ±5%, the value obtained for the ratio would lie between 0.62 and 0.78.

Further improvement is only possible by increasing the number of spots to 10^6 or by fixing p_f within 1% (Fig. 3.10 C, *red*; and Fig. 3.10 D, *Left*) and observing 10,000 spots (±0.02). However, this assumes that p_f is known exactly, as we do in the simulations. Under experimental conditions, a 2 to 5% variation in p_f is often observed due to variations in pre-bleaching or GFP maturation rate. If we fix p_f to a value 5% too high, the result for the ratio would be consistently off by ~10% (Fig. 3.10 D, *Right, red*). Here, it would be advisable to leave p_f free to vary within ±5%, which would find the correct ratio in most cases (Fig. 3.10 D, *Right, blue*).

To summarize, most accurate results would be obtained when 1) collecting sufficient data points (>1,000), 2) allowing for some colocalization (<30%), and 3) fitting the data both with a fixed p_f and a variable p_f that varies within a small range (±5% of the predetermined value), since it is unlikely that p_f is constant in an experimental setting.

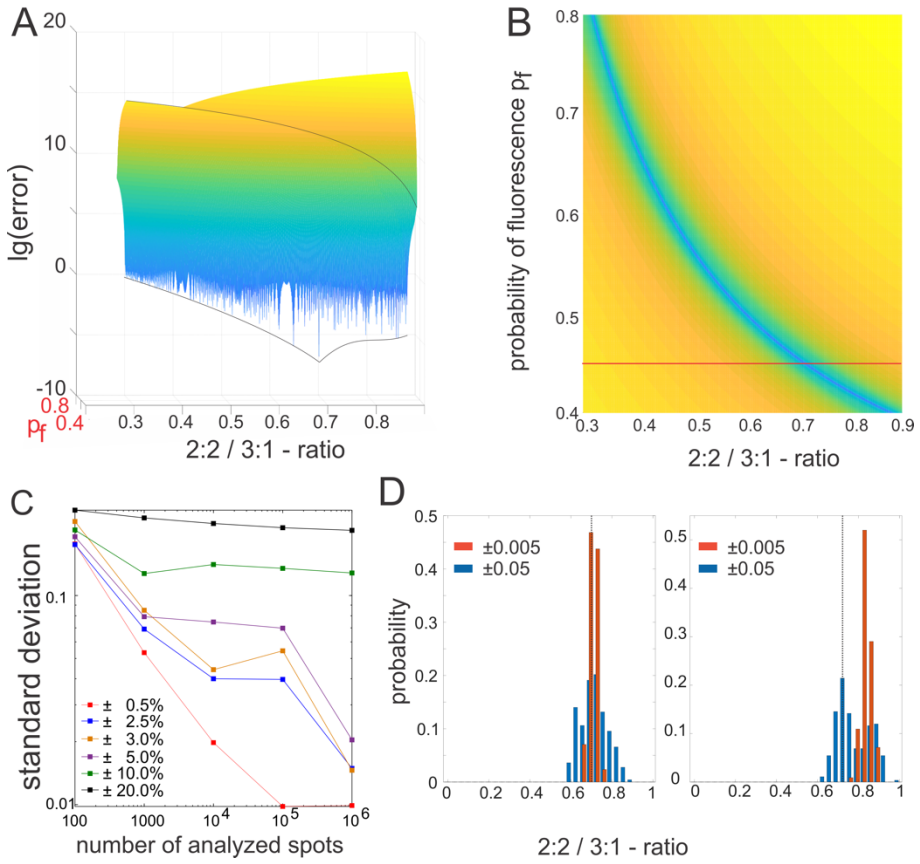

Figure 3.10 Model for channel assembly

A and **B)** Error landscape for the step histogram from single subunit counting data obtained from simulated data (10,000 spots). The error is given in logarithmic scale and denotes the deviation of the correct from the calculated step histogram for any given set of parameters p_f and the ratio between a 2:2 and 3:1 stoichiometry in a heterogenic population. Colocalization allows for a single minimum in the error landscape. The red line in B indicates the correct p_f. **C)** Accuracy of finding the correct parameters. Shown is the 1-σ width of the normal distribution of the found values (e.g., D) with a midpoint in the correct value for the 2:2/3:1-ratio. With a fixed (±0.005) p_f, the ratio can be determined with 1% accuracy when analyzing 100,000 points. **D)** Ratios found by fitting the histograms of simulated 10,000 spots when restricting the p_f to the correct (Left) and 5% too low (Right) value. P_f was allowed to vary 0.5% (red) or 5% (blue).

3.5 Discussion

KvS subunits display, compared to the ubiquitously expressed Kv2 subunits, a more restricted expression pattern. It is, therefore, expected that the KvS subunits tune the expression and localization of Kv2 currents in order to meet the tissue-specific requirements, as has been confirmed by the involvement of different KvS subunits in several (patho-) physiological processes (for review, see ref. 47). This makes them potential therapeutic targets, especially since it was demonstrated that Kv2.1/Kv6.4 channels are modulated differently by the well-characterized drug 4-aminopyridine compared to Kv2.1 homotetramers and other Kv2/KvS heterotetramers (40). It has been shown and confirmed by our TEA experiments (Fig. 3.8) that the pharmacological characteristics of heteromeric Kv channel complexes are affected by the stoichiometry of the subunits involved (26, 48, 49). The differential pharmacological response underlines the importance to know the exact stoichiometries of these heterotetrameric Kv2/KvS channels. Furthermore, our data show that there is also a significant 8-mV hyperpolarizing shift in the voltage dependence of inactivation between a 2:2 or 3:1 stoichiometry (Table 3.1 and Figs. 3.6 and 3.7). Although this shift seems on first sight small, the amount of inactivated channels at physiological relevant resting membrane potentials almost doubles. At −70 and −60 mV the amount of inactivated channels is in a 3:1 stoichiometry ∼10 and 20% (Fig. 3.7), whereas in the 2:2 stoichiometry, it amounts to ∼20 and 35%, respectively (Fig. 3.6). A recent paper on Kv2.1-related neurodevelopmental disorders documented a spectrum of Kv2.1 mutations (50). Among pathogenic mutations that did not affect current density, negative shifts in the voltage-dependence of inactivation in the order of 10 to 20 mV were observed that would sufficiently reduce channel availability, resulting in a loss of function (50).

Tetramerization of Kv channels is guided by the N-terminal T1-domain, which facilitates the assembly of compatible subunits and prevents the addition of incompatible subunits into the channel tetramer (51-54). For example, removal of the T1 domain from the incompatible subunits Kv2.1 and Kv1.4 resulted in the coassembly of these subunits into a functional channel (51). Yeast two-hybrid assays and Förster resonance energy transfer analysis have shown that the T1 domain of KvS subunits interacts with that of Kv2.1, but not with their own, suggesting that no functional

KvS homotetramers can be formed and that Kv2/KvS heterotetramers cannot contain more than two KvS subunits (30, 37, 44-46). This has been supported by the observation that Kv2.1/Kv9.3 heterotetramers consist of three Kv2.1 subunits and one Kv9.3 subunit (20), proposing that a similar 3:1 stoichiometry applies to all Kv2/KvS heterotetramers. While our results confirmed that concatemeric Kv2.1/Kv6.4 channels with a 3:1 stoichiometry are functional (Fig. 3.7), they also showed that Kv2.1/Kv6.4 channels adopt a 2:2 configuration independent of the expression ratio when assembled from monomers (Figs. 3.1 and 3.9). The functionality of Kv2.1/Kv6.4 channels with a 2:2 configuration was further evidenced with dimeric and tetrameric constructs that indicated that the position of the silent Kv6.4 and Kv2.1 subunit have to alternate to yield functional channels. Although it was previously not reported that Kv2.1/KvS channels with a 2:2 configuration are functional, it agrees with the general scheme that Kv channels assemble by dimerization of dimers in which the dimeric interaction sites differ from those mediating monomer–monomer interactions (18).

Since Kv6.4 subunits do not interact directly, it is very unlikely that Kv6.4 dimers are formed, which implies that not more than two Kv6.4 subunits can be incorporated into a Kv2.1/Kv6.4 heterotetramer, although the single subunit counting data did not explicitly exclude this possibility at high Kv6.4 levels. The subsequent assembly of two Kv2.1/Kv6.4 dimers into a functional channel can occur by at least two possible ways: The Kv2.1/Kv6.4 dimers assemble into a tetramer without any interaction between the two Kv6.4 subunits, or the dimerization of the Kv2.1 and Kv6.4 monomers induces conformational changes that allows the Kv6.4 subunits to interact with each other. However, in the latter case it might be expected that the Kv6.4 subunits can be positioned side by side in the Kv2.1/Kv6.4 heterotetramer. Our data indicate that such a positional arrangement does not produce functional Kv2.1/Kv6.4 heterotetramers (Fig. 3.6A) and disfavors this scenario. The adjacent position of two Kv6.4 subunits would also be difficult to reconcile with the specific interactions between N and C termini in the heteromeric complex (37) and it has been shown that parts of the S6 play a key role in stable heteromer formation (43).

Other heterotetrameric Kv channels can assemble with a random subunit stoichiometry and arrangement, depending on the ratio between the involved subunits (22-26). For example, Kv7.2/Kv7.3 heterotetramers display a fixed 2:2 stoichiometry when cells express an equal

amount of both subunits, but varying this ratio results in Kv7.2/Kv7.3 heterotetramers with a variable stoichiometry (25). This raises the possibility that cells can modulate Kv currents through endogenous changes in subunit expression level. Our present study demonstrated that Kv2.1/Kv6.4 channels can functionally express in variable 3:1 or 2:2 stoichiometry when using concatemers, but predominantly expresses in 2:2 stoichiometry when coexpressed. The predominant 2:2 stoichiometry in the single subunit counting data are reflected in the electrophysiological properties of the Kv2.1-Kv6.4 dimer and Kv2.1-Kv6.4-Kv2.1-Kv6.4 tetramer constructs, which strongly resemble the properties of Kv2.1+Kv6.4 coexpression. A detailed analysis of the electrophysiological data (see SI Appendix) describes how the contribution of each subunit to the properties of the channel can be estimated. This analysis suggests that the behavior of Kv2.1 and Kv6.4 subunits in the coexpressions is consistent with the behavior observed in the concatemeric constructs in 2:2 stoichiometry.

The analysis also shows that the voltage dependence of Kv6.4 subunits is far shifted toward more polarized potentials compared to Kv2.1, in agreement with previous findings (35). Consequently, Kv6.4 subunits control inactivation. Activation, on the other hand, is controlled by the Kv2.1 subunits, since all subunits need to be activated to open the channel.

Interestingly, the Kv6.4 subunits seem to influence the apparent gating charge of the Kv2.1 subunits associated with activation—cutting them in half—without changing the midpoint of activation. We should note here that the apparent gating charges were determined from channel opening, assuming a single voltage-dependent step for activation, and therefore does not directly reflect the actual gating charges found in the primary sequence of the voltage-gated ion channels. As the actual charges remain unaltered and allosteric influence of the electric field is highly unlikely, the reduced apparent charge suggests that the Kv6.4 subunits do not allow the gating charges responsible for the final pore opening to move through the entire electric field. This steric hindrance of the Kv2.1 subunits to reach their final state is consistent with the mismatch in the S6 of Kv2.1 and Kv6.4, as suggested by Pisupati et al. (43).

The thorough analysis of the electrophysiological data thus confirmed the findings from the single subunit counting measurements. Our subunit counting analysis introduced a method to

reliably interpret any single subunit counting data and thereby eliminated any ambiguity in model selection. In particular, the inclusion of colocalization—in addition to increasing the number of data points—allows direct evaluation of the likelihoods among different models and removes the ambiguity in the probability of fluorescence. We expect that the analysis algorithm provides clear criteria for model selection and will make single subunit counting useful in the interpretation of heteromeric macromolecules such as ion channels but also the large family of G-protein-coupled receptors.

3.6 Methods

3.6.1 Electrophysiology

Ltk$^-$ cells (mouse fibroblasts; ATCC CCL 1.3), which showed low endogenous K^+ currents, were cultured in Dulbecco's modified Eagle medium supplemented with 10% horse serum and 1% penicillin/streptomycin under a 5% CO_2 atmosphere. Cells were transiently transfected by using Lipofectamine 2000 (ThermoFisher) with the appropriate amount of channel complementary DNA (cDNA), as indicated in the figure legends. A total of 0.5 µg of enhanced GFP (eGFP) was cotransfected as transfection marker. Cells transfected with dimeric constructs were incubated at 37 °C for 16 to 24 h. Tetrameric constructs were incubated at 25 °C for 48 h to aid protein folding. Cells were subsequently enzymatically dissociated with trypsin and used for electrophysiological analysis.Whole-cell currents were recorded at ∼21 °C by using an Axopatch-200B amplifier and digitized by using a Digidata-1440A acquisition system. Command voltages and data storage were controlled with the pClamp (Version 10.2) software (all Molecular Devices). Patch pipettes were pulled from 1.2-mm borosilicate glass (WPI) and subsequently heat polished. This yielded patch pipettes with a resistance of 1 to 3 MΩ in the solutions used. Extracellular bath solution contained (in mM): 145 NaCl, 4 KCl, 1 $MgCl_2$, 1.8 $CaCl_2$, 10 HEPES and 10 glucose, with the pH adjusted to 7.35 with NaOH. The patch pipettes were filled with an intracellular solution containing (in mM): 110 KCl, 5 K_2ATP, 2 $MgCl_2$, 10 HEPES and 5 K_4-BAPTA adjusted to pH 7.2 with KOH. Junction potentials were zeroed with the filled pipette in the bath solution. Cells were excluded from analysis if the voltage error exceeded 5mV after series resistance compensation. Cells were continuously superfused with extracellular solution.

3.6.2 Concatemer Design

Human Kv2.1 and Kv6.4 were both cloned in the mammalian expression vector peGFP-N1 (Clontech) as described previously (30). Concatemeric constructs were created by the sequential insertion of individual subunits into peGFP-N1. Adjacent subunits shared a unique restriction-enzyme (RE) site and were segregated by a linker sequence of 30 to 36 bp, which was added to the individual subunits before they were inserted into the concatemer. Both the appropriate RE sites and the linker sequences were introduced by PCR amplification using the QuickChange site-directed mutagenesis kit (Agilent) and mutant primers. The presence of the desired modifications and the accuracy of the final sequence were confirmed by DNA sequencing.

3.6.3 Western Blot

Concatemeric constructs (10 μg of cDNA per 75-cm^2 culture dish) were transiently transfected into human embryonic kidney 293 (HEK293) cells by using Lipofectamine 2000 according to the manufacturer's guidelines. Cells were cultured in minimal essential medium supplemented with 10% fetal bovine serum, 1% penicillin/streptomycin, and 1% nonessential amino acids under a 5% CO_2 atmosphere in a humidified 37 °C incubator. After harvesting, the cells were lysed by adding lysis buffer, consisting of phosphate-buffered saline (PBS) supplemented with 5 mM ethylendiaminetetraacetic acid, 1% Triton X-100, and a complete protease inhibitor mixture (Roche Diagnostics). The lysed cells were denatured in NuPAGE lithium dodecylsulfate sample buffer for 30 min at 37 °C. The samples were separated on a NuPAGE 3 to 8% Tris–acetate gel and then transferred to a poly(vinylidene fluoride) membrane, which was subsequently blocked with 5% nonfat milk powder in PBS. Concatemers were detected by overnight incubation of mouse Kv2.1 antibodies (K89/34, University of California Davis/NIH NeuroMab Facility), followed by incubation with horseradish peroxidase-labeled anti-mouse immunoglobulin G (GE Healthcare) and enhanced chemiluminescence detection by using the WesternBright Sirius Chemiluminescent Detection kit (Advansta), according to the manufacturer's guidelines.

3.6.4 Pulse Protocols and Data Analysis

Voltage protocols were adjusted based on the biophysical properties of the channels, as shown in the figures. Holding potential was –80 mV, and the interpulse interval ranged from 15 to 30 s to prevent channels from accumulating in the inactivated state. The voltage dependence of activation and inactivation was fitted to a Boltzmann equation: $y = 1/1/[1 + \exp(-(V-V_{1/2})/k)]$, in which V represents the applied voltage, $V_{1/2}$ the voltage at which 50% of the channels are open or inactivated, and k the slope factor. Activation and deactivation time constants were determined by fitting the activating and deactivating currents with a single- or double-exponential function. Results are presented as mean ± SEM with n the number of analyzed cells. One-way ANOVA with pairwise comparison between groups was used to find statistical significance in the midpoint of channel inactivation and in TEA sensitivity between WT Kv2.1 tetramer, the Kv2.1-Kv6.4-Kv2.1-Kv2.1 tetramer (3:1 stoichiometry) and the Kv2.1-Kv6.4-Kv2.1-Kv6.4 tetramer (2:2 stoichiometry). P values lower than 0.05 were considered statistically significant. Data were analyzed by using pClamp10 and Sigmaplot (Version 11; Systat).

3.6.5 Expression of Kv2/KvS in Xenopus oocytes

Kv2.1 and Kv6.4-GFP were fused into the pBSta and pSP64 vector, respectively, as described previously (55) and cRNA was *in vitro* transcribed by using a T7 mMachine kit (Invitrogen), according to the manufacturer's protocol. Oocytes from *X. laevis* were surgically obtained, according to protocols approved by the Comité de déontologie de l'expérimentation sur les animaux de l'Univeristé de Montréal. Follicular membrane was removed enzymatically with collagenase type 1A (1 mg/mL; catalog no. C9891, Sigma) in a Ca^{2+}-free solution. Oocytes were injected with varying ratios of Kv2.1 and Kv6.4–GFP RNA (in ng: 23+0, 23+23, 3+6, 3+12 and 3+24) and incubated for 18 to 48 h at 18 °C.

Oocytes were treated with neuraminidase (1 U/mlL and hyaluronidase (1 mg/mL) for 4 to 5 minutes at room temperature to enzymatically remove the extracellular matrix. Subsequently, oocytes were transferred into a hyperosmotic solution (in mM: 250 KCl, 1 MgCl, 1 ethylen glycol tetraacetic acid, 50 sucrose and 10 HEPES, pH 7.4), and the vitelline membrane was manually removed.

Nº 1 glass coverslips were cleaned in the sequence: sonication (at 37 kHz and T = 60°C) in Alconox 1% in H_2O and two times in anhydrous ethanol. Coverslips were rinsed with H_2O after each sonication step and, finally, dried under a steady-filtered nitrogen stream. For imaging, the injected and pretreated oocytes were placed onto the cleaned coverslips with the animal pole facing down (in mM) 115 N-methyl glucamine, 50 sucrose, 10 HEPES and 2 $Ca(OH)_2$, adjusted to pH 7.4 with methyl-sulfonic acid.

3.6.6 Imaging Photobleaching Using Total Internal Reflection Fluorescence

Fluorescence was recorded by using an Axiovert-200 microscope (Zeiss). Excitation was achieved in total internal reflection fluorescence (TIRF) configuration using a 488-nm laser (PhoXx, Omicron). For TIRF imaging, the laser light was reflected at an angle sufficient to achieve total reflection and only evanescent excitation in the region within ~300 nm above the coverslip, thus eliminating background fluorescence emerging from the cytosol. Excitation intensity was 3.7 mW/mm^2. Emission was collected with a 60X numerical aperture-1.49 objective (Olympus) and filtered by a bandpass emission filter (ET525/50 nm) in combination with a laser line reflecting dichroic mirror (Z405/488/561/635, Chroma). Images were recorded with a backlit 128x128 pixel electron-multiplying charge-coupled device (EMCCD) camera (iXon+ 860BV, Andor) at a sampling rate of 20 Hz.

3.6.7 Single Subunit Counting Analysis

Spot detection and trace analysis were carried out by using the automated algorithm *PIF* (Progressive Idealization and Filtering) (9) to achieve objective criteria for acceptance and rejection of movies and single spots and to avoid user bias. PIF, was specifically designed to automatically detect fluorescent spots; filter fluorescence traces to remove background, thus increasing signal-to-noise ratio; and, finally, count bleaching steps (9). The following parameters were used for *spot detection*: The *selection of a spot* was limited to one neighbor (3 x 3 pixels), and the *minimum signal/noise ratio (dF/F)* was set to 10%. Since noninjected oocytes did not add fluorescent spots beyond the background of the cleaned coverslips, the *minimum fluorescence intensity amplitude* was set to 0. The *spot overlap limit* was restricted to sigma = 1.25. The

following parameters were used for *step detection*: Changes in the *minimal* and *maximal step amplitude* did not influence the final histograms, so they were left at 0 and 1 x 10^6, respectively. The *total fluorophore photobleach* length was set to 100%. All other trace quality control parameters were kept at their default setting.

The region of interest (ROI) function was used to remove out-of-focus areas. Once the initial analysis was completed, step frequency histograms were accepted according to the following criteria: 1) No spot movement was detected; 2) the global photobleaching decay displayed an exponential decay with three time constants; 3) spot density was below 0.04 spots/(total number of pixels) in ROI; and 4) not more than 70% of the traces were rejected. The final histogram was fitted to a binomial distribution of fourth order for Kv2.1-GFP, resulting in a probability of fluorescence (GFP maturation efficiency) of $p_f = 0.48$. This parameter reflects the fact that the chromophore matures only in a fraction of all GFP proteins. The distribution histograms of Kv2.1/Kv6.4-GFP measurements were best fitted with a binomial distribution of second order while maintaining a fixed p_f of 0.48. Results are presented with n as the number of accepted spots.

The models for different stoichiometries were evaluated by *weighted relative likelihoods* (56, 57) given by

$$ {}^{w}rL_i = \frac{rL_i}{\sum_k rL_k} \qquad [1] $$

with i indexing the stoichiometry, and the sum over k includes all possible stoichiometries and the relative likelihoods rL_i

$$ rL_i = \exp\left(\frac{AIC_{min} - AIC_i}{2}\right) \qquad [2] $$

Here, AIC defines the Akaike information criterion (58)

$$ AIC_i = 2 \cdot f - 2\ln\left(L_i\right) \qquad [3] $$

with *f* the number of free parameters in the model *i*, and *Li* the likelihood of the model *i:*

$$ \ln\left(L_i\right) = \sum_{k=\#steps} n_k \cdot ln\left(p_{k,i}\right) \qquad [4] $$

n_k represents the absolute number of experimentally observed events with k photobleaching steps, and $p_{k,i}$ describes the probability to find *k* photobleaching steps according to model (stoichiometry) *i*,

$$p_{k,i} = \sum_{w \geq \frac{k}{i}} \frac{{p_{col}}^{w-1}}{(w-1)!} e^{-p_{col}} \binom{w \cdot i}{k} p_f^k \cdot \left(1 - p_f\right)^{w \cdot i - k} \quad [5]$$

representing a Poisson-weighted sum of binomials, with p_{col} the probability of finding two channels within a diffraction-limited spot and *w* the number of channels in the spot. p_f is, again, the probability of fluorescence.

We chose to use the weighted relative likelihoods and AIC instead of Bayesian-based estimators since the number of free parameters for all models remains constant. In this context, the penalty for additional free parameters in the Bayesian Information Criterion disappears.

The distribution for heterogenous populations had to consider the colocalization of channels with different stoichiometry. Noncolocalized spots (i.e., single channels) were calculated as a linear superposition of the distributions respective for the three stoichiometries 3:1 ($\vec{M}$), 2:2 ($\vec{D}$) and 1:3 ($\vec{T}$). Colocalized spots with two or more channels were calculated by exponentiation of the original distribution weighted by a Poisson distribution representing the probability of finding more than one channel in one spot. The final distribution $\vec{S}$ was thus

$$\vec{S} = \left[\sum_{i=1}^{\infty} \frac{{p_{col}}^{i-1}}{(i-1)!} e^{-p_{col}} \cdot \left(p_{3:1}\vec{M} + p_{2:2}\vec{D} + p_{1:3}\vec{T}\right)^i\right] \cdot \vec{x} \quad [6]$$

where $p_{j:k}$ represent the fraction of the three populations with

$$p_{3:1} + p_{2:2} + p_{1:3} = 1. \quad [7]$$

$\vec{M}$ signifies the monomer (3:1) stoichiometry. It is a square matrix with

$$\vec{M}_{i,j} = \begin{cases} p_f & if\ i = j \\ 1 - p_f & if\ i = j + 1 \\ 0 & else \end{cases} \quad [8]$$

$\vec{D}\ and\ \vec{T}$ signify the dimer (2:2) and trimer (3:1) stoichiometries with $\vec{D} = \vec{M}^2$ and $\vec{T} = \vec{M}^3$.

The matrices are converted into a vector containing the distributions via multiplication with the vector $\vec{x}$

with $x_i = \begin{cases} 1 & if\ i = 1 \\ 0 & else \end{cases}$.

3.6.8 Simulations

Simulated data were generated according to the above equations, assuming Poisson (shot) noise for each probability. We chose different conditions; shown here are p_f = 0.55; p_{col} = 0.1, and dimer/monomer ratio = 0.7. We simulated 10,000 distributions each for 100, 1,000, 10,000, 100,000 and 1,000,000 spots. For randomly picked distributions from each ensemble (>1,000), we determined the best-fitting parameters. Since the parameters were not normally distributed, we determined the interval within which 68% (1-σ) of the data were found. All simulations and analysis was done in Matlab (Mathworks) with in-house-written routines.

3.7 Data Availability

All data discussed in the paper will be available

3.8 Acknowledgements

We thank Evy Mayeur, Gerda Van de Vijver, and Mireille Marsolais for the technical assistance. This work was supported by Research Foundation–Flanders grants G.0449.11N and G.0443.12N (to D.J.S.); Canadian Institutes of Health Research Grant MOP-136894 (to RB); and Natural Sciences and Engineering Research Council Grant (NSERC) Grant RGPIN-2017-06871 (to R.B.). L.M. was supported by fellowships of the Deutscher Akademischer Austauschdienst and the NSERC Training Program in Cellular dynamics of macromolecular complexes.

3.9 Supplemental Material

Analysis of Electrophysiology Kinetics

In this section, we investigate how the electrophysiological kinetics of activation and inactivation inform us on the stoichiometry of the Kv2.1-Kv6.4 heteromers.

3.9.1 Inactivation

We will first examine inactivation as it is most effected by the Kv2.1:Kv6.4 co-expression in a 1:8 ratio compared to the kinetics of WT Kv2.1 channels. Kv2.1 channels undergo U-type inactivation, which can be entered from the open but also directly from non-conductive states (S1, S2). In the polarized range that we investigated here, inactivation is predominated by inactivation from the activated pre-open state(s). In models describing U-type inactivation, the voltage dependence is governed by the activation of the voltage sensors (S1, S2, S3, S4). We assumed that the voltage sensors activate independently, and the inactivated state can be entered as soon at least one voltage sensor is in the activated state (S3, S4).

If we now assume that the subunits inactivate independently, then the probability that a Kv2.1 monomer is inactivated $p_{i,2}$ would follow a Boltzmann distribution proportional to activation of that subunit,

$$p_{i,2} = \left[1 + \exp\left(-\frac{z_{i,2}\,F}{RT}(V - V_0)\right)\right]^{-1} \qquad \text{(eq. S1)}$$

with F the Faraday constant, R the gas constant, T the temperature in Kelvin (300 K) and $z_{i,2}$ the apparent charge on the monomer that is associated with inactivation (i.e. the gating charge that determines the slope of the inactivation curve). The probability of inactivation P_i of the tetrameric Kv2.1 channel would then be proportional to the probability that none of the subunits are activated:

$$P_i = 1 - (1 - p_{i,2})^4. \qquad \text{(eq. S2)}$$

Under these assumptions, we obtained the voltage dependence of inactivation for the control experiments of Kv2.1-channels (inactivation curves) with the above equations and obtained a

$z_{i,2}$ = 3.1 and V_0 = -3.7. In the dimeric and tetrameric constructs (Kv2.1-Kv2.1 and Kv2.1-Kv2.1-Kv2.1-Kv2.1) the midpoint V_0 was shifted slightly towards hyperpolarization by 5-6 mV without significantly altering the slope of the inactivation curve and the gating charge.

In the dimeric constructs Kv2.1-Kv6.4 and Kv6.4-Kv2.1 as well as the tetrameric Kv2.1-Kv6.4-Kv2.1-Kv6.4 constructs, two monomers each of Kv2.1 and Kv6.4 are present. The probability would still be proportional to activation of the voltage sensors but with two different voltage dependencies. The inactivation probability becomes

$$P_i = 1 - (1 - p_{i,2})^2 \cdot (1 - p_{i,6})^2 \qquad \text{(eq. S3)}$$

where $p_{i,6}$ represents the probability of a single Kv6.4 to inactivate:

$$p_{i,6} = \left[1 + \exp\left(-\frac{z_{i,6}\,F}{RT}(V - V_0)\right)\right]^{-1} \qquad \text{(eq. S4)}$$

Assuming that the Kv2.1 behavior did not alter by the presence of the Kv6.4 subunits, we can derive the behavior of a single Kv6.4 with $z_{i,6}$ = 2.8 ± 0.4 and V_0 = -52.0 ± 1.9 mV. [values of the three different constructs were: Kv2-Kv6 a $z_{i,6}$ = 2.96 and V_0 = -50.2 mV, for Kv6-Kv2 a $z_{i,6}$ = 2.97 and V_0 = -54.0 mV, for the Kv2-Kv6-Kv2-Kv6 tetramer a $z_{i,6}$ = 2.32 and V_0 = -51.8 mV].

In the Kv2.1-Kv6.4-Kv2.1-Kv2.1 construct with only a single Kv6.4, P_i becomes

$$P_i = 1 - (1 - p_{i,2})^3 \cdot (1 - p_{i,6}), \qquad \text{(eq. S5)}$$

which produces $z_{i,6}$ = 2.9 and V_0 = -50.6 mV. The behavior (values) of the Kv6.4 monomer did not alter in the 3:1-tetramer compared to the 2:2-constructs, and we can therefore assume that the obtained $z_{i,6}$ and V_0 values are Kv6.4s intrinsic properties. The above results suggest that, under the assumption of independently inactivating subunits, both Kv2.1 and Kv6.4 monomers behave consistently in all stoichiometries, and only the number of subunits alters.

Under these premises, the values obtained for Kv6.4 can now be compared with those obtained from co-expressing Kv2.1 and Kv6.4 in a 1:8 ratio. First, assuming a 2:2 stoichiometry, P_i is calculated according to eq. S3. With unaltered $p_{i,2}$, we obtain for $p_{i,6}$: $z_{i,6}$ = 2.9 and V_0 = -50.9 mV. These values are consistent with those found for all dimers and tetramers.

In contrast, if we assume a 3:1 stoichiometry, P_i is calculated according to eq. S5, which results in a $z_{i,6}$ = 3.5 and V_0 = -59.1 mV. These values are significantly different than the intrinsic values of Kv6.4 determined above. Thus, while our model can be made consistent with a 3:1 stoichiometry, this is only possible by significantly shifting the values for Kv6.4 with respect to the concatemers. Considering the strong shift towards hyperpolarized potentials between Kv6.4 (-52.0 mV) and Kv2.1 (-3.7 mV), we can also deduce that inactivation is purely governed by the Kv6.4 subunits in the tetramers in physiologically relevant scenarios without influencing the intrinsic properties of the Kv2.1 monomers.

3.9.2 Activation

The effect on activation by co-expression seems more subtle. In fact, the midpoint of activation is only marginally altered, whereas the major effect is found to be on the apparent gating charge z_a. In contrast to inactivation, all four voltage sensors need to be activated for a homotetrameric Kv2.1 to open. The probability for activation P_a – equaling G/Gmax – becomes

$$P_a = p_{a,2}^4 \qquad \text{(eq. S6)}$$

with the probability $p_{a,2}$ of a Kv2.1 monomer to be activated

$$p_{a,2} = \left[1 + \exp\left(-\frac{z_{a,2}\,F}{RT}(V - V_0)\right)\right]^{-1} \qquad \text{(eq. S7)}$$

From the activation kinetics of the homotetrameric Kv2.1, we thus obtain $z_{a,2}$ = 2.2 and V_0 = -14.3 mV. In the dimeric and tetrameric homo-constructs, V_0 alters to -19.4 mV with the same $z_{a,2}$.

In the dimeric and tetrameric heteromers in a 2:2 stoichiometry, one would assume that P_a would be the geometric superposition of the independent probabilities according to

$$P_a = p_{a,2}^2 \cdot p_{a,6}^2, \qquad \text{(eq. S8)}$$

where $p_{a,6}$ is the probability of activation for a single Kv6.4 monomer. However, it was not possible to fit the data with this model using the above V_0 and $z_{a,2}$ values for Kv2.1. This indicates that the probability of *activation* for Kv2.1 is altered by the presence of Kv6.4. Such a cross-influence is perfectly feasible since we are monitoring pore opening following cooperative steps

instead of voltage sensor movement. Since the early closed state transitions of each voltage sensor occur independently, we can lump them into a single closed state. We then considered only the final 1-step transition to opening.

We fitted the dimeric and tetrameric 2:2 heteromers according to equation S8, while, this time, leaving the parameters of Kv2.1 free to alter, too. We then find that the Kv6.4 monomers have to be continuously activated (far shifted to hyperpolarizing potentials), whereas the Kv2.1 subunits keep their initial midpoint of activation V_0 but alter their apparent gating charge to half the original value ($z_{a,2}$ = 1.0 ± 0.1, V_0 = -22.0 mV ± 3.1 mV).

The 3:1-tetramer (Kv2.1-Kv6.4-Kv2.1-Kv2.1) shows a similar pattern with three Kv2.1 subunits with an apparent gating charge reduced to $z_{a,2}$ = 1.4 and V_0 = -25 mV, when fitted according to

$$P_a = p_{a,2}^3 \cdot p_{a,6}. \qquad \text{(eq. S9)}$$

Alternatively, Kv6.4 might only affect the adjacent Kv2.1 subunits. In this case, the 3:1-tetramer can also be described by one Kv2.1 behaving like wildtype and two with $z_{a,2}$ = 1.15 and V_o = -27.6 mV.

Thus, for all constructs, with both the 2:2 stoichiometries (Kv2-Kv6, Kv6-Kv2, Kv2-Kv6-Kv2-Kv6) and the 3:1 stoichiometry (Kv2-Kv6-Kv2-Kv2), we find a reduced apparent gating charge of $z_{a,2}$ = 1.1 ± 0.1 in the Kv2.1 adjacent to Kv6.4, assuming a single voltage-dependent activation step.

If we now compare the values obtained from the heteromeric co-expression of Kv2.1 and Kv6.4, we find that it behaves like two Kv2.1 with the reduced $z_{a,2}$ = 1.1 and V_0 = -14.9, as expected for a pure 2:2 stoichiometry. A 3:1 stoichiometry does not fit as well and would require a $z_{a,2}$ = 0.77 with a shift of V_0 = -32 mV, assuming that only the adjacent Kv2.1 are affected. Thus, while our model can fit both the homotetramer and concatemers, the experimental data of the co-expressed heteromers is not compatible with a 3:1 stoichiometry while keeping Kv2.1's midpoint of activation constant.

To summarize: (i) assuming independently activating subunits both for activation and inactivation as described above, the electrophysiological data of Kv2.1:Kv6.4 channels assembled

from monomers are consistent with a pure 2:2 stoichiometry, excluding the presence of predominantly heteromeric Kv2.1:Kv6.4 channels with 3:1 stoichiometry. (ii) Kv6.4 voltage dependence is strongly shifted to more hyperpolarized potentials both for inactivation and activation. As a consequence, inactivation is governed by Kv6.4 and activation by Kv2.1. (iii) Presence of Kv6.4 lowers the gating charge of the neighboring Kv2.1 subunits for activation. While the 1-step gating model with independently acting subunits that we used here likely does not completely describe Kv2.1/Kv6.4 gating, we find consistent results for the homotetramer and concatemers. The parameters of the heteromers assembled from Kv2.1 and Kv6.4 monomers are consistent with a predominantly 2:2 stoichiometry.

Supplemental Table S3.1: Biophysical properties of homotetrameric Kv2.1 and heterotetrameric Kv2.1/Kv6.4 channels composed of monomers, dimers or tetramers

	Activation								
	$V_{1/2}$	k	n	$V_{1/2}$	z_{app}	#	#	$V_{1/2}$	z_{app}
monomer									
Kv2.1	6.1 ± 2.2	9.0 ± 0.4	7	-14.3	2.2	4			
Kv2.1 + Kv**6.4**	7.9 ± 0.7	20.2 ± 0.7	3	-14.9	1.1	2			
				-29.2	0.98	3			
dimer									
Kv2.1-Kv2.1	5.6 ± 2.4	10.9 ± 1.5	7	-19.2	1.8	4			
Kv2.1-Kv**6.4**	-4.6 ± 1.0	18.4 ± 0.6	3	-25.2	1.16	2			
Kv**6.4**-Kv2.1	2.4 ± 2.7	21.6 ± 2.5	4	-21.9	0.98	2			
tetramer									
Kv2.1-Kv2.1-Kv2.1-Kv2.1	1.8 ± 2.8	9.4 ± 0.6	5	-19.5	2.5	4			
Kv2.1-Kv**6.4**-Kv2.1-Kv2.1 (3:1)	1.7 ± 2.9	14.9 ± 1.8	4	-25.0	1.36	3			
Kv2.1-Kv**6.4**-Kv2.1-Kv**6.4** (2:2)	5.7 ± 3.1	21.9 ± 0.3	5	-19.0	0.97	2			
	Inactivation								
	$V_{1/2}$	k	n	$V_{1/2}$	z_{app}	#	#	$V_{1/2}$	z_{app}
monomer									
Kv2.1	-18.2 ± 2.3	6.4 ± 0.5	7	-3.7	3.1	4			
Kv2.1 + Kv**6.4**	-59.2 ± 2.5	7.4 ± 1.2	3	-3.7	3.1	2	2	-50.9	2.9
				-3.7	3.1	3			
							1	-59.1	3.5
dimer									
Kv2.1-Kv2.1	-23.4 ± 2.2	5.6 ± 0.9	7	-10.7	3.5	4			
Kv2.1-Kv**6.4**	-58.4 ± 0.7	7.3 ± 0.3	3	-10.7	3.5	2	2	-50.2	3.0
Kv**6.4**-Kv2.1	-62.5 ± 1.9	7.3 ± 0.2	4	-10.7	3.5	2	2	-54.3	3.0
tetramer									
Kv2.1-Kv2.1-Kv2.1-Kv2.1	-21.0 ± 1.9	5.6 ± 0.4	6	-10.2	3.4	4			
Kv2.1-Kv**6.4**-Kv2.1-Kv2.1 (3:1)	-54.8 ± 2.4	8.6 ± 0.7	10	-10.2	3.4	3	1	-50.6	2.9
Kv2.1-Kv**6.4**-Kv2.1-Kv**6.4** (2:2)	-62.8 ± 1.6	9.4 ± 0.9	9	-10.2	3.4	2	2	-51.8	2.3

Values are given as mean ± SEM and n the number of cells analyzed. The midpoints of activation and inactivation ($V_{1/2}$), represented in mV, and the slope factor k in mV/*e*-fold were obtained from a single Boltzmann fit. The columns on the right reflect the transitions of the single subunits resulting in the same voltage dependences as fitted on the left. The # indicates how many subunits were assumed to contribute. z_{app} represents the apparent gating charge, assuming an electric free energy difference $z_{app}F\ (V-V_{1/2})$.

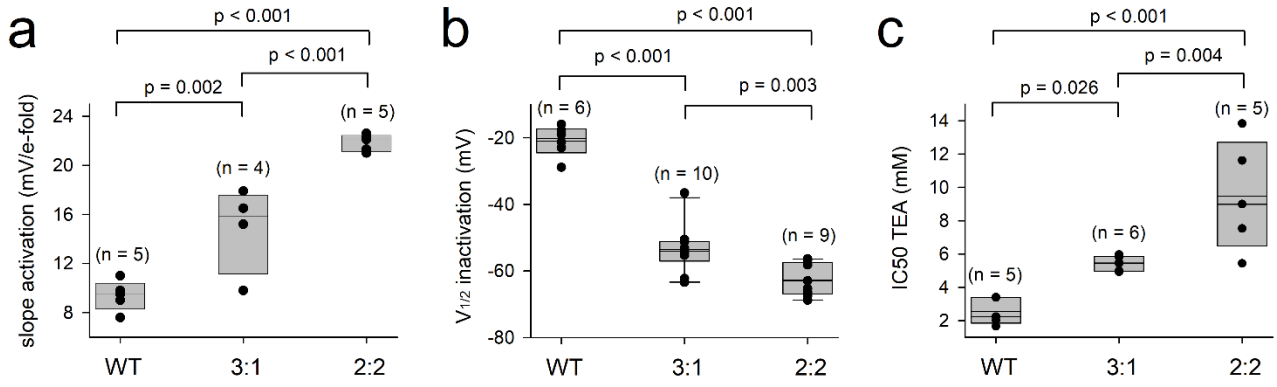

Figure 3.S1 Supplementary Figure

Single values and box plot for the tetrameric concatemers Kv2.1-Kv2.1-Kv2.1-Kv2.1 (WT), Kv2.1-Kv6.4--Kv2.1-Kv2.1 (3:1) and Kv2.1-Kv6.4-Kv2.1-Kv6.4 (2:2) are shown of (**a**) the slope factor of activation, (**b**) the $V_{½}$ of inactivation and (**c**) the IC50 value for TEA inhibition. One-way ANOVA with pairwise analysis between the three models was performed for each parameter (slope, V1/2 or TEA) and the statistical significance added to the figure. Values between parentheses indicate the number (n) of cells analyzed.

3.10 References

1. M. H. Ulbrich, E. Y. Isacoff, Subunit counting in membrane-bound proteins. *Nat Methods* **4**, 319-321 (2007).
2. V. Dunsing *et al.*, Optimal fluorescent protein tags for quantifying protein oligomerization in living cells. *Sci Rep* **8**, 10634 (2018).
3. N. Durisic *et al.*, Stoichiometry of the human glycine receptor revealed by direct subunit counting. *J Neurosci* **32**, 12915-12920 (2012).
4. N. Durisic, L. Laparra-Cuervo, A. Sandoval-Alvarez, J. S. Borbely, M. Lakadamyali, Single-molecule evaluation of fluorescent protein photoactivation efficiency using an in vivo nanotemplate. *Nat Methods* **11**, 156-162 (2014).
5. F. Fricke, J. Beaudouin, R. Eils, M. Heilemann, One, two or three? Probing the stoichiometry of membrane proteins by single-molecule localization microscopy. *Sci Rep* **5**, 14072 (2015).
6. A. G. Godin *et al.*, Spatial Intensity Distribution Analysis Reveals Abnormal Oligomerization of Proteins in Single Cells. *Biophys J* **109**, 710-721 (2015).
7. P. Li, Y. Miao, A. Dani, M. Vig, alpha-SNAP regulates dynamic, on-site assembly and calcium selectivity of Orai1 channels. *Mol Biol Cell* **27**, 2542-2553 (2016).
8. C. Liesche *et al.*, Automated Analysis of Single-Molecule Photobleaching Data by Statistical Modeling of Spot Populations. *Biophys J* **109**, 2352-2362 (2015).
9. H. McGuire, M. R. Aurousseau, D. Bowie, R. Blunck, Automating single subunit counting of membrane proteins in mammalian cells. *J Biol Chem* **287**, 35912-35921 (2012).
10. K. O. Nagata, C. Nakada, R. S. Kasai, A. Kusumi, K. Ueda, ABCA1 dimer-monomer interconversion during HDL generation revealed by single-molecule imaging. *Proc Natl Acad Sci U S A* **110**, 5034-5039 (2013).
11. K. Wong, S. J. Briddon, N. D. Holliday, I. D. Kerr, Plasma membrane dynamics and tetrameric organisation of ABCG2 transporters in mammalian cells revealed by single particle imaging techniques. *Biochim Biophys Acta* **1863**, 19-29 (2016).
12. Y. Yu *et al.*, Structural and molecular basis of the assembly of the TRPP2/PKD1 complex. *Proc. Natl. Acad. Sci. U. S. A* **106**, 11558–11563 (2009).
13. B. Hille, *Ionic channels of excitable membranes* (Sinauer Associates, Sunderland, Mass., ed. 2, 1991).
14. M. Li, Y. N. Jan, L. Y. Jan, Specification of subunit assembly by the hydrophilic amino- terminal domain of the *Shaker* potassium channel. *Science* **257**, 1225-1230 (1992).
15. N. V. Shen, X. Chen, M. M. Boyer, P. J. Pfaffinger, Deletion analysis of K^+ channel assembly. *Neuron* **11**, 67-76 (1993).

16. G. A. Gutman *et al.*, International Union of Pharmacology. LIII. Nomenclature and molecular relationships of voltage-gated potassium channels. *Pharmacol. Rev* **57**, 473-508 (2005).

17. E. Bocksteins, D. J. Snyders, Electrically silent Kv subunits: their molecular and functional characteristics. *Physiology (Bethesda)* **27**, 73-84 (2012).

18. L. Tu, C. Deutsch, Evidence for dimerization of dimers in K+ channel assembly. *Biophys. J* **76**, 2004-2017 (1999).

19. T. Jegla, L. Salkoff, A novel subunit for *Shal* K^+ channels radically alters activation and inactivation. *J. Neurosci* **17**, 32-44 (1997).

20. D. Kerschensteiner, F. Soto, M. Stocker, Fluorescence measurements reveal stoichiometry of K+ channels formed by modulatory and delayed rectifier {alpha}-subunits. *Proc. Natl. Acad. Sci. U. S. A* **102**, 6160-6165 (2005).

21. E. T. Powers, D. L. Powers, A perspective on mechanisms of protein tetramer formation. *Biophys J* **85**, 3587-3599 (2003).

22. M. Kitazawa, Y. Kubo, K. Nakajo, The Stoichiometry and Biophysical Properties of the Kv4 Potassium Channel Complex with K+ Channel-interacting Protein (KChIP) Subunits Are Variable, Depending on the Relative Expression Level. *J. Biol. Chem* **289**, 17597-17609 (2014).

23. M. Kitazawa, Y. Kubo, K. Nakajo, Kv4.2 and Accessory Dipeptidyl Peptidase-like Protein 10 (DPP10) Subunit Preferentially Form a 4:2 (Kv4.2:DPP10) Channel Complex. *J. Biol. Chem* **290**, 22724-22733 (2015).

24. K. Nakajo, M. H. Ulbrich, Y. Kubo, E. Y. Isacoff, Stoichiometry of the KCNQ1 - KCNE1 ion channel complex. *Proc Natl Acad Sci U S A* **107**, 18862-18867 (2010).

25. A. P. Stewart *et al.*, The kv7.2/kv7.3 heterotetramer assembles with a random subunit arrangement. *J. Biol. Chem* **287**, 11870-11877 (2012).

26. H. Yu *et al.*, Dynamic subunit stoichiometry confers a progressive continuum of pharmacological sensitivity by KCNQ potassium channels. *Proc Natl Acad Sci U S A* **110**, 8732-8737 (2013).

27. E. R. Liman, J. Tytgat, P. Hess, Subunit stoichiometry of a mammalian K^+ channel determined by construction of multimeric cDNAs. *Neuron* **9**, 861-871 (1992).

28. A. Naso, R. Montisci, F. Gambale, C. Picco, Stoichiometry Studies Reveal Functional Properties of KDC1 in Plant Shaker Potassium Channels. *Biophys. J* **91**, 3673-3683 (2006).

29. M. S. Shapiro, W. N. Zagotta, Stoichiometry and arrangement of heteromeric olfactory cyclic nucleotide-gated ion channels. *Proc Natl Acad Sci U S A* **95**, 14546-14551 (1998).

30. N. Ottschytsch, A. Raes, D. Van Hoorick, D. J. Snyders, Obligatory heterotetramerization of three previously uncharacterized Kv channel alpha -subunits identified in the human genome. *Proc. Natl. Acad. Sci. U. S. A* **99**, 7986-7991 (2002).

31. N. A. Minassian, M. C. Lin, D. M. Papazian, Altered Kv3.3 channel gating in early-onset spinocerebellar ataxia type 13. *J Physiol* **590**, 1599-1614 (2012).

32. L. Heginbotham, R. MacKinnon, The aromatic binding site for tetraethylammonium ion on potassium channels. *Neuron* **8**, 483-491 (1992).

33. M. P. Kavanaugh *et al.*, Multiple subunits of a voltage-dependent potassium channel contribute to the binding site for tetraethylammonium. *Neuron* **8**, 493-497 (1992).

34. K. McCormack, L. Lin, L. E. Iverson, M. A. Tanouye, F. J. Sigworth, Tandem linkage of *Shaker* K^+ channel subunits does not ensure the stoichiometry of expressed channels. *Biophys. J* **63**, 1406-1411 (1992).

35. E. Bocksteins *et al.*, Conserved negative charges in the N-terminal tetramerization domain mediate efficient assembly of Kv2.1 and Kv2.1/Kv6.4 channels. *J. Biol. Chem* **284**, 31625-31634 (2009).

36. E. Bocksteins, A. J. Labro, D. J. Snyders, D. P. Mohapatra, The electrically silent Kv6.4 subunit confers hyperpolarized gating charge movement in Kv2.1/Kv6.4 heterotetrameric channels. *PLoS. ONE* **7**, e37143 (2012).

37. E. Bocksteins *et al.*, The subfamily-specific interaction between Kv2.1 and Kv6.4 subunits is determined by interactions between the N- and C-termini. *PLoS One* **9**, e98960 (2014).

38. J. P. David, J. I. Stas, N. Schmitt, E. Bocksteins, Auxiliary KCNE subunits modulate both homotetrameric Kv2.1 and heterotetrameric Kv2.1/Kv6.4 channels. *Sci. Rep* **5**, 12813 (2015).

39. N. Ottschytsch, A. L. Raes, J. P. Timmermans, D. J. Snyders, Domain analysis of Kv6.3, an electrically silent channel. *J. Physiol* **568**, 737-747 (2005).

40. J. I. Stas, E. Bocksteins, A. J. Labro, D. J. Snyders, Modulation of Closed-State Inactivation in Kv2.1/Kv6.4 Heterotetramers as Mechanism for 4-AP Induced Potentiation. *PLoS. ONE* **10**, e0141349 (2015).

41. J. Lu, J. M. Robinson, D. Edwards, C. Deutsch, T1-T1 interactions occur in ER membranes while nascent Kv peptides are still attached to ribosomes. *Biochem* **40**, 10934-10946 (2001).

42. R. MacKinnon, G. Yellen, Mutations affecting TEA blockade and ion permeation in voltage-activated K+ channels. *Science* **250**, 276-279 (1990).

43. A. Pisupati *et al.*, The S6 gate in regulatory Kv6 subunits restricts heteromeric K(+) channel stoichiometry. *J Gen Physiol* **150**, 1702-1721 (2018).

44. M. Mederos y Schnitzler *et al.*, Mutation of histidine 105 in the t1 domain of the potassium channel kv2.1 disrupts heteromerization with kv6.3 and kv6.4. *J. Biol. Chem* **284**, 4695-4704 (2009).

45. M. A. Post, G. E. Kirsch, A. M. Brown, Kv2.1 and electrically silent Kv6.1 potassium channel subunits combine and express a novel current. *FEBS Lett* **399**, 177-182 (1996).

46. M. Stocker, M. Hellwig, D. Kerschensteiner, Subunit assembly and domain analysis of electrically silent K^+ channel alpha-subunits of the rat Kv9 subfamily. *J. Neurochem* **72**, 1725-1734 (1999).

47. E. Bocksteins, Kv5, Kv6, Kv8, and Kv9 subunits: No simple silent bystanders. *J. Gen. Physiol* jgp.201511507 [pii];10.1085/jgp.201511507 [doi] (2016).

48. A. Al-Sabi, S. K. Kaza, J. O. Dolly, J. Wang, Pharmacological characteristics of Kv1.1- and Kv1.2-containing channels are influenced by the stoichiometry and positioning of their alpha subunits. *Biochem J* **454**, 101-108 (2013).

49. A. Al-Sabi *et al.*, Arrangement of Kv1 alpha subunits dictates sensitivity to tetraethylammonium. *J. Gen. Physiol* **136**, 273-282 (2010).

50. S. K. Kang *et al.*, Spectrum of KV 2.1 Dysfunction in KCNB1-Associated Neurodevelopmental Disorders. *Ann Neurol* **86**, 899-912 (2019).

51. T. E. Lee, L. H. Philipson, A. Kusnetsov, D. J. Nelson, Structural determinant for assembly of mammalian K^+ channels. *Biophys. J* **66**, 667-673 (1994).

52. N. V. Shen, P. J. Pfaffinger, Molecular recognition and assembly sequences involved in the subfamily-specific assembly of voltage-gated K^+ channel subunit proteins. *Neuron* **14**, 625-633 (1995).

53. L. W. Tu *et al.*, Voltage-gated k+ channels contain multiple intersubunit association sites. *J. Biol. Chem* **271**, 18904-18911 (1996).

54. J. Xu, W. Yu, Y. N. Jan, L. Y. Jan, M. Li, Assembly of voltage-gated potassium channels. *J. Biol. Chem* **270**, 24761-24768 (1995).

55. Z. Batulan, G. A. Haddad, R. Blunck, An intersubunit interaction between S4-S5 linker and S6 is responsible for the slow off-gating component in Shaker K+ channels. *J Biol Chem* **285**, 14005-14019 (2010).

56. E. J. Wagenmakers, S. Farrell, AIC model selection using Akaike weights. *Psychonomic bulletin & review* **11**, 192-196 (2004).

57. C. A. Vandenberg, R. Horn, Inactivation viewed through single sodium channels. *J Gen Physiol* **84**, 535-564 (1984).

58. H. Akaike, Ed., *Information theory and an extension of the maximum likelihood principle* (Akadémiai Kiadó, Budapest, Hungary, 1973), pp 267-281.

S1. Klemic KG, Shieh CC, Kirsch GE, & Jones SW (1998) Inactivation of Kv2.1 potassium channels. *Biophys J* 74(4):1779-1789.

S2. Cheng YM*, et al.* (2011) Molecular determinants of U-type inactivation in Kv2.1 channels. *Biophys J* 101(3):651-661.

S3. Kaulin YA, De Santiago-Castillo JA, Rocha CA, & Covarrubias M (2008) Mechanism of the modulation of Kv4:KChIP-1 channels by external K+. *Biophys J* 94(4):1241-1251.

S4. Bahring R, Barghaan J, Westermeier R, & Wollberg J (2012) Voltage sensor inactivation in potassium channels. *Front Pharmacol* 3:100.

Chapter 4

The Putative Pain Sensor TACAN Assembles as Tetramer

Lena Moeller[1],Hélène Klein[2], Rikard Blunck[3,1]

1 Department of Biochemistry, Université de Montréal, Montréal, Canada

2 Department of Physiology, Université de Montréal, Montréal, Canada

3 Department of Physics, Université de Montréal, Montréal, Canada

Unpublished

Author Contributions

I performed the experiments, analyzed the data and wrote the manuscript.

Hélène Klein designed and created the plasmids as well as the stable cell line.

Rikard Blunck designed the research, helped with the data analysis and edited the manuscript.

4.1 Abstract

The body's ability to perceive and react to stimuli from the environment is fundamental for survival. The molecular player forming the complex responsible for transducing noxious touch stimuli has remained elusive for a long time. The mechanosensitive cation channel TACAN was recently suggested to be part of the molecular machinery responsible for transducing these pain signals in vertebrates. It is predicted to comprise six transmembrane helices, but the channel structure remains unsolved. Here, we investigate TACAN's oligomeric state using single subunit counting experiments by tethering purified channel complexes solubilized in detergent onto nickel-nitrilotriacetic acid functionalized coverslips, thereby increasing the signal to background ratio. We found that solubilizing the channels in *n*-Dodecyl β-D-maltoside allowed for more efficient tethering compared to Fos-Choline-14. Our subunit counting results showed that SEC-purified TACAN exists in various oligomeric states. Depending on the SEC fraction, we observed tetramers, trimer and dimers, suggesting that native TACAN channels assemble as tetramers, which are unstable when solubilized and purified.

4.2 Introduction

The underlying molecular mechanisms of how the body perceives and reacts to stimuli are not fully understood. The field of sensory perception has received much attention and a multitude of studies investigate the underlying processes. These studies can be divided into two subfields. The first investigates the perception of taste, smell and sight which depend on various G-protein coupled receptors (GPCRs). Small tasty or odorant molecules and photons activate different members of this receptor family, respectively (1-3). Activation of the receptors lead to signal transduction via secondary messengers that ultimately transform the external stimuli into electrical signals in neurons (4, 5).

The second field investigates the perception of sound and touch as well as proprioception which depend on mechanosensation. Unlike GPCR-mediated signal transduction, the molecular mechanisms underlying mechanosensation are less understood. Because of the rapid response time to mechanical stimuli, it has been postulated that the primary sensor is an ion channels (6,

7). Since these ion channels are less abundant than GPCRs that are highly expressed in sensory cells, possible candidates for mechanically activated channels remained for a long time unknown.

Of all sensory perception, the mechanism of sensing pain is the least understood. Recently published work identified TACAN as a mechanosensitive non-selective cation channel that is involved in pain sensing in vertebrates (8). Currently, the protein structure or even the oligomeric state of TACAN remain elusive. In the absence of a high-resolution structure, single subunit counting has been successfully applied to determine the number of protein complex subunits (9, 10). Single subunit counting is based on the stepwise photochemical destruction of fluorescent molecules linked to subunits of protein complexes and counting the photobleaching steps. Here, we investigate TACAN's oligomeric state via two separate single subunit counting approaches. In the first approach, we performed experiments directly in cells. Due to some limitations of the technique, i.e. high background fluorescence, we then performed the experiments by tethering purified fluorescently labeled channel complexes onto nickel-nitrilotriacetic acid (Ni-NTA) functionalized coverslips.

4.3 Results

4.3.1 GFP Background Fluorescence and Clustering of TACAN in Cells

Single subunit counting experiments are a direct method to study the number of subunits in unknown protein complexes and are typically performed in mammalian cells or *Xenopus* oocytes. TACAN was recently identified as a non-selective cation channel that generates mechanosensitive currents and is involved in pain sensing (11). The channel's structure including topology or oligomeric state remain unknown. To determine the oligomeric state of TACAN, we first conducted subunit counting experiments in transiently transfected HEK cells, which have been shown to functionally express the channel in the plasma membrane (8).

To resolve individual protein complexes, single subunit counting experiments rely on low protein expression and a good signal to noise ratio. We transfected HEK cells with super-folder monomeric GFP-tagged TACAN (TACAN-GFP) in varying conditions. Compared to control transfections of GluK2-GFP and Kv2.1-GFP which are both trafficked to the membrane (13, 14),

TACAN-GFP expression led to high background fluorescence and to protein clusters beyond the diffraction limit (figure 4.1a). To reduce background fluorescence, single subunit counting experiments are performed in TIRF mode. The evanescent excitation illuminates fluorescently labeled proteins in the plasma membrane (PM) and dissipates within approximately 300 nm above the coverslip. Since the intensity of the excitation decreases exponentially with the distance to the coverslip and the speed of bleaching depends on the excitation intensity, the speed of bleaching will depend on the distance from the coverslip. Fluorophores attached to proteins inserted in the plasma membrane bleach fastest and those located further inside the cell – but still within the first 300 nm – bleach with a slower speed. Typically, we find the exponential bleaching trace of an entire cell illuminated in TIRF mode described by three time constants. The fastest time constant represents contamination directly on the coverslip, the intermediate represents fluorophores in the plasma membrane while the slowest represents the fluorophores further away from the coverslip, i.e. in the intracellular of the cell (13). Comparing TACAN's exponential bleaching traces with those of the sfmGFP-tagged plasma membrane protein controls GluK2 and Kv2.1 shows that bleaching is slower and incomplete (figure 4.1b). This suggests that only a fraction of TACAN subunits traffics to the plasma membrane. We then investigated if this background fluorescence is comparable to background fluorescence originating from fluorescently tagged proteins located in the ER. To this aim, we compared the overall bleaching of TACAN-GFP to Kv6.4-GFP which gets trapped in the ER and to co-expressed Kv2.1/Kv6.4-GFP channels which traffic partially to the plasma membrane but also suffer from background fluorescence originating from untrafficked Kv6.4-GFP. In comparison, TACAN-GFP was slower and slightly less complete (figure 4.1b). While expressing Kv6.4-GFP resulted in diffuse background fluorescence and GluK2-GFP and Kv2.1-GFP in uniform expression of single channels in the plasma membrane observed as distinct spots, expression of TACAN-GFP resulted not only in diffuse background fluorescence but also in larger fluorescent spots (clusters) (figure 4.1a).

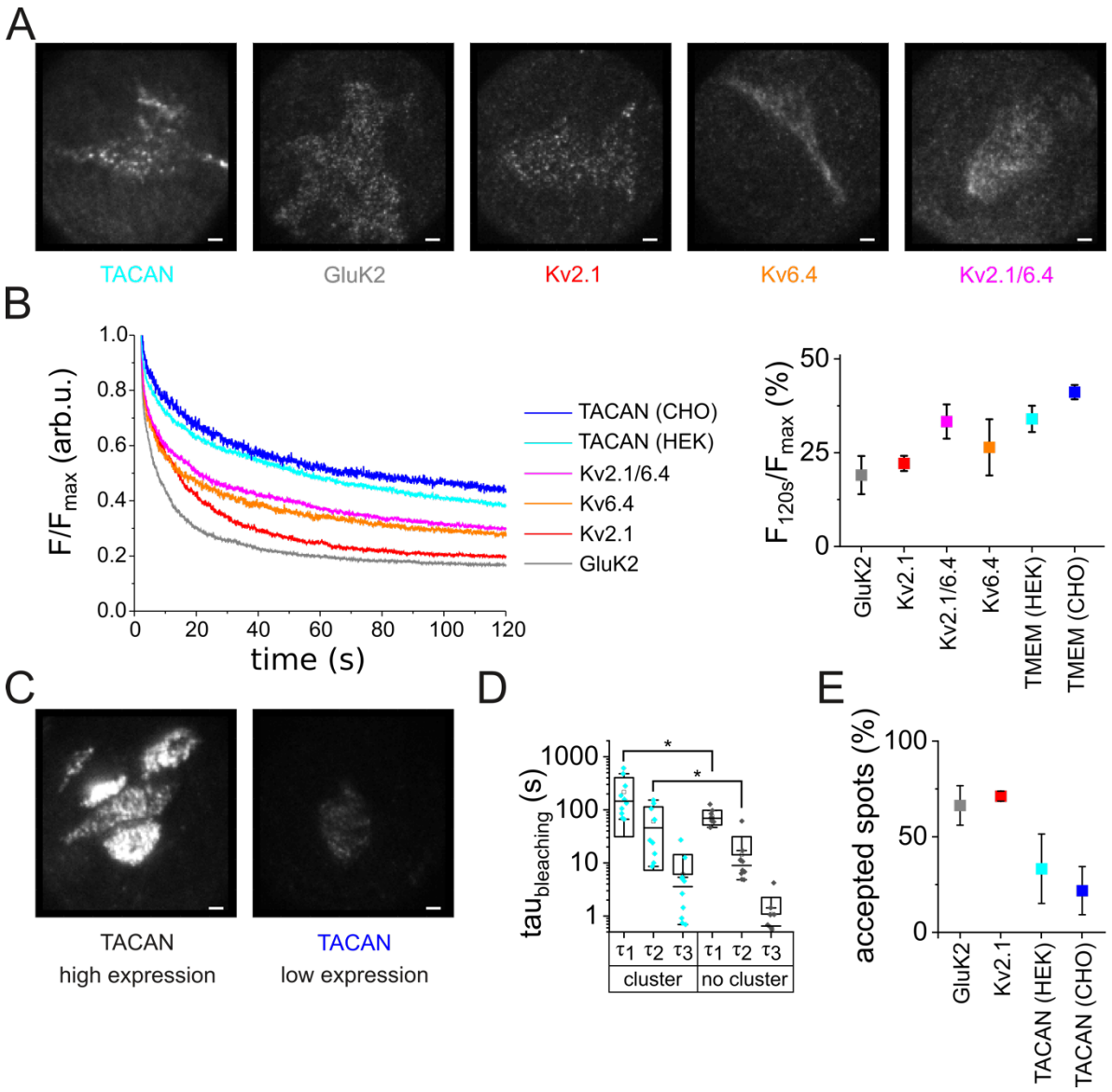

Figure 4.1 TACAN expression in cells compared to other GFP-tagged plasma membrane proteins (**A**) Representative frames of recorded movies of HEK cells expressing (from left to right) TACAN-GFP, GluK2-GFP, Kv2.1-GFP, Kv6.4-GFP, Kv2.1/Kv6.4-GFP recorded in TIRF configuration. (Scale bars 2 µm.) (**B**) Left, representative global bleaching traces of recorded movies from HEK cells expressing GluK2-GFP (grey), Kv2.1-GFP (red), Kv6.4-GFP (orange), Kv2.1/Kv6.4-GFP (magenta) and TACAN-GFP (cyan) and CHO cells expressing TACAN-GFP at lower densities (blue). Right, normalized remaining fluorescence after two minutes, n=5. (**C**) Representative frames of recorded movies of CHO cells expressing His6-TACAN-GFP at high densities (left) and lower densities (right). (Scale bars 2 µm.) (**D**) Bleaching time constants of clusters compared to areas of the cell that did not have clusters, n=10 (**E**) Fraction of accepted spots from SSC movies for membrane proteins GluK2 and Kv2.1 compared to TACAN expressed in CHO and HEK, n=5.

To further study these TACAN clusters we first wanted to rule out the possibility of artefacts originating from the transient transfection and expressed TACAN-GFP in stable CHO cells. The expression level of TACAN-GFP in the stable CHO cell line varied widely (figure 4.1c). We selected those CHO cells that expressed levels of TACAN-GFP appropriate for single molecule analysis (figure 4.1c, right). In the overall bleaching trace (figure 4.1b), the fluorescence not originating from the plasma membrane (slow bleaching time) was still dominating, and we still observed cluster formation. Comparing the bleaching time constants of the clusters to the regions of the cell devoid of clusters in both stably and transient transfected cells showed that the slow and intermediate time constants were significantly slowed (figure 4.1d). The distribution of the time constants suggested that, although a fraction of TACAN traffics to the plasma membrane, the majority is located in the intracellular space where it forms clusters. We previously found a similar behavior in Kv6.4-GFP (14) that are known to remain in the ER. We therefore propose that much of TACAN does not traffic to the membrane. We did not further investigate, however, in which intracellular membrane TACAN clusters are found. In addition to the ER, possible locations for the intracellular clusters are a pool of recycled TACAN located in endosomes or other organelle membranes. Since the clusters were observed throughout the entire cell, it is unlikely that TACAN expressed here exclusively in the nuclear envelope as has been previously reported in adipocytes (15).

4.3.2 Subunit Counting of Immobilized Purified Protein

As a result of high background fluorescence and clustering, a lot of detected fluorescent spots were rejected by the spot and bleaching step detection program (figure 4.1e), rendering the single subunit counting results unreliable. Therefore, we were unable to obtain reliable single subunit counting data from TACAN expressed in cells. Expressing the protein in *Xenopus* oocytes has been one way to circumvent the problem of background fluorescence from the ER, as the endogenous, overexpressed or injected melanin blocks fluorescence from the intracellular side (16). Here, we pursued a tethering approach as an alternative method. To this aim, we expressed TACAN in bacteria and studied the channel in purified form. Membrane bound proteins have been mostly studied in cells or lipid environments, but soluble complexes have been immobilized via biotin or

antibodies to perform subunit counting studies (Mini review (17, 18)). Rather than introducing a new tag, we decided to utilize the existing His_6-tag for tethering the His_6-TACAN-GFP onto a Ni-NTA functionalized coverslip (supplemental figure S4.1) (12).

First, we aimed at immobilizing His6-TACAN-GFP purified in FC14 onto Ni-NTA coverslips to record bleaching movies. We added protein in excess of available binding sites (11-68 nM) to facilitate binding and detect immobilized fluorescent spots on the coverslip. Observation in epifluorescence mode confirmed that the majority of the protein remains in solution and doesn't bind to the Ni-NTA functionalized coverslips. This was further confirmed by precipitating the protein onto the coverslip. Adding the protein to buffer without detergent immediately resulted in the appearance of spots at a density beyond the camera's resolution. However, even after incubating the protein for 20 minutes in the presence of FC14 detergent, we only observed an average of 69$\pm$37 spots per movie. We therefore investigated whether changing the detergent to DDM would allow to tether more complexes onto the coverslip and increase the number of detected spots. We isolated the protein in FC14 but exchanged the detergent to DDM in the final step of purification. Adding 7-30 times less DDM-solubilized protein (1.5-3 nM) compared to samples solubilized in FC14 resulted in an over 3-fold increase of immobilized channels. In average we detected 255$\pm$98 spots per movie of which 61.9 $\pm$ 6.3 % were accepted for step histograms (figure 4.2a representative movies).

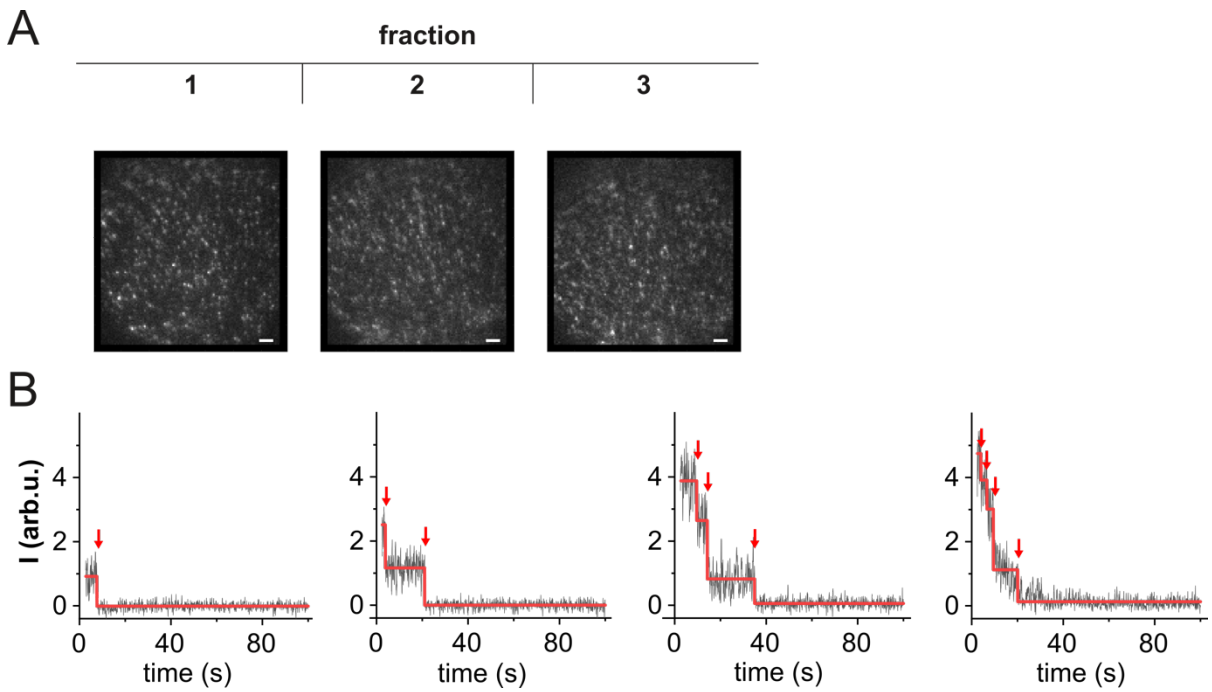

Figure 4.2 Single subunit counting on NI-NTA coverslips in DDM
(**A**) Representative frames of recorded movies of His_6-TACAN-GFP purified and tethered in DDM buffer from three different fractions as indicated on top. (Scale bar 2 µm.) (**B**) Representative intensity time traces (black) of a single spot fitted by PIF (red) with one to four bleaching steps (red arrow).

We analyzed each relevant fraction collected during the size-exclusion chromatography independently and found different oligomeric states for each fraction. Fractions that eluted closer to the column's void volume had higher numbers of subunits per spots. The first fraction was collected 1 mL after the void volume to avoid potential protein aggregates and we observed primarily one to four photobleaching steps (figure 4.2b and 4.3a, first graph). For photobleaching recordings of the second fraction, we saw a drastic shift in the step frequency histograms to lower numbers of bleaching steps compared to the previous fraction (figure 4.3a, second graph). We collected the third peak of the size exclusion chromatography and again immobilized protein complexes onto the coverslips. Similar to the previous fraction, step frequency histograms showed primarily one to three bleaching steps (figure 4.3a, third graph). As a result of incomplete maturation of the GFP chromophore and pre-bleaching prior to recording bleaching movies, not all GFP molecules are visible, resulting in a binomial distribution of bleaching step frequencies.

In order to determine the oligomeric states of TACAN in these different fractions, we first determined the probability of GFP fluorescence (p_f). The maturation of GFP depends on the protein expression conditions, while pre-bleaching depends on the experimental conditions. Given that the three fractions were purified from the same culture and handled identically following the purification, we reasonably assumed p_f to be identical for all fractions. We determined the most likely probability of fluorescence for all three fractions simultaneously (see *Methods*). Very low ($p_f < 0.25$) and higher ($p_f > 0.65$) GFP probabilities were very unlikely, while two to three maxima were found between p_f 0.3 and 0.6 (figure 4.3b). We fitted the step frequency histograms of all three fractions to binomial distributions of N^{th} order, where N corresponds to the number of subunits in the TACAN complex and kept p_f fixed to the different maxima. Lower p_f values then predicted higher oligomeric states, whereas higher p_f values predicted lower oligomeric states (table 4.1). For example, fixing p_f to 0.387 resulted in best binomial fits of fifth, fourth and third order for the three fractions, respectively, while overall lower oligomeric states were predicted when we increased p_f to 0.461, which resulted in best binomial fits of fourth, third and third order for the three fractions, respectively. Independent of the p_f value, we consistently found that the first fraction was predicted to contain channels of higher oligomeric states compared to later fractions. We propose that the channel complex of the highest oligomeric state represents the native channel and that lower oligomeric states found in later fractions are due to protein disintegration. However, we could not yet determine the most probable oligomeric state for the native channel complex, since the likelihoods for the different p_f maxima were too similar. To determine the most likely number of subunits in the first fraction, which is likely to contain the native channel, we fitted the respective step frequency histogram to various binomial distributions and let p_f free to vary between 0.3 and 1. The best fit was obtained for a binomial distribution of fourth order, suggesting that (native) TACAN channels in the first fraction are composed of four subunits (not shown). Knowing the oligomeric state of the first fraction, we were then able to identify the "best" p_f value for all three fractions. To this end, we checked which p_f maxima that we found earlier (figure 4.3b) predicts a tetrameric assembly for the first fraction and determined the "best" p_f to be 0.461. Fixing p_f to this value allowed us to identify the oligomeric states of channels contained in the second and third fraction. Assuming

that each fraction only composes one population of TACAN channels that don't mix, we found that the second and third fraction both contain trimeric TACAN complexes (figure 4.3c).

Table 4.1. Oligomeric states obtained by different p_f values

	Fraction		
pf	1	2	3
0.323	hexamer	pentamer	tetramer
0.387	pentamer	tetramer	trimer
0.461	tetramer	trimer	trimer
0.538	trimer	trimer	dimer

Oligomeric states were determined by finding the best fitting binomial distribution of N^{th} order for each fraction keeping p_f fixed to the different maxima shown in figure 4.2d. N corresponds to the number of subunits.

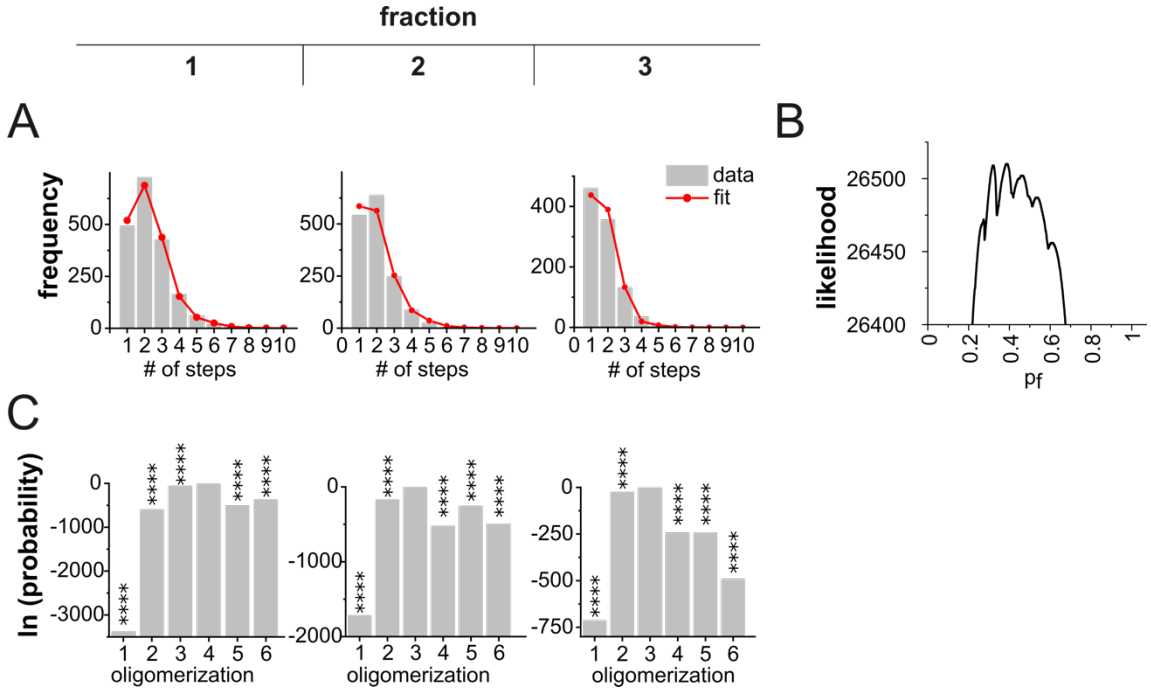

Figure 4.3 Single subunit counting analysis

(**A**) PIF automated analysis result showing step frequency distributions (grey bars) for the three independent fractions as indicated on top. For fits, the probability of fluorescence p_f was fixed to 0.461 and distributions were best fitted with binomial distributions of fourth (left) and third (center and right) order (red). (**B**) Likelihood for different p_f values determined for all three fractions simultaneously. (**C**) Log likelihoods for the step frequency distributions in (A) for monomeric to hexameric oligomeric states with p_f limited 0.461. Significance was determined with respect to the tetramer for the first fraction (left) and to trimer for the second and third fraction (center and right). ****P > 0.9999.

Since our results suggested that the protein is not stable in isolated form, it was likely that we find mixtures of different oligomeric forms in the fractions. To test this, we fitted binomial distributions that would account for populations with heterogenous oligomeric state (table 4.2). For the first fraction, we found that the distribution was best fitted with a pure tetrameric distribution with no fraction of dimers or trimers. In contrast, the fit of the step frequency distribution of the second fraction was improved when a mixed population of 49.5% trimers and 50.5% tetramers was allowed. Following this trend of degradation of the tetrameric TACAN complex, the fit of the third fraction was improved by accounting for a mixed population of 66.5% trimers and 33.5% dimers. Other mixed population fit less well (table 4.2). In summary, our data show that the highest oligomeric state of purified TACAN channels is tetrameric. We suggest that this represents the native channel as found in the plasma membrane. Our results also illustrate that DDM-solubilized TACAN is unstable and disintegrates into trimers and dimers.

Table 4.2. Distribution of mixed populations in DDM

	Stoichiometry						
	monomer	dimer	trimer	tetramer	p_c	p_f	Significance
				1	0.151	0.461	
Fraction 1		0		1	0.151	0.461	1
			0	1	0.151	0.461	1
			1		0.272	0.461	
Fraction 2			**0.495**	**0.505**	**0.077**	**0.461**	**0.0212**
		0.18		0.82	0.015	0.461	1
			1		0.089	0.461	
		0.335	**0.665**		**0.206**	**0.461**	**0.0084**
Fraction 3		0.492		0.508	0.037	0.461	0.0471
	0.08	0.165	0.755		0.182	0.461	0.0167
		0.409	0.279	0.313	0.092	0.461	0.1184

Significance was determined for fits with fixed p_f with respect to the best pure oligomeric state (grey). Bold numbers highlight the fit with the highest probability.

4.4 Discussion

Overall, our initial experiments in cells demonstrate that TACAN is primarily localized in intracellular compartments and only a fraction is trafficked to the plasma membrane. Previous biotinylation assays of stably transfected CHO cells also confirm this (11) and another study reported TACAN (also known as TMEM120A) in the nuclear envelope membrane of adipocytes (15). Our recordings resulted in a diffuse fluorescence signal and cluster formation throughout the cell. The diffuse background fluorescence is often observed when the membrane protein does not traffic to the plasma membrane but remains in the ER (as for Kv6.4). Since the outer membrane of the nuclear envelope is continuous with the ER membrane, TACAN might well be located in both membranes, resulting in diffuse background fluorescence. Without further experiments, it remains unknown whether TACAN localizes in one specific intracellular compartment. We analyzed the protein sequence for subcellular localization signals using the LocSigDB database (19). The search found, among other, less well defined, signals (supplementary table 4.1), a dilysine C-terminal ER-retention signal. A similar C-terminal dilysine KKXX motif has been shown to be involved in ER targeting (20), which also depends on the correct length between the last transmembrane helix and the C-terminus (21). Proteins with short 13aa C-termini traffic to the plasma membrane despite the presence of a retention motif, but proteins with 18aa and longer C-termini that carry this motif remain in the ER. According to the previously published sequence prediction of TACAN, the channel has a 14 amino acid long C-terminus (11), which might result in a mixed localization of protein complexes in the plasma membrane and complexes that remain in the ER. Additionally to the diffuse background fluorescence, we observed intracellular cluster formation. The identity of the organelles containing these TACAN clusters remains unknown, but it is possible that the mechanosensitive action of TACAN serves distinct purposes in the plasma membrane and in the intracellular space.

Our subunit counting results suggest that SEC-purified TACAN solubilized in DDM is not homogenous and exists in various oligomeric states. Although we found the highest oligomeric state to be tetrameric, mixed populations of tetramers, trimers and dimers were more likely for later fractions. A plausible explanation for our results, is the possibility that the functional channel

complex is instable and falls apart as a result of the detergent extraction. This is crucial, especially for future attempts at solving the protein structure since heterogenous protein samples are difficult to crystalize and complicate the interpretation of electron microscopy images. We showed that the first fraction of the SEC purification features the largest channel complex with four subunits and no trimers or dimers. We suggest that this oligomeric state represents the native channel. Subsequent fractions might then contain non-native channel arrangements of lower oligomeric states. The observation of trimers suggests that the interactions at all four subunit interfaces are comparable. This raises the question if TACAN channels assemble by successively adding monomers to the complex. This would be untypical, since other tetrameric protein assemblies that form in the ER, and more specifically, voltage-gated potassium channels have been reported to assemble as dimers of dimers (22, 23).

While we assume that the heterogeneity in the oligomeric states is caused by unstable proteins in detergent micelles, an alternative explanation for these different oligomeric states could be a physiologically relevant heterogeneity. A heterogeneity in TACAN localization was observed in cells and might be accompanied by distinct oligomeric arrangements. It is, for instance, unclear, whether the tetramer is required to form the ion conduction pathway as it is the case for most hexahelical cation channels, or whether the monomer is the pore-forming unit, and entire channels co-assemble to one complex. Such an oligomerization independent of function is for instance seen for voltage-gated proton channels (Hv (24-26)). The channels might thus assemble dependent on function or localization.

In summary, we show that TACAN expresses not only in the plasma membrane where it has been previously shown to be mechanosensitive but also in the intracellular of the cell where it might serve a different purpose. Furthermore, we suggest that native TACAN channels comprise four subunits that might not be assembled as dimers of dimers.

4.5 Methods

4.5.1 Cleaning of Coverslips

To minimize background fluorescence on the single molecule level, coverslips underwent a thorough cleaning procedure. No. 1 glass coverslips were cleaned in a staining jar by sonication (at 37 kHz and T = 60°C) in Alconox 1% in MilliQ H_2O and 2 times in anhydrous ethanol. Coverslips were rinsed with MilliQ H_2O (deionized to >18 MOhm·cm) after each sonication step. These "ultra-clean" coverslips were stored in deionized, 0.2 µm-filtered H_2O and dried under a steady stream of filtered nitrogen directly before use. For cell culture, the ultra-clean coverslips were glued using Sylgard 184 (Dow Corning) to the bottom of 35 mm culture dishes and sterilized by UV radiation overnight.

4.5.2 Cell Culture

HEK 293T cells were cultured in DMEM supplemented with 10% FBS and 1% penicillin/streptomycin in a 5% CO_2-atmosphere. Cells were plated on ultra-clean N°1 glass coverslip petridishes coated with poly-D-lysine and transiently transfected with 50-150 ng superfolder monomeric (sfm) GFP-TACAN (referred to as TACAN-GFP) in pRK5 missing the SV40 origin of replication using calcium phosphate and varying amount of cDNA. Removing the SV40 origin of replication is important to better control the expression levels, since this feature would otherwise allow the replication of plasmid DNA in the cytoplasm in HEK 293T cells. All following steps were performed in the dark or under red light. 6His-GFP-TACAN was expressed at 37°C for 8-18 hours. For comparison sfmGFP tagged Kv2.1, 6.4 and GluK2 were transfected under the same conditions.

4.5.3 Stable CHO Cell Line Expressing TACAN-GFP

CHO K1 cells were transfected with 2 µg of sfmGFP-TACAN (referred to as TACAN-GFP)in a pcDNA3.1 vector using lipofectamine. Expressing clones were selected with 600 µg/mL neomycine applied for 14 days. Stably transfected cells were plated onto ultra-clean N°1 glass coverslip petridishes and kept in the dark until fixation (1-6 days). HEK and CHO cells were fixed

in 4% EM-grade formaldehyde in PBS for 24 hours and washed three times with PBS before imaging.

4.5.4 Protein Purification

The protein has been expressed and purified as published previously (11) with minor modifications. 6His-sfmGFP-TACAN-pET27a (we refer to the protein as TACAN-GFP) was transformed into *E. coli* DE3-pLys (Rosetta) competent cells. 100mL of pre-culture was grown overnight in LB medium supplemented with 15 µg/mL kanamycin and 34 µg/ml chloramphenicol at 37°C. 1L of culture was inoculated with 10 mL of pre-culture. Once OD_{600} 0.8 was reached, IPTG (final concentration of 0.5 mM) and glycerol 50 mL/L culture (~5%) were added to induce 6His-GFP-TACAN expression. From this point on, the protein was protected from light exposure and expressed at 20°C over night. Cells were collected and resuspended at a concentration of 1 g/14 mL with resuspension buffer (0.5 M NaCl, 50 mM HEPES, 10% glycerol, pH adjusted to 7.50 with KOH) containing 2 pellets of protease inhibitor (mini complete EDTA-free, Sigma) and 4-(2-Aminoethyl)benzenesulfonyl fluoride hydrochloride (0.25 mM, Sigma). The suspension was kept on ice at all times. Cells were lyzed by passing through a cell disrupter (Emulsiflex C5, Avestin) 3 times at 10,000 psi. Unbroken cells and debris were subsequently removed by centrifugation (18 000g, 15 min). The supernatant was ultracentrifuged at 100,000 g for 2h at 4°C and the pellet (membranes) was collected. Membranes were resuspended in 2 mL/g of pellet in buffer (0.5 M NaCl, 50 mM HEPES, 10% glycerol, pH adjusted to 7.5 with KOH) and mechanically homogenized. Fos-choline-14 (FC14, 2%, Avanti) was added and agitated for 2h at 4°C. Non-soluble debris was removed by centrifugation at 100,000 g for 30 min. Proteins were bound to Co-resin (Talon superflow) equilibrated in buffer (0.5 M NaCl, 20 mM HEPES, 10% glycerol,10 mM imidazole, 0.02% Fos-choline-14, pH adjusted to 7.5 with KOH) and washed with 25 mM imidazole in a FPLC (Äkta purifier, GE Lifesciences). The protein was eluted at 400 mM imidazole and the appropriate fractions pooled and concentrated. TACAN was further purified by size-exclusion on a Superdex 200 10/300GL column (GE Healthcare Life Sciences) in SEC buffer (0.5 M NaCl, 20 mM HEPES, 5 % glycerol, 0.02% *n*-Dodecyl β-D-maltoside (DDM), pH adjusted to 7.5 with KOH).

4.5.5 Coverslips Functionalized with Ni-NTA

N°1 glass coverslips were cleaned as described above. Coverslips and staining jar were dried under a steady stream of filtered nitrogen and subjected to a 24-hour treatment of aqua regia (nitric acid and hydrochloric acid at a molar ratio of 1:3). Coverslips were functionalized following published protocols (12). Coverslips were treated for 24h each with piranha solution and 1% (3-Glycidyloxypropyl)trimethoxysilane in toluene. Between the steps, they were washed with deionized, filtered H_2O and dried under a steady stream of nitrogen. Access toluene and GPTMS were washed away with toluene and 4 rounds of anhydrous ethanol and dried under nitrogen. The coverslips were then glued onto 35mm bottomless petri dishes with Sygard 184 (Dow Corning). 10mM AB-NTA was added to the surface and incubated for 3 hours. Next, a 1-hour treatment of $NaBH_4$ to reduce remaining epoxy-groups was followed by 4 rounds of washing with MilliQ H_2O and a final 1-hour incubation with 10mM $NiCl_2$. The coverslips were rinsed in SEC buffer before adding protein. 6His-GFP-TACAN was added, incubated for 5 minutes and washed with SEC buffer to remove unbound protein and reduce background fluorescence.

4.5.6 Single Subunit Counting

Fluorescence bleaching was recorded using an Axiovert-200 microscope (Zeiss). All samples were excited at an intensity of 3.7 mW/mm^2 in TIRF configuration using a 488-nm laser (PhoXx, Omicron). For TIRF imaging, the laser light is reflected at an angle sufficient for total reflection of the light and only evanescent excitation in the region within ~300 nm above the coverslip, thus limiting background fluorescence emerging from internal cell compartments or the solution. Emission was collected with a 60X NA-1.49 objective (Olympus) and filtered by a bandpass emission filter (ET525/50 nm) in combination with a laser line reflecting dichroic mirror (Z405/488/561/635, Chroma). Images were recorded with a backlit 128x128 pixel EMCCD camera (iXon+ 860BV, Andor) at a sampling rate of 20 Hz.

4.5.7 Analysis of Bleaching Movies

To avoid user bias, spot and step detection was carried out using the automated algorithm *PIF* (13). The following parameters were used for spot and step detection: The selection of a spot was limited to one neighbor (3 × 3 pixels), and the minimum signal/noise ratio (dF/F) was set to 12%. The minimum fluorescence intensity amplitude was set to 0. Minimal and maximal step amplitude were left at 0 and 1×10^6, respectively. The total fluorophore photobleach length was set to 100%. All parameters were kept at their default setting.

The obtained step distribution histograms were converted into oligomeric states using maximum relative weighted likelihoods as published previously (14). To determine the probability of fluorescence (p_f) for purified TACAN-GFP, we fitted the step frequency distributions of the three fractions simultaneously with p_f values ranging from 0 to 1. The p_f for all three fractions had to be identical, while parameters for the oligomeric state and colocalization of spots were independent. The error was calculated as the sum of all errors, i.e. the log likelihood for all points of all distributions instead of just for one distribution.

4.6 Acknowledgments

We would like to thank Mireille Marsolais for technical support in mutagenesis. This work was funded by the Canadian Institutes of Health Research (PJT169160 to R.B.) and the Natural Science and Engineering Research Council of Canada (RGPIN-2017-06871 to R.B.).

4.7 Supplemental Material

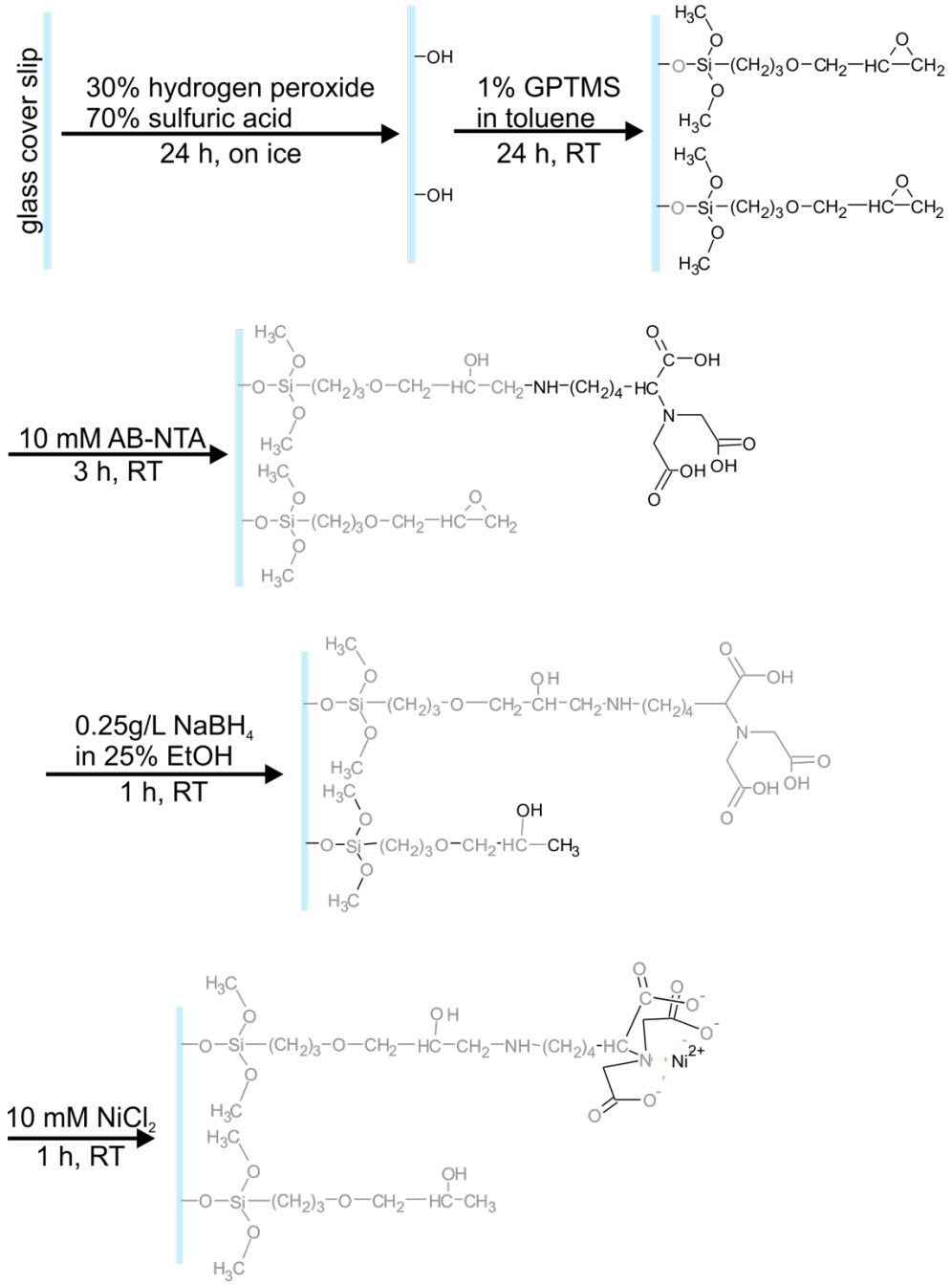

Figure S4.1 Schematic representation of Ni-NTA functionalized coverslip preparation
The different steps of the chemical reaction are depicted in black. First the coverslip is treated with piranha solution to introduce silanol sites on the surface. Next GPTMS is added to link epoxy-terminated substrates to the glass surface. The epoxy group then cross-links with the amine group of aminobutyl-NTA. Epoxy sites that did not react with AB-NTA are then reduced by sodium borohydrate. In the final step, divalent nickel ions are chelated by the NTA. Protocol from Cheng et al., 2011 (12).

Supplemental table S4.1 Search Results for Subcellular Localization Signals

signal	amino acid position	Subcellular localization
Yxx[VILFWCM]	107-111, 132-136, 138-142, 171-175, 215-219, 228-232	Lysosome
KxxxQ	54-59, 217-222, 331-336	Lysosome
DxE	14-17, 95-98	Endoplasmic reticulum
SKK	339-342	Endoplasmic reticulum
[HK]xK	66-69, 134-137, 329-332	Endoplasmic reticulum
LxxKN	100-105	Golgi

Six different localization signals were found using the LocSigDB database (19). x - occurrence of any amino acid, [] - various amino acids at this position are possible.

4.8 References

1. L. Buck, R. Axel, A novel multigene family may encode odorant receptors: a molecular basis for odor recognition. *Cell* **65**, 175-187 (1991).
2. P. A. Hargrave *et al.*, The structure of bovine rhodopsin. *Biophys Struct Mech* **9**, 235-244 (1983).
3. M. A. Hoon *et al.*, Putative mammalian taste receptors: a class of taste-specific GPCRs with distinct topographic selectivity. *Cell* **96**, 541-551 (1999).
4. U. Gether, B. K. Kobilka, G protein-coupled receptors. II. Mechanism of agonist activation. *J Biol Chem* **273**, 17979-17982 (1998).
5. E. N. Pugh, Jr., Variability in single photon responses: a cut in the Gordian knot of rod phototransduction? *Neuron* **23**, 205-208 (1999).
6. M. Chalfie, Neurosensory mechanotransduction. *Nat Rev Mol Cell Biol* **10**, 44-52 (2009).
7. D. P. Corey, A. J. Hudspeth, Response latency of vertebrate hair cells. *Biophys J* **26**, 499-506 (1979).
8. L. Beaulieu-Laroche *et al.*, TACAN Is an Ion Channel Involved in Sensing Mechanical Pain. *Cell* **180**, 956-967 e917 (2020).
9. S. K. Das, M. Darshi, S. Cheley, M. I. Wallace, H. Bayley, Membrane protein stoichiometry determined from the step-wise photobleaching of dye-labelled subunits. *Chembiochem* **8**, 994-999 (2007).
10. M. H. Ulbrich, E. Y. Isacoff, Subunit counting in membrane-bound proteins. *Nat Methods* **4**, 319-321 (2007).
11. L. Beaulieu-Laroche *et al.*, TACAN Is an Ion Channel Involved in Sensing Mechanical Pain. *Cell* **180**, 956-967.e917 (2020).
12. W. Cheng *et al.*, Ultrasensitive scanometric strategy for detection of matrix metalloproteinases using a histidine tagged peptide-Au nanoparticle probe. *Chem Commun (Camb)* **47**, 2877-2879 (2011).
13. H. McGuire, M. R. Aurousseau, D. Bowie, R. Blunck, Automating single subunit counting of membrane proteins in mammalian cells. *J Biol Chem* **287**, 35912-35921 (2012).
14. L. Moller, G. Regnier, A. J. Labro, R. Blunck, D. J. Snyders, Determining the correct stoichiometry of Kv2.1/Kv6.4 heterotetramers, functional in multiple stoichiometrical configurations. *Proc Natl Acad Sci U S A* 10.1073/pnas.1916166117 (2020).
15. D. G. Batrakou, J. I. de Las Heras, R. Czapiewski, R. Mouras, E. C. Schirmer, TMEM120A and B: Nuclear Envelope Transmembrane Proteins Important for Adipocyte Differentiation. *PLoS One* **10**, e0127712 (2015).

16. E. E. L. Lee, F. Bezanilla, Methodological improvements for fluorescence recordings in Xenopus laevis oocytes. *J Gen Physiol* **151**, 264-272 (2019).

17. R. J. Arant, M. H. Ulbrich, Deciphering the subunit composition of multimeric proteins by counting photobleaching steps. *Chemphyschem* **15**, 600-605 (2014).

18. N. Groulx, H. McGuire, R. Laprade, J. L. Schwartz, R. Blunck, Single molecule fluorescence study of the Bacillus thuringiensis toxin Cry1Aa reveals tetramerization. *J Biol Chem* **286**, 42274-42282 (2011).

19. B. R. King, C. Guda, ngLOC: an n-gram-based Bayesian method for estimating the subcellular proteomes of eukaryotes. *Genome Biol* **8**, R68 (2007).

20. J. Shin, R. L. Dunbrack, Jr., S. Lee, J. L. Strominger, Signals for retention of transmembrane proteins in the endoplasmic reticulum studied with CD4 truncation mutants. *Proc Natl Acad Sci U S A* **88**, 1918-1922 (1991).

21. M. J. Vincent, A. S. Martin, R. W. Compans, Function of the KKXX motif in endoplasmic reticulum retrieval of a transmembrane protein depends on the length and structure of the cytoplasmic domain. *J Biol Chem* **273**, 950-956 (1998).

22. L. Tu, C. Deutsch, Evidence for dimerization of dimers in K+ channel assembly. *Biophys J* **76**, 2004-2017 (1999).

23. E. T. Powers, D. L. Powers, A perspective on mechanisms of protein tetramer formation. *Biophys J* **85**, 3587-3599 (2003).

24. H. P. Koch *et al.*, Multimeric nature of voltage-gated proton channels. *Proc Natl Acad Sci U S A* **105**, 9111-9116 (2008).

25. S. Y. Lee, J. A. Letts, R. Mackinnon, Dimeric subunit stoichiometry of the human voltage-dependent proton channel Hv1. *Proc Natl Acad Sci U S A* **105**, 7692-7695 (2008).

26. F. Tombola, M. H. Ulbrich, E. Y. Isacoff, The voltage-gated proton channel Hv1 has two pores, each controlled by one voltage sensor. *Neuron* **58**, 546-556 (2008).

Chapter 5

Stable DPP6 Propeller Formation Required for Modulating Kv4.2 Gating Kinetics

Lena Moeller[1], Rikard Blunck[2,1]

1 Department of Biochemistry, Université de Montréal, Montréal, Canada

2 Department of Physics, Université de Montréal, Montréal, Canada

Unpublished

Author Contributions

I performed the experiments, analyzed the data and wrote the manuscript.

Rikard Blunck designed the research, helped with the data analysis and edited the manuscript.

5.1 Abstract

Rapidly inactivating voltage-gated potassium currents in the brain and heart are governed by ternary channel complexes of pore-forming Kv4 α-subunits, cytosolic K(+) channel interacting proteins (KChIPs) and transmembrane dipeptidyl aminopeptidase-like proteins (DPPLs). Coexpression of DPPLs increases current amplitude and accelerates channel inactivation and recovery from inactivation. The underlying mechanism of altered channel gating is not well understood. DPPLs feature an approximately 700 amino acid long C-terminal extracellular domain, which comprises a proximal inactive α/β-hydrolase domain and a distal eight-bladed β-propeller. The extracellular domain is responsible for increased surface expression of the channel complex, but it remains unclear which parts of the extracellular domain are responsible for altering Kv4's gating properties. Here, we investigate how different C-terminally truncated DPP6 variants affect macroscopic Kv4.2 channel behavior. Electrophysiological interrogation demonstrates a strong link between the length of DPP6's extracellular domain, peak current and accelerated activation and inactivation kinetics. More specifically, our results show that the second half of the propeller domain of DPP6 is responsible for drastically accelerated inactivation in the presence and absence of KChIP revealing the importance of a stable β-propeller domain and possibly DPP6 dimer formation. We hypothesize that the formation of a multimeric DPP6 extracellular domain leads to a positioning of DPP6's extracellular domain directly on top of the ion channel whereas truncated DPP6 variants fail to multimerize and therefore establish a more flexible conformation that does not destabilize the open channel state as efficiently. The proximal α/β-hydrolase domain does not directly modify the biophysical channel properties but might aid proper positioning of the extracellular domain on top of the channel.

5.2 Introduction

The voltage-gated potassium channel family member Kv4 is expressed in the brain and heart, where it is responsible for the rapidly activating and inactivating somatodendric subthreshold A-type current (I_{SA}) and the cardiac transient outward current (I_{to}), respectively (1-5). Heterologous expression of Kv4, however, does not result in currents matching the properties of the native currents. In the brain and heart, the biophysical properties of the channel are modulated to the tissue specific requirements by auxiliary subunits. Here, Kv4 channels form complexes with the cytosolic Kv channel interacting proteins (KChIP) and transmembrane dipeptidyl aminopeptidase-like proteins (DPP6 and DPP10) (6-9).

Due to its importance in the central nervous system and heart, alterations of functional DPP6 levels have been linked to neurological and cardiac disorders. Mice knockout models demonstrate that DPP6-loss leads to impaired learning and memory formation (10). In line with this, mutations leading to decreased DPP6 expression in humans have been linked to microcephaly and mental retardation (11) as well as neurodegenerative dementia like Alzheimer's disease (12). Autism spectrum disorder (13, 14), sporadic amyotrophic lateral sclerosis (15, 16), Gilles de la Tourette syndrome (17) and antipsychotics-induced involuntary body movements (tardive dyskinesia) in Schizophrenics (18) have also been associated with alterations in the DPP6 gene. In the heart, a gain of function variant and increased DPP6 mRNA levels in the myocardium are the likely underlying mechanism for idiopathic ventricular fibrillation which is an important factor in sudden cardiac death (19, 20).

The dipeptidyl aminopeptidase-like proteins (DPPLs) are related to the CD26/DPPIV enzyme, but a substitution in the catalytic site of serine to aspartate in DPP6 and to glycine in DPP10 and altered conformation revealed by crystallography renders it enzymatically inactive (21-23). The enzymatically inactive α/β-hydrolase domain together with an eight-bladed β-propeller domain form the approximately 700 amino acid long extracellular part of the protein, which follows the short cytoplasmic N-terminal domain and single transmembrane helix. It was found that DPPL traffics to the plasma membrane in the absence of Kv4 α-subunits (24-26) and when coexpressed with the pore forming subunits, DPPL redistributes Kv4.2 to the plasma membrane (27, 28),

increase single channel conductance (29) and accelerate channel activation, inactivation and recovery from inactivation (7, 30). KChIP1-3 also increase Kv4 trafficking and stabilization in the membrane (28) but slow the early phase of inactivation (6, 31). The effects on Kv4 gating are further fine-tuned by different isoforms of the auxiliary subunits (32-35).

The channel gating of Kv4 has been studied in detail (36, 37). The structure-function relationship for open state inactivation (OSI) in Kv4 is well understood and is very similar to N-type inactivation (NTI) in Shaker channels, where the binding of the cytosolic N-terminus of Kv4 in the ion-conducting pore blocks the channel in its open state (38-40). However, in native Kv4 channel complexes, NTI is inhibited by KChIP, which sequesters the N-terminal inactivation domain of Kv4 (31, 38, 41, 42). The inhibition of NTI by KChIP manifests itself in macroscopic currents as slowed initial inactivation. Rather than inactivating via NTI, Kv4 channels preferentially undergo closed state inactivation (CSI) (37, 43). The involvement of the S4S5 linker and C-terminal part of the S6 helix in CSI has been revealed (36, 44, 45). Additionally, the structural determinants of gating modulation by auxiliary subunits have been studied. While KChIP interacts mainly with the cytoplasmic N-terminus of the channel, DPPL interacts with the channel in the membrane. Here, DPPL's transmembrane helix and Kv4's voltage sensing domain (VSD) are involved in protein-protein interaction (26, 27, 46, 47). This interaction between the transmembrane helices of DPPL and the VSD influences channel gating, but other parts of the about 100 kDa auxiliary subunit are also involved in the modulation of channel behavior. N-terminal splice variants DPP6a and DPP10a are suggested to confer NTI by blocking the ion-conducting pore when NTI is inhibited by KChIP or truncation of Kv4's N-terminus. But the shorter N-terminal splice variant DPP6-S does not cause NTI (48). The large extracellular domain comprising the α/β-hydrolase and β-propeller was found to be vital for increased channel expression and interaction with the extracellular matrix (47, 49). Its effect on channel gating, however, remains elusive.

Here, we investigated how different C-terminal domains of DPP6 affect macroscopic channel behavior. Electrophysiological interrogation of different C-terminally truncated DPP6 constructs revealed the importance of a stable β-propeller domain.

5.3 Results

5.3.1 DPP6 Extracellular Domain Alters Gating Properties

Previous studies have shown that Kv4.2 alone does not account for the native somatodendric subthreshold rapidly activating and inactivating, referred to as A-type, current characteristics found in neurons of the central nervous system, but that coexpression of DPP6 is necessary (7, 54). The general role of DPP-like proteins in the brain is to accelerate channel inactivation and enhance preferential closed state inactivation (30). Until now, it is unknown which parts of the auxiliary subunit are responsible for these altered gating properties. Here, we investigate the functional role of the extracellular domain of DPP6.

We deleted the extracellular domain (DPP6-T132X) and coexpressed the truncated construct with Kv4.2 in *Xenopus* oocytes. The obtained current traces displayed distinct properties (figure 5.1). In agreement with previous results (29, 33), full-length DPP6-WT significantly increased average peak current (I_{max}) about seven-fold from 3.2 ± 2.1 µA to 21.6 ± 12.3 µA (figure 5.1a). The truncated DPP6-T132X, in contrast, increased peak current only three-fold to 9.83 ± 6.34 µA. Furthermore, DPP6-WT resulted in a significantly more complete inactivation with 12.9 ± 3.7 % of peak current remaining in the steady state compared to 16.4 ± 6.4% for Kv4.2 in the absence of DPP6 (figure 5.1b). The more complete current inactivation of DPP6-WT is a result of a destabilized open state. The truncated DPP6-T132X inactivated to 16.7 ± 3.6 % of the maximum current, which was undistinguishable from Kv4.2 currents in the absence of DPP6. While the effect might not seem physiologically relevant, it shows that the effect of DPP6-WT on Kv4.2 inactivation is removed by truncation of the C-terminus beyond T132.

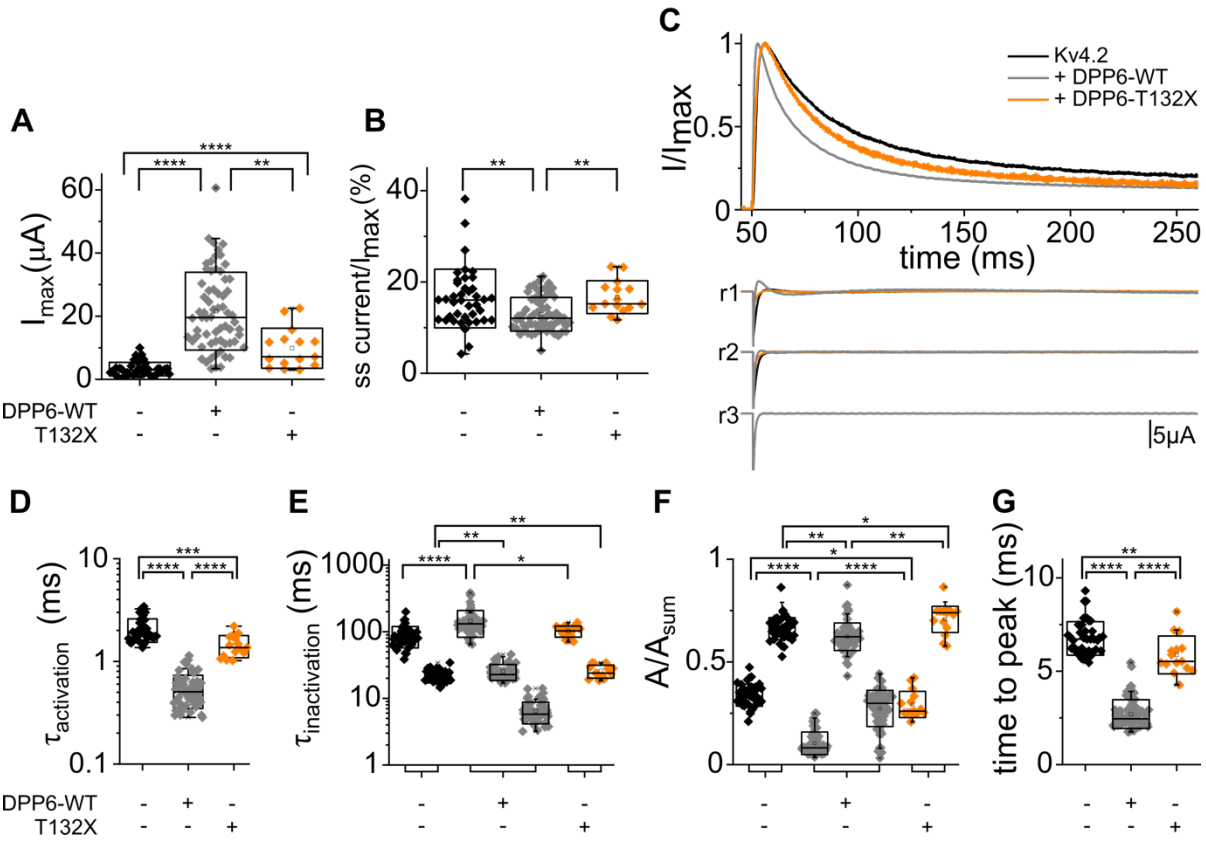

Figure 5.1 Electrophysiological properties of Kv4.2/DPP6-T132X compared to Kv4.2 alone and Kv4.2/DPP6-WT.

A) Peak currents obtained at test pulse of +100 mV. **B**) Steady state current at the end of +100 mV test pulse normalized to peak current. **C**) Representative current traces and residual currents of 100 mV test pulse fitted to exponential of first, second or thirds order as indicated (r1-r3, respectively). **D**) Time constants of activation at + 100 mV test pulse. **E**) Time constants of inactivation at +100 mV test pulse. **F**) Relative amplitudes of inactivation time constants at +100 mV test pulse in the same order as in D (left slow, right fast). **G**) Time to peak at +100 mV test pulse. Kv4.2 n=40, Kv4.2/DPP6-T132X n=15, Kv4.2/DPP6-WT n=65. * P < 0.05, ** P < 0.005, *** P < 0.0005, **** P < 0.00005, additional significances can be found in the supplementary table S5.1.

Not only peak and steady state current levels, but also DPP6's effect on activation and inactivation kinetics largely depends on the extracellular domain (figure 5.1c-e). We fitted the activation time course with a single exponential (figure 5.1d). DPP6-WT significantly accelerated Kv4.2 activation (7, 55). While truncation of the extracellular domain at T132X also resulted in accelerated activation kinetics compared to Kv4.2, the effect was less pronounced compared to the full length DPP6. These results suggest that the extracellular domain is responsible for drastically accelerating activation kinetics. We also observed altered inactivation kinetics and

fitted the inactivation time course with a sum of exponential decays (figure 5.1c,e). These complex inactivation kinetics reflect a mixture of different populations within the ensemble of channels. Two exponentials were necessary to accurately describe the inactivation of Kv4.2 (τ_1 = 88.5 $\pm$ 31.2 ms, τ_2 = 21.4 $\pm$ 4.3 ms) and Kv4.2/DPP6-T132X (τ_1 = 102.3 $\pm$ 19.6 ms, τ_2 = 25.8 $\pm$ 5.7 ms), reflecting at least two distinct channel populations in the open state. In the presence of DPP6-WT, a third exponential component became necessary to account for the fast, initial current decay of Kv4.2/DPP6-WT (τ_1 = 145.4 $\pm$ 62.8 ms, τ_2 = 25.4 $\pm$ 6.8 ms, τ_3 = 6.5 $\pm$ 2.3 ms), reflecting the presence of an additional channel population in the open state. Coexpression with the truncated DPP6 (T132X) disposed of the fast time constant observed in the presence of the full-length DPP6, illustrating that the drastic acceleration of inactivation by the presence of an additional open channel state depends on the extracellular domain. Although the inactivation kinetics of DPP6-T132X were more comparable to Kv4.2 in the absence of DPP6 than in the presence of full-length DPP6, the overall current decay remained faster than Kv4.2 alone. Compared to Kv4, it was not the time constants themselves that altered in the presence of DPP6-T132X but the relative amplitudes between the two decay times (figure 5.1f). Such a shift in relative amplitudes is observed when the two distinct open channel populations redistribute due to the stabilization or destabilization of one open state compared to the other. The relative amplitudes of the time constants (A/A_{sum}) significantly shifted towards the faster time constants with 0.71 $\pm$ 0.06 for DPP6-T132X compared to Kv4.2 alone (0.66 $\pm$ 0.05), illustrating that destabilization of the open state leads to a redistribution between the different populations within the ensemble of channel states.

The differences in inactivation were also reflected in the time it took to reach peak amplitude (figure 5.1g). As expected for a superposition of an exponential increase for activation and exponential decay for inactivation, faster inactivation overcame the accelerated activation at an earlier time, leading to earlier peak amplitude. Full-length DPP6 reached peak current almost three times as quickly as Kv4 alone in 2.7 $\pm$ 0.8 ms as opposed to 6.8 $\pm$ 0.9 ms. DPP6-T132X reached the peak current in 5.9 $\pm$ 1.0 ms, which was slightly faster than Kv4 alone, but significantly slower than DPP6-WT. Overall the truncation of the extracellular domain of DPP6 led

to lower peak currents, slowed channel activation, the loss of fast inactivation and resulted in gating properties much more like Kv4.2 alone than full-length DPP6.

5.3.2 The Extracellular Domain of DPP6 is Located in Proximity to the S4 Helix

To better understand how the extracellular domain of DPP6 is arranged in respect to the Kv4 α-subunit and to investigate whether truncations affect the interaction, we used voltage clamp fluorometry (VCF). The VCF technique is a powerful tool to simultaneously investigate the structure and function of ion channel complexes. This technique is based on site-directed fluorescent labeling of the complex. Voltage-dependent structural rearrangements can lead to an altered chemical environment of the fluorophore, resulting in a change in brightness (quenching or unquenching). Since this modulation of the fluorescent properties is based on the local environment (2-3 Å), this method is ideal to investigate the proximity of Kv4 to DPP6. We labeled the extracellular part of the voltage-sensing S4 helix with the cysteine-reactive tetramethylrhodamine-maleimide (TMRM) fluorophore (figure 5.2a) at position A288C and measured voltage-dependent fluorescence changes. In other Kv channels, the voltage-induced outward movement of the labeled S4 helix results in a change of the fluorescence signal (52, 56-58), but the same movement did not result in a fluorescence change when labeling homologous position in Kv4.2. Coexpression of full-length DPP6, on the other hand, led to voltage-induced quenching of the fluorophore (figure 5.2b), illustrating a close proximity of DPP6 and the S4 helix of Kv4.2.

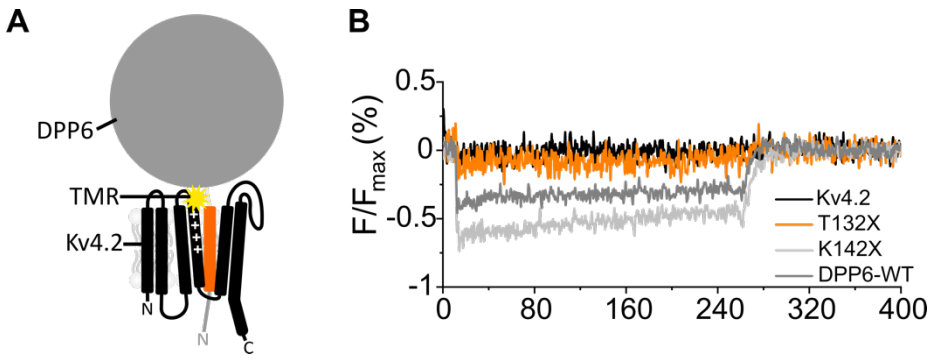

Figure 5.2 Voltage-clamp fluorometry.
A) Cartoon illustrating the TMR labeling position (yellow star) of Kv4.2 at position A288C. One subunit each of Kv4.2 in black and DPP6 in orange/grey are illustrated. **B**) Representative fluorescence traces of TMR labeled Kv4.2-A288C/KChIP in the presence of DPP6-T132X and DPP6-K140X compared to DPP6-WT.

We next verified whether the truncated DPP6-T132X still interacts with Kv4. When we coexpressed the truncated DPP6-T132X, we observed a fluorescence change smaller than the full-length DPP6 induced signal (figure 5.2b), indicating that the truncated version is expressed in the plasma membrane and interacts with the channel but that the quenching efficiency is decreased compared to the full-length DPP6. A bigger change in fluorescence compared to DPP6-WT and DPP6-T132X caused by a slightly longer DPP6-K142X (figure 5.2b) is not surprising since the C-terminus of DPP6-K140X extends out of the plasma membrane and is more flexible thereby increasing quenching efficiency. Although we have previously applied VCF to quantify channel properties (57-60), here we simply interpret a negative change in fluorescence as an indicator for a close proximity between the top of the S4 helix and the DPP6 β-subunit. The presented VCF data is in agreement with the observation by Lin et al. (47) reporting that a DPP6 truncation similar to our T132X still traffics to the plasma membrane. Moreover, our data illustrates that the extracellular domain is not necessary for trafficking to the membrane and DPP6's interaction with the channel. More specifically, it demonstrates that DPP6's transmembrane helix is in close proximity to the S4 helix of Kv4.2 and that the interaction between Kv4 and DPP6 is increased by the extracellular domain of DPP6.

5.3.3 Majority of Propeller Domain Responsible for Channel Gating Properties

The truncation of the extracellular domain at T132X significantly affected the electrophysiological properties of the channel complex, decreasing peak currents and slowing activation and inactivation kinetics, while maintaining a close proximity to the channel's S4 helix. These results suggest that DPP6 interacts with the alpha subunit through the transmembrane helix and that additional interactions between the α-subunit and the extracellular domain are necessary to confer drastic gating modulations. We thus aimed at narrowing down which part of the extracellular domain of DPP6 is responsible for the increased peak currents and the accelerated activation and inactivation kinetics. We truncated DPP6 progressively from the C-terminus (K241X, R322X, N351X, D484X, H581X, K711X) removing subdomains according to the crystal structure (figure 5.3a and table 5.1). To study their gating properties, we coexpressed the

resulting constructs with Kv4.2 in *Xenopus* oocytes. VCF experiments (figure 5.3b) confirmed trafficking of these truncations to the plasma membrane together with Kv4.2.

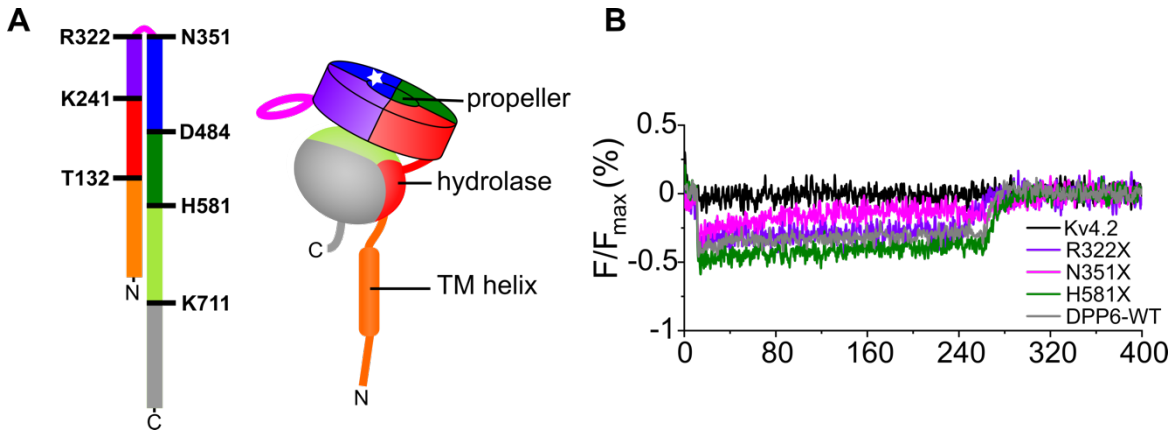

Figure 5.3 Voltage-clamp fluorometry.
A) Cartoon illustrating the different DPP6 truncations. Truncation sites indicated by one letter code and position corresponding to the crystal structure. White star highlights the site of disulfide bridge formation between residues C411 and C418. **B**) Representative fluorescence traces of TMR labeled Kv4.2-A288C/KChIP in the presence of DPP6-R322X, -N351X, -H581X and DPP6-WT.

Table 5.1: Truncations of the extracellular domain of DPP6 and their structural properties

truncation	structure
K241X	beginning of α/β-hydrolase + ¼ of β-propeller intact
R322X	beginning of α/β-hydrolase + ½ of β-propeller intact (loop removed)
N351X	beginning of α/β-hydrolase + ½ of β-propeller intact (loop intact)
D484X	beginning of α/β-hydrolase + ¾ of β-propeller intact
H581X	beginning of α/β-hydrolase + β-propeller intact
K711X	last ½ of α/β-hydrolase removed
ΔProp	β-propeller removed, α/β-hydrolase intact

When we compared the functional expression level based on the peak current amplitude to the expression of the progressive truncations (figure 5.4a), we found a sharp transition between N351X and D484X. Like DPP6-T132X, DPP6-K241X, -R322X and -N351X had similar peak currents to Kv4 whereas the longer DPP6 variants (D484X, H581X and K711X) reached higher peak currents

comparable to DPP6-WT. Interestingly, only D484X achieved comparable expression to DPP6-WT, while the two longer truncations had slightly lower currents.

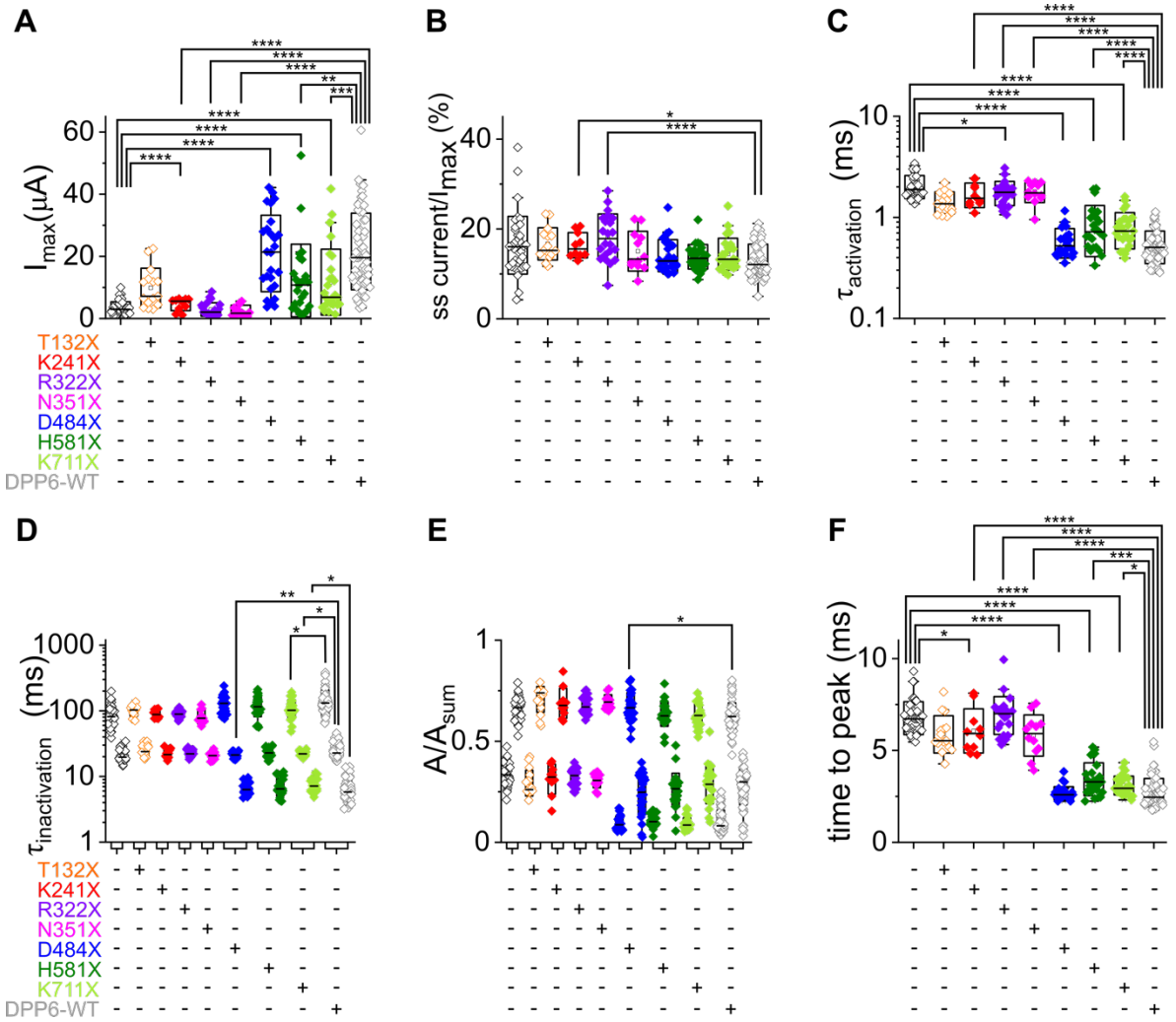

Figure 5.4 Electrophysiological properties of DPP6 truncations.
Kv4.2/DPP6-K241X, Kv4.2/DPP6-R322X, Kv4.2/DPP6-N351X, Kv4.2/DPP6-D484X, Kv4.2/DPP6-H581X and Kv4.2/DPP6-K711X compared to Kv4.2 and Kv4.2/DPP6-WT. **A**) Peak currents obtained at test pulse of +100 mV. **B**) Steady state current at the end of +100 mV test pulse normalized to peak current. **C**) Time constants of activation at + 100 mV test pulse. **D**) Time constants of inactivation at +100 mV test pulse. **E**) Relative amplitudes of inactivation time constants at +100 mV test pulse. **F**) Time to peak at +100 mV test pulse. Kv4.2/DPP6-K241X n=10, Kv4.2/DPP6-R322X n=22, Kv4.2/DPP6-N351X n=12, Kv4.2/DPP6-D484X n=26, Kv4.2/DPP6-H581X n=25 and Kv4.2/DPP6-K711X n=27. * $P < 0.05$, ** $P < 0.005$, *** $P < 0.0005$, **** $P < 0.00005$, additional significances can be found in the supplementary table S5.2.

Although the fraction of inactivation of full-length DPP6 was significantly lower compared to Kv4.2 and DPP6-T132X (figure 5.1b), other DPP6 truncations were undistinguishable from Kv4.2 (figure 5.4b). However, when we compared the steady state currents of truncated DPP6s to the full-length DPP6, we saw that longer DPP6 truncations (D484X and longer) were more comparable to full-length DPP6 steady state currents than shorter truncations. Like DPP6-T132X, DPP6-K241X and -R322X featured significantly higher steady state currents compared to the full-length DPP6. This transition in relative steady state current amplitudes was not as prominent as the transition in peak current amplitudes. As for peak current amplitudes, a more obvious transition between D484X and N351X, i.e. in the second half of the beta-propeller, was observed in the activation kinetics (figure 5.4c). Although shorter truncations featured accelerated activation kinetics compared to Kv4.2, they remained significantly slower compared to full-length DPP6. In contrast, truncations at D484 and longer were more comparable to DPP6-WT. This sharp transition was also observed in inactivation kinetics (figure 5.4d). The faster inactivation of full-length DPP6 with an additional fast initial component (described by a third time constant) was absent in T132X. The same is true for DPP6-K241X, -R322X and -N351X. The faster inactivation with the fast, initial component appeared in the longer DPP6-D484X, -H581X and -K711X. The time constants for these longer truncations were comparable to the ones of DPP6-WT mediated inactivation. The relative amplitudes of the shorter truncations were comparable to Kv4.2 alone (figure 5.4e). Here, approximately one-third of the decay is attributed to the slow time constant. For the longer constructs and DPP6-WT, the relative amplitudes of the slow time constant were clustered at around 10%. Relative amplitudes for the intermediate and fast time constants were scattered around 60% and 25%, respectively. Time constants and relative amplitudes for D484X, H581X and K711X were almost undistinguishable from DPP6-WT.

The altered activation and inactivation kinetics were also reflected in the time to peak (figure 5.4f). Overall, the three longer truncations (D484X, H581X and K711X) had shorter time to peak around 3 ms, which were only marginally slower than DPP6-WT (2.7$\pm$0.77 ms). Time to peak averaged around 6 ms for shorter truncations (K241X, R322X, N351X) and were closer to Kv4 alone (6.76 $\pm$ 0.9 ms). R322X and N351X were the closest to Kv4 alone, and K241X was slightly, but significantly faster.

Our data demonstrate a strong link between the length of DPP6's extracellular domain, peak current and accelerated activation and inactivation kinetics. More specifically, the region between N351X and D484X plays an essential role in conferring DPP6's effect on these channel characteristics. The crystal structure of DPP6's extracellular domain suggests that the propeller loop (R322-N351) is important for dimer formation (23), and biochemical studies have suggested a 4:4 stoichiometry of Kv4.2 to DPP6 (dimer of dimers) (61). Truncating DPP6 directly after the β-propeller loop (N351X) did not result in DPP6-WT-like properties, whereas truncating DPP6 at D484X resulted in comparable channel complex properties to complexes that comprise full-length DPP6. The longer D484X truncation leaves three-quarters of the propeller domain intact including the loop at the midpoint of the domain. Expressing three-quarters of the propeller domain allows for disulfide bridge formation at C411-C418 in propeller blade 5, which could stabilize the loop-loop interaction between two DPP6 subunits, so that longer DPP6 subunits might interact with other DPP6 subunits more stable than shorter truncations that, in contrast, might fail to form dimers. Removing this cysteine bridge in blade 5 by alanine substitution mutation (which probably leads to misfolding) results in 40-50% reduced surface expression (47). We hypothesized that shorter truncations (T132X, K241X, R322X and N351X) and misfolded propeller domains as for the C411A-C418A mutation might then lead to altered stoichiometries between DPP6 and the channel.

The DPP6 extracellular domain dependent increase in peak currents could have several reasons. First, the proper dimerization of DPP6's extracellular domain could result in increased trafficking of Kv4.2 as well as anchoring of the channel complex in the plasma membrane. It has been shown that the full-length DPP6-WT increases Kv4.2 trafficking to the plasma membrane 9-fold (62). A similar increase in trafficking might be also observed when the propeller domain is partially intact, as we hypothesize for the D484X truncation. This would increase the number of channel complexes in the plasma membrane and thereby the macroscopic currents. Another reason for increased peak currents could be an increase in the single channel conduction. Therefore, we should not exclude the possibility that longer DPP6 truncations exhibit increased single channel conductance like the almost 2-fold increase for the full-length DPP6 (29). Since both mechanisms have been reported to be responsible for increased currents when the full-

length DPP6 subunit is coexpressed, it is possible that longer DPP6 truncations also increase the current amplitude through both mechanisms.

Another reason that might play a role in the diminished DPP6 function when the extracellular domain is removed, is a change in the DPP6 expression level. If shorter truncations expressed less compared to longer ones, we would expect more Kv4.2 channel complexes without DPP6 subunits to be present in the plasma membrane, which would result in overall more Kv4-like properties. To test, if the altered properties of DPP6 truncations might be caused by lowered DPP6 expression, we increased the relative amount of truncated DPP6-T132X cRNA 9-fold (1:1 cRNA weight ratio) and thereby the amount of available auxiliary subunits and checked if some of the channel modulation properties could be rescued. We found that peak and steady state currents nor the activation time constant were significantly changed (figure 5.5a-c). However, inactivation was accelerated when more DPP6-T132X was expressed. This was reflected in the fast time constant of inactivation, which was significantly accelerated by approximately 1.5-fold (figure 5.5d) as well as the relative amplitudes, which shifted towards the faster time constant (figure 5.5e). Although an acceleration in inactivation is expected to overtake activation at an earlier time and therefore shift the peak amplitude to earlier times, the acceleration of inactivation by higher expression levels of DPP6-T132X was not enough to significantly alter time to peak values (figure 5.5f). Given that we were able to change at least one of the current properties by increasing the relative amount of available DPP6-T132X subunits, we propose that shorter truncations might not express as well as longer truncations and that the diminished effect of DPP6 can be partly rescued by expressing more DPP6 subunits. Additionally, the fact that the inactivation kinetics can be accelerated by more available DPP6 subunits suggests that the DPP6 stoichiometry is flexible at least for shorter truncations and that the effect on the biophysical properties of the channel complex gradually changes depending on the number of DPP6 subunits that bind to the channel complex. However, increasing the relative amount of shorter DPP6 truncations did not increase peak currents nor decrease steady state currents, furthermore, it did not introduce a fast inactivation component described by a third time constant, suggesting that these properties are solely governed by the extracellular domain rather than the number of DPP6 subunits bound to the channel.

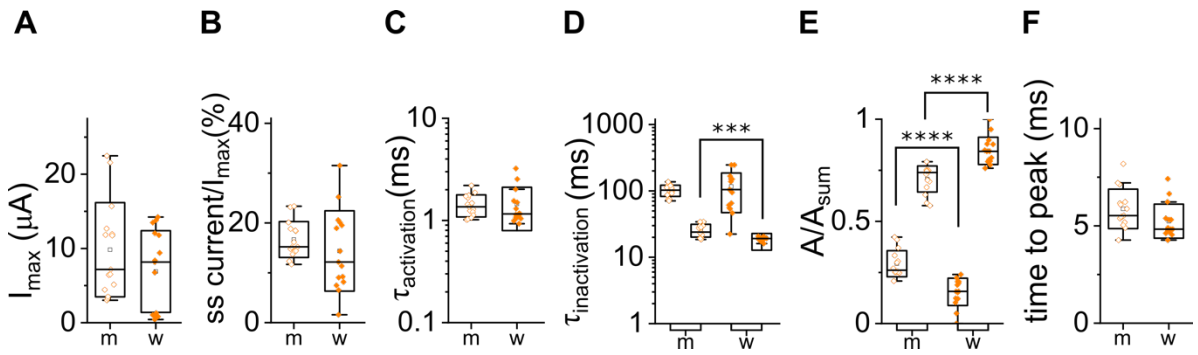

Figure 5.5 Electrophysiological properties of DPP6-T132X coexpressed with Kv4.2 cRNA in molar ratios (m) compared to weight ratios (w).
A) Time constants of inactivation at +100 mV test pulse. **B**) Relative amplitudes of inactivation time constants at +100 mV test pulse. Molar ratio n=15, weight ratio n=15. * $P < 0.05$, ** $P < 0.005$, *** $P < 0.0005$, **** $P < 0.00005$, additional significances can be found in the supplementary table S5.3.

5.3.4 Effect of DPP6 Extracellular Domain on Gating Properties in the Presence of KChIP

It has been previously demonstrated that Kv4.2 features a N-terminal autoinhibitory peptide, similar to the ball-and-chain inactivation particle in Shaker (63), that mediates a vestigial form of N-type inactivation from the open state (39). This fast open state inactivation has been shown to be impaired when auxiliary subunit KChIP is coexpressed as it is thought to bind to the proximal N-term of Kv4 and prevents it from blocking the pore (6, 31, 37, 41, 42). We coexpressed KChIP to verify that the DPP6 mediated channel inactivation mechanism is independent from the N-term mediated fast OSI and investigate if the abrupt transition of DPP6's influence dependent on the truncation is preserved in the absence of fast inactivation. To ensure the suppression of NTI, we used splice variant DPP6-S, that unlike DPP10a and DPP6a (DPP6-E) does not have the N-terminal MNQTA motif that produces NTI in the presence of KChIP or deletion of the alpha subunit's N-term (48).

The drastic difference in gating properties of longer truncations (D484X and longer) in comparison to shorter C-termini was not obvious in the peak current when KChIP2 was coexpressed, indicating that, in the ternary complex, the peak current amplitude is governed by

KChIP rather than the length of the extracellular domain. Coexpression of KChIP2 with Kv4.2 resulted in a more than 4-fold increase in peak current to 14.95 ± 6.01 µA (figure 5.6a). This effect was, however, smaller than the previously observed 7-fold increase mediated by coexpression of DPP6-WT (figure 5.1a). The individual peak current-increasing effects of DPP6 and KChIP were not additive and coexpressing KChIP in the presence of full-length DPP6 resulted in lower average peak currents of 10.9 ± 7.2 µA. These results are in agreement with other publications on the ternary Kv4/DPPL/KChIP complex (54, 64). Coexpressing the truncated DPP6-T132X with KChIP led to non-significant increase of peak current to 13.9 ± 5.7 µA, and the significant decrease in peak current amplitude in the presence of full-length DPP6 was lost. Since no significant change between the full-length DPP6 and DPP6-T132X was observed, we did not expect any changes for the other truncations. This was found to be true, with the exception of DPP6-D484X, which showed significantly reduced peak current amplitudes compared to Kv4.2 in the presence of KChIP. However, these peak currents did not significantly change compared to DPP6-WT currents. Generally peak current amplitudes varied around 5 to 10 µA around the mean value, while coexpression of KChIP/DPP6-D484X resulted in less deviation (8.1 ± 3.16 µA). Since, expression levels, and therefore peak current amplitudes, not only depend on the respective protein constructs but also on several external factors, such as oocyte and RNA quality as well as precise RNA injection, we propose that less variations are caused by more consistent external factors that influence the expression level.

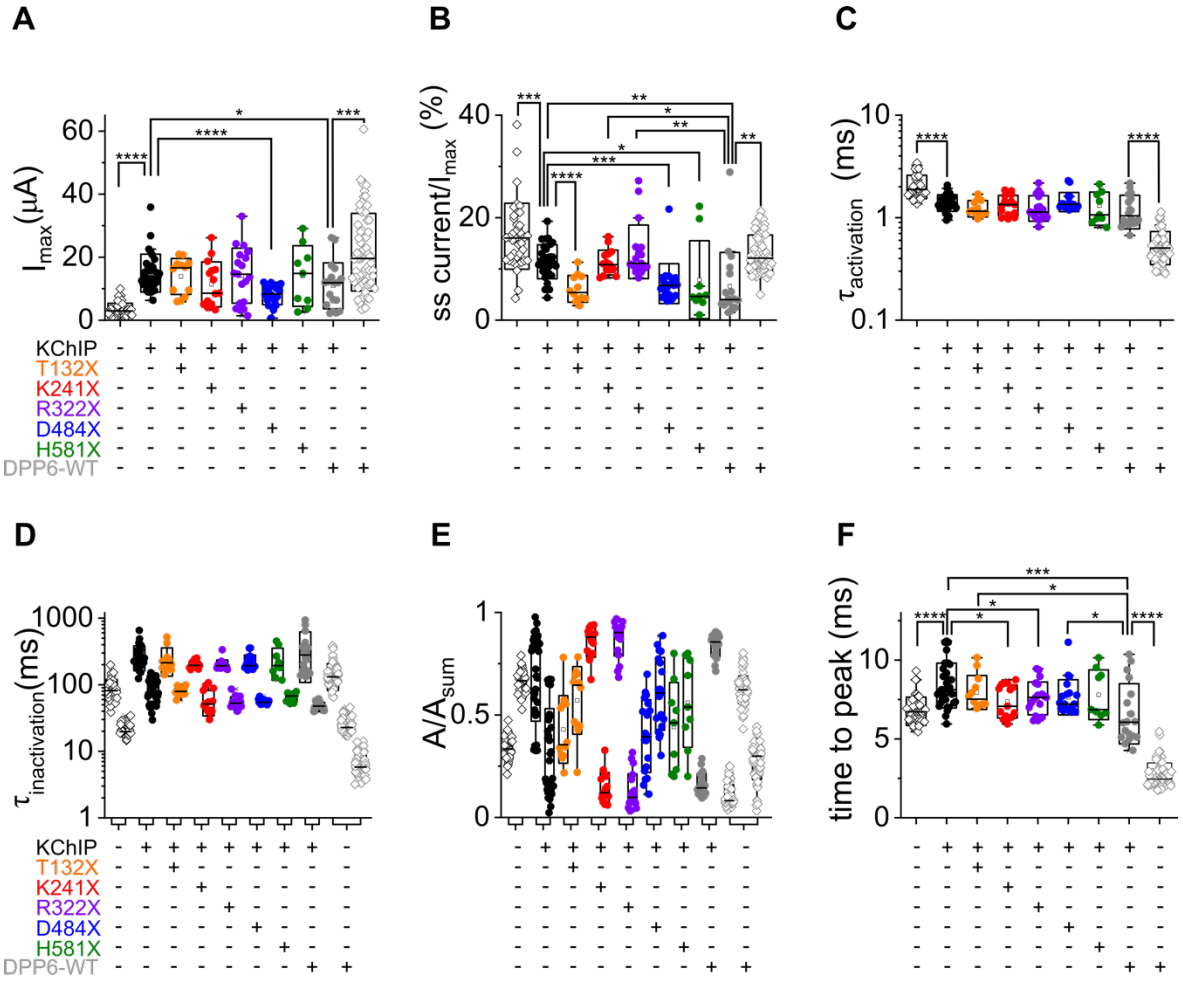

Figure 5.6 Electrophysiological properties of DPP6 truncations in the presence of KChIP compared to Kv4.2/KChIP and Kv4.2/KChIP/DPP6-WT.
A) Peak currents obtained at test pulse of +100 mV. **B**) Steady state current at the end of +100 mV test pulse normalized to peak current. **C**) Time constants of activation at + 100 mV test pulse. **D**) Time constants of inactivation at +100 mV test pulse. **E**) Relative amplitudes of inactivation time constants at +100 mV test pulse. **F**) Time to peak at +100 mV test pulse. Kv4.2/KChIP n=31, Kv4.2/KChIP/DPP6-T132X n=12, Kv4.2/KChIP/DPP6-K241X n=15, Kv4.2/KChIP/DPP6-R322X n=19, Kv4.2/KChIP/DPP6-D484X n=19, Kv4.2/KChIP/DPP6-H581X n=9 and Kv4.2/KChIP/DPP6-WT n=18. * $P < 0.05$, ** $P < 0.005$, *** $P < 0.0005$, **** $P < 0.00005$, additional significances can be found in the supplementary table S5.4.

For all constructs, KChIP binding led to approximately 1.5-fold more complete inactivation (shown for Kv4.2 and DPP6-WT in figure 5.6b) and the degree of inactivation varied as a function of the length of DPP6's extracellular domain (figure 5.6b). In the presence of KChIP, DPP6-N241X and -R322X featured steady state current levels comparable to Kv4.2/KChIP, while stronger

inactivation was observed for DPP6-D484X and longer DPP6 subunits. Interestingly, DPP6-T132X also resulted in stronger inactivation in the presence of KChIP, that was indiscernible from full-length DPP6 in the presence of KChIP. This result implies that the N-terminal part and transmembrane helix of DPP6 affect inactivation, although to a smaller degree than the full-length DPP6.

In the presence of KChIP, the drastic shift in activation time constants with longer DPP6 truncations, as previously observed in the absence of KChIP (figure 5.4c), was no longer observed (figure 5.6c). The time constants of activation were around 1 ms and indistinguishable for all conditions, illustrating that KChIP binding governs channel activation kinetics. It is quite intriguing that KChIP alters the channel properties from the cytosol, whereas we are manipulating the extracellular domain of DPP6. Rather than a direct competition between KChIP and DPP6, we propose that KChIP allosterically interacts with the channel which results in conformational changes of the α-subunits. This proposed change in the Kv4 subunit then prevents DPP6 from conferring its extracellular domain dependent channel activation modulation.

KChIP influenced the inactivation time constants distinctly for the different DPP6 constructs. The most drastic difference compared to the inactivation in the absence of KChIP, was the loss of the fast time constant for DPP6 truncations D484X and longer. The time constants of the shorter truncations also changed, albeit less drastically, and were overall slower than in the absence of KChIP (figure 5.6d). As a result, the fast and slow time constants of inactivation of differently truncated DPP6 subunits were undiscernible from one another. Although KChIP coexpression resulted in overall slowed inactivation kinetics, a distinct acceleration of inactivation kinetics was observed for longer truncations (D484X and H581X) and full-length DPP6. Rather than being observable in the time constants, the shift towards faster inactivation kinetics depended on the redistribution of the relative amplitudes of the exponential terms (figure 5.6e). The relative amplitude shifted significantly towards the faster time constant for truncations D484X and longer. This shift was most pronounced for the full-length DPP6 subunit (~16 % slow), but was also observed for longer truncations D484X (40 $\pm$ 18% slow) and H581X (44 $\pm$ 21 % slow). Although the fractional amplitudes were not as separated as for the full-length DPP6, the fractional amplitudes

of the longer DPP6-D484X and -H581X truncations clearly differed from the shorter truncations (T132X, K241X and R322X) in the presence of KChIP. In the presence of KChIP, DPP6-T132X inactivated faster than Kv4.2/KChIP. However, inactivation was still slower than the longer truncations DPP6-D484X and -H581X in the presence of KChIP. This indicates that, while the C-terminus of DPP6 does play a role on the acceleration of inactivation by DPP6, even in the absence of the C-terminus inactivation is accelerated. However, this effect is much less pronounced compared to the effect conferred by the longer truncations (D484X and H581X) and full-length DPP6.

We previously observed a shift in time to peak towards faster times with longer DPP6 in the absence of KChIP (figure 5.6f), however, this shift disappeared in the presence of KChIP, indicating that KChIP binding governs the activation kinetics and peak current is reached before channels start to inactivate significantly. This resulted in comparable time to peak values for Kv4.2 alone and all DPP6 truncations, while the full-length KChIP/DPP6-WT reached the peak slightly faster.

We concluded earlier that the abrupt change in channel gating seen with longer truncations of DPP6 in the absence of KChIP (figure 5.4) was mediated by the beginning of the 2nd half of the β-propeller (residues N351 to D484). The same region plays an important role for the accelerated inactivation kinetics in the absence of NTI. Instead of introducing another time constant to describe the current decay, a redistribution of relative amplitudes towards the faster phase caused the changes. The shift of fractional amplitudes is a result of a DPP6-dependent redistribution of channel populations, suggesting that DPP6 truncation results in a shift towards a more stable open channel state compared to the full-length DPP6-WT. This indicates that not only the cytosolic N-terminus of DPP6 is important for accelerated Kv4 inactivation (48) but also its extracellular C-terminal domain. More specifically, our results suggest that the stabilization of DPP6 dimer formation by the second part of the propeller (D484X) leads to redistribution of states and destabilization of open state independent of the presence of KChIP, while KChIP governs channel activation kinetics and shifts the equilibrium towards CSI.

5.3.5 Contribution of α/β-Hydrolase Domain on Channel Gating Properties

Even the longest truncation DPP6-K711X, where we removed only the last half of the α/β-hydrolase of DPP6 did not inactivate as rapidly as the full-length DPP6. This indicated that the peptidase domain has a modulatory effect on the alpha subunit. We therefore investigated the effect of the peptidase domain in the absence of the β-propeller domain. We tested this new construct (DPP6-ΔProp) in the presence and absence of KChIP and compared the effects on the channel gating properties.

Coexpression of DPP6-ΔProp in the presence and absence of KChIP resulted in peak and steady state currents that were undistinguishable from Kv4 currents with and without KChIP (figure 5.7a,b). We also did not observe any noticeable changes in the activation and inactivation kinetics when we coexpressed DPP6-ΔProp. Instead, the activation kinetics for DPP6-ΔProp were undistinguishable from Kv4 (figure 5.7c). As seen for shorter truncations, DPP6-ΔProp's inactivation was best fitted with two exponentials and the time constants of inactivation for DPP6-ΔProp without KChIP were comparable to the inactivation time constants of Kv4.2 alone (figure 5.7d, diamonds). Although not reflected in the inactivation time constants, DPP6-ΔProp inactivated, like DPP6-T132X, on average faster than Kv4.2. This was reflected in the fractional amplitudes. The loss of the fast time component, that we previously observed for longer truncations, resulted in fractional amplitudes of DPP6-ΔProp similar to Kv4.2 alone, where the majority of decay was attributed to the fast component (29.0 ± 4.0 % slow) (figure 5.7e, diamonds). Despite the similarity to Kv4.2 alone, for DPP6-ΔProp, the distribution was slightly shifted toward the faster time constant, explaining the overall accelerated inactivation kinetics compared to Kv4.2.

As for other DPP6 truncations, binding of KChIP affected the inactivation kinetics independent of the DPP6 subunit and slowed the average time constants for DPP6-ΔProp. Additionally, in the presence of KChIP, the fractional amplitudes shifted towards the slow component (86.4 ± 5.9 % slow) as seen previously for shorter truncations and Kv4 alone. In accordance with the gating kinetics, time to peak of DPP6-ΔProp in the presence and absence of KChIP was comparable to Kv4.2 (figure 5.7f), mirroring the overall similarity to the channel properties without DPP6.

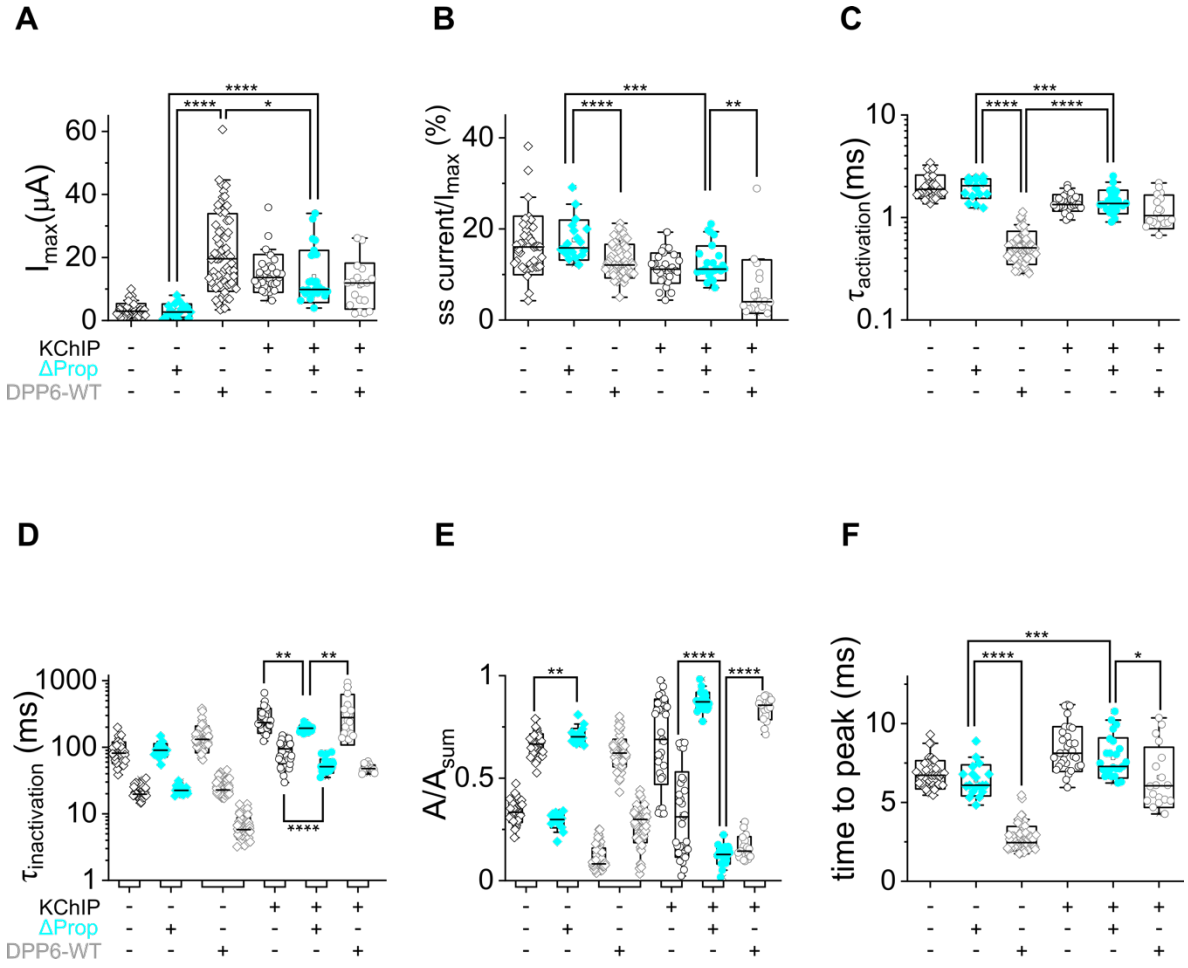

Figure 5.7 Electrophysiological properties of DPP6-ΔProp in the presence and absence of KChIP. Kv4.2/DPP6-ΔProp and Kv4.2/KChIP/DPP6-ΔProp compared to Kv4.2, Kv4.2/KChIP, Kv4.2/DPP6-WT and Kv4.2/KChIP/DPP6-WT. **A**) Peak currents obtained at test pulse of +100 mV. **B**) Steady state current at the end of +100 mV test pulse normalized to peak current. **C**) Time constants of activation at + 100 mV test pulse. **D**) Time constants of inactivation at +100 mV test pulse. **E**) Relative amplitudes of inactivation time constants at +100 mV test pulse. **F**) Time to peak at +100 mV test pulse. Kv4.2/DPP6-ΔProp n= 19 and Kv4.2/KChIP/DPP6-ΔProp n=29. * $P < 0.05$, ** $P < 0.005$, *** $P < 0.0005$, **** $P < 0.00005$, additional significances can be found in the supplementary table S5.5.

Overall, the α/β-hydrolase domain did not directly contribute to the acceleration of activation, inactivation and increased peak currents. Furthermore, removing the peptidase domain also does not affect DPP6 trafficking to nor Kv4.2 amounts in the plasma membrane (47). We suggest that this domain may help in the positioning of the propeller domain but is not crucial for its effect on Kv4.2 channel kinetics. It remains elusive, whether the α/β-hydrolase domain has a functional significance.

5.4 Discussion

Electrophysiological studies have demonstrated the effect of the N-termini of DPP10a, DPP6a and Kv4.2 on fast N-type like inactivation (39, 48, 65). But until now, no in-depth analysis of the biophysical property-rendering character of the about 700 amino acid long extracellular domains of DPP6 have been available. To understand in more detail the role of the extracellular domain of DPP6, we examined the effects of C-terminal deletions of auxiliary subunit DPP6-S on Kv4.2 channel gating. Our data show that removal of the extracellular domain results in reduced peak currents and slower activation and inactivation kinetics. However, compared to Kv4.2/KChIP, the truncated DPP6-T132X featured accelerated inactivation kinetics in the absence of NTI, suggesting that the N-terminal part and transmembrane helix of DPP6 affects inactivation, albeit much less than the full-length DPP6. More specifically, our results show that the second half of the propeller domain of DPP6 is responsible for drastically accelerated inactivation in the presence and absence of KChIP. We demonstrate that in the absence of KChIP the propeller domain controls the rapid component of inactivation (addition of 3rd time constant). In the presence of KChIP, it controls the speed of inactivation by shifting the relative amplitudes of inactivation time constants towards the fast component. The same domain is responsible for accelerated activation kinetics in the absence of KChIP, lowering the energy barrier of channel opening. Interestingly, KChIP binding on the cytosolic side overshadows any activation-accelerating effect of DPP6's extracellular domain and governs activation kinetics. Our results illustrate a destabilizing effect of DPP6 on transition and open channel states, which depends on the region between N351X and D484X. Considering DPP6's crystal structure of the extracellular domain (23), we suggest that this

region at the midpoint of the propeller domain is crucial for the dimer formation of DPP6 and furthermore, that this multimerization is key for the increased peak currents and profound and accelerated inactivation conferred by the extracellular domain.

Multimerization of the extracellular domain by longer truncations could increase peak currents by increasing the unitary conductance. Two negatively charged amino acids in the N-term have been shown to be responsible for DPP6's effect on single channel conductance (29). In the same study, it was proposed that these amino acid side chains assemble as a ring of eight negative charges when four DPP6 subunits bind to the channel complex. This ring is hypothesized to be positioned in proximity to the intracellular opening of the ion channel pore, where it locally increases the K^+ concentration by electrostatic interactions. If, as we propose, truncated DPP6 subunits fail to multimerize as efficiently as full-length DPP6 subunits, less negative charges would be present at the intracellular mouth of the channel, so that K^+ ions are less efficiently concentrated, which ultimately results in a decreased unitary conductance.

Without further experiments, it remains unclear what mechanism causes the destabilization effect of the extracellular DPP6 domain on the open channel state. Increasing the relative amount of available truncated DPP6 subunits accelerated inactivation kinetics but left the other properties unchanged, suggesting that a truncated extracellular domain results in a decreased subunit expression and altered DPP6 stoichiometry that can be changed by overexpression of the shorter DPP6 subunit. However, only the longer DPP6 subunits, that proposedly form stable dimers (and dimer of dimers) through the propeller domain, confer drastic changes in the channel properties. We further hypothesize that the longer extracellular domain affects the channel gating directly. It is possible that the formation of a multimeric DPP6 extracellular domain leads to a positioning of DPP6's extracellular domain directly on top of the ion channel whereas truncated DPP6 variants fail to multimerize and therefore establish a more flexible conformation that does not interact with the top of the channel directly and ultimately failing at destabilizing the open state as efficiently. Coexpressed DPP6 subunits with properly folded propeller domains might then not only be in direct contact with the VSD (as illustrated by our VCF data) but also with the pore domain. This positioning might facilitate CSI by destabilizing the open channel state. Destabilizing the open state would shift the equilibrium towards the closed state from where the

channels accumulate in a closed inactivated state. The mechanism of CSI is not well understood, but it is characterized by a distinct desensitized conformation of the voltage sensor and uncoupled S6 gate (45). We proposed that the extracellular domain is positioned in proximity to the voltage sensing domain. There, it might be involved in interactions with the S4 helix that favor the desensitized conformation.

Because Kv4.2 features open-state inactivation (OSI), i.e. N-type like inactivation (NTI), and closed-state inactivation (CSI), we examined the gating properties of Kv4.2 in the presence of KChIP to understand which gating pathway is affected by the extracellular domain of DPP6. It has been shown, that the KChIP auxiliary subunit inhibits fast NTI by sequestering the N-terminus of Kv4 (6, 31, 38, 41).Binding of KChIP in a 1:1 ratio to the channel's N-terminal domain removes NTI. As a result, inactivation follows the slower kinetics of CSI and inactivation is more complete. Coexpression of full-length DPP6 destabilizes the open channel state (redistributing the channel population towards faster inactivation) in an extracellular domain-dependent manner, while the cytosolic KChIP subunits shift the equilibrium towards closed inactivated channels independently of the length of the extracellular DPP6 domain.

Rather than being the pure result of channel gating modifications induced by properly positioned DPP6 subunits on top of the channel, the accelerated inactivation kinetics conferred by longer DPP6 subunits in the presence of KChIP could be a result of an altered ternary channel complex stoichiometry. Two scenarios could explain this. The first scenario involves a homogenous channel ensemble comprising a dynamic, DPP6-dependent amount of KChIP subunits per complex. A shift towards less KChIP subunits per channel complex in the presence of longer DPP6 subunits could then explain accelerated inactivation kinetics. In this case, a single unbound N-terminal of Kv4.2 could lead to NTI and thereby accelerate the macroscopic inactivation kinetics. We hypothesized, that coexpression of DPP6 with longer extracellular domains leads to multimerization of DPP6. A partial loss of KChIP subunits on the cytosolic site could be explained by a direct competition between an increased number of DPP6 subunits per channel complex and KChIP. Such a shared binding site has not been reported and, we propose, is unlikely, given that KChIP binds to the N-terminal Kv4 domain, while DPP6 interacts with Kv4's S4 helix as our VCF data demonstrated (42). Alternatively, the proper positioning of the

multimeric DPP6 could induce a conformational change of the α-subunit that results in a weaker interaction with KChIP and ultimately a loss of KChIP subunits. However a DPP6 induced loss of KChIP subunits seems improbable, since biochemical experiments have led to believe that Kv4.2, KChIP and full-length DPP6 adopt a 1:1:1 arrangement, although the biochemical experiments actually resulted in a 1:2:1 stoichiometry which was interpreted as an experimental artifact (61). Another study conducted subunit counting experiments and demonstrated that DPP10 (another DDP-like auxiliary subunit) does not affect the Kv4.2/KChIP stoichiometry and that the number of KChIP subunits depends on the expression level of KChIP (66). Not only these biochemical studies suggest that coexpression with full-length DPP6 leave the number of KChIP subunits unchanged, but also our own data cannot be reconciled with the idea of DDP6-dependent KChIP stoichiometry changes. KChIP binding leads to more complete inactivation, so that a decreased number of KChIP in the channel complex would then, opposed to what we observed, increase steady state currents.

The second scenario of altered ternary channel complex stoichiometries involves mixed populations of ternary channel complexes. Here, two distinct populations of channel complexes might exist in the presence of KChIP, one with and one without DPP6 (62). If DPP6 variants with a short extracellular domain fail to interact with Kv4.2 as efficiently as longer DPP6 variants and DPP6-WT or shorter DPP6 truncations are less well expressed, more complexes without DPP6 could be present in the plasma membrane. Assuming that DPP6 subunits with shorter extracellular domains exhibit identical channel gating modification characteristics as the individual full-length DPP6 subunit, the observed change in gating kinetics would be solely a result of a reduced number of DPP6 containing channel complexes. Such a redistribution towards complexes without DPP6 in the presence of KChIP would result in overall slowed inactivation kinetics and lower maximum macroscopic currents. However, increasing the amount of available DPP6-T132X subunits 9-fold did not result in channel properties identical to the full-length subunit, strengthening the idea that the extracellular domain confers a distinct channel modulation and that differently truncated DPP6 subunits do not exhibit identical channel gating modification characteristics. However, the slowed inactivation kinetics in the presence of KChIP might be a mixed result of directly altered channel modification through the shorter extracellular

domain as well as a reduced number of DPP6 containing channel complex as a result of reduced expression of the shorter subunits. This scenario could be further tested by single subunit counting experiments (67-69), which could confirm if DPP6 truncations truly lead to mixed populations of channel complexes with and without DPP6 or if DPP6 stoichiometries are more variable within a channel complex (25) depending on the length of the extracellular domain as suggested by our results obtained from increased DPP6-T132X subunit amounts.

In summary, the presented research revealed the importance of a stable β-propeller domain and possibly DPP6 dimer formation as key determinants for increased peak currents and accelerated Kv4.2 activation and inactivation kinetics. How the multimerization of DPP6 subunits confers its channel modulating action remains unanswered, but the close interaction between the DPP6 subunit and S4 voltage-sensing helix hints at a direct allosteric effect on channel gating properties.

5.5 Methods

5.5.1 Molecular Biology

The DPP6 numbering is based on 1XFD crystal structure (23). All C-terminal DPP6-S truncations were generated by removing nucleotides from the 3'-end of the DPP6-S gene in a pRAT vector using the Gibson Assembly kit (NEB) and appropriate primers. Truncations are called after their last amino acid position, i.e. T132X has deleted positions V133-D865, K241X, N351X, R322X, D484X, H581X, K711X. The DPP6-ΔProp construct was generated by removing all residues between H144 and N579 by Gibson assembly. In this construct, residues H144 and N579 served as linkers between the two a/ß-hydrolase parts. The Kv4.2-A288C construct was generated in a pRAT vector by QuickChange site-directed mutagenesis (Stratagene) using appropriate primers (50). All cDNA clones were sequenced to verify mutations. All constructs were in vitro transcribed using mMachine T7 (Invitrogen) and cRNA was purified following the kit's instruction for lithium

chloride precipitation. RNA for Kv4.2 and for auxiliary subunits were mixed in equal molar ratios before injection.

5.5.2 Expression in Xenopus Oocytes

Oocytes were surgically obtained from *Xenopus laevis* and the follicular membrane was removed by treatment with collagenase type 1A (Sigma-Aldrich) in Ca^{2+}-free standard oocyte solution containing (in mM) 102 NaCl, 3 KCl, 1 $MgCl_2$, 4.6 HEPES, pH 7.2 adjusted with NaOH (0.0024g/35ml per 3-5 bags of oocytes). Oocytes of stage V and VI were selected and kept in Barth medium supplemented with 5% horse serum. 24-72h after surgery, if not specified otherwise, oocytes were injected with 46 nL of 1.64 µM Kv4.2 cRNA and if applicable equal molar amounts of cRNA encoding auxiliary subunits. For simplicity, coexpressions are denoted by slashes, e.g. Kv4/DPP6-WT/KChIP. For weight ratios, 46 ng of each Kv4.2 and DPP6-T132X were injected, which equates to molar ratios of 1:8.98. 46 nl of pre-mixed cRNA were injected into each oocyte using a nano-injector (Drummond Scientific). After injection, oocytes were incubated at 18°C in Barth medium (without serum). Electrophysiological recordings were performed 18-33 hours after injection of cRNA and VCF measurements after 3 days. N states the number of oocytes recorded for each condition; data were obtained from at least 3 independent oocyte preparations.

5.5.3 Electrophysiology and Voltage Clamp Fluorometry

All electrophysiology and voltage clamp fluorometry recordings were performed as described at room temperature (~18°C) with a CA-1B amplifier (Dagan Corp.) and analyzed using GPatch software (Department of Anesthesiology, University of California, Los Angeles)(51-53). Capacitance currents were subtracted offline using scaled subtraction with a negative pulse of -100 mV or maximally -140 mV as reference. 250-300 ms depolarizing test pulses ranging from -140 to +100 mV were applied. The holding potential was -90 mV. External solution contained (in mM) 5 KOH, 110 *N*-methyl-D-glucamine (NMG), 10 HEPES and 2 $Ca(OH)_2$, pH 7.1 adjusted with methane sulfonic acid. Internal solution contained (in mM) 115 KOH, 10 HEPES and 2 EDTA, pH 7.1 adjusted with methane sulfonic acid.

In voltage clamp fluorometry (VCF) experiments, voltage-dependent fluorescence changes from fluorophores covalently bound to the extracellular end of the S4 (position A288C in Kv4.2) were measured simultaneously to the current. Oocytes were labeled with freshly prepared 5 µM TMRM in labeling solution containing (in mM) 115 KOH, 10 HEPES and 2 $Ca(OH)_2$, pH 7.1 adjusted with methane sulfonic acid for 20 minutes at room temperature before recording. Currents were measured as described above and fluorescence was recorded using a Photomax 200 photodiode detection system (Dagan) attached to an upright microscope (Axioskop 2FS; Zeiss) with an ex-545/25, dc-570, em-605/70 filter set.. Bleaching effects were removed by scaled subtraction using the first sweep as reference.

5.5.4 Data Analysis

To compare effects of DPP6 truncations on the Kv4.2 gating properties we analyzed the peak current at 100 mV (I_{max}). The current-voltage relationships of A-type currents activation at 100 mV were fitted with first order exponential increases. The inactivation at 100 mV was fitted to first-, second- or third-order exponential decays. Residual currents were obtained by subtracting the exponential fit from the current trace. To ensure the comparability of fractional amplitudes, all exponentials were extrapolated to 0.75 ms after the onset of test pulse -where Kv4.2 + DPP6 was half activated- and the end of the recording. We observed higher variations in the relative amplitudes for longer DPP6 truncations in the presence of KChIP. When time constants for KChIP/DPP6-H581X were fixed to mean, the relative amplitudes were more clustered suggesting that fractional amplitudes might compensate for some extremer time constants. Figure 6e presents the unrestricted relative amplitudes. Time to peak describes the time from the onset of test pulse to the peak current. Significance was determined by one-way ANOVA using Origin (OriginLabs).

5.6 Acknowledgements

We would like to thank Mireille Marsolais for technical support in mutagenesis. This work was funded by the Canadian Institutes of Health Research (PJT169160 to R.B.) and the Natural Science and Engineering Research Council of Canada (RGPIN-2017-06871 to R.B.).

5.7 Supplemental Material

Supplemental Table S5.1 : One-way ANOVA analysis for figure 5.1

Figure 5.1				Prop>F	
A	Imax	Kv4.2	DPP6-T132X	<0.00005	****
		Kv4.2	DPP6-WT	0	****
		DPP6-WT	DPP6-T132X	0.00060	**
B	ss current/Imax	Kv4.2	DPP6-T132X	0.86623	NS
		Kv4.2	DPP6-WT	0.00069	**
		DPP6-WT	DPP6-T132X	0.00062	**
D	tau activation	Kv4.2	DPP6-WT	0	****
		Kv4.2	DPP6-T132X	0.00009	***
		DPP6-WT	DPP6-T132X	0	****
E	tau slow	Kv4.2	DPP6-T132X	0.11800	NS
		Kv4.2	DPP6-WT	<0.00005	****
		DPP6-WT	DPP6-T132X	0.01053	*
	tau fast	Kv4.2	DPP6-T132X	0.00323	**
		Kv4.2	DPP6-WT	0.00124	**
		DPP6-WT	DPP6-T132X	0.83505	NS
F	A slow	Kv4.2	DPP6-T132X	0.01121	*
		Kv4.2	DPP6-WT	0	****
		DPP6-WT	DPP6-T132X	0	****
	A fast	Kv4.2	DPP6-T132X	0.01121	*
		Kv4.2	DPP6-WT	0.00200	**
		DPP6-WT	DPP6-T132X	<0.00005	****
G	time to peak	Kv4.2	DPP6-T132X	0.00288	**
		Kv4.2	DPP6-WT	0	****
		DPP6-WT	DPP6-T132X	0	****

One-way ANOVA with pairwise analysis between the different conditions was performed and the statistical significance was denoted as asterisks for clarity. NS, not significant, * $P < 0.05$, ** $P < 0.005$, *** $P < 0.0005$, **** $P < 0.00005$

Supplemental Table S5.2 : One-way ANOVA analysis for figure 5.4

Figure 5.4				Prop>F	
A	Imax	Kv4.2	DPP6-K241X	0.08470	NS
		Kv4.2	DPP6-R322X	0.00000	****
		Kv4.2	DPP6-N351X	0.27501	NS
		Kv4.2	DPP6-D484X	<0.00005	****
		Kv4.2	DPP6-H581X	<0.00005	****
		Kv4.2	DPP6-K711X	<0.00005	****
		DPP6-WT	DPP6-K241X	<0.00005	****
		DPP6-WT	DPP6-R322X	<0.00005	****
		DPP6-WT	DPP6-N351X	<0.00005	****
		DPP6-WT	DPP6-D484X	0.82053	NS
		DPP6-WT	DPP6-H581X	0.00150	**
		DPP6-WT	DPP6-K711X	0.00044	***
B	ss current/Imax	Kv4.2	DPP6-K241X	0.99846	NS
		Kv4.2	DPP6-R322X	0.26022	NS
		Kv4.2	DPP6-N351X	0.50748	NS
		Kv4.2	DPP6-D484X	0.09739	NS
		Kv4.2	DPP6-H581X	0.06347	NS
		Kv4.2	DPP6-K711X	0.15133	NS
		DPP6-WT	DPP6-K241X	0.00604	*
		DPP6-WT	DPP6-R322X	<0.00005	****
		DPP6-WT	DPP6-N351X	0.07959	NS
		DPP6-WT	DPP6-D484X	0.18734	NS
		DPP6-WT	DPP6-H581X	0.27874	NS
		DPP6-WT	DPP6-K711X	0.07930	NS
C	tau activation	Kv4.2	DPP6-K241X	0.06621	NS
		Kv4.2	DPP6-R322X	0.04717	*
		Kv4.2	DPP6-N351X	0.11488	NS
		Kv4.2	DPP6-D484X	<0.00005	****
		Kv4.2	DPP6-H581X	<0.00005	****
		Kv4.2	DPP6-K711X	<0.00005	****
		DPP6-WT	DPP6-K241X	<0.00005	****
		DPP6-WT	DPP6-R322X	<0.00005	****
		DPP6-WT	DPP6-N351X	<0.00005	****
		DPP6-WT	DPP6-D484X	0.31407	NS
		DPP6-WT	DPP6-H581X	<0.00005	****
		DPP6-WT	DPP6-K711X	<0.00005	****
D	tau slow	DPP6-WT	DPP6-D484X	0.32125	NS
		DPP6-WT	DPP6-H581X	0.09367	NS
		DPP6-WT	DPP6-K711X	0.01051	*
	tau middle	DPP6-WT	DPP6-D484X	0.00315	**
		DPP6-WT	DPP6-H581X	0.06976	NS
		DPP6-WT	DPP6-K711X	0.01484	*
	tau fast	DPP6-WT	DPP6-D484X	0.80263	NS
		DPP6-WT	DPP6-H581X	0.16387	NS
		DPP6-WT	DPP6-K711X	0.04691	*
E	A slow	Kv4.2	DPP6-K241X	0.22317	NS
		Kv4.2	DPP6-R322X	0.18151	NS
		Kv4.2	DPP6-N351X	0.05793	NS
		DPP6-WT	DPP6-D484X	0.45220	NS
		DPP6-WT	DPP6-H581X	0.76150	NS
		DPP6-WT	DPP6-K711X	0.28602	NS
	A middle	DPP6-WT	DPP6-D484X	0.00599	*
		DPP6-WT	DPP6-H581X	0.44323	NS
		DPP6-WT	DPP6-K711X	0.68019	NS
	A fast	Kv4.2	DPP6-K241X	0.22317	NS
		Kv4.2	DPP6-R322X	0.18151	NS
		Kv4.2	DPP6-N351X	0.05793	NS
		DPP6-WT	DPP6-D484X	0.09328	NS
		DPP6-WT	DPP6-H581X	0.45446	NS
		DPP6-WT	DPP6-K711X	0.09328	NS

Figure 5.4				Prop>F	
E	time to peak	DPP6-WT	DPP6-D484X	0.84869	NS
		DPP6-WT	DPP6-H581X	0.00025	***
		DPP6-WT	DPP6-K711X	0.01947	*
		DPP6-WT	DPP6-K241X	0	****
		DPP6-WT	DPP6-R322X	0	****
		DPP6-WT	DPP6-N351X	0	****
		Kv4.2	DPP6-D484X	0	****
		Kv4.2	DPP6-H581X	0	****
		Kv4.2	DPP6-K711X	0	****
		Kv4.2	DPP6-K241X	0.04714	*
		Kv4.2	DPP6-R322X	0.57051	NS
		Kv4.2	DPP6-N351X	0.57051	NS

One-way ANOVA with pairwise analysis between the different conditions was performed and the statistical significance was denoted as asterisks for clarity. NS, not significant, * $P < 0.05$, ** $P < 0.005$, *** $P < 0.0005$, **** $P < 0.00005$

Supplemental Table S5.3 : One-way ANOVA analysis for figure 5.5

Figure 5.5		Prop>F	
A	Imax	0.18609	NS
B	ss current/Imax	0.32258	NS
C	tau activation	0.91459	NS
D	tau slow	0.44380	NS
	tau fast	0.00032	***
E	A slow	<0.00005	****
	A fast	<0.00005	****

One-way ANOVA with pairwise analysis between weight ratio and molar ratio injection conditions was performed and the statistical significance was denoted as asterisks for clarity. NS, not significant, * $P < 0.05$, ** $P < 0.005$, *** $P < 0.0005$, **** $P < 0.00005$

Supplemental Table S5.4 : One-way ANOVA analysis for figure 5.6

Figure 5.6				Prop>F	
A	Imax	Kv4.2	Kv4.2 + KChIP	0	****
		DPP6-T132X	DPP6-T132X KChIP	0.09692	NS
		DPP6-K241X	DPP6-K241X + KChIP	0.00743	*
		DPP6-R322X	DPP6-R322X + KChIP	0	NS
		DPP6-D484X	DPP6-D484X + KChIP	0.00006	***
		DPP6-H581X	DPP6-H581X + KChIP	0.68258	NS
		Kv4.2 + KChIP	DPP6-T132X KChIP	0.60103	NS
		Kv4.2 + KChIP	DPP6-K241X + KChIP	0.08243	NS
		Kv4.2 + KChIP	DPP6-R322X + KChIP	0.69563	NS
		Kv4.2 + KChIP	DPP6-D484X + KChIP	<0.00005	****
		Kv4.2 + KChIP	DPP6-H581X + KChIP	0.72612	NS
		DPP6-WT + KChIP	DPP6-T132X KChIP	0.24444	NS
		DPP6-WT + KChIP	DPP6-K241X + KChIP	0.85425	NS
		DPP6-WT + KChIP	DPP6-R322X + KChIP	0.23293	NS
		DPP6-WT + KChIP	DPP6-D484X + KChIP	0.13245	NS
		DPP6-WT + KChIP	DPP6-H581X + KChIP	0.35629	NS
		DPP6-WT + KChIP	Kv4.2 + KChIP	0.04146	*
B	ss current/Imax	Kv4.2	Kv4.2 + KChIP	0.00021	***
		DPP6-T132X	DPP6-T132X + KChIP	<0.00005	****
		Kv4.2 + KChIP	DPP6-T132X + KChIP	<0.00005	****
		Kv4.2 + KChIP	DPP6-K241X + KChIP	0.86230	NS
		Kv4.2 + KChIP	DPP6-R322X + KChIP	0.11407	NS
		Kv4.2 + KChIP	DPP6-D484X + KChIP	0.00014	***
		Kv4.2 + KChIP	DPP6-H581X + KChIP	0.04917	*
		DPP6-WT + KChIP	DPP6-T132X + KChIP	0.80484	NS
		DPP6-WT + KChIP	DPP6-K241X + KChIP	0.01544	*
		DPP6-WT + KChIP	DPP6-R322X + KChIP	0.00150	**
		DPP6-WT + KChIP	DPP6-D484X + KChIP	0.77089	NS
		DPP6-WT + KChIP	DPP6-H581X + KChIP	0.65674	NS
		DPP6-WT + KChIP	DPP6-WT	0.00145	**
		DPP6-WT + KChIP	Kv4.2 + KChIP	0.00145	**
C	tau activation	Kv4.2	Kv4.2 + KChIP	<0.00005	****
		Kv4.2 + KChIP	DPP6-T132X + KChIP	0.05139	NS
		Kv4.2 + KChIP	DPP6-K241X + KChIP	0.44295	NS
		Kv4.2 + KChIP	DPP6-R322X + KChIP	0.13569	NS
		Kv4.2 + KChIP	DPP6-D484X + KChIP	0.61861	NS
		Kv4.2 + KChIP	DPP6-H581X + KChIP	0.38369	NS
		Kv4.2 + KChIP	DPP6-WT + KChIP	0.05266	NS
		DPP6-WT + KChIP	DPP6-T132X + KChIP	0.85128	NS
		DPP6-WT + KChIP	DPP6-K241X + KChIP	0.33337	NS
		DPP6-WT + KChIP	DPP6-R322X + KChIP	0.62292	NS
		DPP6-WT + KChIP	DPP6-D484X + KChIP	0.06214	NS
		DPP6-WT + KChIP	DPP6-H581X + KChIP	0.61655	NS
		DPP6-WT	DPP6-WT + KChIP	<0.00005	****
D	tau slow	Kv4.2 + KChIP	Kv4.2	<0.00005	****
		Kv4.2 + KChIP	DPP6-T132X + KChIP	0.48444	NS
		Kv4.2 + KChIP	DPP6-K241X + KChIP	0.01552	*
		Kv4.2 + KChIP	DPP6-R322X + KChIP	0.00784	*
		Kv4.2 + KChIP	DPP6-D484X + KChIP	0.06902	NS
		Kv4.2 + KChIP	DPP6-H581X + KChIP	0.38084	NS
		Kv4.2 + KChIP	DPP6-WT + KChIP	0.08627	NS
		DPP6-WT + KChIP	DPP6-T132X + KChIP	0.14349	NS
		DPP6-WT + KChIP	DPP6-K241X + KChIP	0.01886	*
		DPP6-WT + KChIP	DPP6-R322X + KChIP	0.00877	*
		DPP6-WT + KChIP	DPP6-D484X + KChIP	0.02326	*
		DPP6-WT + KChIP	DPP6-H581X + KChIP	0.16404	NS
		DPP6-WT + KChIP	DPP6-WT	<0.00005	****
		DPP6-T132X + KChIP	DPP6-T132X	<0.00005	****
	tau fast	DPP6-WT + KChIP	DPP6-WT	0	****
		DPP6-T132X + KChIP	DPP6-T132X	<0.00005	****
		Kv4.2 + KChIP	Kv4.2	<0.00005	****
		Kv4.2 + KChIP	DPP6-T132X + KChIP	0,29458	NS

Figure 5.6				Prop>F	
D	tau fast	Kv4.2 + KChIP	DPP6-K241X + KChIP	0,0018	**
	(continued)	Kv4.2 + KChIP	DPP6-R322X + KChIP	4,72132E-5	****
		Kv4.2 + KChIP	DPP6-D484X + KChIP	6,83034E-5	***
		Kv4.2 + KChIP	DPP6-H581X + KChIP	0.03386	*
		Kv4.2 + KChIP	DPP6-WT + KChIP	0.00001	****
		DPP6-WT + KChIP	DPP6-T132X + KChIP	0	****
		DPP6-WT + KChIP	DPP6-K241X + KChIP	0.11292	NS
		DPP6-WT + KChIP	DPP6-R322X + KChIP	0.06349	NS
		DPP6-WT + KChIP	DPP6-D484X + KChIP	0.00007	***
		DPP6-WT + KChIP	DPP6-H581X + KChIP	0.00001	****
E	A slow	Kv4.2 + KChIP	Kv4.2	<0.00005	****
		Kv4.2 + KChIP	DPP6-T132X + KChIP	0.00063	**
		Kv4.2 + KChIP	DPP6-K241X + KChIP	0.00237	***
		Kv4.2 + KChIP	DPP6-R322X + KChIP	0.00032	***
		Kv4.2 + KChIP	DPP6-D484X + KChIP	0.00002	****
		Kv4.2 + KChIP	DPP6-H581X + KChIP	0.00503	*
		Kv4.2 + KChIP	DPP6-WT + KChIP	0.00002	****
		DPP6-WT + KChIP	DPP6-WT	0.00042	***
		DPP6-WT + KChIP	DPP6-T132X + KChIP	<0.00005	****
		DPP6-WT + KChIP	DPP6-K241X + KChIP	<0.00005	****
		DPP6-WT + KChIP	DPP6-R322X + KChIP	<0.00005	****
		DPP6-WT + KChIP	DPP6-D484X + KChIP	<0.00006	****
		DPP6-WT + KChIP	DPP6-H581X + KChIP	0.00002	****
	A fast	Kv4.2 + KChIP	Kv4.2	<0.00005	****
		Kv4.2 + KChIP	DPP6-T132X + KChIP	0.00063	**
		Kv4.2 + KChIP	DPP6-K241X + KChIP	0.00237	**
		Kv4.2 + KChIP	DPP6-R322X + KChIP	0.00032	***
		Kv4.2 + KChIP	DPP6-D484X + KChIP	0.00002	****
		Kv4.2 + KChIP	DPP6-H581X + KChIP	0.00503	*
		Kv4.2 + KChIP	DPP6-WT + KChIP	<0.00005	****
		DPP6-WT + KChIP	DPP6-WT	0	****
		DPP6-WT + KChIP	DPP6-T132X + KChIP	<0.00005	****
		DPP6-WT + KChIP	DPP6-K241X + KChIP	<0.00005	****
		DPP6-WT + KChIP	DPP6-R322X + KChIP	<0.00005	****
		DPP6-WT + KChIP	DPP6-D484X + KChIP	<0.00005	****
		DPP6-WT + KChIP	DPP6-H581X + KChIP	0.00002	****
F	time to peak	Kv4.2	Kv4.2 + KChIP	0	****
		Kv4.2 + KChIP	DPP6-T132X + KChIP	0.33746	NS
		Kv4.2 + KChIP	DPP6-K241X + KChIP	0.01821	*
		Kv4.2 + KChIP	DPP6-R322X + KChIP	0.03452	*
		Kv4.2 + KChIP	DPP6-D484X + KChIP	0.05774	NS
		Kv4.2 + KChIP	DPP6-H581X + KChIP	0.29504	NS
		Kv4.2 + KChIP	DPP6-WT + KChIP	0.00049	***
		DPP6-WT + KChIP	DPP6-T132X + KChIP	0.03459	*
		DPP6-WT + KChIP	DPP6-K241X + KChIP	0.16685	NS
		DPP6-WT + KChIP	DPP6-R322X + KChIP	0.06009	NS
		DPP6-WT + KChIP	DPP6-D484X + KChIP	0.04765	*
		DPP6-WT + KChIP	DPP6-H581X + KChIP	0.11442	NS
		DPP6-WT + KChIP	DPP6-WT	0	****

One-way ANOVA with pairwise analysis between the different conditions was performed and the statistical significance was denoted as asterisks for clarity. NS, not significant, * $P < 0.05$, ** $P < 0.005$, *** $P < 0.0005$, **** $P < 0.00005$

Supplemental Table S5.4 : One-way ANOVA analysis for figure 5.7

Figure 5.7				Prop>F	
A	Imax	Kv4.2	DPP6-dProp	0.85281	NS
		DPP6-WT	DPP6-dProp	<0.00005	****
		DPP6-WT	DPP6-dProp + KChIP	0.00550	*
		Kv4.2 + KChIP	DPP6-dProp + KChIP	0.61595	NS
		DPP6-WT + KChIP	DPP6-dProp + KChIP	0.21388	NS
		DPP6-dProp	DPP6-dProp + KChIP	<0.00005	****
B	ss current/Imax	Kv4.2	DPP6-dProp	0.47434	NS
		DPP6-WT	DPP6-dProp	0.00001	****
		DPP6-WT	DPP6-dProp + KChIP	0.60934	NS
		Kv4.2 + KChIP	DPP6-dProp + KChIP	0.26314	NS
		DPP6-WT + KChIP	DPP6-dProp + KChIP	0.00067	**
		DPP6-dProp	DPP6-dProp + KChIP	0.00045	***
C	tau activation	Kv4.2	DPP6-dProp	0.46562	NS
		DPP6-WT	DPP6-dProp	0.00000	****
		DPP6-WT	DPP6-dProp + KChIP	<0.00005	****
		Kv4.2 + KChIP	DPP6-dProp + KChIP	0.53796	NS
		DPP6-WT + KChIP	DPP6-dProp + KChIP	0.05096	NS
		DPP6-dProp	DPP6-dProp + KChIP	0.00030	***
D	tau slow	Kv4.2	DPP6-dProp	0.62193	NS
		DPP6-WT	DPP6-dProp	0.00053	**
		DPP6-WT	DPP6-dProp + KChIP	0.00050	**
		Kv4.2 + KChIP	DPP6-dProp + KChIP	0.00069	**
		DPP6-WT + KChIP	DPP6-dProp + KChIP	0.00164	**
		DPP6-dProp	DPP6-dProp + KChIP	0.00000	****
	tau fast	Kv4.2	DPP6-dProp	0.18029	NS
		DPP6-WT	DPP6-dProp	<0.00005	****
		DPP6-WT	DPP6-dProp + KChIP	<0.00005	****
		Kv4.2 + KChIP	DPP6-dProp + KChIP	0.00000	****
		DPP6-WT + KChIP	DPP6-dProp + KChIP	0.12112	NS
		DPP6-dProp	DPP6-dProp + KChIP	<0.00005	****
E	A slow	Kv4.2	DPP6-dProp	0.00194	**
		DPP6-WT	DPP6-dProp	<0.00005	****
		DPP6-WT	DPP6-dProp + KChIP	<0.00005	****
		Kv4.2 + KChIP	DPP6-dProp + KChIP	0.00002	****
		DPP6-WT + KChIP	DPP6-dProp + KChIP	0.00000	****
		DPP6-dProp	DPP6-dProp + KChIP	<0.00005	****
	A fast	Kv4.2	DPP6-dProp	0.00194	**
		DPP6-WT	DPP6-dProp	<0.00005	****
		DPP6-WT	DPP6-dProp + KChIP	<0.00005	****
		Kv4.2 + KChIP	DPP6-dProp + KChIP	0.00002	****
		DPP6-WT + KChIP	DPP6-dProp + KChIP	0.00000	****
		DPP6-dProp	DPP6-dProp + KChIP	<0.00005	****
F	time to peak	Kv4.2	DPP6-dProp	0.17101	NS
		DPP6-WT	DPP6-dProp	<0.00005	****
		DPP6-WT	DPP6-dProp + KChIP	<0.00005	****
		Kv4.2 + KChIP	DPP6-dProp + KChIP	0.12696	NS
		DPP6-WT + KChIP	DPP6-dProp + KChIP	0.01530	*
		DPP6-dProp	DPP6-dProp + KChIP	0.00023	***

One-way ANOVA with pairwise analysis between the different conditions was performed and the statistical significance was denoted as asterisks for clarity. NS, not significant, * $P < 0.05$, ** $P < 0.005$, *** $P < 0.0005$, **** $P < 0.00005$

5.8 References

1. T. J. Baldwin, M. L. Tsaur, G. A. Lopez, Y. N. Jan, L. Y. Jan, Characterization of a mammalian cDNA for an inactivating voltage-sensitive K+ channel. *Neuron* **7**, 471-483 (1991).
2. M. Segal, M. A. Rogawski, J. L. Barker, A transient potassium conductance regulates the excitability of cultured hippocampal and spinal neurons. *J Neurosci* **4**, 604-609 (1984).
3. J. E. Dixon *et al.*, Role of the Kv4.3 K+ channel in ventricular muscle. A molecular correlate for the transient outward current. *Circ Res* **79**, 659-668 (1996).
4. P. Serodio, C. Kentros, B. Rudy, Identification of molecular components of A-type channels activating at subthreshold potentials. *J Neurophysiol* **72**, 1516-1529 (1994).
5. B. Rudy *et al.*, Region-specific expression of a K+ channel gene in brain. *Proc Natl Acad Sci U S A* **89**, 4603-4607 (1992).
6. W. F. An *et al.*, Modulation of A-type potassium channels by a family of calcium sensors. *Nature* **403**, 553-556 (2000).
7. M. S. Nadal *et al.*, The CD26-related dipeptidyl aminopeptidase-like protein DPPX is a critical component of neuronal A-type K+ channels. *Neuron* **37**, 449-461 (2003).
8. S. Radicke, D. Cotella, E. M. Graf, U. Ravens, E. Wettwer, Expression and function of dipeptidyl-aminopeptidase-like protein 6 as a putative beta-subunit of human cardiac transient outward current encoded by Kv4.3. *The Journal of physiology* **565**, 751-756 (2005).
9. L. Waldschmidt, V. Junkereit, R. Bahring, KChIP2 genotype dependence of transient outward current (Ito) properties in cardiomyocytes isolated from male and female mice. *PLoS One* **12**, e0171213 (2017).
10. L. Lin *et al.*, DPP6 Loss Impacts Hippocampal Synaptic Development and Induces Behavioral Impairments in Recognition, Learning and Memory. *Front Cell Neurosci* **12**, 84 (2018).
11. C. Liao *et al.*, Loss-of-function variation in the DPP6 gene is associated with autosomal dominant microcephaly and mental retardation. *Eur J Med Genet* **56**, 484-489 (2013).
12. R. Cacace *et al.*, Loss of DPP6 in neurodegenerative dementia: a genetic player in the dysfunction of neuronal excitability. *Acta Neuropathol* **137**, 901-918 (2019).
13. S. Girirajan *et al.*, Refinement and discovery of new hotspots of copy-number variation associated with autism spectrum disorder. *Am J Hum Genet* **92**, 221-237 (2013).
14. C. R. Marshall *et al.*, Structural variation of chromosomes in autism spectrum disorder. *Am J Hum Genet* **82**, 477-488 (2008).
15. S. Cronin *et al.*, A genome-wide association study of sporadic ALS in a homogenous Irish population. *Hum Mol Genet* **17**, 768-774 (2008).

16. M. A. van Es *et al.*, Genetic variation in DPP6 is associated with susceptibility to amyotrophic lateral sclerosis. *Nat Genet* **40**, 29-31 (2008).

17. P. Prontera *et al.*, DPP6 gene disruption in a family with Gilles de la Tourette syndrome. *Neurogenetics* **15**, 237-242 (2014).

18. S. Tanaka *et al.*, DPP6 as a candidate gene for neuroleptic-induced tardive dyskinesia. *Pharmacogenomics J* **13**, 27-34 (2013).

19. M. Alders *et al.*, Haplotype-sharing analysis implicates chromosome 7q36 harboring DPP6 in familial idiopathic ventricular fibrillation. *Am J Hum Genet* **84**, 468-476 (2009).

20. D. B. Ding *et al.*, A novel mutation of dipeptidyl aminopeptidase-like protein-6 in a family with suspicious idiopathic ventricular fibrillation. *QJM* **111**, 373-377 (2018).

21. Y. Kin, Y. Misumi, Y. Ikehara, Biosynthesis and characterization of the brain-specific membrane protein DPPX, a dipeptidyl peptidase IV-related protein. *J Biochem* **129**, 289-295 (2001).

22. S. Y. Qi, P. J. Riviere, J. Trojnar, J. L. Junien, K. O. Akinsanya, Cloning and characterization of dipeptidyl peptidase 10, a new member of an emerging subgroup of serine proteases. *Biochem J* **373**, 179-189 (2003).

23. P. Strop, A. J. Bankovich, K. C. Hansen, K. C. Garcia, A. T. Brunger, Structure of a human A-type potassium channel interacting protein DPPX, a member of the dipeptidyl aminopeptidase family. *J Mol Biol* **343**, 1055-1065 (2004).

24. B. D. Clark *et al.*, DPP6 Localization in Brain Supports Function as a Kv4 Channel Associated Protein. *Front Mol Neurosci* **1**, 8 (2008).

25. M. Kitazawa, Y. Kubo, K. Nakajo, Kv4.2 and accessory dipeptidyl peptidase-like protein 10 (DPP10) subunit preferentially form a 4:2 (Kv4.2:DPP10) channel complex. *J Biol Chem* **290**, 22724-22733 (2015).

26. X. Ren, Y. Hayashi, N. Yoshimura, K. Takimoto, Transmembrane interaction mediates complex formation between peptidase homologues and Kv4 channels. *Mol Cell Neurosci* **29**, 320-332 (2005).

27. E. Zagha *et al.*, DPP10 modulates Kv4-mediated A-type potassium channels. *J Biol Chem* **280**, 18853-18861 (2005).

28. E. Seikel, J. S. Trimmer, Convergent modulation of Kv4.2 channel alpha subunits by structurally distinct DPPX and KChIP auxiliary subunits. *Biochemistry* **48**, 5721-5730 (2009).

29. Y. A. Kaulin *et al.*, The dipeptidyl-peptidase-like protein DPP6 determines the unitary conductance of neuronal Kv4.2 channels. *J Neurosci* **29**, 3242-3251 (2009).

30. H. H. Jerng, Y. Qian, P. J. Pfaffinger, Modulation of Kv4.2 channel expression and gating by dipeptidyl peptidase 10 (DPP10). *Biophys J* **87**, 2380-2396 (2004).

31. E. J. Beck, M. Bowlby, W. F. An, K. J. Rhodes, M. Covarrubias, Remodelling inactivation gating of Kv4 channels by KChIP1, a small-molecular-weight calcium-binding protein. *The Journal of physiology* **538**, 691-706 (2002).

32. J. Maffie, T. Blenkinsop, B. Rudy, A novel DPP6 isoform (DPP6-E) can account for differences between neuronal and reconstituted A-type K(+) channels. *Neurosci Lett* **449**, 189-194 (2009).

33. M. S. Nadal, Y. Amarillo, E. Vega-Saenz de Miera, B. Rudy, Differential characterization of three alternative spliced isoforms of DPPX. *Brain Res* **1094**, 1-12 (2006).

34. H. H. Jerng, P. J. Pfaffinger, Incorporation of DPP6a and DPP6K variants in ternary Kv4 channel complex reconstitutes properties of A-type K current in rat cerebellar granule cells. *PLoS One* **7**, e38205 (2012).

35. H. H. Jerng, P. J. Pfaffinger, Multiple Kv channel-interacting proteins contain an N-terminal transmembrane domain that regulates Kv4 channel trafficking and gating. *J Biol Chem* **283**, 36046-36059 (2008).

36. H. H. Jerng, M. Shahidullah, M. Covarrubias, Inactivation gating of Kv4 potassium channels: molecular interactions involving the inner vestibule of the pore. *J Gen Physiol* **113**, 641-660 (1999).

37. R. Bahring, L. M. Boland, A. Varghese, M. Gebauer, O. Pongs, Kinetic analysis of open- and closed-state inactivation transitions in human Kv4.2 A-type potassium channels. *The Journal of physiology* **535**, 65-81 (2001).

38. R. Bahring *et al.*, Conserved Kv4 N-terminal domain critical for effects of Kv channel-interacting protein 2.2 on channel expression and gating. *J Biol Chem* **276**, 23888-23894 (2001).

39. M. Gebauer *et al.*, N-type inactivation features of Kv4.2 channel gating. *Biophys J* **86**, 210-223 (2004).

40. H. H. Jerng, M. Covarrubias, K+ channel inactivation mediated by the concerted action of the cytoplasmic N- and C-terminal domains. *Biophys J* **72**, 163-174 (1997).

41. M. Pioletti, F. Findeisen, G. L. Hura, D. L. Minor, Jr., Three-dimensional structure of the KChIP1-Kv4.3 T1 complex reveals a cross-shaped octamer. *Nat Struct Mol Biol* **13**, 987-995 (2006).

42. B. Callsen *et al.*, Contribution of N- and C-terminal Kv4.2 channel domains to KChIP interaction [corrected]. *The Journal of physiology* **568**, 397-412 (2005).

43. K. Dougherty, J. A. De Santiago-Castillo, M. Covarrubias, Gating charge immobilization in Kv4.2 channels: the basis of closed-state inactivation. *J Gen Physiol* **131**, 257-273 (2008).

44. R. Bahring, M. Covarrubias, Mechanisms of closed-state inactivation in voltage-gated ion channels. *The Journal of physiology* **589**, 461-479 (2011).

45. J. Barghaan, R. Bahring, Dynamic coupling of voltage sensor and gate involved in closed-state inactivation of kv4.2 channels. *J Gen Physiol* **133**, 205-224 (2009).

46. K. Dougherty, M. Covarrubias, A dipeptidyl aminopeptidase-like protein remodels gating charge dynamics in Kv4.2 channels. *J Gen Physiol* **128**, 745-753 (2006).

47. L. Lin, L. K. Long, M. M. Hatch, D. A. Hoffman, DPP6 domains responsible for its localization and function. *J Biol Chem* **289**, 32153-32165 (2014).

48. H. H. Jerng, K. Dougherty, M. Covarrubias, P. J. Pfaffinger, A novel N-terminal motif of dipeptidyl peptidase-like proteins produces rapid inactivation of KV4.2 channels by a pore-blocking mechanism. *Channels (Austin)* **3**, 448-461 (2009).

49. L. Lin *et al.*, DPP6 regulation of dendritic morphogenesis impacts hippocampal synaptic development. *Nat Commun* **4**, 2270 (2013).

50. T. M. Shih, A. L. Goldin, Topology of the Shaker potassium channel probed with hydrophilic epitope insertions. *J Cell Biol* **136**, 1037-1045 (1997).

51. Z. Batulan, G. A. Haddad, R. Blunck, An intersubunit interaction between S4-S5 linker and S6 is responsible for the slow off-gating component in Shaker K+ channels. *J Biol Chem* **285**, 14005-14019 (2010).

52. A. Cha, F. Bezanilla, Characterizing voltage-dependent conformational changes in the Shaker K+ channel with fluorescence. *Neuron* **19**, 1127-1140 (1997).

53. M. Taglialatela, L. Toro, E. Stefani, Novel voltage clamp to record small, fast currents from ion channels expressed in Xenopus oocytes. *Biophys J* **61**, 78-82 (1992).

54. Y. Amarillo *et al.*, Ternary Kv4.2 channels recapitulate voltage-dependent inactivation kinetics of A-type K+ channels in cerebellar granule neurons. *The Journal of physiology* **586**, 2093-2106 (2008).

55. H. H. Jerng, P. J. Pfaffinger, M. Covarrubias, Molecular physiology and modulation of somatodendritic A-type potassium channels. *Mol Cell Neurosci* **27**, 343-369 (2004).

56. L. M. Mannuzzu, M. M. Moronne, E. Y. Isacoff, Direct physical measure of conformational rearrangement underlying potassium channel gating. *Science* **271**, 213-216 (1996).

57. T. Kalstrup, R. Blunck, Dynamics of internal pore opening in K(V) channels probed by a fluorescent unnatural amino acid. *Proc Natl Acad Sci U S A* **110**, 8272-8277 (2013).

58. J. Zhao, R. Blunck, The isolated voltage sensing domain of the Shaker potassium channel forms a voltage-gated cation channel. *Elife* **5** (2016).

59. G. A. Haddad, R. Blunck, Mode shift of the voltage sensors in Shaker K+ channels is caused by energetic coupling to the pore domain. *J Gen Physiol* **137**, 455-472 (2011).

60. T. Kalstrup, R. Blunck, S4-S5 linker movement during activation and inactivation in voltage-gated K(+) channels. *Proc Natl Acad Sci U S A* **115**, E6751-E6759 (2018).

61. H. Soh, S. A. Goldstein, I SA channel complexes include four subunits each of DPP6 and Kv4.2. *J Biol Chem* **283**, 15072-15077 (2008).

62. N. C. Foeger, A. J. Norris, L. M. Wren, J. M. Nerbonne, Augmentation of Kv4.2-encoded currents by accessory dipeptidyl peptidase 6 and 10 subunits reflects selective cell surface Kv4.2 protein stabilization. *J Biol Chem* **287**, 9640-9650 (2012).

63. T. Hoshi, W. N. Zagotta, R. W. Aldrich, Biophysical and molecular mechanisms of Shaker potassium channel inactivation. *Science* **250**, 533-538 (1990).

64. H. H. Jerng, P. J. Pfaffinger, Modulatory mechanisms and multiple functions of somatodendritic A-type K (+) channel auxiliary subunits. *Front Cell Neurosci* **8**, 82 (2014).

65. J. Barghaan, M. Tozakidou, H. Ehmke, R. Bahring, Role of N-terminal domain and accessory subunits in controlling deactivation-inactivation coupling of Kv4.2 channels. *Biophys J* **94**, 1276-1294 (2008).

66. M. Kitazawa, Y. Kubo, K. Nakajo, The stoichiometry and biophysical properties of the Kv4 potassium channel complex with K+ channel-interacting protein (KChIP) subunits are variable, depending on the relative expression level. *J Biol Chem* **289**, 17597-17609 (2014).

67. S. K. Das, M. Darshi, S. Cheley, M. I. Wallace, H. Bayley, Membrane protein stoichiometry determined from the step-wise photobleaching of dye-labelled subunits. *Chembiochem* **8**, 994-999 (2007).

68. L. Moller, G. Regnier, A. J. Labro, R. Blunck, D. J. Snyders, Determining the correct stoichiometry of Kv2.1/Kv6.4 heterotetramers, functional in multiple stoichiometrical configurations. *Proc Natl Acad Sci U S A* 10.1073/pnas.1916166117 (2020).

69. M. H. Ulbrich, E. Y. Isacoff, Subunit counting in membrane-bound proteins. *Nat Methods* **4**, 319-321 (2007).

Chapter 6 – Discussion

To better understand how specific ion channel complexes function, we investigated the structural details of three channel complexes using fluorescence and electrophysiological techniques. In chapter four, we used a direct structural technique to determine the oligomeric state of the novel ion channel TACAN. Here, we performed single subunit counting experiments on purified channel complexes tethered by the commonly utilized 6His-tag since the traditional single subunit counting technique performed in cells did not result in acceptable bleaching movies. This allowed us to investigate the oligomeric state of this channel, which otherwise would have been impossible due to a poor signal to background ratio in cells. In contrast to this direct structural technique, in the fifth chapter, we used functional measurements and deduced information about the complex formation from the effect of mutagenesis on the complex function. Rather than investigating the number and effect of α-subunits, we took a closer look at the auxiliary subunit DPP6 in Kv4.2 channel complexes and studied the effect of individual domains within the β-subunit on channel gating. Finally, in chapter three, we addressed a very complex problem with a dynamically changing complex assembly. Here, we had to combine both structural and functional techniques to elucidate the structural details of heteromeric Kv2.1/6.4 channels. The effect of entire α-subunits in the heteromeric assemblies was electrophysiologically investigated by our collaborators. This work supported our single subunit counting experiments aimed at identifying the channel complex stoichiometry. To determine the most probable stoichiometric model, we used an analysis method aimed at reducing confirmation bias.

6.1 Investigating the Structure of Kv2.1/6.4 Heteromers

This study was designed to investigate the stoichiometry of Kv2.1/6.4 heterotetramers. Until then it was assumed that all Kv2/KvS heteromers adopt a 3:1 arrangement, like Kv2.1/9.3. While our manuscript was under review, Pisupati et al. published subunit counting data on Kv2.1/6.4 that was undistinguishable from our own data but interestingly, they came to a different conclusion. This highlighted the need for a more rigorous subunit counting analysis method that would limit confirmation bias and distinguish which stoichiometry is the most probable.

Compared to typical publications presenting subunit counting data, we collected far more data points and applied the new relative weighted likelihood model selection method to confidently determine a stoichiometric model for Kv2.1/6.4 channels. Importantly, we also did not reject spots that featured more than the theoretically possible number of photobleaching steps. These spots originate from colocalized channels within a diffraction limited spot and are crucial for unbiased analysis of the step frequency histogram, since removing them would misrepresent the lower number of bleaching steps. The inclusion of colocalization makes it possible to directly compare the likelihoods of different models. This is key, since a thorough analysis should not only demonstrate that one model describes the data well, but that other models fit less well. As a result of this effort and opposed to previously published Kv2/KvS arrangements in a 3:1 stoichiometry, we showed that the stoichiometry of heteromeric Kv channels with silent subunits is more flexible and that under physiological conditions Kv2.1 and 6.4 express in a 2:2 stoichiometry.

The rigorous analysis of subunit counting data together with the complementary electrophysiological investigation on concatemeric channel complex resulted in a convincing architectural channel model where Kv2.1 and 6.4 subunits are arranged in an alternating fashion. The possibility of a 2:2 stoichiometric arrangement with alternating Kv2/KvS subunits was not entirely surprising considering that Kv channels are thought to assemble as dimers of dimers (1). While subunit counting experiments cannot distinguish between functional and electrically silent channels, concatemers elucidate the functionality of fixed arrangements of subunits. This showed that channels with more than three silent subunits are not functional. However, subunit counting data demonstrated that at higher Kv6.4 expression levels, these non-functional channels might still traffic to the plasma membrane. How these channels would form is not understood given that the tetramerization domains of Kv6.4 subunits are not self-compatible and don't interact with each other in the ER. Indeed, expressing Kv6.4 in the absence of Kv2 subunits, leads to retention in the ER. An ER retention signal is not present in KvS subunits, suggesting that they might not traffic forward due to misfolding. Our observation of possible 1:3 Kv2.1/6.4 heterotetramers in the plasma membrane at high Kv6.4 expression levels would then propose that a single Kv2.1 subunit rescues Kv6.4 misfolding and allows for channel arrangements with

three Kv6.4 subunits. However, allowing mixed population with one, two or three Kv6.4 subunits per channel complex added an additional variable to the analysis which might explain the better fit without being physiological relevant.

Biasing the stoichiometry in the opposite direction towards Kv2.1 subunits showed that Kv2.1/6.4 channels with a 3:1 arrangement are functional but unlikely to form under physiological conditions. Using concatemers with a single silent subunit verified that these 3:1 arrangements are functional. These channels exhibited gating properties in between Kv2.1 homotetramers and heterotetramers comprising two Kv6.4 subunits, illustrating that incorporation of Kv6.4 subunits progressively alters channel activation and inactivation. In cells expressing individual subunits as opposed to concatemers, a 3:1 arrangement could not be observed because the cDNA ratio has to be biased towards Kv6.4 (which results in a 2:2 arrangement) since otherwise Kv2.1 homotetramers overshadow the contribution of heteromers in the ensemble. However, subunit counting experiments at equal RNA ratios are possible when only the silent subunit is fluorescently labeled and homomeric Kv2.1 channels remain invisible. Under these conditions, our subunit counting data suggests that the number of Kv6.4 subunits is not decreased and that the 2:2 heteromeric channel stoichiometry remains unchanged. Comparing our results with Kv2.1/9.3 heteromers shows that KvS subunits feature distinct preferences for specific stoichiometries and that Kv2/KvS arrangements have variable stoichiometries depending on the KvS subunit.

We consistently observed colocalized channels within a diffraction limited spot (~ 300 nm diameter). We argued that channels are stochastically distributed and that there is a 10 – 20 % probability of finding two channels in a diffraction limited spot. However, it would be possible that channels at this expression level start to interact with each other and therefore are observed more often as colocalized. To unequivocally reject the possibility of a direct interaction of channels that results in the observation of colocalized channels, one could perform Förster resonance energy transfer (FRET) experiments to determine the distance between two channels. If these Kv channels are found to interact directly, it would be worthwhile to further study their function.

Our work was limited to heterologous expression systems and might not represent the full picture. As for Kv4.2 channel complexes, native Kv2.1/6.4 channels in neurons are further influenced by auxiliary subunits which were not present in our study. The β-subunit KCNE5, which is also expressed in the brain, has been shown to modulate Kv2.1 homomers and 2.1/6.4 heteromers in distinct ways (2). Since KCNE5 modulates the biophysical properties of Kv2.1/6.4, but not of Kv2.1 homomeric, channels significantly, it would be intriguing to investigate the effect of KCNE5 on the functionality of Kv2.1/6.4 arrangements in a 1:3 stoichiometry. Our results on concatemers showed, that these 1:3 stoichiometric arrangements are non-functional, while our subunit counting experiments did not exclude the possibility of expressing such channels in the plasma membrane. It could be yet another cellular mechanism to finetune channel function if a small population of Kv2.1/6.4 channels in a 1:3 arrangement becomes functional in the presence of an auxiliary subunit, making them physiologically relevant. David et al. also studied the interaction between the α- and β-subunits and performed FRET experiments between Kv2.1/6.4 α-subunits and KCNE5 (2). Although FRET experiments can be used to study stoichiometries (3, 4), David et al. did not investigate the Kv2.1:KCNE5 stoichiometry. To better understand by which mechanisms KCNE5 modulates Kv2.1 and Kv2.1/6.4 channels, it would be interesting to examine if coexpression of Kv6.4 alters the Kv2.1:KCNE5 stoichiometry. Furthermore, it remains unknown, if and how KCNE5 affects the Kv2.1/6.4 stoichiometry. Considering that KCNE5, like DPP6, traffics to the plasma membrane in the absence of Kv2.1 or Kv2.1/6.4 and does not rescue Kv6.4 retention in the ER, its presence is more likely to affect channels that are not retained in the ER but expressed in the plasma membrane (2). In the plasma membrane, channels are already fully assembled, so that it is unlikely that KCNE could alter their stoichiometry by actively exchanging subunits. However, when mixed populations of heteromeric channels with different stoichiometries traffic to the plasma membrane, KCNE could distinctly affect the retrograde trafficking of one of the populations. As a result, one of the populations might be more (or less) likely to remain in the plasma membrane, so that it is more (or less) likely to observe this stoichiometry.

Another limitation of the subunit counting technique in general is the requirement for very low expression so that single channels can be optically resolved. This, however, is not

representative of Kv2.1 expression in neurons. Here, Kv2.1 channels have been reported to largely localize in non-conducting clusters in the plasma membrane (5). These clusters are also observed when Kv6.4 (and KCNE5) is coexpressed in HEK cells (2) but it remains unknown if and how these clusters influence heteromeric channel functionality, stability and stoichiometry. SSC only studies what expresses regardless of the functionality whereas electrophysiology investigations are blind to electrically silent channels and non-conducting clusters. Obtaining single molecule structural and functional data simultaneously would be a major improvement, especially when channels exist in such a heterogenous ensemble. Ideally such studies should be performed in native cells that express possible auxiliary subunits. But due to being limited to low expression, traditional SSC cannot be performed successfully in neurons.

SSC in *Xenopus* oocytes is accompanied by specific challenges. SSC in HEK cells have the advantage that they can be fixed in formaldehyde to eliminate movement of proteins which is a key factor for sufficient signal quality. However, when we expressed Kv2.1/6.4 in HEK cells, as shown in chapter four, the signal to background ratio was poor due to background fluorescence originating from untrafficked labeled subunits. This was also a major problem when expressing TACAN in HEK or CHO cells, where a significant amount of TACAN did not traffic to the plasma membrane but remained in the intracellular of the cell. In the case of TACAN, we hypothesized that the intracellular TACAN is located in the ER (discussed further in 6.2). To avoid high background fluorescence, we expressed Kv2.1/6.4 in oocytes. However, fixing them in formaldehyde similar to HEK cells was not successful. To access the plasma membrane, one needs to first mechanically remove the vitelline membrane that surrounds the oocyte and gives it its stability. Once this membrane is removed, oocytes become extremely fragile and difficult to handle making it impossible to fixate them at this stage. In addition to the lateral movement of fluorescent spots, unfixed proteins in oocytes also diffuse away from the focal plane. The oocyte's plasma membrane is highly invaginated so that proteins observed in TIRF can diffuse laterally as well as in and out of the focal plane. These invaginations also result in a non-uniform focus across the field of observation so that entire areas that are out of focus have to be excluded from the analysis. In fact, a lot of bleaching movies recorded from oocytes have to be rejected due to poor focus or movement of fluorescent spots.

SSC experiments would benefit from an improved signal to background ratio (SBR) in fluorescent recordings. This can be achieved by using brighter fluorophores. Unfortunately, we did not explore the possibility of using mNeonGreen, a smaller and approximately three times brighter fluorescent protein (FP) compared to GFP, which is not a *Aequorea Victoria* GFP variant but is derived from *Branchiostoma lanceolatum* (6, 7). Improving the maturation rate of GFP would also improve SSC experiments, as it would increase the probability of fluorescence (p_f). Apart from the super-folder monomeric GFP, the D'Avanzo laboratory tested other quickly maturing fluorescent proteins (FPs), of which none resulted in an significantly improved p_f value compared to sfmGFP (Y. Lussier, personal communication, August 2020). Although other publication reported probabilities of fluorescence of up to 80 % (8-11), we repeatedly determined fluorescence probabilities around 50 % (12, 13). Rather than using brighter FPs or FPs with higher probabilities of fluorescence, optimized organic fluorophores could be used to label the protein of interest since these fluorophores are typically brighter than GFP. Several approaches could be employed to achieve protein labeling with these smaller dyes. A common method utilizes thiol reactive fluorophores, which we used previously with purified proteins (14) and in chapter five for ensemble fluorescence measurements of overexpressed Kv4 channels. The proper choice of thiol reactive fluorophores is crucial to reduce the risk of introducing additional background fluorescence. For example, tetramethylrhodamine maleimide (TMRM) easily passes the plasma membrane in mammalian cells leading to background fluorescence from the intracellular of the cell, whereas methanethiosulfonate sulforhodamine (MTSR) does not penetrate mammalian cells (15). Additionally, endogenous proteins with accessible cysteines can also be labeled, which leads to unspecific labeling. This can be reduced by blocking these cysteines with the non-fluorescent 3-Mercaptopropionic acid (MPA) prior to expressing the protein of interest. The thiol (sulfhydryl) group of MPA forms a disulfide bond with the thiol group of the cysteine sidechain, thereby decreasing the number of endogenous cysteines that can be linked to a thiol-reactive fluorescent label. However, depending on the time between MPA blocking and the experiments, protein recycling and newly expressed endogenous membrane proteins still lead to unspecific labeling that could be too high for single molecule experiments. Alternatively to thiol-reactive fluorescent

labels, more specific labeling techniques, such as unnatural amino acid based click chemistry, could be used (16).

A second approach to increase the SBR in fluorescent recordings, is to reduce background fluorescence. This can be achieved by expressing the membrane protein of interest in *Xenopus* oocytes rather than smaller cells. In oocytes, the ER is located further away from the plasma membrane compared to smaller cells, so that fluorescently tagged untrafficked proteins trapped in the ER are not excited in TIRF illumination. Additionally, the SBR in SSC experiments performed in *Xenopus* oocytes can be drastically improved when the plasma membrane of the dark animal pole, rather than the bright vegetal pole, is observed. Here, the pigmented cortex shields from background fluorescence. Alternatively, as presented in chapter four, *ex vivo* experiments can be performed on purified proteins to eliminate background fluorescence originating from untrafficked proteins. If, however, undisrupted native assemblies, e.g. in neurons, are to be investigated, zero-mode waveguides (ZMWs) could be used (17). These aluminum-based nanostructures are cylindrical holes of 30 to 300 nm diameter in a 50 to 200 nm tick metallic layer mounted onto a glass substrate (17). ZMWs with hole sizes *d* don't propagate wavelengths above the critical wavelength $\lambda_c = 1.7d$. Instead, the light is confined to a very small volume (in the order of 0.03-100 x 10^{-21} L) as the intensity decreases exponentially at the glass surface (18, 19). Richards et al. used 150 nm diameter ZMWs for SSC experiments and were able to spatially isolate membrane complexes in wells even at high protein densities (19). Using 150 nm holes and 488 nm light as excitation, which is above the critical wavelength, allowed them to eliminate any background from the cell. Unfortunately, the use of ZMWs remains limited since nanofabrication techniques are expensive and not readily available. However, it is promising that brighter FPs and more specific labeling techniques for optimized organic fluorophores are developed alongside improvements on reducing background fluorescence in order to improve SSC data.

Our rigorous analysis method of weighted maximum likelihoods is applicable to any subunit counting data as shown in chapters three and four and we anticipate that our work will serve as a guideline to researchers to solidify their analysis and stoichiometric model selection. Manual data analysis is heavily biased towards the "good looking" fluorescent spots and time traces, introducing significant observer bias. Using automated spot detection and bleaching step fitting

algorithms like PIF, the Progressive Idealization and Filtering software we used to analyze our bleaching movies, allows for bigger data sets to be analyzed and eliminates user bias. However, programs like PIF only produce bleaching step frequency histograms, which need to be analyzed and interpreted by the researcher. This subsequent step easily introduces confirmation bias, i.e. the tendency to favor a model that best fits with one's prior believes, which can be avoided by rigorously analyzing data sets with standardized methods. Published subunit counting data are often limited to a few hundred spots, dismiss colocalized spots, overestimate the probability of fluorescence and don't investigate other possible stoichiometries. Our SSC data analysis, presented in chapter three, offers a guideline to avoid these pitfalls and illustrates the need for sufficient data points and the inclusion of spots originating from colocalization. Under these conditions, the most probable stoichiometry can even be determined when the probability of fluorescence is allowed to vary. Importantly, the presented weighted likelihood method interrogates several possible stoichiometries and mixtures thereof and mathematically determines the confidence of each model. Furthermore, the addition of the presented model selection method to existing automated analysis programs would make the interpretation of SSC data much more reliable and objective. This could even include a feature that determines how many more data points need to be collected in order to confidently choose a stoichiometric model.

6.2 Investigating the Oligomeric State of TACAN

This study was designed to investigate the oligomeric state of the novel ion channel TACAN by single subunit counting. Because of the high background fluorescence observed in cells, these experiments were performed on purified proteins. We used a previously described functionalization technique to covalently link Ni-NTA to the surface of glass coverslips and extended its use to SSC experiments.

Here, we present, for the first time, a structural investigation of TACAN. Until now, no structural data for this new ion channel was available. Based on hydrophobicity, it is predicted that each subunit features six transmembrane helices but no crystal or electron microscopy structure is available yet. Utilizing the 6His-tag that was used to purify the protein and Ni-NTA

functionalized coverslips, we performed SSC experiments *ex vivo*. Using the same analysis approach as described in chapter three, we reported variable oligomeric states that depended on the fraction of the size exclusion chromatography. According to our analysis, TACAN channels are tetramers but unstable when detergent-solubilized. This instability is not entirely surprising considering that mechanosensitive channels are often highly sensitive to specific hydrophobic interactions between the plasma membrane and the transmembrane helices. For example, phospholipid alkyl sidechains are located in distinct pockets formed by transmembrane helices of MscS, a mechanosensitive channel from E. coli (20), and between each MscS subunit, a phospholipid headgroup binds tightly to the extracellular T2-T3 loop (21). Detergent molecules interfere with these interactions and replace a majority of lipids surrounding the channel. At the same time, solubilizing the channel in detergent molecules changes the lateral pressure on the channel, which might be necessary to keep it stable (22). This drastic change in environment could then result in unstable channel complexes.

The stability of an ion channel depends on noncovalent interactions between subunits. In addition to interactions between the transmembrane helices of different subunits, TACAN channels could be further stabilized by intra- or extracellular domains if these domains interact with each other. Interestingly, TACAN is predicted to feature a 135 amino acids long intracellular N-terminal which might help stabilizing the complex. Similarly, T1 domains that regulate Kv channel assembly also increase Kv channel stability by increasing the number of non-covalent inter-subunit interactions. It is currently unknown if the N-terminal domain of TACAN, similarly to the tetramerization T1 domain in Kv channels, is involved in channel stability and assembly. Although the T1 domain and the N-terminal sequence of TACAN show no sequence homology, and are therefore predicted to have distinct structures, the cytoplasmic N-terminal domain of TACAN could be long enough to assembles, like T1 domains, as a “hanging gondola” below the ion channel (23). It remains to be tested, if the N-terminal TACAN domains interact with each other and self-assemble. In addition to intersubunit interactions, auxiliary subunits potentially contribute to stabilizing ion channels. DPP6 subunits potentially stabilize Kv4 channel complexes by acting as brackets that interact with themselves as well as with the channel positioned at the center. It is currently unknown if native TACAN channels are stabilized by auxiliary subunits and

which intersubunit interactions hold the complex together. Unfortunately, SSC experiments in physiologically more relevant environments, i.e., in cells, were not possible, so it remains uncertain if native TACAN channels form obligatory tetramers in the plasma membrane or if more flexible oligomeric states are possible too. However, considering that other ion channels, like potassium channels, have stable oligomerization states in the plasma membrane and misfolded proteins remain in the intracellular compartment of the cell, we propose that the highest oligomeric state purified and observed in out SSC experiments, i.e. the tetrameric state, is the native state found in the plasma membrane.

The cause and purpose of the intracellularly localized TACAN remain uncertain. As for Kv6.4, when we expressed TACAN in cells, we observed a significant amount of channels in the intracellular compartment. TACAN seems to be retained in the ER. While Kv6.4's retention is suggested to be caused by misfolding, we hypothesized that TACAN's retention might be due to a dilysine motif at the C-terminus. However, our analysis does not exclude that channels are prohibited from anterograde trafficking due to misfolding or improper assembly, resulting in distinct localized populations in the PM and intracellular compartment with different oligomeric states. Additionally, we have seen, in the context of chapter three and five, that many ion channels show improved trafficking when coexpressed with other alpha or auxiliary subunits. Kv6.4 traffics to the plasma membrane in the presence of Kv2.1, while Kv4.2's expression in the plasma membrane is enhanced by coexpression with KChIP and DPP6. In a similar fashion, TACAN's trafficking could be affected by other subunits that have not been identified yet and that are missing in heterologous expression systems. Furthermore, we observed the formation of TACAN clusters. Opposed to non-conducting Kv2.1 clusters that are observed in the plasma membrane, we found TACAN clusters to be localized in the intracellular space. It remains unknown if these clusters originate from endosomes that recycle plasma membrane TACAN or if other organelles are involved and if TACAN localization in these clusters serves a distinct functional role.

One important limitation of performing SSC of purified proteins from bacterial expression systems is the absence of post-translational modifications. These modifications could be important for protein stability, its conformation and interaction with other macromolecules, but

it is unclear how post-translational modifications influence TACANs assembly. Expression in mammalian cell lines mimics native protein processing more closely than recombinant expression in bacteria. When only small amounts of protein are required, i.e. for SSC, it could be advantageous to purify the protein from mammalian cell cultures, which might increase channel stability and represents the assembly in a more physiological way.

Another important limitation of the presented work is the missing functional evaluation of the purified protein. As opposed to studying Kv2.1/6.4 heteromers with two complementary approaches, the presented research on TACAN solely depends on SSC data. However, TACANs functionality has been previously demonstrated and we only slightly modified the protocol that our laboratory developed to purify TACAN for functional studies in the original publication (24). This originally published purification was performed in FC14 and purified channels were reconstituted into small unilamellar lipid vesicles to be functionally tested in planar lipid bilayers. It is possible that the reconstitution into a lipid environment helps stabilizing the channel complex. For the SSC experiments, we followed the purification protocol in FC14, but TACAN solubilized in FC14 did not bind efficiently to Ni-NTA functionalized coverslips. Hence, we switched to DDM in the final size exclusion chromatography to improve tethering efficiencies. The protein did not precipitate, but it is unclear if the switch of detergents disrupts the integrity of the channel and if lipids are necessary to keep the channel assembly intact.

The possibility of unstable channel complexes has important implications for researchers aiming at solving the channel structure. Since we only slightly modified the purification protocol described in the publication that first described TACAN, it is likely that other researchers follow the same instructions. Especially when the channels are purified from membrane fractions that include the plasma membrane as well as other organelle membranes and the channel is not subsequently reconstituted into lipid vesicles, but remains detergent-solubilized, heterogeneous and/or unstable channel assemblies could exist and lead to mixed oligomeric arrangements. Avoiding heterogeneous mixtures of different assemblies is a key in order to produce high quality EM structures. Reconstituting the mechanosensitive channel into lipid nanodiscs could help stabilize the protein complex in a more native environment, while still being able to determine

the structure (21, 25). Alternatively, amphipols, amphiphilic surfactants, can stabilize membrane proteins in a detergent free environment (26).

A potential advantage of SSC experiments performed on purified proteins is the possibility to efficiently label the protein with brighter fluorophores. Since the protein of interest is isolated from the cell, it is easy to specifically label it with optimized organic fluorophores without introducing unspecific labeling. Thiol-reactive fluorophores, like Alexa-maleimides, can be used when the protein has not more than one, endogenous or engineered, accessible cysteine. Unfortunately, TACAN possesses eight cysteines of which only three are predicted to be inaccessible, i.e., positioned in the transmembrane helices. Having potentially five cysteines per subunit that are fluorescently labeled, would make it challenging to resolve bleaching events and accurately count steps even with an automated analysis software, especially when the subunits arrange as tetramers.

The use of Ni-NTA functionalized coverslips is not limited to SSC experiments but rather lends itself for studying dynamic movements in purified proteins. I initially established this technique in our laboratory to study the subunit specific movements of the ionotropic glutamate receptor AMPA, which is responsible for the fast excitatory transmission in the central nervous system, and a soluble protein, the enzyme fructose-bisphosphate aldolase, involved in glycolysis. While we did not follow through with these projects, they show that Ni-NTA functionalized coverslips expand the toolkit to study structure function relations on a single molecule level. This is especially valuable when studying protein complexes that have asymmetric arrangements (like AMPA) and whose subunits might undergo distinct conformational changes that would average out in ensemble measurements.

As an alternative to separate experiments, simultaneous SSC and electrophysiological experiments could study the functionality of specific stoichiometric arrangements. For Kv2.1/6.4, we performed these structural and functional experiments separately. Here, we observed potential 1:3 assemblies in the plasma membrane using the SSC technique and only electrophysiological investigation of the respective concatemer showed that these channels were electrically silent. While studies on concatemeric constructs are valuable to study the

functionality of specific internal subunit arrangements (e.g. adjacent or alternating), they don't investigate native complexes assembled by individual subunits. When only the function and oligomeric state, but not the internal arrangement of subunits, is of interest, simultaneous structural and functional investigations could provide all the necessary data. In order to obtain structural and functional data of ion channels like TACAN and Kv2.1/6.4 simultaneously, one could record the single channel currents in planar lipid bilayers and perform SSC at the same time. However, to resolve single channel currents, only very few channels can be present in the membrane, drastically limiting the size of the data set. If at all possible, obtaining even just a few hundred fluorescent spots that can be analyzed for SSC would require months of experiments. Advances in automated high throughput bilayer formation, as for example developed by Ionera (Freiburg, Germany), would drastically accelerate such a project. Additionally, the analysis algorithm would have to be extended to include a powerful spot tracking feature since channels are expected to diffuse in the bilayer. Such tracking algorithms are already used for single molecule tracking (27-30). A simultaneous SSC and electrophysiology approach would be helpful for investigating TACAN, for which we hypothesized that functional channels are tetrameric, but also purified trimeric and dimeric channels that might be nonfunctional. Simultaneous experiments could then help solve if four subunits are necessary to form an ion channel with a central ion conducting pore (as it is the case for Kv channels) or if each subunit forms a distinct ion conducting pore (as has been reported for voltage gated proton channels (31-33)), so that lower oligomeric arrangements might also be conducting.

6.3 Investigating the Function of Distinct DPP6 Domains

The research described in chapter five was designed to investigate the effect of distinct extracellular regions of the auxiliary subunit DPP6 on Kv4.2 channel gating. Deletion of the entire extracellular domain led to drastically altered channel properties, suggesting that the extracellular part is involved in channel modulation. We studied which part of the extracellular domain confers the modification by progressively truncating the DPP6 extracellular domain and recording macroscopic currents.

Until now, the effect of the approximately 700 amino acids long extracellular domain of DPP6 on channel gating remained unknown. It was previously proposed that this part of the auxiliary subunit is involved in cell adhesion by interacting with the extracellular matrix (EM) (34). It is reasonable to assume, that the interaction of DPP6 with the EM as well as with the Kv4 subunits stabilizes Kv4 channels in the plasma membrane. Additionally, Lin et al. demonstrated that properly folded ß-propeller domains are important for DPP6 trafficking to the plasma membrane (35). Based on the research presented in chapter five, we propose, that the β-propeller additionally has an important modulatory effect on gating kinetics of the Kv4 channel complex.

Our findings suggest that DPP6 interacts with and modulates Kv4 channels through several interaction sites. While all DPP6 isoforms are suggested to interact with Kv4's VSD through the transmembrane helix (36), DPP6 isoforms with the N-terminal MNQTA motif also interact with the internal channel pore and confer NTI when Kv4's N-termini are sequestered by KChIP (37). In addition to these studies, our results show that the extracellular domain interacts with the α-subunit and destabilizes the open channel through a mechanism that has not been further investigated yet. Our electrophysiological interrogation of progressively C-terminally truncated DPP6 subunits demonstrated a strong link between the length of DPP6's extracellular domain, peak current and accelerated activation and inactivation kinetics. More specifically, our results showed that the second half of DPP6's propeller domain is responsible for drastically accelerated inactivation in the presence and absence of KChIP. Based on the crystal structure of the isolated extracellular domain, we proposed that a stable β-propeller domain and possibly DPP6 dimer formation are key determinants for altered channel properties. We hypothesized that the formation of a multimeric DPP6 extracellular domain leads to a positioning of DPP6's extracellular domain directly on top of the ion channel whereas truncated DPP6 variants fail to multimerize and therefore establish a more flexible conformation that does not destabilize the open channel state as efficiently. How the multimerization of DPP6 subunits confers its channel modulating action remains unanswered, but the close interaction between the DPP6 subunit and S4 voltage-sensing helix demonstrated by VCF experiments hints at an allosteric effect on channel gating properties. Our research lays a foundation to further identify interaction sites of DPP6's

extracellular domain and Kv4 and the underlying structural determinants for DPP6 dependent channel gating modifications.

Although we did not study the stoichiometry or subunit arrangement of Kv4/DPP6 channel complexes as we did for Kv2.1/6.4 heteromeric channels, we propose that only the proper positioning of DPP6 subunits in regard to Kv4.2 subunits elicits the maximal effect as a result of specific interactions that allosterically modulate the channel. Similarly, we saw in chapter three that the specific arrangement of distinct Kv2.1 and Kv6.4 subunits is of great importance for channel function. There, we showed that Kv6.4 subunits cannot be positioned adjacent to each other in order for the heteromeric channel to be functional. While concatemeric studies of Kv2.1/6.4 channels helped to identify the functional arrangement of the heteromeric channel, a comparable approach of concatemeric Kv4/DPP6 channels illustrated that Kv4/DPP6 channel complexes preferentially form 4:4 assemblies (38). Kv4/DPP10 channel complexes, on the other hand, are suggested to assemble in a 4:2 arrangement as investigated by SSC experiments (39). This is interesting, since both studies suggest that Kv4/DPPL arrangements form by adding DPPLs as multiples of dimers to the channel complex.

To my knowledge, it has not been studied how dimeric or tetrameric DPPL subunits are arranged in respect to Kv4 subunits but several scenarios are possible. Since we and others showed that DPP6 is positioned in proximity to the voltage-sensing S4 helix (40), the extracellular domain is likely to be positioned over the voltage-sensing domain. As shown below, two DPPL subunits could interact with Kv4 tetramers in at least two ways. If each DPPL subunit interacts with Kv4 subunits in a symmetric way, the propeller loops would be positioned diagonally over the channel pore (figure 6.1, left bottom). This arrangement is further supported by studies on concatemers comprising two Kv4 and one DPP6 subunit resulting in a 4:2 channel arrangement where opposite Kv4 subunits are linked to DPP6. Similarly to Kv6.4 in Kv2.1 channel complexes as well as KChIP in Kv4 channel complexes (41), these 4:2 Kv4/DPP6 concatemeric channels have been shown to shift channel properties progressively compared to concatemers comprising one subunit of Kv4 and DPP6 each (resulting in a 4:4 channel arrangement) (38). The diagonal arrangement of 4:2 Kv4/DPP6 concatemeric channels is similar to the one we observed in chapter three for Kv2.1/6.4 channels. Alternatively to a symmetric diagonal arrangement, the two DPPL

subunits could have distinct orientations and interactions with Kv4, so that the propeller loops are positioned more towards the periphery of the ion conducting pore and the entire channel complex becomes asymmetric (figure 6.1, left top).

Likewise, channels with four DPPL subunits could be arranged in two different ways. Since the soluble extracellular domain crystallized as dimers, it is plausible that four DPPLs interact in a dimer of dimer fashion so that the two pairs of propeller loops are positioned on either side over the channel pore (figure 6.1, right top). Alternatively, four pore loops could interact and be positioned directly on top of the ion conducting pore (figure 6.1, right bottom). This second scenario would feature additional inter-subunit propeller loop interactions that differ from the previously published interactions determined by x-ray crystallography (42). This however, would mean that the interaction sites between DPPL and Kv4 subunits are identical for all intersubunit interaction sites. Furthermore, this arrangement would make it more likely that 4:1 or 4:3 Kv4/DPPL assemblies exist. Then, similarly to Kv6.2 subunits which progressively altered Kv2 properties, DPPLs might alter channel properties gradually with every DPP6 subunit rather than with every DPP6 dimer added to the complex. However, it remains uncertain if these 4:1 and 4:3 arrangements exist and modulate channel properties progressively.

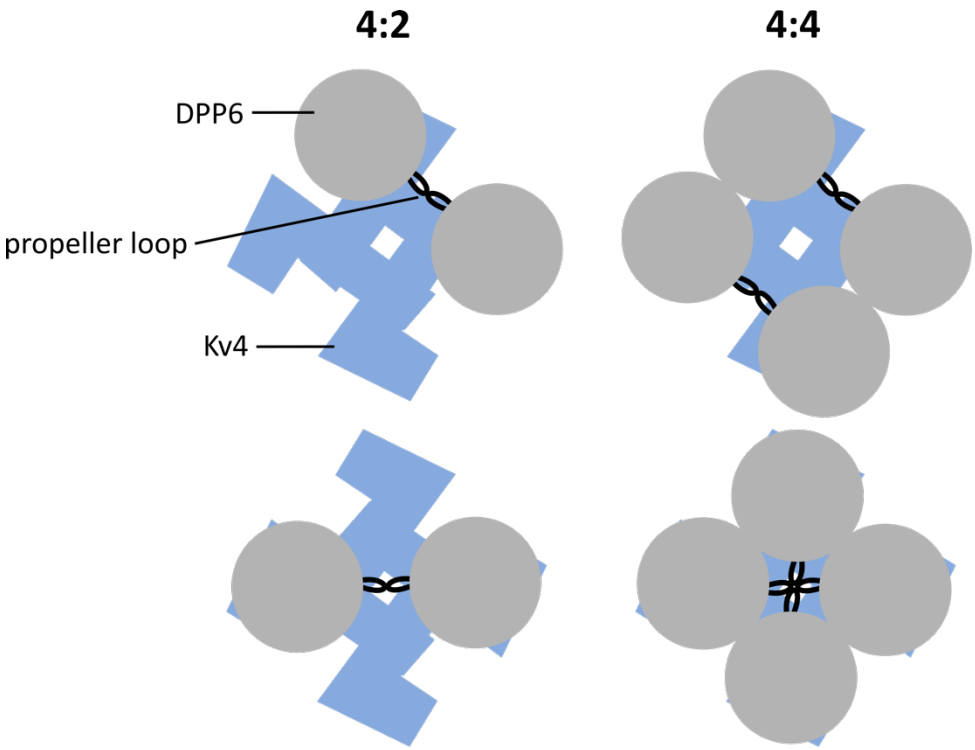

Figure 6.1 Kv4/DPPL arrangements
Cartoon representation of different Kv4/DPPL stoichiometries and symmetries viewed from the extracellular. Four Kv4 subunits represented in blue with two (left) and four (right) DPPL subunits with distinct (top) and identical (bottom) interaction sites between DPPL and Kv4 subunits.

Identifying specific interaction sites between Kv4 subunits and the extracellular DPP6 domain would be of great value to better understand the relative position of DPP6 as well as the structural detail of the open-state channel destabilization mechanism. While we were working on the research presented in chapter five, we tried to identify possible interaction sites between DPP6's extracellular domain and Kv4 subunits using VCF. As shown in chapter five, we observed that the presence of DPP6's extracellular domain can be visualized by labeling the top of the voltage sensor domain at position A288C and following the voltage-pendent fluorescence changes that are only visible when DPP6 is present. We hypothesized that the reverse is possible too and that labeling of DPP6 at a position close to the S4 would report the voltage-induced movement of the S4 helix thereby identifying residues in the extracellular domain that are in proximity to the top of this helix. We tested four positions in the β-propeller loop, three positions in the α/β-hydrolase and one position in the first quarter of the β-propeller domain. Unfortunately, none of these positions resulted in a sizeable fluorescence change. The absence of a fluorescence change,

however, should not be interpreted as a lack of interaction. The fluorophore is sensitive to its chemical environment and the absence of a fluorescence change signal can have several reasons. First, the fluorophore might not encounter a quencher or move together with the quencher, so that the direct environment remains the same. Secondly, the fluorophore could move between different environments without resulting in a fluorescence change. It is important to only interpret the presence of a fluorescence change rather than basing conclusions on the absence of a signal. Obviously, there are many more positions to be tested in the approximately 700 amino acid long extracellular domain. In the future, this search for potential labeling and interaction sites could be aided by computational models of Kv4/DPP6 complexes (43).

The presented study was limited to investigating an ensemble of channel complexes, but studying single channels could help solve some unanswered questions. First, we do not know if DPP6 truncations effect the channel complex stoichiometry. Although we hypothesized that truncated DPP6 subunits fail to dimerize, we did not perform any experiments that would test this idea. Förster resonance energy transfer (FRET) experiments are well-suited to study the distance between molecules. The FRET technique uses two different fluorophores as energy donor and acceptor. The basis for the energy transfer is the spectral overlap of the emission of the donor and the excitation of the acceptor and the donor-acceptor distance dependence of the energy transfer efficiency (44). Performing FRET experiments on truncated DPP6 subunits and comparing the obtained distances between each truncated DPP6 subunit to the ones of the full-length DPP6, could help verify our hypothesis. We also do not know if the potentially altered DPP6 stoichiometry caused by truncated extracellular domains might affect KChIP binding. This would be interesting to investigate as it would suggest a long-range allosteric effect since we manipulate the extracellular domain, whereas KChIP is located intracellularly and does not interact directly with DPP6. For now, we cannot exclude the possibility that DPP6 truncations result in conformational changes of the α-subunit that might alter KChIP binding. Therefore, SSC experiments on truncated DPP6 subunits in Kv4.2 as well as experiments on KChIP in truncated DPP6/Kv4 channel complexes could help to better understand the effect of shorter DPP6 extracellular domains on the stoichiometry of the channel complex. Moreover, these experiments

could illustrate if DPP6 truncation results in mixed populations of Kv4 channels with and without DPP6 or KChIP.

Another unanswered question concerns the increased macroscopic currents in the presence of longer DPP6 variants. At this point, it is worth discussing the effect of accelerated inactivation kinetics on the peak currents. Longer DPP6 truncations activated and inactivated faster than shorter truncations. As mentioned before, an acceleration in inactivation is expected to overtake activation at an earlier time and therefore shifts the peak amplitude to earlier times. Additionally, the maximum current might not fully develop, since a significant number of channels start to inactivate before all channels are opened. Therefore, the maximum currents are lower than theoretically possible for fast inactivating variants. This effect is diminished when KChIP is co-expressed. Here, the inactivation is slowed and the majority of channels opens before a significant amount of channels closes. In addition to altered activation and inactivation kinetics, other factors influence the macroscopic current peak amplitude. We did not examine if larger peak currents in longer DPP6 variants (D484X and longer) are due to an increased number of channel complexes in the plasma membrane, an increased single channel conductance (γ) or a combination of the two. It was shown that full-length DPP6 almost doubles Kv4.2's unitary conduction from ~4 pS to ~7.5 pS, which depends on two negatively charged amino acids at the N-terminus of the DPP6 subunit (45). These residues have been hypothesized to form a ring of eight negatively charged amino acids when the channel complex comprises four DPP6 subunits. This negatively charged ring, in turn, is proposed to increase the local K^+ concentration at the internal mouth of the channel pore. It would be worthwhile investigating if the increase in γ, as hypothesized, depends on the number of DPP6 subunits in the complex. Such a dependence on the number of subunits would also support our hypothesis that C-terminally truncated DPP6 fail to multimerize as efficiently as full-length DPP6 subunits, which then manifests itself as reduced peak current amplitudes for shorter truncations. Single channel patch clamp recordings of concatemeric Kv4/DPP6 constructs and Kv4.2 in the presence of our progressively truncated DPP6 variants, could demonstrate if the increase in unitary conductance depends on the number of DPP6 subunits bound to the channel complex and if the stoichiometry and single channel conduction depend on DPP6's extracellular domain.

Future studies will have to identify the structural details of how the DPP6's extracellular domain destabilizes the open channel state. While finding answers to this question is of great academic interest, rational drug design could also benefit from such an advancement of knowledge. For now, treating malfunctioning Kv4 channels is challenging, since they are ubiquitously expressed, so that many potential treatments would cause severe side effects. Identifying specific, and tissue specific, modulation mechanisms could then translate to developing very specific pharmaceuticals. To this aim, VCF experiments could be exploited to study dynamic structure function relations. While chapter five presented VCF experiments as a tool to examine the presence of DPP6, this technique allows to correlate functional and fluorescence kinetic data. Observing similar kinetics then suggests that the movement observed by the fluorescence change is associated to the functional event. However, interpreting such data remains difficult, as one cannot easily determine if the change in fluorescence is a cause or effect of the functional event. Nevertheless, this technique has been applied successfully to study structure function relations in ion channels (46-51). Employing such a strategy to study changes in the presence and absence of DPP6 could drastically advance our understanding on how exactly this auxiliary subunit affects the gating mechanism and potentially help identifying new therapeutic treatments for DPP6 related neurological and cardiac diseases (52-57).

6.4 Concluding Remarks

The work presented in this thesis portrays the fundamental structural investigation of diverse biological ion channel complexes. We investigated the oligomeric state of the novel TACAN channel (chapter four), the stoichiometry of heteromeric Kv2.1/6.4 channel complexes (chapter three) and the structure-function relation of Kv4.2 channels with their tissue-specific modulatory DPP6 subunits (chapter five).

Through our research, we gained new insights into how these ion channel complexes assemble and how they are modulated by α- and β-subunits. To our knowledge, we are the first to report a structural investigation of the mechanosensitive channel TACAN. Here, we determined the oligomeric state of the homomeric channel. Understanding how many subunits are comprised in a biological assembly lays an important foundation to then investigate how these complexes

function in their most basic configuration, before potential modulatory α- and/or β-subunits alter the channel function. Such modulations of channels was studied in the third and fifth chapter. In the former, we investigated modulatory α-subunits that contribute to the pore-forming complex and showed that the architecture of heteromeric Kv2/KvS channels is more variable than previously believed. The ability of Kv2 to incorporate not only one (3), but also two modulatory subunits ultimately adds to a greater diversity of channel configurations and modulation. However, many ion channel complexes are not only modulated by pore-forming α-subunits, but also by binding to auxiliary β-subunits, which alter the channel function through distinct allosteric interactions. We investigated the modulatory effect of the β-subunit DPP6 in Kv4.2 channel complexes. To better understand the molecular mechanisms, we examined the function of distinct DPP6 subunit domains and showed that not only the N-terminal domain and transmembrane helix are important for the modulatory function (36, 37), but also the extracellular domain. These three projects were primarily of academic interest, but we hope that the deeper understanding of these ion channel assemblies will help future scientists to solve unanswered questions, especially in respect to ion channel related diseases.

Although we studied distinct channel complexes from the two fields of mechanosensitive and voltage-gated ion channels, we observe some common themes. Finding tetrameric TACAN channels raised the question if these channels assemble via the same pathway as other tetrameric protein complexes, including Kv channels, that are formed as dimers of dimers (1). Our discussion on DPP6 assembly also lead to the question if, in the plasma membrane, DPPL auxiliary subunits are added to the tetrameric Kv4.2 channel as multiples of dimers. To determine why the dimer of dimer tetramerization pathway is dominant in homotetramer formation, Powers and Powers modeled the kinetics of tetramerization (58). They found that a tetramerization pathway that successively adds monomers to the complex results in the accumulation of non-tetrameric intermediates and argued that these intermediates could be harmful to the organism, so that the dimer of dimer pathway evolved as the dominant tetramerization pathway (58). Interestingly, we found a significant amount of TACAN subunits trapped in the intracellular compartment of the cell. It remains uncertain, if these subunits are trapped due to an ER-retention signal or due to misfolding. Maybe these untrafficked complexes are such non-tetrameric intermediates that

accumulate during the complex formation. Rather than being detrimental to the organism, such intracellular, possibly non-tetrameric, TACAN complexes might have adopted a second function which remains unknown. Likewise, DPP6 might serve several functions, as it is expressed in the plasma membrane even in the absence of Kv4 channels (39, 59, 60).

Although the work presented in this thesis primarily investigates the structure of channel complexes, the discussion led to questions about channel stability. We reported that purified, solubilized TACAN channels disintegrate into lower oligomeric complexes and argued that the lateral pressure of the native lipid environment is important to keep the complex stable. Additionally, we raised the question whether not only the transmembrane helices but also the N-terminal TACAN domains, similar to the T1 domains in potassium channels, are involved in intersubunit interactions. For now, the interaction interfaces between the subunits as well as the function of the N-terminal TACAN domain remain unidentified. If the N-terminal domain does not contribute to the channel stability by increasing the intersubunit interaction sites, it might still stabilize the channel in its native environment through interactions with other molecules. Similarly, DPP6 interacts with the extracellular matrix, which anchors the channel complex in the membrane stabilizing it further (34). Like Kv channels, TACAN might interact with auxiliary subunits that have not been identified yet. These potential auxiliary subunits might help stabilizing the complex under physiological conditions. Especially subunits that interact with the α-subunits as well as with themselves could increase channel complex stability. We proposed that DPP6 adopts such a bracket-like arrangement by interacting with the channel via the transmembrane helix and with other DPP6 subunits through the propeller domain. We hypothesized that truncated DPP6 subunits with short extracellular domains fail to oligomerize, which could result in less stable channel complexes compared to complexes that comprise full-length DPP6 subunits.

A feature that appears to be shared between distinct protein assemblies is the progressive alteration of their function by modulatory subunits. In chapter three, the research performed by our collaborators showed that the progressive incorporation of Kv6.4 subunits into Kv2.1 channels shifts the gating properties stepwise. Similarly, DPP6 binding to Kv4.2 channels is proposed to alter the channel properties incrementally (38). This is interesting, as it suggest that

the modulatory effect could be fine-tuned depending on the expression level of the modulatory subunits. It remains unclear if this is a regulatory mechanism found under physiological conditions. One argument against this was presented by our SSC results obtained for Kv2.1/6.4 heteromers which preferentially formed 2:2 arrangements independent of the relative cRNA amount injected. However, other factor might be important too, such as preferential retrograde trafficking of a distinct channel assembly or preferential trafficking to the plasma membrane for example aided by auxiliary subunits. Opposed to the progressive alteration of channel function by modulatory subunits, the potassium channel α-subunits act cooperatively during gating. Here all four voltage sensors need to be activated for the channel to open, rather than opening the channel step by step with the activation of each individual voltage sensor (61-63). A multitude of allosteric interactions govern channel gating and future research will need to elucidate the underlying molecular mechanisms.

Fundamental research performed *ex vivo* or in heterologous expression systems, as presented in this thesis, remains crucial for better understanding biological assemblies and their modulation in a more controlled environment. Building on this foundation, future research can be designed to be more and more complex. Ultimately, studies performed in native environments, where channel assemblies are most stable and potential modulatory subunits are present, will contribute to better understanding complex interactions of macromolecular complexes.

6.5 References

1. L. Tu, C. Deutsch, Evidence for dimerization of dimers in K+ channel assembly. *Biophys J* **76**, 2004-2017 (1999).
2. J. P. David, J. I. Stas, N. Schmitt, E. Bocksteins, Auxiliary KCNE subunits modulate both homotetrameric Kv2.1 and heterotetrameric Kv2.1/Kv6.4 channels. *Sci Rep* **5**, 12813 (2015).
3. D. Kerschensteiner, F. Soto, M. Stocker, Fluorescence measurements reveal stoichiometry of K+ channels formed by modulatory and delayed rectifier alpha-subunits. *Proc Natl Acad Sci U S A* **102**, 6160-6165 (2005).
4. J. Zheng, M. C. Trudeau, W. N. Zagotta, Rod cyclic nucleotide-gated channels have a stoichiometry of three CNGA1 subunits and one CNGB1 subunit. *Neuron* **36**, 891-896 (2002).
5. K. M. O'Connell, R. Loftus, M. M. Tamkun, Localization-dependent activity of the Kv2.1 delayed-rectifier K+ channel. *Proc Natl Acad Sci U S A* **107**, 12351-12356 (2010).
6. N. C. Shaner *et al.*, A bright monomeric green fluorescent protein derived from Branchiostoma lanceolatum. *Nat Methods* **10**, 407-409 (2013).
7. L. Hostettler *et al.*, The Bright Fluorescent Protein mNeonGreen Facilitates Protein Expression Analysis In Vivo. *G3 (Bethesda)* **7**, 607-615 (2017).
8. V. Dunsing *et al.*, Optimal fluorescent protein tags for quantifying protein oligomerization in living cells. *Sci Rep* **8**, 10634 (2018).
9. A. G. Godin *et al.*, Spatial Intensity Distribution Analysis Reveals Abnormal Oligomerization of Proteins in Single Cells. *Biophys J* **109**, 710-721 (2015).
10. M. H. Ulbrich, E. Y. Isacoff, Subunit counting in membrane-bound proteins. *Nat Methods* **4**, 319-321 (2007).
11. N. Durisic *et al.*, Stoichiometry of the human glycine receptor revealed by direct subunit counting. *J Neurosci* **32**, 12915-12920 (2012).
12. H. McGuire, M. R. Aurousseau, D. Bowie, R. Blunck, Automating single subunit counting of membrane proteins in mammalian cells. *J Biol Chem* **287**, 35912-35921 (2012).
13. Y. Lussier *et al.*, Disease-linked mutations alter the stoichiometries of HCN-KCNE2 complexes. *Sci Rep* **9**, 9113 (2019).
14. N. Groulx, H. McGuire, R. Laprade, J. L. Schwartz, R. Blunck, Single molecule fluorescence study of the Bacillus thuringiensis toxin Cry1Aa reveals tetramerization. *J Biol Chem* **286**, 42274-42282 (2011).
15. R. Blunck, D. M. Starace, A. M. Correa, F. Bezanilla, Detecting rearrangements of shaker and NaChBac in real-time with fluorescence spectroscopy in patch-clamped mammalian cells. *Biophys J* **86**, 3966-3980 (2004).

16. R. Pantoja, E. A. Rodriguez, M. I. Dibas, D. A. Dougherty, H. A. Lester, Single-molecule imaging of a fluorescent unnatural amino acid incorporated into nicotinic receptors. *Biophys J* **96**, 226-237 (2009).

17. M. J. Levene *et al.*, Zero-mode waveguides for single-molecule analysis at high concentrations. *Science* **299**, 682-686 (2003).

18. J. Korlach, S. W. Turner, "Zero-Mode Waveguides" in Encyclopedia of Biophysics, G. C. K. Roberts, Ed. (Springer Berlin Heidelberg, Berlin, Heidelberg, 2013), 10.1007/978-3-642-16712-6_499, pp. 2793-2795.

19. C. I. Richards *et al.*, Live-cell imaging of single receptor composition using zero-mode waveguide nanostructures. *Nano Lett* **12**, 3690-3694 (2012).

20. C. Pliotas *et al.*, The role of lipids in mechanosensation. *Nat Struct Mol Biol* **22**, 991-998 (2015).

21. B. Reddy, N. Bavi, A. Lu, Y. Park, E. Perozo, Molecular basis of force-from-lipids gating in the mechanosensitive channel MscS. *Elife* **8** (2019).

22. K. M. Callenberg, N. R. Latorraca, M. Grabe, Membrane bending is critical for the stability of voltage sensor segments in the membrane. *J Gen Physiol* **140**, 55-68 (2012).

23. W. R. Kobertz, C. Williams, C. Miller, Hanging gondola structure of the T1 domain in a voltage-gated K(+) channel. *Biochemistry* **39**, 10347-10352 (2000).

24. L. Beaulieu-Laroche *et al.*, TACAN Is an Ion Channel Involved in Sensing Mechanical Pain. *Cell* **180**, 956-967 e917 (2020).

25. M. A. Schuler, I. G. Denisov, S. G. Sligar, Nanodiscs as a new tool to examine lipid-protein interactions. *Methods Mol Biol* **974**, 415-433 (2013).

26. C. Tribet, R. Audebert, J. L. Popot, Amphipols: polymers that keep membrane proteins soluble in aqueous solutions. *Proc Natl Acad Sci U S A* **93**, 15047-15050 (1996).

27. C. Manzo, M. F. Garcia-Parajo, A review of progress in single particle tracking: from methods to biophysical insights. *Rep Prog Phys* **78**, 124601 (2015).

28. A. Kusumi *et al.*, Paradigm shift of the plasma membrane concept from the two-dimensional continuum fluid to the partitioned fluid: high-speed single-molecule tracking of membrane molecules. *Annu Rev Biophys Biomol Struct* **34**, 351-378 (2005).

29. H. Shen *et al.*, Single Particle Tracking: From Theory to Biophysical Applications. *Chem Rev* **117**, 7331-7376 (2017).

30. S. Hou, J. Exell, K. Welsher, Real-time 3D single molecule tracking. *Nat Commun* **11**, 3607 (2020).

31. H. P. Koch *et al.*, Multimeric nature of voltage-gated proton channels. *Proc Natl Acad Sci U S A* **105**, 9111-9116 (2008).

32. S. Y. Lee, J. A. Letts, R. Mackinnon, Dimeric subunit stoichiometry of the human voltage-dependent proton channel Hv1. *Proc Natl Acad Sci U S A* **105**, 7692-7695 (2008).

33. F. Tombola, M. H. Ulbrich, E. Y. Isacoff, The voltage-gated proton channel Hv1 has two pores, each controlled by one voltage sensor. *Neuron* **58**, 546-556 (2008).

34. L. Lin *et al.*, DPP6 regulation of dendritic morphogenesis impacts hippocampal synaptic development. *Nat Commun* **4**, 2270 (2013).

35. L. Lin, L. K. Long, M. M. Hatch, D. A. Hoffman, DPP6 domains responsible for its localization and function. *J Biol Chem* **289**, 32153-32165 (2014).

36. K. Dougherty, M. Covarrubias, A dipeptidyl aminopeptidase-like protein remodels gating charge dynamics in Kv4.2 channels. *J Gen Physiol* **128**, 745-753 (2006).

37. H. H. Jerng, K. Dougherty, M. Covarrubias, P. J. Pfaffinger, A novel N-terminal motif of dipeptidyl peptidase-like proteins produces rapid inactivation of KV4.2 channels by a pore-blocking mechanism. *Channels (Austin)* **3**, 448-461 (2009).

38. H. Soh, S. A. Goldstein, I SA channel complexes include four subunits each of DPP6 and Kv4.2. *J Biol Chem* **283**, 15072-15077 (2008).

39. M. Kitazawa, Y. Kubo, K. Nakajo, Kv4.2 and accessory dipeptidyl peptidase-like protein 10 (DPP10) subunit preferentially form a 4:2 (Kv4.2:DPP10) channel complex. *J Biol Chem* **290**, 22724-22733 (2015).

40. K. Dougherty, J. A. De Santiago-Castillo, M. Covarrubias, Gating charge immobilization in Kv4.2 channels: the basis of closed-state inactivation. *J Gen Physiol* **131**, 257-273 (2008).

41. M. Kitazawa, Y. Kubo, K. Nakajo, The stoichiometry and biophysical properties of the Kv4 potassium channel complex with K+ channel-interacting protein (KChIP) subunits are variable, depending on the relative expression level. *J Biol Chem* **289**, 17597-17609 (2014).

42. P. Strop, A. J. Bankovich, K. C. Hansen, K. C. Garcia, A. T. Brunger, Structure of a human A-type potassium channel interacting protein DPPX, a member of the dipeptidyl aminopeptidase family. *J Mol Biol* **343**, 1055-1065 (2004).

43. M. Morin (2019) Étude numérique de la formation du complexe protéique formé du canal potassique humain Kv4.2 et de sa sous-unité bêta DPP6.2. in *Physics* (Université de Montréal, Montreal).

44. J. R. Lakowicz, *Principles of fluorescence spectroscopy* (Springer Science+Business Media,LLC, New York, USA, ed. 3, 2006).

45. Y. A. Kaulin *et al.*, The dipeptidyl-peptidase-like protein DPP6 determines the unitary conductance of neuronal Kv4.2 channels. *J Neurosci* **29**, 3242-3251 (2009).

46. Z. Batulan, G. A. Haddad, R. Blunck, An intersubunit interaction between S4-S5 linker and S6 is responsible for the slow off-gating component in Shaker K+ channels. *J Biol Chem* **285**, 14005-14019 (2010).

47. T. Kalstrup, R. Blunck, Dynamics of internal pore opening in K(V) channels probed by a fluorescent unnatural amino acid. *Proc Natl Acad Sci U S A* **110**, 8272-8277 (2013).

48. T. Kalstrup, R. Blunck, S4-S5 linker movement during activation and inactivation in voltage-gated K(+) channels. *Proc Natl Acad Sci U S A* **115**, E6751-E6759 (2018).

49. A. Cha, F. Bezanilla, Characterizing voltage-dependent conformational changes in the Shaker K+ channel with fluorescence. *Neuron* **19**, 1127-1140 (1997).

50. L. M. Mannuzzu, M. M. Moronne, E. Y. Isacoff, Direct physical measure of conformational rearrangement underlying potassium channel gating. *Science* **271**, 213-216 (1996).

51. A. Pantazis, N. Savalli, D. Sigg, A. Neely, R. Olcese, Functional heterogeneity of the four voltage sensors of a human L-type calcium channel. *Proc Natl Acad Sci U S A* **111**, 18381-18386 (2014).

52. L. Lin *et al.*, DPP6 Loss Impacts Hippocampal Synaptic Development and Induces Behavioral Impairments in Recognition, Learning and Memory. *Front Cell Neurosci* **12**, 84 (2018).

53. C. Liao *et al.*, Loss-of-function variation in the DPP6 gene is associated with autosomal dominant microcephaly and mental retardation. *Eur J Med Genet* **56**, 484-489 (2013).

54. S. Girirajan *et al.*, Refinement and discovery of new hotspots of copy-number variation associated with autism spectrum disorder. *Am J Hum Genet* **92**, 221-237 (2013).

55. C. R. Marshall *et al.*, Structural variation of chromosomes in autism spectrum disorder. *Am J Hum Genet* **82**, 477-488 (2008).

56. M. Alders *et al.*, Haplotype-sharing analysis implicates chromosome 7q36 harboring DPP6 in familial idiopathic ventricular fibrillation. *Am J Hum Genet* **84**, 468-476 (2009).

57. D. B. Ding *et al.*, A novel mutation of dipeptidyl aminopeptidase-like protein-6 in a family with suspicious idiopathic ventricular fibrillation. *QJM* **111**, 373-377 (2018).

58. E. T. Powers, D. L. Powers, A perspective on mechanisms of protein tetramer formation. *Biophys J* **85**, 3587-3599 (2003).

59. B. D. Clark *et al.*, DPP6 Localization in Brain Supports Function as a Kv4 Channel Associated Protein. *Front Mol Neurosci* **1**, 8 (2008).

60. X. Ren, Y. Hayashi, N. Yoshimura, K. Takimoto, Transmembrane interaction mediates complex formation between peptidase homologues and Kv4 channels. *Mol Cell Neurosci* **29**, 320-332 (2005).

61. J. L. Ledwell, R. W. Aldrich, Mutations in the S4 region isolate the final voltage-dependent cooperative step in potassium channel activation. *J Gen Physiol* **113**, 389-414 (1999).

62. M. Pathak, L. Kurtz, F. Tombola, E. Isacoff, The cooperative voltage sensor motion that gates a potassium channel. *J Gen Physiol* **125**, 57-69 (2005).

63. W. N. Zagotta, T. Hoshi, R. W. Aldrich, Shaker potassium channel gating. III: Evaluation of kinetic models for activation. *J Gen Physiol* **103**, 321-362 (1994).